# SHEAR STRENGTH AND BEHAVIOR OF FLAT SLAB STRUCTURES REINFORCED WITH HEADED SHEAR STUDS

**by**

**Thai Xuan Dam**

**A dissertation submitted in partial fulfillment**
**of the requirements of the degree of**
**Doctor of Philosophy**
**(Civil Engineering)**
**in the University of Michigan**
**2016**

**Doctoral Committee:**

**Professor James K. Wight, Chair**
**Professor James R. Barber**
**Associate Professor Jason P. McCormick**
**Professor Gustavo J. Parra-Montesinos, University of Wisconsin - Madison**
**Professor Sherif El-Tawil**

# DEDICATION

To my beloved family members

for their boundless love and support

# ACKNOWLEDGEMENTS

I would like to express the deepest appreciation to Professor James K. Wight and Professor Gustavo J. Parra-Montesinos, co-chairs of my doctoral thesis committee, for their invaluable guidance and support throughout this study. Without their guidance and persistent help, this dissertation would not have been possible.

I would also like to thank the other members in my doctoral thesis committee, Professor Sherif El-Tawil, Professor Jason P. McCormick, and Professor James R. Barber for offering helpful comments and advice throughout this study.

I would like to thank the Vietnam Education Foundation Fellowship Program and The University of Michigan for the financial supports for this study. I would also like to acknowledge Neil Hammill at Decon USA for his donation of the shear studs used in this study.

I would also like to thank the technicians in the Structures Laboratory, Robert Spence, Robert Fisher, and Jan Pantolin for their useful suggestions and help during the laboratory work. Sincere thanks are due to Alex DaCosta, Matt Fadden, Xiaohu Fan, Antonio Conforti, Zhichao Liu, and specially Monthian Setkit and Hamza Bilal for their help on the experimental work.

Last but not least, I would especially like to thank my family members, including my mom, Thanh Vu, my parents-in-law Hung Pham and Duyen Than, my beloved wife Hanh Pham, my adorable son Nam Dam and daughter Anh Dam, and my brothers Trinh Dam, Hoang Dao, Thang Pham, and Tung Le for their endless love, encouragement, and support.

# TABLE OF CONTENTS

# LIST OF TABLES

# LIST OF FIGURES

# LIST OF APPENDICES

# LIST OF ACRONYMS

| | |
|---|---|
| ACI | = Amecican Concrete Insitute |
| ACI 318 | = Building Code Requirements for Structural Concrete and Commentary |
| CAN/CSA | = Canadian Building Code / Canadian Standards Association |
| EC 2 | = European Building Code |
| FIB | = Fédération Internationale du Béton |
| ABAQUS/CAE | = ABAQUS Complete Abaqus Environment |
| F.E. | = Finite Element |
| CDP | = Concrete Damaged Plasticity |

# LIST OF NOTATIONS

$b$ = perimeter of a loaded area (in. or mm)

$b_0$ = perimeter of critical section (in. or mm)

$c$ = distance from the centroid of the critical shear-perimeter to the location where $v_u$ is being calculated (in. or mm)

$c_1$ = dimension of column measured in the direction of the span under consideration (in. or mm)

$c_2$ = dimension of column perpendicular to dimension $c_1$ (in. or mm)

$d$ = effective depth of slab (in. or mm) — distance from extreme compression fiber to centroid of longitudinal tension reinforcement

$d_b$ = diameter of reinforcement bars or shear studs

$d_c$ = diameter of a circle column (in. or mm)

$f_c'$ = compressive strength of concrete (psi or MPa)

$\sqrt{f_c'}$ = square root of compressive strength of concrete (psi or MPa)

$f_t$ = tensile strength of concrete (psi or MPa)

$f_y$ = yield strength of flexural reinforcement (psi or MPa)

$f_{yt}$ = yield strength of shear studs (psi or MPa)

$h_c$ = dimension of a square column (in. or mm)

$h_v$ = height of shearhead (in. or mm)

$jd$ = distance from the centroid of compression area to the centroid of tension reinforcement (in. or mm)

$l$ = span of isolated slab-column specimens (in. or mm), distance between the centers of two opposite supports about the center of the slab

$l_v$ = length of shearhead arms (in. or mm)

$L$ = average span of flat plate system (in. or mm), distance between the centers of adjacent columns

$m_r$ = radial bending moment component in slabs (lb-in./in. or N-m/m)

$M_u$ = factored moment being transferred at slab-column connections (lb-in. or N-m)

$m_\theta$ = tangential bending moment component in slabs (lb-in./in. or N-m/m)

$n$ = proportion of slab flexural tension reinforcement that placed across the column

$n_a$ = number of arms in a shearhead system

$q$ = uniform load on slabs (psf or kN/m$^2$)

$r$ = radial direction (axis) in the cylindrical coordinate system

$s$ = spacing between reinforcement bars or shear studs (in. or mm)

$s_0$ = spacing between the first row of shear studs and column faces or corners (in. or mm)

$t$ = thickness of slab (in. or mm)

$v$ = shear stress computed at critical section due to shear force $V$ (psi or MPa)

$v_c$ = shear strength, expressed as a stress, corresponding to $V_c$ (psi or MPa)

$v_n$ = nominal shear strength, expressed as a stress (psi or MPa)

$v_s$ = shear strength, expressed as a stress, corresponding to $V_s$ (psi or MPa)

$v_u$ = shear stress due to factor loads (psi or MPa)

$z$ = vertical axis in the cylindrical coordinate system

$J_c$ = an effective polar moment of inertia for the critical section (in.$^4$ or mm$^4$)

$M_p$ = plastic flexural strength of shearhead arms (lb-in. or N-m)

$V$ = concentric shear force transfer at slab-column connections (lb or kN)

$V_c$ = nominal shear strength provided by concrete (lb or kN)

$V_n$ = nominal shear strength (lb or kN)

$V_s$ = nominal shear strength provided by shear studs (lb or kN)

$V_u$ = factored shear being transferred at slab-column connections (lb or kN)

$\alpha_s$ = constant used to indicate the location of slab-column connections

$\alpha_v$ = relative flexural stiffness of a shearhead arm to surrounding slab regions

$\beta$ = ratio of long-side to short-side dimensions of a rectangular column

$\lambda$ = the factor for lightweight-aggregate concrete

$\theta$ = tangential direction (axis) in the cylindrical coordinate system

$\phi$ = strength reduction factor

$\gamma_v$ = fraction of the moment transferred by shear stresses on the critical section

# CHAPTER 1
# INTRODUCTION

## 1.1 BACKGROUND AND MOTIVATION

### 1.1.1 Research Background

In the history of reinforced concrete structures, the first flat slabs are believed to have been invented and built by Claude A. P. Turner in America[1, 2], and by Robert Maillart in Switzerland[3] in the early 20th century. These first flat slabs, as shown in Fig. 1-1, were called mushroom slabs because the top of the columns was flared out to support the slabs directly without the use of joist (beam) and girder systems. Flat slab structures are economical and highly efficient in terms of optimizing interior space and minimizing story height due to the absence of beam systems, and thus they have been widely used all over the world.


a) by Claude A. P. Turner (1869-1955) b) by Robert Maillart (1872-1940)

*Fig. 1-1: Flat slab structures (mushroom slabs) built in 1900s*

*(a) J. Hoffmann warehouse, Milwaukee, Wisconsin[2] and (b)Warehouse Giesshübel in Zürich, Switzerland (Photograph courtesy of Хрюша at wikipedia.org)*

For industrial slabs, which often support heavy loads in excess of 100 psf and have spans of 20 to 30 ft, column capitals and/or drop panels (Fig. 1-2a) are often used to increase shear

strength and stiffness of slab regions near columns. For slabs that support relatively light loads, e.g. slabs in apartments or similar buildings, they can be supported directly by columns without drop panels or column capitals (Fig. 1-2b). These systems, referred to as flat plates, significantly reduce the cost of formwork and expedite construction, and thus, they are preferred in modern construction.

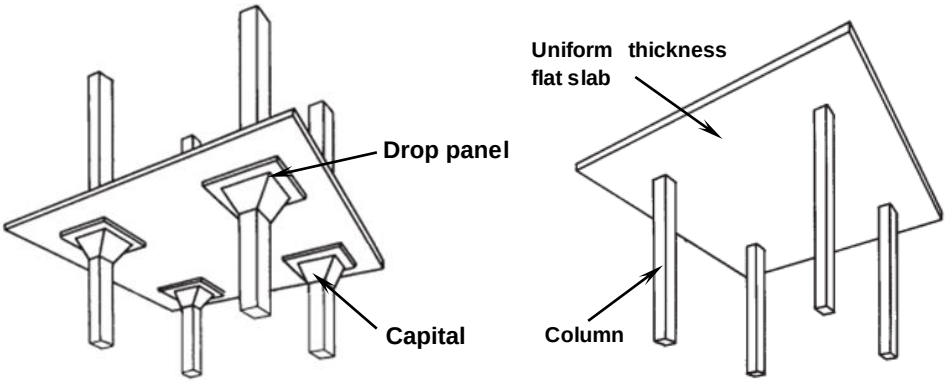


*a) Flat slab with drop panels and capitals* *b) Flat plate*

*Fig. 1-2: Flat slab systems[3]*

In design of flat plate systems, structural engineers must consider two major problems: 1) large deflections at midspan of the slabs and 2) punching shear failure at column-to-slab connections. The former problem is often associated with long-span slab systems, in which the slab thickness is designed to be relatively thin to lower the self-weight of slabs. The reduction in slab thickness, on the other hand, reduces the flexural stiffness of slab systems, and thus, increases vertical deflections at midspan. To deal with this issue, prestressing methods[4] are often used to control the vertical deflections of slabs. The other problem associated with flat plate systems is more complicated. Although punching shear failure, a three-dimensional shear failure in slab regions near the supporting column, has been extensively studied for a century, no theoretical treatment for this failure is generally accepted. Most Building Codes, such as the ACI 318[5], Eurocode 2[6], and CAN/CSA A23.3[7], thus use empirical or semi-empirical approaches for shear design of slab-column connections. This research investigation studies the punching shear failure problem and compares test results with design recommendations in the ACI Building Code[5].

The development of a punching shear failure at slab-column connections may be similar to web-shear failures in beams[8, 9]. Shear force and moment transfer at a slab-column connection

results in high shear stresses near the mid-depth of the slab region around the column. When the principle tensile stress at these locations reaches the tensile strength of the concrete, shear (or inclined) cracks are initiated. The inclined cracks then extend upward to the top of the slab and downward to the edge of the supporting area, as shown in Fig. 1-3 (a). The inclined cracks propagate around the column to form a truncated cone (Fig. 1-3b), and a failure takes place when the inclined crack surface separates the slab completely from the column.

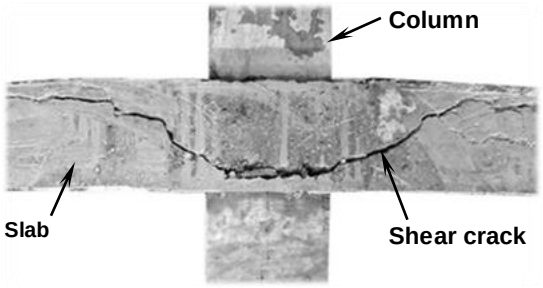


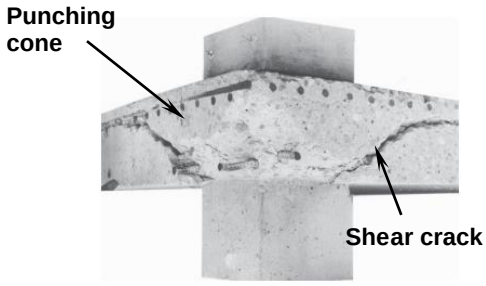


*a) Shear cracks in a cut section near a column* *b) 3-D view of failure surface*[3]

*Fig. 1-3: Punching shear failure*

Punching shear failures are brittle in nature and may lead to the collapse of the entire floor system. Load redistribution in the floor system after an initial punching shear failure may cause an overload at adjacent slab-column connections, and these connections may also fail due to punching shear. These sequential failures at slab-column connections may result in the collapse of all or most of the floor system, as shown in Fig. 1-4.

The shear strength of slab-column connections can be increased by using higher strength concrete, larger column sections, thicker slabs, and/or shear reinforcement. Shear reinforcement is placed vertically in slab regions around the column to control the opening and growth of inclined cracks and provide additional shear strength to slab-column connections. The ACI Code[5] permits the use of different types of shear reinforcement for slabs, including single- or multiple-leg stirrups, shearheads, and headed shear studs. In modern construction, headed shear studs are often preferred because, compared with other shear reinforcement, they have less interference with slab flexural reinforcement.

a) b)

*Fig. 1-4: Collapse of flat plate buildings due to punching shear failure*

*a) Pipers Row parking, Wolverhampton, UK, 1997*[10]

*b) Eaton Place parking, Christchurch CBD, New Zealand. 2011*[11]

Headed shear studs are usually welded to a steel plate to facilitate installation (Fig. 1-5), and this assembly is normally referred to as a stud rail[12, 13]. In North America, stud rails are typically placed in an orthogonal (or cruciform) layout around the columns, as shown in Fig. 1-6 (a), to reduce interferences with slab flexural reinforcement. In this layout, shear studs are arranged in orthogonal strips that extend out from column faces and are parallel to the principle directions of slab flexural reinforcement. The ACI Code[5] specifies the maxium spacing between peripheral lines of shear studs and the distance from the column faces to the first line of studs, so the shear studs should cross any potential inclined crack. The ACI Code also specifies that spacing between two adjacent parallel stud rails should be smaller than $2d$ ($d$ is the effective flexural depth of the slab), so slab regions between these stud rails are effectively reinforced by the adjacent shear studs.

*Fig. 1-5: A rail of headed shear studs (stud rail)*[14]

### 1.1.2 Research Motivation

A potential issue with an orthogonal layout of shear studs is that large regions of the slab extending out from the corners of the columns may be essentially unreinforced in shear. As shown in Fig. 1-6 (a), the distance measured in the diagonal directions between two adjacent studs for the outermost peripheral line of shear studs may significantly exceed $2d$ as the length of the stud rails increase. Thus, the slab regions between those shear studs are essentially unreinforced in shear. The ACI Code[5] defines the perimeter ($b_0$) for the outer critical section as a continuous polygon that is located $d/2$ beyond the outermost peripheral line of shear studs (Fig. 1-6a). Consequently, for an orthogonal stud layout, the perimeter of the outer critical section may include some slab regions that are essentially unreinforced in shear. This issue can be addressed by placing stud rails that project radially out from the corners of the column (Fig. 1-6b), referred to as a radial layout.

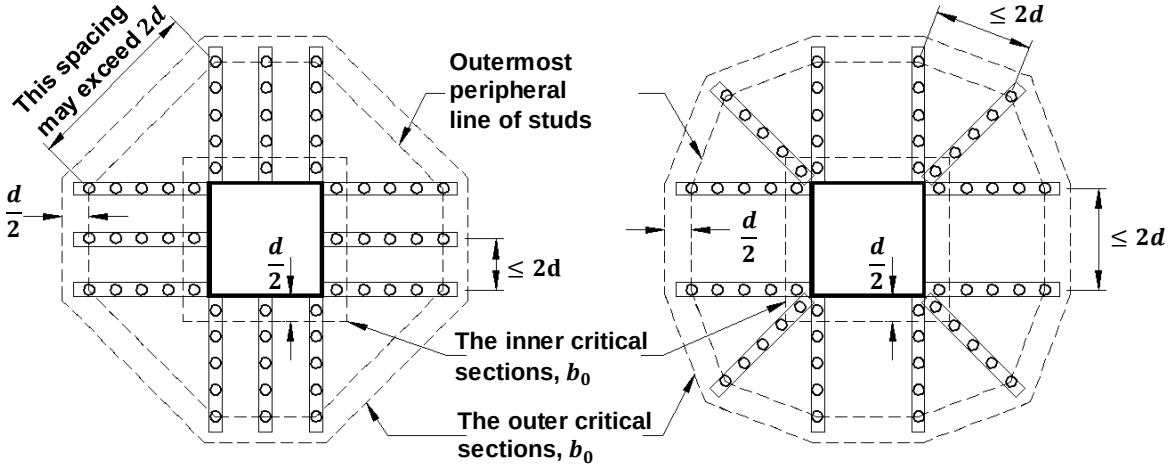


*a) an orthogonal layout* *b) a radial layout*

*Fig. 1-6: Configurations of shear studs and critical sections for internal columns*

Research investigations have been conducted to assess the effect of a radial layout versus an orthogonal layout of shear studs on the behavior and shear strength of slab-column connections, but the results have been conflicting. Test results reported by Birkle and Dilger[15], and Ferreira et al[16] indicated that shear strength of slab-column connections with shear studs arranged in either a radial or orthogonal layout are similar. However, other research investigations conducted by Broms[17] and DaCosta and Parra-Montesinos[18] have indicated that there is a significant difference in behavior and shear strength of slab-column connections where shear studs are used

in either an orthogonal or radial layout. Test results reported by those researchers[17, 18] showed that 1) an orthogonal layout of shear studs provided lower shear strength and less ductility to slab-column connections than a radial stud layout and 2) measured shear strength for the test specimens was substantially lower than the corresponding nominal shear strength given by the ACI Code[5].

Test results reported by Broms[17] and DaCosta and Parra-Montesinos[18] have raised major concerns over the safety of flat plate systems that have been built with headed shear stud reinforcement in North America. The apparently conflicting research results have also indicated that the percentage of flexural reinforcement in slab regions near the columns may have a significant effect on shear failures of slab-column connections. For public safety, additional investigations of the behavior and shear strength of slab-column connections reinforced with shear studs are required.

## 1.2 OBJECTIVES

The main objectives of this research investigation were to evaluate: 1) the shear strength of gravity-loaded reinforced concrete slab-column connections with or without headed shear stud reinforcement; and 2) the effects of different layouts of headed shear studs and the percentage of slab flexural reinforcement on the behavior and shear strength of slab-column connections.

To accomplish these research objectives, five full-scale interior slab-column connections were tested to failure under simulated gravity loading. Test specimens were simply supported along the edge of the slab to simulate the contra-flexural line (zero bending moment) around the column in a flat plate system. The primary parameters for the tests were the average slab flexural reinforcement ratio (0.87% and 1.25%) and the layout of shear studs (radial or orthogonal layout).

Apart from the experimental study, three-dimensional finite element models were developed to simulate the behavior of reinforced concrete slab-column connections tested in this research investigation. The finite element program ABAQUS/CAE[19] was used because it offers convenient methods to simulate the interaction between reinforcement and concrete in three-dimensional models. The finite element models developed for this investigation were useful for

evaluating the effect of other parameters on the behavior and shear strength of reinforced concrete slab-column connections.

## 1.3 ORGANIZATION OF THESIS

This thesis is organized into six chapters. Chapter 1 presents an introduction and the objectives of the study. A literature review of previous work related to this study is provided in Chapter 2. The experimental program is presented in Chapter 3, including the design of test specimens, construction of specimens, loading method, and other test-related aspects. Results from the tests of five slab-column connections described in Chapter 3 are evaluated in Chapter 4. Comparisons between results from the test specimens in this study and prior research investigations and design recommendations for reinforced concrete slab-column connections are presented in Chapter 5. Chapter 6 presents finite element modeling of the test specimens and simulation results. Conclusions and recommendations derived from this research investigation are given in Chapter 7.

# CHAPTER 2
# LITERATURE REVIEW

This chapter presents an overview of different topics related to this research investigation. First, background information is presented in Section 2.1. Then, the ACI Code provisions for two-way shear in slabs are reviewed in Section 2.2. After that, Sections 2.3 and 2.4 discuss the effects of different shear stud layouts and the slab flexural reinforcement ratio on the behavior and shear strength of slab-column connections. The effects of other factors are presented in Section 2.5, and lastly, finite element modeling of slab-column connections is reviewed in Section 2.6.

## 2.1 BACKGROUND

### 2.1.1 Typical Cracks in Slab Regions near Columns

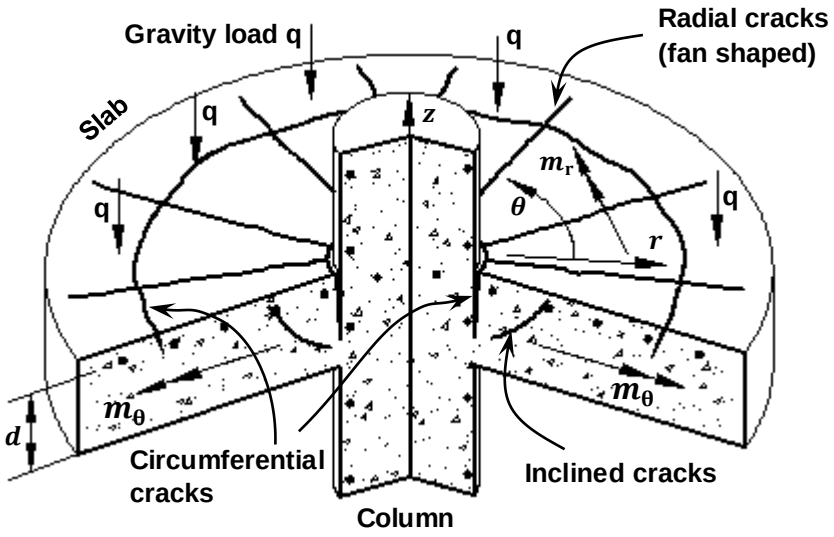


*Fig. 2-1: Typical cracks and bending moments at slab-column connections*[20]

Typical cracks in slab regions near the supporting column include flexural and inclined (shear) cracks, as shown in Fig. 2-1. The flexural cracks, induced by bending moments, consist

of circumferential (tangential) and radial (fan-shaped) cracks[8]. The first circumferential cracks form at the column periphery, and the later circumferential cracks are parallel to the column faces and located at different distances from the column. The radial cracks, on the other hand, are perpendicular to the column faces. They initiate near the column and extend radially away from the column, perpendicular to the circumferential cracks. The flexural cracks can be observed on the slab tension surface, while inclined cracks propagate inside slab regions near the column (Fig. 2-1). These inclined cracks develop around the column to form a truncated conical surface (Fig. 1-3b). If a slab-column connection is reinforced with shear reinforcement, more inclined cracks may form in slab regions further away from the column.

### 2.1.2 Bending Moments in Slabs

In the cylindrical coordinate system ($r, \theta$, z) shown in Fig. 2-1, a bending moment at one point in the slab can be decomposed into two components, a radial ($m_r$) and tangential moment ($m_\theta$). The radial moment component is perpendicular to the radial direction ($r$), and it causes the circumferential cracks. The tangential moment component is parallel to the radial direction and causes the radial cracks.

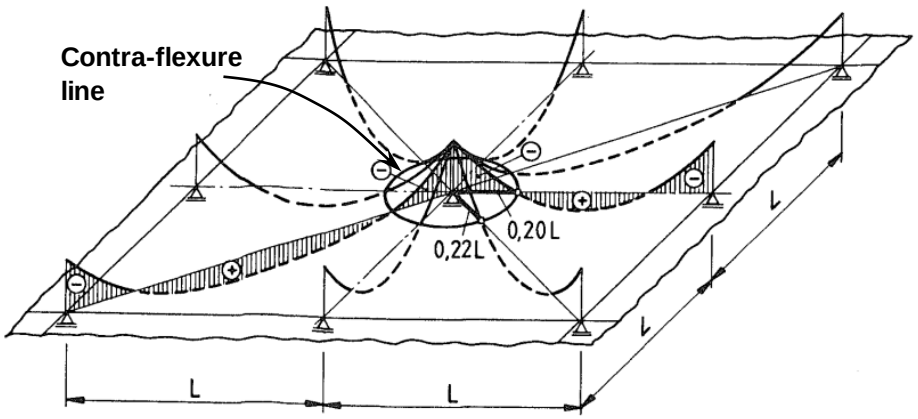


*Fig. 2-2: Distribution radial bending moment[20]*

Fig. 2-2 shows the distribution of a radial bending moment (elastic analyses[20]) around an interior column when a flat plate system supports a uniform gravity load. It can be seen that positive radial moments (causing tension at the bottom of slab) are located at midspan regions, while negative radial moments are located near the columns A closed line separating the negative and positive radial moment regions, referred to as a contra-flexure line, can be approximated as a

circle with a diameter of $0.4L$ ($L$ is span length) located asymmetrically around the column (Fig. 2-2).

For typical test specimens, slab regions bounded by a contra-flexure line are usually combined with the column (Fig. 2-2). This isolated slab-column connection is typically supported along the slab periphery and loaded at the column, so the distribution of bending moments in these specimens is similar to that in flat plate systems (Fig. 2-2). Radial ($m_r$) and tangential moments ($m_\theta$) in the slab for this test setup, according to elastic analyses by Timoshenko and Woinowsky-Krieger[21], are given in Eq. (1) and (2), respectively. In these equations, $l = 0.4\,L$ and $d_c$ are the slab and column diameters, respectively, and $V$ is the applied load at the column. The moment diagrams (Fig. 2-3) show that $m_r$ and $m_\theta$ are both highest at the column faces, and they decrease as the distance from the column increases. The rate of decrease for the radial moments is higher than for the tangential moments. Thus, while the radial moments decrease to zero at the slab periphery, the tangential moments decrease only 50 to 70 percent of the maximum value, depending on the column and slab sizes.

$$m_r = \frac{V}{8\pi}\left[2\,ln\left(\frac{l}{2r}\right) + \frac{d_c^2}{4r^2} - \frac{d_c^2}{l^2}\right] \qquad (1)$$

$$m_\theta = \frac{V}{8\pi}\left[2ln\left(\frac{l}{2r}\right) + 2 - \frac{d_c^2}{4r^2} - \frac{d_c^2}{l^2}\right] \qquad (2)$$

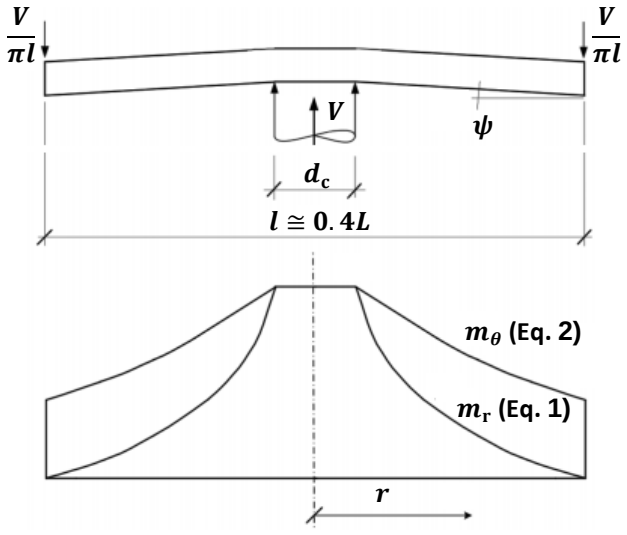


*Fig. 2-3: Distribution bending moments in a test slab[22]*

## 2.2 REVEW OF THE ACI CODE PROVISIONS FOR SHEAR STRENGTH OF SLAB-COLUMN CONNECTIONS

### 2.2.1 Slab-Column Connections without Shear Reinforcement

A report[23] published in 1916 by a Joint Committee appointed by a number of professional societies is considered as the first standard specification for concrete in the United States[24]. In this report, the pure shear stress ($v$) in a slab, calculated at a section close to the perimeter of the column, is given as,

$$v = \frac{V}{bt} \tag{3}$$

in which, $V$ is a shear force, b is the column perimeter (e.g., $b = \pi d_c$ for a circular column with diameter $d_c$), and $t$ is the total thickness of a slab. This calculated stress ($v$) was required to not exceed the allowable value of $0.06f_c'$ ($f_c'$ is the compressive strength of slab concrete) to prevent vertical sliding failure at the perimeter of the column. This allowable shear stress was increased to $0.075f_c'$ and $0.1f_c'$ in the 1916 and 1920 ACI Standards[25, 26], respectively.

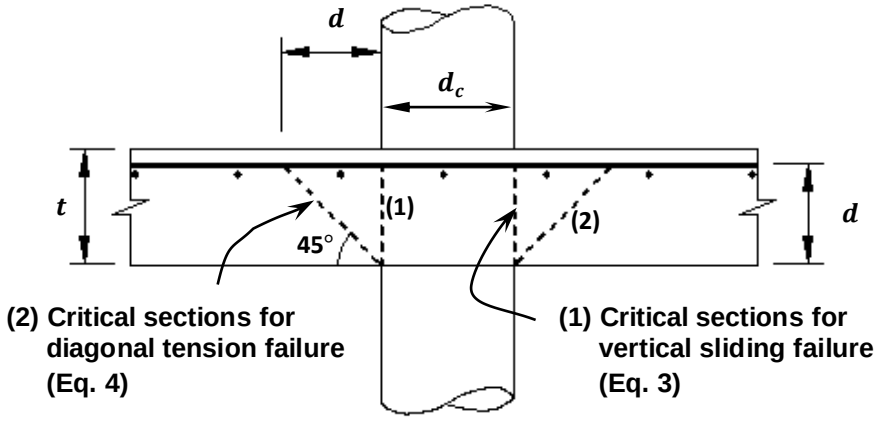


*Fig. 2-4: Critical sections for shear failure specified by the 1920 ACI Standard[26]*

"Diagonal tension failure" for slabs was introduced in the ACI Standard published in 1917[27], but no design specification for a diagonal tension failure at slab-column connections was given until the 1920 ACI Standard[26]. In the 1920 ACI Standard, a clear distinction was made between diagonal tension failure and vertical sliding failure. While vertical sliding failure was controlled by the shear stress (Eq. 3) calculated at a critical section following the periphery of the column (section 1 in Fig. 2-4), diagonal tension failure was governed by the shear stress

calculated on the surface of the frustum of a cone or pyramid passing through the periphery of the column and having a base angle of 45 degrees (section 2 in Fig. 2-4). The diagonal tension shear stress is given in Eq. (4), where $b_0$ is a perimeter of an equivalent vertical section located at a distance of $d/2$ from the column faces, and $d$ is the effective depth of a slab. The calculated shear stress was specified to not exceed $0.035f_c'$.

$$v = \frac{V}{b_0 d} \tag{4}$$

The effect of slab flexural reinforcement distribution on the allowable shear stress at slab-column connections was considered in the report of the Joint Committee in 1924[28]. In this report, the shear stress was computed at a distance of $t - 1.5$ in. (approximately equal to $d$) from column faces, and the allowable shear stress was specified as $0.02f_c'(1+ n)$, where $n$ was defined as the ratio of the area of slab flexural tension reinforcement placed across the column to the total area of slab flexural tension reinforcement within the column strip, and $n \geq 0.25$. Thus, an increase in slab flexural reinforcement across the column ($n$) increased the shear strength of slab-column connections, but the allowable shear stress was limited to $0.03f_c'$.

Provisions for shear strength of slab-column connections in the report of the 1924 Joint Committee[28] were adopted by the ACI Standards. In the 1941 ACI Building Regulations for Reinforced Concrete[29], the calculated shear stress at a distance $t - 1.5$ in. from the column faces was limited to the value of $0.02\,f_c'$ if $n \leq 0.25$, or $0.03f_c'$ if $n > 0.5$. These design specifications for punching shear in slab-column connections remained mainly unchanged through the 1947 and 1951 versions of the ACI Building Code (ACI 318)[30, 31]. In the 1956 ACI Code[32], only slight changes were made. The shear stress was calculated at the critical section located at a distance $d$ away from the column perimeter, and the allowable shear stresses of $0.02f_c'$ and $0.03f_c'$ were limited to 85 and 100 psi, respectively.

$$v_u = \frac{V_u}{bd} = 4\left(\frac{d}{d_c} + 1\right)\sqrt{f_c'} \quad \text{(psi)} \tag{5}$$

$$v_u = \frac{V_u}{bd} = 0.33\left(\frac{d}{d_c} + 1\right)\sqrt{f_c'} \quad \text{(MPa)} \tag{5M}$$

The ACI-ASCE Committee 326[33] in 1962 proposed an expression (Eq. 5) for ultimate shear strength ($v_u$) of slab-column connections. In this expression, $v_u$ was computed at a vertical section around the column, and the measure of diagonal tension resistance was given in terms of $\sqrt{f_c'}$ (instead of $f_c'$), as proposed by Moe[24] in 1961. As shown in Fig. 2-5, the expression presented a lower bound for the measured punching shear strength of slabs and footings from almost all of the tests reported to that time. In order to simplify Eq. (5), ACI-ASCE Committee 326 suggested that ultimate shear stress should be computed at a vertical section located at $d/2$ from the periphery of the column. The perimeter of this critical section was computed as $b_0 = \pi(d_c + d) = 3(d/d_c + 1)$, so $v_u$ was expressed as a function of $\sqrt{f_c'}$ (Eq. 6). This simpler equation was shown[33] to be equivalent to the expression for ultimate shear strength of slabs given by the 1956 ACI Code[32].

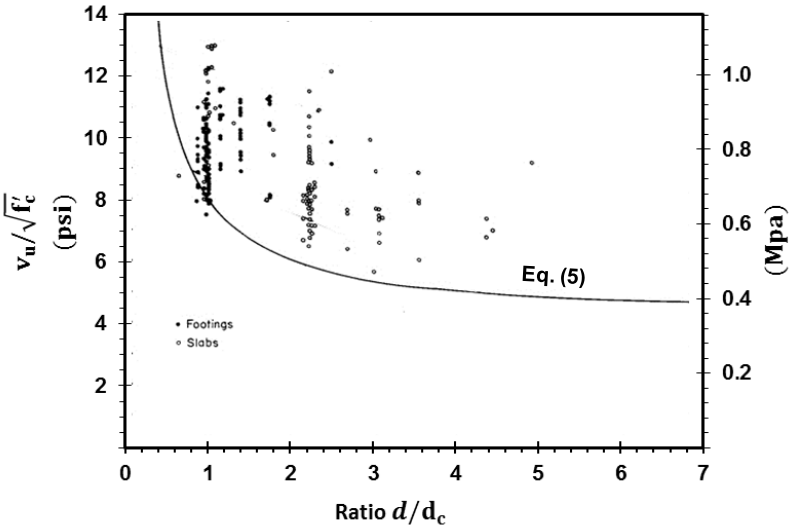


*Fig. 2-5: Punching shear strength proposed by ACI-ASCE Committee 326[33]*

$$v_u = \frac{V_u}{b_0 d} = 4\sqrt{f_c'} \quad \text{(psi)} \qquad (6)$$

$$v_u = \frac{V_u}{b_0 d} = 0.33\sqrt{f_c'} \quad \text{(MPa)} \qquad (6M)$$

The design specifications for punching shear in flat plate structures were changed significantly in the 1963 ACI Code[34] with regard to the locations of critical sections, the allowable shear stresses, and the ultimate shear strength of slab-column connections. Based on

the report by ACI-ASCE Committee 326[33], the 1963 ACI Code defined the critical section for diagonal tension failure at $d/2$ from the periphery of the column. The nominal shear stresses computed at this critical section, given in Eqs. (4) and (6), was limited to $2\sqrt{f_c'}$ and $4\sqrt{f_c'}$ psi ($0.17\sqrt{f_c'}$ and $0.33\sqrt{f_c'}$ MPa) for Working Stress Design (WSD) and Ultimate Strength Design (USD), respectively. The specification for Ultimate Strength Design remains unchanged in the current ACI Code[5] provisions for two-way shear strength.

In the 1971 ACI Code[35] provisions for punching shear at slab-column connections, only ultimate strength (USD) was used and the calculation of shear stress induced by unbalanced moments was introduced. Factored shear stress ($v_u$) induced by factored shear ($V_u$) and unbalanced moment ($M_u$) at a slab-column connection was given in Eq. (7),

$$v_u = \frac{V_u}{b_0 d} + \frac{\gamma_v M_u c}{J_c} \leq \phi v_n \qquad (7)$$

where, $\gamma_v$ is the fraction of the moment that is transferred by eccentric shear stresses, $c$ is the measurement from the centroid of the critical-shear perimeter to the edge of the perimeter where the shear stress ($v_u$) is being calculated, and $J_c$ is an effective polar moment of inertia for the critical shear section. The factor shear stress calculated from Eq. (7) was specified to not exceed the reduced nominal shear strength of the connection, expressed as a stress, $\phi v_n$ ($\phi$ is a strength reduction factor, taken as 0.75 for shear design). For slab-column connections without shear reinforcement, the nominal shear strength was provided by only concrete ($v_n = v_c$), and was calculated by the formula given in Eq. (8), in which $\lambda$ is the factor for lightweight-aggregate concrete defined in the text of the 1971 ACI Code[35].

$$v_c = 4\lambda\sqrt{f_c'} \quad \text{(psi)} \qquad (8)$$

$$v_c = 0.33\lambda\sqrt{f_c'} \quad \text{(MPa)} \qquad (8M)$$

Significant changes were made in the ACI Code of 1977[36] to account for the effect of the geometry of column cross sections on punching shear strength, and to introduce a concept of *transfer width* in slabs for carrying moment transfer. Based on the report by the ACI-ASCE Committee 426[8] with regard to the effect of geometry of loaded areas, the 1977 ACI Code added a new lower bound for shear strength (Eq. 9) of slab-column connections without shear

reinforcement. Eq. (9) results in a lower shear strength than Eq. (8), if β, the ratio of long-side to short-side dimensions of a rectangular column, exceeds the value of 2. As β increases, the two-way shear effect in slab regions near supports is reduced, and for very large values of β, e.g. slabs supported by walls, the shear strength given by Eq. (9) becomes $2\lambda\sqrt{f_c'}$ psi ($0.17\ \lambda\sqrt{f_c'}$ MPa), which is equal to one-way shear strength specified for beams. The 1977 ACI Code also introduced a *transfer width*, in which the slab flexural reinforcement was required to carry a fraction of the moment being transferred at the connection, $(1-\gamma_v)M_u$. The transfer width included the column width and extended $1.5t$ ($t$ is the slab thickness) on each side of the column.

$$v_c = \left(2 + \frac{4}{\beta}\right)\lambda\sqrt{f_c'} \quad \text{(psi)} \tag{9}$$

$$v_c = 0.083\left(2 + \frac{4}{\beta}\right)\lambda\sqrt{f_c'} \quad \text{(MPa)} \tag{9M}$$

After the ACI Code of 1977[36], the expressions for punching shear strength remained unchanged until the 1989 version[37] of the ACI Code, where a new lower bound for punching shear strength was developed, as given in Eq. (10). The new expression was to account for the effect of a large $b_0/d$ ratio on shear strength of slab-column connections without shear reinforcement. This effect was presented by Vanderbilt in 1972[38], in which he found that an increase of the ratio $b_0/d$ decreased punching shear strength of slab-column connections. In Eq. (10), a constant $\alpha_s$ is equal to 40, 30, and 20 for interior, edge, and corner columns, respectively. Eq. (10) governs the punching shear strength of an interior slab-column connection that has a column with square cross section if the dimension of a column exceeds 4 times of the depth of a slab.

$$v_c = \left(2 + \alpha_s\frac{d}{b_0}\right)\lambda\sqrt{f_c'} \quad \text{(psi)} \tag{10}$$

$$v_c = 0.083\left(2 + \alpha_s\frac{d}{b_0}\right)\lambda\sqrt{f_c'} \quad \text{(MPa)} \tag{10M}$$

Three expressions for punching shear strength of slab-column connection without shear reinforcement, given in Eq. (8), (9), and (10), have not been changed since the 1989 ACI Code[37]. In the current ACI Code[5] these expressions are presented in Table 22.6.5.2. Nominal

shear strength, given as a stress, of slab-column connection without shear reinforcement is the least of the three expressions, as given in Eq. (11).

$$v_c = \quad \text{the least of } \textit{Eq. (8), (9),} \text{ and } \textit{(10)} \qquad \textit{(11)}$$

For slab-column connections that have $v_u/\phi$, computed by Eq. (7), larger than the nominal shear strength given in Eq. (11), shear reinforcement can be used to increase shear strength. The next section presents a review of the ACI Code provisions for shear strength of slab-column connections with shear reinforcement, including stirrups, shearheads, and headed shear studs.

### 2.2.2 Slab-Column Connections with Shear Reinforcement

Although various shear reinforcement systems have been tested and used to increase shear strength of slab-column connections since 1930s[39, 40], procedures for design of shear reinforcement in slabs were not developed until 1962 by the ACI-ASCE Committee 326[33]. Based on the report of this Committee, the 1963 ACI Code[34] specified stirrups (similar to stirrups used for beams) as a shear reinforcement system for slabs. After that, shearheads, a shear reinforcement system consisting of steel sections, was included in the 1971[35] version of the ACI Code. In 2008, headed shear stud reinforcement for slab-column connections was introduced in the ACI Code[41]. Since then, no additional shear reinforcement system has been added to the ACI Code. In the current ACI Code[5], design specifications for shear strength of slab-column connections with stirrups, shearheads, and headed shear studs are given in Section 22.6.

#### *2.2.2.1 Stirrups*

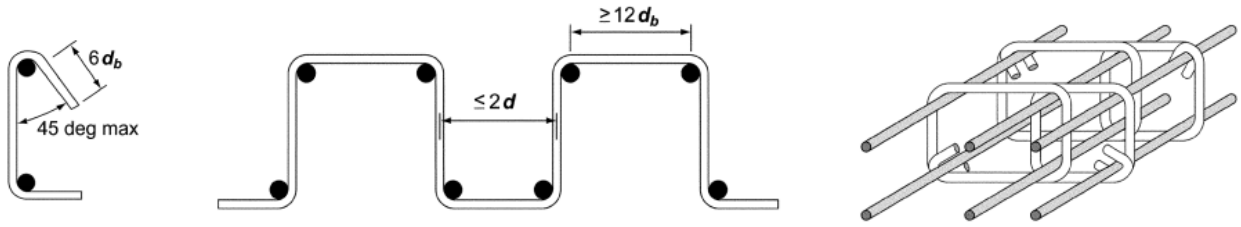


*a. single leg stirrups* *b. multiple leg stirrups* *c. close stirrups*

*Fig. 2-6: Stirrups for flat slab systems[41]*

Design specifications for stirrups were initiated in the 1963 ACI Code[34], and significantly changed in the 1971 ACI Code[35]. In the 1963 version of the ACI Code, single- or multiple-leg

stirrups were permitted for use only in slabs greater than 10 in. thick, but the design strength of stirrups was limited to 50 percent of the specified yielding strength of stirrups ($f_{yt}$). For slabs with a thickness of less than 10 in., on the other hand, stirrups were assumed to be ineffective. These imposed restrictions were due to the limitations of test data and concerns over anchorage capacity provided at the bends (hooks) of stirrups. In the 1971 ACI Code, with more established data, design of shear reinforcement for slabs was permitted to use the full specified yield strength of shear reinforcement, given that shear reinforcement was properly anchored and detailed. In the 2014 ACI Code[5], stirrups are permitted to be used in slabs that have an effective flexural depth ($d$) of at least 6 in. and 16 times of the diameter of stirrups. The stirrups are required to engage the slab flexural reinforcement at both the top and bottom of the slab, as shown in Fig. 2-6.

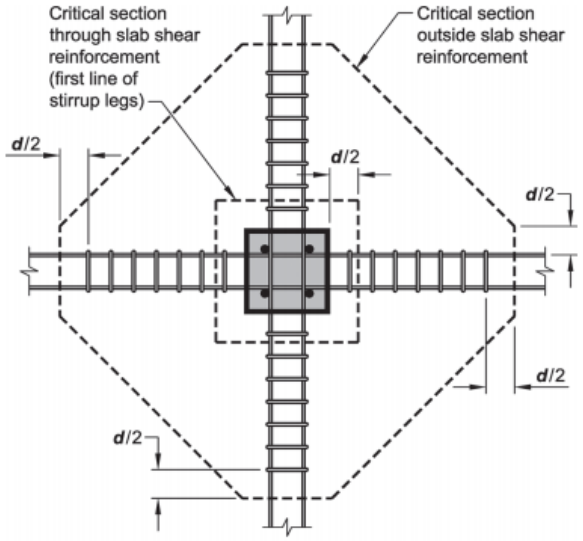


*Fig. 2-7: Critical sections for two-way shear in slabs with stirrups[41]*

Provisions for shear strength of slab-column connections reinforced with stirrups have not been significantly changed since the 1971 ACI Code[35]. For flat plate structures, shear strength of a slab-column connection is required to be checked at two critical sections located at $d/2$ from the perimeter of a column (referred as inner critical section) and at $d/2$ beyond the outermost stirrups (referred as outer critical section), as shown in Fig. 2-7. Nominal shear strength calculated at the inner critical section, given as a stress ($v_n$), is the sum of shear strength provided by concrete ($v_c$) and stirrups ($v_s$), as given in Eq. (12).

$$v_n = v_c + v_s \tag{12}$$

Shear strength provided by concrete ($v_c$) is limited to $2\lambda\sqrt{f'_c}$ psi ($0.166\,\lambda\sqrt{f'_c}$ MPa). Shear strength provided by stirrups ($v_s$) is calculated from Eq. (13),

$$v_s = \frac{A_v f_{yt}}{b_0 s} \tag{13}$$

in which $A_v$ is the sum of the area of all stirrup legs on one peripheral line of stirrups, $b_0$ is the perimeter of the critical section, $s$ is the spacing between peripheral lines of shear reinforcement, and $f_{yt}$ is the yield strength of shear reinforcement. For the outer critical section, nominal shear strength of a slab-column connection is provided by the concrete only, and thus $v_n = v_c = 2\lambda\sqrt{f'_c}$ psi ($0.166\lambda\sqrt{f'_c}$ MPa). The maximum design shear stress ($v_u$) for slab-column connections with stirrups, calculated at the inner critical section, is specified as $6\phi\lambda\sqrt{f'_c}$ psi ($0.5\phi\lambda\sqrt{f'_c}$ MPa).

#### *2.2.2.2 Shearheads*

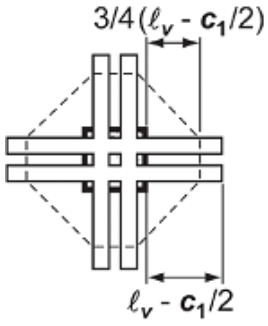


*(an eight-arms shearhead)*

*Fig. 2-8: Critical sections for two-way shear in slabs with shearhead[41]*

The 1971 ACI Code[35] design procedures for shear strength of slab-column connections reinforced with shearheads, originally developed by Corley and Hawkins[42], have been maintained in the current ACI Code[5]. In these design procedures, the length and cross section of shearhead arms (Fig. 2-8) were designed to ensure that the design shear force ($V_u$) was attained as the flexural strength of the shearhead was reached. Thus, the plastic flexural strength ($M_p$) of each shearhead was specified to be larger than the required plastic flexural strength given in Eq. (14),

$$M_p \geq \frac{V_u}{2\phi n_a}\left[h_v + \alpha_v\left(l_v - \frac{c_1}{2}\right)\right] \quad (14)$$

where, $n_a$ was the number of arms in a shearhead system, $h_v$ and $l_v$ were the height and length of shearhead arms, $\alpha_v$ was a ratio of flexural stiffness of a shearhead arm to flexural stiffness of the surrounding slab regions, and $c_1$ is a dimension of the column in the direction parallel to a shearhead arm. For slab-column connections without moment transfer, design shear stress ($v_u$) calculated at the inner critical section located at $d/2$ from the periphery of the column, is limited to $\phi 7\sqrt{f_c'}$ psi ($\phi 0.58\sqrt{f_c'}$ MPa). Shearhead arms are extended away from the column faces to ensure that design shear stress ($v_u$), calculated at the outer critical section located at 3/4 of the extended length of shearhead arms (Fig. 2-8), does not exceed $\phi 4\sqrt{f_c'}$ psi ($\phi 0.33\sqrt{f_c'}$ MPa).

#### *2.2.2.3 Headed shear studs*

Design specifications for shear strength of slab-column connections reinforced with headed shear stud reinforcement were developed by ACI Committee 421[43] in 1999, and have been recommended by the ACI Code since 2008[41]. Nominal shear strength of slab-column connections in flat plate structures is specified at two critical sections, as shown in Fig. 2-8. For the first critical section (inner critical section), located at $d/2$ from the column perimeter, the nominal shear strength of a slab-column connection ($v_n$) is calculated from Eq. (12). Shear strength provided by concrete ($v_c$) is limited to $3\lambda\sqrt{f_c'}$ psi ($0.25\ \lambda\sqrt{f_c'}$ MPa). Shear strength provided by stirrups ($v_s$) is calculated from Eq. (13), in which $A_v$ is the sum of the area of all shear studs on one peripheral line of shear studs, and $s$ is the spacing between peripheral lines of shear studs. For the other critical section, located at $d/2$ from the outermost shear studs, the nominal shear strength is provided by the concrete only, $v_n = v_c = 2\lambda\sqrt{f_c'}$ psi ($0.166\lambda\sqrt{f_c'}$ MPa).

$$v_n = v_c + v_s \quad (12)$$

$$v_s = \frac{A_v f_{yt}}{b_0 s} \quad (13)$$

The maximum design shear stress ($v_u$) calculated at the inner critical section at slab-column connections with headed shear stud reinforcement is permitted to reach $8\phi\lambda\sqrt{f_c'}$ psi ($0.66\phi\lambda\sqrt{f_c'}$ MPa). This specified maximum design shear stress is approximately 30% higher than that for

slab-column connections with stirrups because the mechanical heads of shear studs were assumed to be more effective in providing anchorage than the bends of stirrups [44].

In the 2014 ACI Code[5], the configuration of headed shear studs allowed for interior slab-column connections is shown in Fig. 2-9. Three requirements for spacing shear studs are specified. First, the spacing ($s_0$) between the column perimeter to the closest peripheral line of shear studs is not to exceed $d/2$. Second, the spacing between two adjacent peripheral lines of shear studs ($s$) is limited to $3d/4$ if the design shear stress calculated at the inner critical section $v_u \leq 6\phi\lambda\sqrt{f'_c}$ psi ($0.55\phi\lambda\sqrt{f'_c}$ MPa), and to $d/2$ otherwise. And finally, the spacing between adjacent shear studs on the peripheral line closest to the column is limited to $2d$. The spacing between adjacent shear studs on other peripheral lines beyond the innermost stud line, however, is not limited. Thus, in North America, headed shear studs have been typically placed in an orthogonal layout, as shown in Fig. 2-9, to facilitate construction.

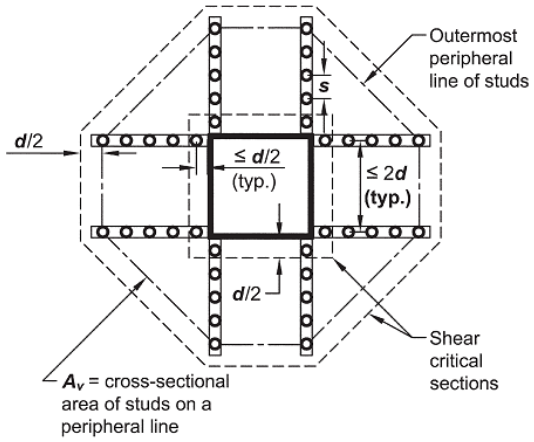


*Fig. 2-9: Critical sections for two-way shear in slabs with headed shear studs[5]*

A potential issue with an orthogonal layout of shear studs is that large regions of the slab extending out from the corners of the columns are essentially unreinforced in shear. This issue can be addressed by using stud rails that project radially out from the corners of the column (Fig. 1-6b), referred to as a radial layout. Research investigations that have studied the effect of different shear stud layouts are presented in Section 2.3.

## 2.3 EFFECT OF SHEAR STUD LAYOUT ON PUNCHING SHEAR STRENGTH

This section presents a review of research investigations on the effects of a radial and orthogonal layout of shear studs on the behavior and shear strength of slab-column connections under simulated gravity loads. A limited number of research investigations related to this topic have been reported and test results from these investigations have shown an apparent conflict. Some investigations indicated that shear strength of slab-column connections with shear studs arranged in either a radial or orthogonal layout were similar, while other investigations have indicated that there was a significant difference in behavior and shear strength of slab-column connection where shear studs were used in either an orthogonal or radial layout.

The use of an orthogonal layout of shear studs was recommended for the first time by Ghali and Dilger in 1980[12, 45], when they observed that an equal increase in shear strength was provided by the shear studs placed either on orthogonal lines parallel to the column faces[45] (orthogonal layout) or on circular lines around the supporting column[12]. The shear studs used for these studies[12, 45] were in the form of slices cut from I-beams and they were placed in regions extending $1.5d$ from the column faces. The column in each test specimen was 12 in. (300 mm) square and it was located at the center of a 71 in. × 71 in. × 6 in. thick slab (1800 mm × 1800 mm × 150 mm). The percentage of flexural tension reinforcement in all slabs was approximately 1.2%. Based on the test results from these studies and some later tests[13, 46], Dilger[47], in 2000, concluded that orthogonal and radial layouts of shear studs were equally effective in providing shear strength to slab-column connections, and for practical reasons, an orthogonal layout was recommended because it minimized interference with slab flexural reinforcement.

In 2007, however, results from the tests reported by Broms[17] indicated that an orthogonal layout of shear studs did not provide an equal strength and deformation capacity in slab-column connections as provided by a radial stud layout. In his report, Specimens 18a and 18b had a similar geometry, as shown in Fig. 2-10. In these specimens, the columns were 12 in. (300 mm) square and the slabs were 7 in. (180 mm) thick. The slabs were supported at 16 points uniformly distributed on a circle with a radius of approximately 48 in. (1215 mm). The average slab flexural tension reinforcement ratio was 1.3 and 1.2% for Specimens 18a and 18b, respectively. For shear reinforcement design, the two specimens were both reinforced with 72 identical shear

studs with a shaft diameter of 0.5 in. (12 mm). For Specimen 18a, the shear studs were welded at a spacing of 2.9 in. (75 mm) to 8 rails and were placed in an orthogonal layout, while for Specimen 18b, the shear studs were welded at a spacing of 4.3 in. (110 mm) to 12 rails placed in a radial (star) layout. Load versus column displacement responses for Specimens 18a and 18b are shown in Fig. 2-11. It can be seen that Specimen 18b, with a radial stud layout, had a higher measured strength and exhibited more ductile behavior than Specimen 18a, with an orthogonal stud layout.

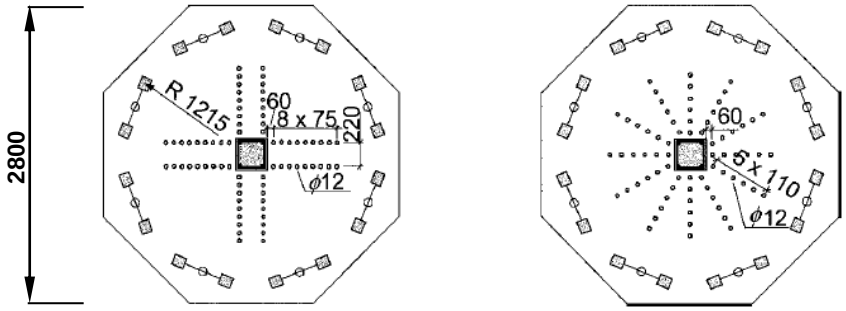


*a. Orthogonal Layout (18a)* *b. Radial Layout (18b)*

*Fig. 2-10: Two connections tested by Broms[17]*

*(units in mm, 1 in. = 25.4 mm)*

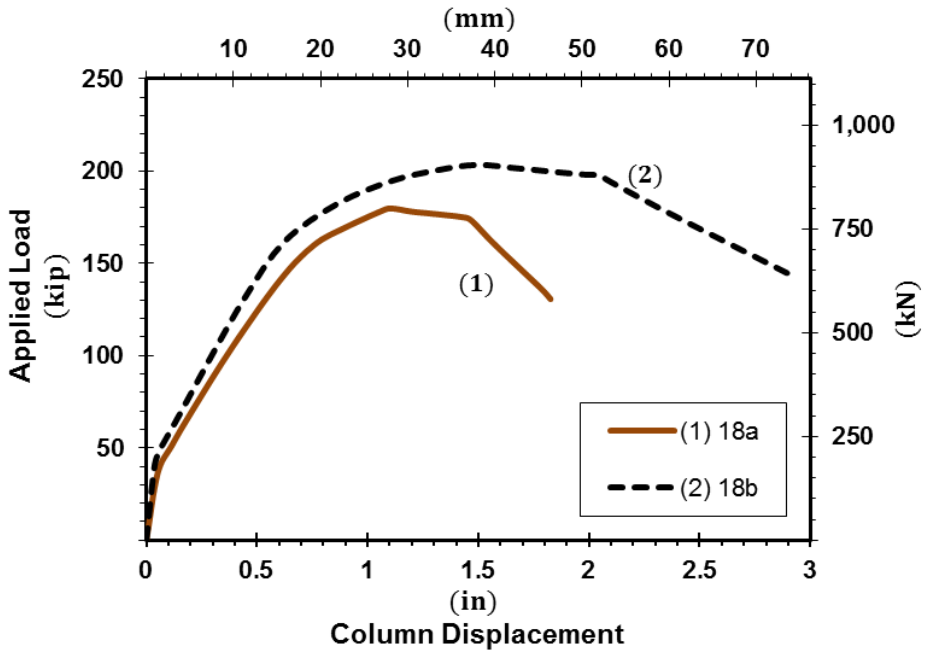


*Fig. 2-11: Test results by Broms[17]*

In 2009, test results reported by Birkle and Dilger[15], however, showed that orthogonal and radial layouts of shear studs were equally effective for shear strength of slab-column connections. In their research investigation, the effects of the two stud layouts were evaluated through 4 slab-column connections with identical geometries and flexural design. Columns in these specimens had 10 in. (250 mm) square cross sections and slabs were regular octagons with a total width of 73 in. (1850 mm), as shown in Fig. 2-12. The percentage of slab flexural reinforcement was 1.5% for all test specimens. The four specimens were divided into two groups depending on the spacing between peripheral lines of shear studs, as shown in Fig. 2-12. For Specimens 2 and 3, the shear studs were equally spaced at approximately 3.5 in. (90 mm) along each rail (Fig. 2-12a and b). For Specimens 5 and 6, the shear studs were spaced at approximately 2.4 in. (60 mm) for the first five stud rows close to the column, but the spacing was increased to 5 in. (120 mm) for the two outer stud rows (Fig. 2-12c and d).

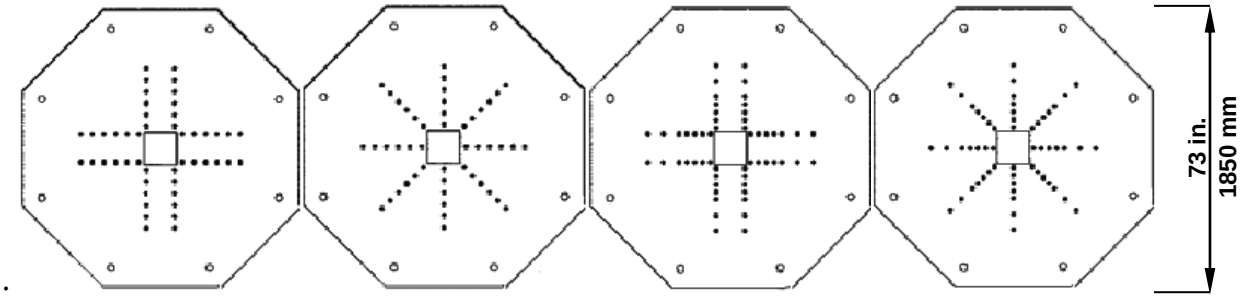


a. Specimen 2 b. Specimen 3 c. Specimen 5 d. Specimen 6

*Fig. 2-12: Specimens tested by Birkle and Dilger[15]*

Load versus displacement relationships for the four specimens are shown in Fig. 2-13. The displacement shown in Fig. 2-13 was measured at the center of columns except for Specimen 2, in which the displacement was measured on the slab at 20 in. (500 mm) from the center of the column. Fig. 2-12 shows that measured strengths for the two specimens in each group were similar. Based on these results, Birkle and Dilger[15] stated that neither the behavior nor strength of slab-column connections were improved by the radial arrangement of stud rails.

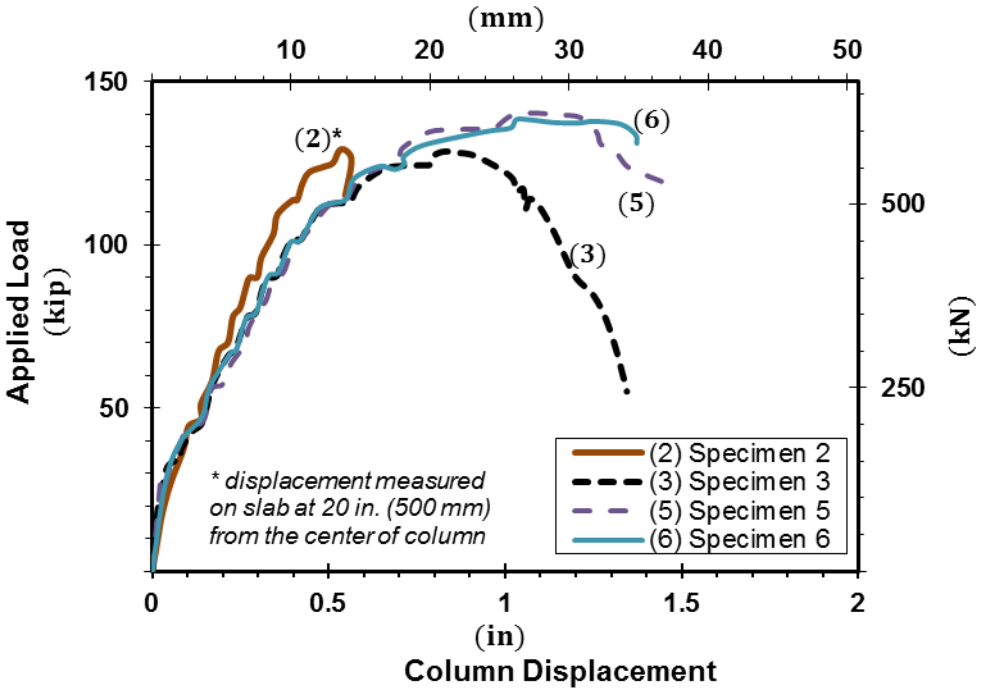


*Fig. 2-13: Experimental results by Birkle and Dilger[15]*

Other test results similar to those from Birkle and Dilger[15] were also reported by Ferreira et al[16], and Bu and Polak[48]. Two slab-column connections were tested by Ferreira et al[16]. These test specimens had a slab flexural tension reinforcement ratio of approximately 1.5% and they were reinforced with stud rails in an orthogonal layout (C4) and a radial layout (C8). Test results indicated that the orthogonal stud layout was as effective as the radial stud layout in terms of proving shear strength to the slab-column connections. In the report by Bu and Polak[48], two pairs of slab-column connections were retrofitted with shear studs in the form of shear bolts through the slabs, and were tested under gravity and lateral load reversals. In each pair of specimens, the same number of shear bolts was used for each slab. The shear bolts were arranged in an orthogonal layout for two specimens and in a radial layout for two other specimens. The average slab flexural tension reinforcement ratio was approximately 1.2% for all test specimens. Based on test results of these pairs of specimens, Bu and Polak[48] concluded that no significant difference was found in the behavior and strength of specimens in each pair.

In contrast to the test results from other studies, poor performance of slab-column connections with an orthogonal layout of shear studs were observed by DaCosta and Parra-Montesinos[18] in 2011. In their research investigation, the effect of shear stud layout was studied through the tests of three pairs of slab-column connections (M1 and M9, M5 and M10, and M8

and M11) under simulated gravity loads. All test specimens were similar in geometry. Slabs in these specimens were 72 in. (1820 mm) square and 8 in. (200 mm) thick, and columns were 6 in. (150 mm) square located at the center of the slabs. The percentage of slab flexural reinforcement was approximately 1.3% for Specimens M8 and M11, and 0.8% for the other two pairs of specimens. A total of 8 stud rails were used in each test specimens and the spacing between the studs on each rail was approximately 0.75$d$ for the pair of M5 and M10, and 0.4$d$ for the other two pairs. Test results for each pair of specimens indicated that the orthogonal layout of shear studs provided lower shear strength and less ductility to slab-column connections than the radial stud layout.

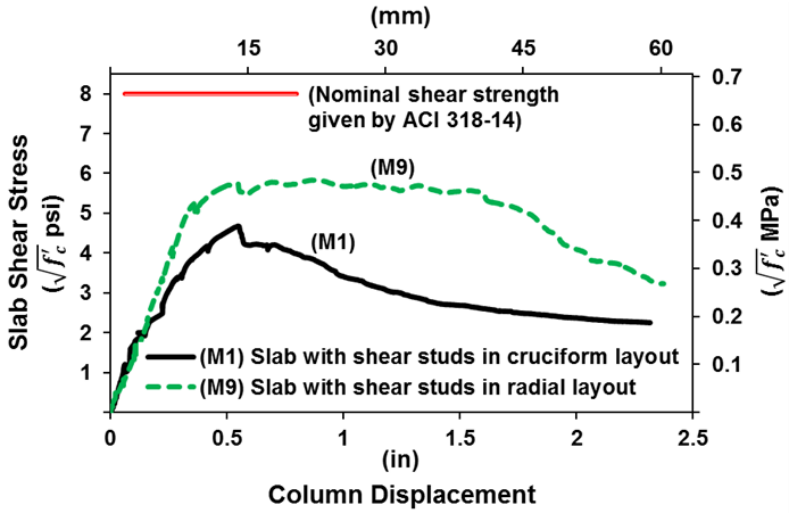


*Fig. 2-14: Experimental results by DaCosta and Parra-Montesinos*[18]

A typical relationship between the applied load, expressed as a slab shear stress, versus column displacement in the DaCosta and Parra-Montesinos study is shown in Fig. 2-14. It can be seen that: 1) shear studs configured in the orthogonal layout (Specimen M1) were substantially less effective than those placed in the radial layout (Specimen M9) in terms of shear strength and ductility, and 2) Specimen M9, with a radial stud layout, experienced significant yielding of slab flexural reinforcement before the punching failure occurred. Fig. 2-14 also indicates that the measured punching shear strength for the two specimens was significantly lower than the nominal shear strength given by the ACI Code[5]. In addition, measured strains in slab flexural bars near the columns in the two specimens significantly exceeded the yield strain of the slab flexural reinforcement. This suggested that yielding of the slab flexural reinforcement, which is

inversely proportional to slab flexural reinforcement ratio, could have a significant effect on shear strength of slab-column connections reinforced with shear stud reinforcement.

Post-test observations of crack patterns in test specimens often show valuable information about specimen failure modes. The typical cracks and failure surfaces in the test slabs[18] from the DaCosta and Parra-Montesinos study are shown in Fig. 2-15. It can be seen that these cracks and failure surfaces developed uniformly around the column in Specimen M9 (Fig. 2-15a), but they did not develop uniformly around the column in Specimen M1 (Fig. 2-15b). For Specimen M1 (with an orthogonal stud layout), the failure surfaces developed above the shear studs and extended downward to the bottom of the slab outside the edges of the shear stud regions. Consequently, slab concrete in large diagonal regions of Specimen M1 (extending from corners of the column) were not engaged by the failure surfaces, and thus these regions appeared to be still intact. These observations indicated that the diagonal slab regions in Specimen M1, without diagonal stud rails, were less effective in resisting shear, and this could be a primary cause for the poor behavior of Specimen M1. These test results raised major concerns regarding to the safety of slab-column connections with a low slab flexural reinforcement ratio and an orthogonal layout of stud rails.

a. Orthogonal Layout (M1) b. Radial Layout (M9)

*Fig. 2-15: Crack patterns induced by shear stud layouts[18]*

Other test results showing the lower effectiveness of an orthogonal stud layout were also presented by Gomes and Regan[49], Carvalho et al[50], and Cheng and Parra-Montesinos[51]. In Gomes and Regant's investigation[48], Specimens 5 and 6 were reinforced with shear studs (slices

cut from I-beams), which were arranged in orthogonal and radial layouts, respectively. The slab flexural reinforcement ratio was approximately 1.3% for both specimens. Test results showed that measured shear strength for Specimen 5 (with an othogonal stud layout) was approximately 20% lower than that for Specimen 6 (with a radial stud layout). Shear strength of the prestressed slab-column connections (L5C and S5R) tested by Carvalho, Melo[50] were also affected by a shear stud layout. Results from this study showed that the measured shear strength for the connection with an orthogonal stud layout (L5C) was 7% lower than that for the connection with a radial stud layout (S5R). In the other investigation by Cheng and Parra-Montesinos[51], Specimen SB3, a nearly full-scale slab-column connection, was reinforced with shear studs in an orthogonal layout. This specimen was tested under simulated gravity load and lateral load reversals. Test results of Specimen SB3 indicated that the design procedures in the ACI Code[41] for shear stud reinforcement were potentially unsafe.

This section has shown that test results from the research investigations on the effect of shear stud layout are conflicting, and these different results might be related to the slab flexural reinforcement ratios. These ratios were often relatively high (above 1.2% e.g.) in the studies that showed an equal effectiveness between an orthogonal and a radial stud layout, but they were lower in the other studies that showed poor behavior for the orthogonal stud layouts. In the following section, the effect of slab flexural reinforcement ratio on the behavior and shear strength of slab-column connections is presented.

## 2.4 EFFECT OF SLAB FLEXURAL REINFORCEMENT RATIO ON PUNCHING SHEAR STRENGTH

Test results for isolated slab-column specimens and flat plate systems have shown that the behavior and measured shear strength of the test specimens were significantly affected by the flexural strength of slab near the columns. This section will review some of those test results.

### 2.4.1 Tests of Isolated Slab-Column Connections

The effect of slab flexural reinforcement ratio was recognized by Hognestad[52] in 1953, when a ratio $\phi_0 = V_u/V_{flex}$ was included in an equation (Eq. 15) for the ultimate shear strength of slabs. This equation was based on test results reported by Richart[53]. In Eq. (15), $V_u$ was the measured shear strength of the slabs, and $V_{flex}$ was the calculated flexural strength of the slabs.

$V_{\text{flex}}$, proportional to the slab flexural reinforcement ratio, was computed using yield line analysis[54]. Equation (15) indicated that measured shear strength of the test specimens increased as the flexural strength $V_{\text{flex}}$ increased. The ratio $\phi_0$ for test results was always less than 1, and thus Hognestad recommended using $\phi_0 = 1$ to estimate punching shear strength of slabs. This recommendation implied that slab flexural reinforcement should be designed such that $V_{\text{flex}}$ was at least equal to the calculated shear strength $V_{\text{u}}$.

$$v_u = \frac{V_u}{7/8\ bd} = \left(0.035 + \frac{0.07}{\phi_0}\right) f_c' + 130 \quad \text{(psi)} \qquad \textit{(15)}$$

In 1961, Moe[24] proposed an expression (Eq. 16) for the ultimate shear strength of slabs and footings, which was dependent on the calculated flexural strength ($V_{\text{flex}}$). To develop Eq. (16), Moe considered a linear interaction between $V_{\text{u}}/V_0$ and $V_{\text{u}}/V_{\text{flex}}$, in which $V_0$ was a fictitious shear strength of slabs that would be obtained if the effect of bending could be eliminated (or when $V_{\text{flex}} = \infty$). Moe[24] assumed that $V_0$ was related to a splitting type failure, so it should be proportional to the square root of the slab concrete strength ($\sqrt{\text{f}_c'}$). Equation (16) indicated that the ultimate punching shear strength of reinforced concrete slabs decreased if the flexural strength $V_{\text{flex}}$ decreased. Combining $\phi_0 = V_{\text{u}}/V_{\text{flex}}$ with Eq. (16) led to Eq. (17), which showed a relationship between ultimate punching shear strength and $\phi_0$. This relationship indicated a similar effect of $\phi_0$ as in Eq. (15) proposed by Hognestad[52].

$$v_u = \frac{V_u}{bd} = \frac{15\left(1 - 0.075\frac{d_c}{d}\right)}{1 + \frac{5.25\ bd\ \sqrt{f_c'}}{V_{\text{flex}}}}\sqrt{f_c'} \quad \text{(psi)} \qquad \textit{(16)}$$

$$v_u = \frac{V_u}{bd} = \left[15\left(1 - 0.075\frac{d_c}{d}\right) - 5.25\ \phi_0\right]\sqrt{f_c'} \quad \text{(psi)} \qquad \textit{(17)}$$

In 1962, the ACI-ASCE Committee 326[33] proposed a lower bound (Eq. 5) for the ultimate shear strength of slab-column connections, but this expression was not dependent on either $V_{\text{flex}}$ or $\phi_0$. In the development of this equation, the ACI-ASCE Committee 326[33] assumed that although $\phi_0$ was an important variable for slab-column specimens, it was not an important variable for practical design of flat plate systems because shear strength of the slab should exceed its flexural strength, or $\phi_0(\text{system}) \geq 1$. Thus, the effect of slab flexural reinforcement

was not included in Eq. (5). In Fig. 2-16, the equation proposed by Committee 326 (Eq. 5) and Moe's equation (Eq. 17) for $\phi_0 = 0.3$ and 1.0, were plotted with the test results available at that time. Fig. 2-16 shows that Eq. (5) was a better lower bound for the test data. This equation was then simplified to Eq. (6) by using a new critical section to compute ultimate shear strength. This critical section was located at $d/2$ from the column faces. Equation (6) and the new critical section became part of the ACI Code in 1963, and are still used in the current ACI Code.

$$v_u = \frac{V_u}{bd} = 4\left(\frac{d}{d_c} + 1\right)\sqrt{f_c'} \quad \text{(psi)} \qquad \textit{Eq. (5)}$$

$$v_u = \frac{V_u}{bd} = 0.33\left(\frac{d}{d_c} + 1\right)\sqrt{f_c'} \quad \text{(MPa)} \qquad \textit{(5M)}$$

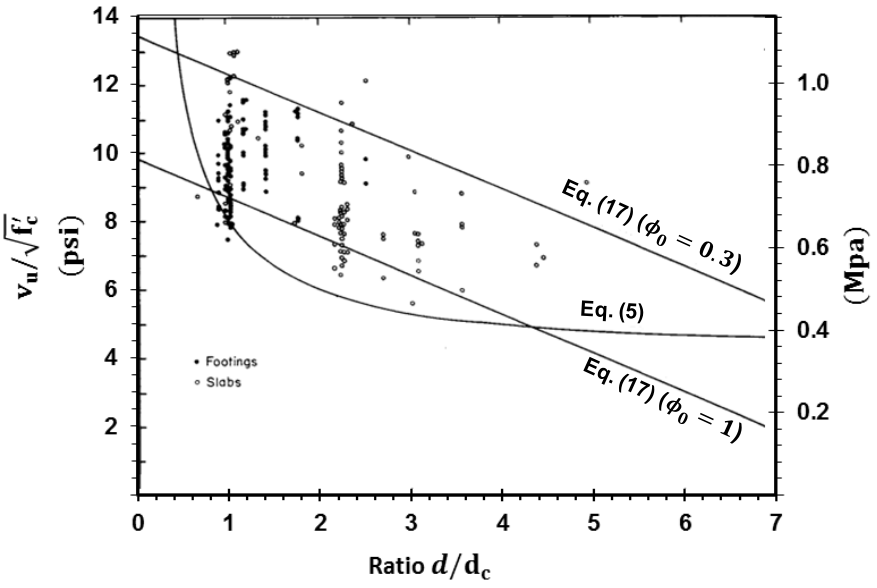


*Fig. 2-16: Punching shear strength proposed by ACI-ASCE Committee 326[33]*

$$v_u = \frac{V_u}{b_0 d} = 4\sqrt{f_c'} \quad \text{(psi)} \qquad \textit{Eq. (6)}$$

$$v_u = \frac{V_u}{b_0 d} = 0.33\sqrt{f_c'} \quad \text{(MPa)} \qquad \textit{(6M)}$$

In 1974, ACI-ASCE Committee 426[8] commented that although test data showed the effect of the calculated flexural strength $V_{\text{flex}}$ on the measured shear strength of slabs, this did not prove that the shear failure mechanism was physically related to the flexural failure mechanism. The

value of $V_{flex}$ might be an indicator of other physically changes, e.g., a decrease in the depth of the flexural compression zone. Committee 426 indicated the need to establish expressions of $\phi_0$ and $V_{flex}$ for slab systems. However, such tests have been very scarce[55] and they have often not focused on the punching shear problem. Results from a few slab system tests (discussed in subsection 2.4.2) indicated that the shear strength of the slab-column connections might be affected by significant yielding of slab flexural reinforcement near the columns.

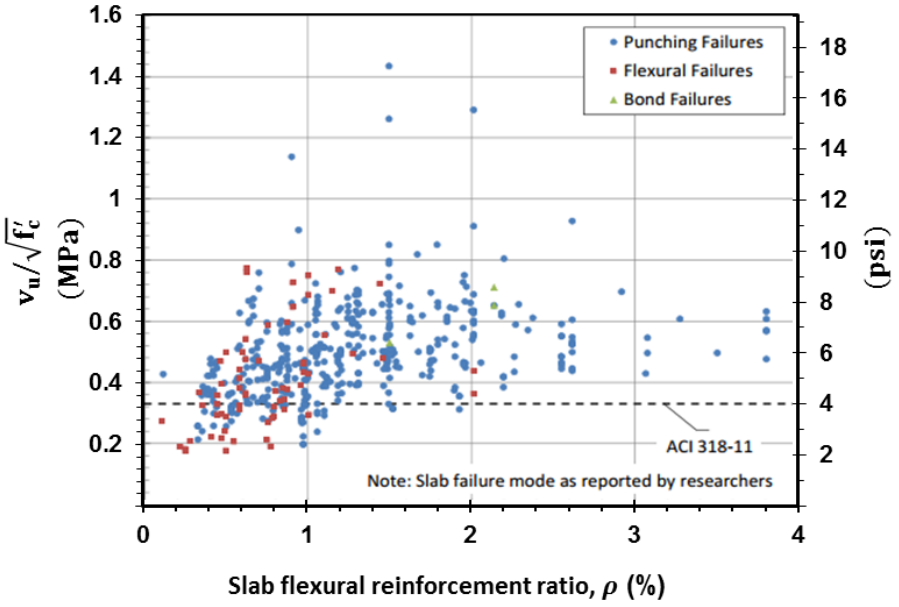


*Fig. 2-17: Measured shear strength vs. a slab flexural reinforcement ratio[56]*

In 2012, test results from 512 slab-column specimens without shear reinforcement were studied by Ospina et al[56]. Measured shear strength, expressed as a stress, for these specimens was plotted versus the slab flexural reinforcement ratio, as shown in Fig. 2-17. The dashed line shown in Fig. 2-17 represents the nominal shear strength given by the ACI Code[5] (Eq. 8 or 6). The figure shows that a significant number of test specimens with a slab flexural tension reinforcement ratio $\rho \leq 1.2\%$ had a measured shear strength lower than the ACI Code[5] calculated shear strength. These results inidcated that the expressions for ultimate punching shear strength of slabs in the ACI Code, which was developed by ACI-ASCE Committee 326[35] (Eq. 5 and 6) based on the test data in 1963, overestimates shear strength of slab-column connections that have a relatively low slab flexural reinforcement ratio.

For slab-column specimens reinforced with shear reinforcement, e.g. headed shear studs, the apparently conflicting results presented in Section 2.3 have also indicated that the slab flexural reinforcement ratio may have a similar effect on the behavior and shear strength of these specimens. This potential effect, however, has not been studied thoroughly. Thus, the effect of slab flexural reinforcement ratio on the behavior and shear strength of slab-column connections reinforced with headed shear studs was studied in this research investigation.

### 2.4.2 Tests of Slab Systems

This section reviews the results from two experimental programs conducted by Hatcher et al[57] at the University of Illinois and Guralnick and La Fraugh[58] at the Portland Cement Association (PCA) laboratories. The primary objective of these tests was to study moments in two-way slab system[59], and thus the slabs were designed so that shear failures were not expected in the tests. The average slab flexural reinforcement ratio was approximately 1% and 0.5% for column and middle strips in these slabs, respectively. Test results from these studies indicated that significant yielding of slab flexural reinforcement near the columns might have a significant effect on the shear strength of slab-column connections in the flat plate systems.

#### *2.4.2.1 Tests of quarter-scale slab systems*

In 1961, Hatcher et al[57] reported test results for two quarter-scale reinforced concrete slab systems, including one flat plate and one flat slab. The tests were conducted to study the behavior of these beamless slab systems. The prototypes for these systems are shown in Fig. 2-18. The flat plate was designed as a slab in a typical apartment building (Fig. 2-18a), while the flat slab, with capitals and drop panels at columns (Fig. 2-18b), was designed as a slab in a building for light storage. The two slab systems were designed in accordance with the empirical method specified in the 1956 ACI Building Code[32]. These slab systems were tested in a series of tests under service loads first, and then they were uniformly loaded on all slab panels until failure. Test results showed that: 1) the flat plate system failed due to the punching shear failure at one interior slab-column connection (Column 7 in Fig. 2-18a), while the flat slab system failed in a flexure mode, 2) the measured load for Column 7 at punching failure was smaller than the calculated punching shear strength given by the ACI Code[34], and 3) significant yielding of slab flexural reinforcement was developed near interior columns before punching shear occurred.

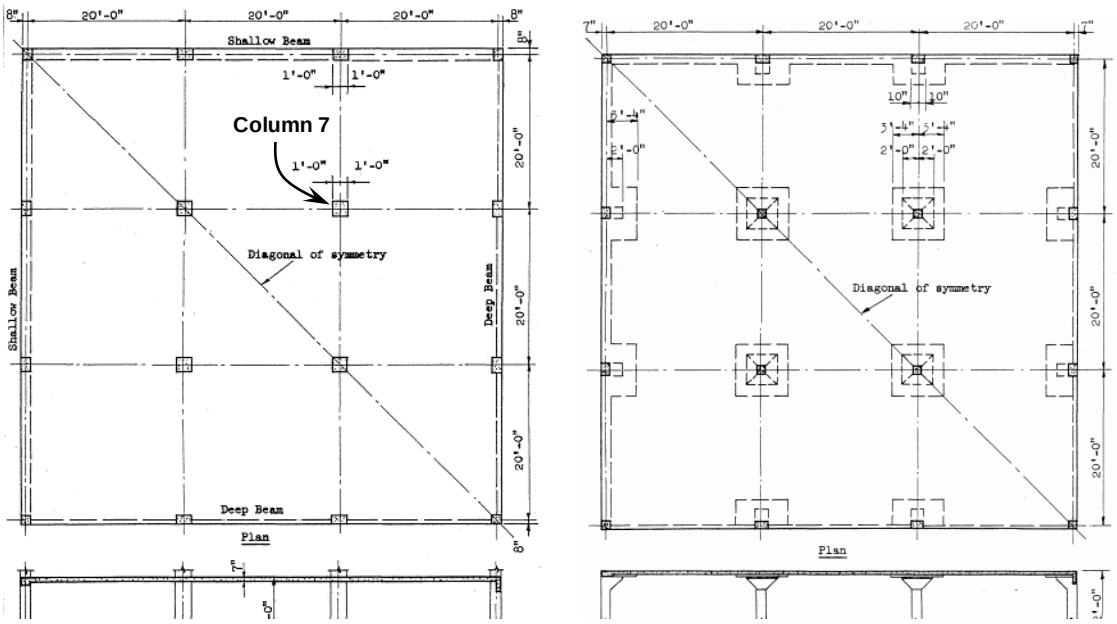


a) flat plate system b) flat slab system

*Fig. 2-18:Prototypes of slab systems tested by Hatcher et al*[57]

Relationships between applied load and slab displacement measured at midspan of the interior panel for the two systems are shown in Fig. 2-19. The flat plate system showed a significant decrease in its stiffness at an applied load of approximately 260 psf (12.4 kPa), and failed when the applied load reached 360 psf (17.2 kPa). This failure was due to the punching shear failure at Column 7, and a sketch that shows the base of punching cone is given in Fig. 2-20 (a). Fig. 2-19 also shows that the load-displacement curve for this system did not level off before failure and the measured stiffness of the system near failure ($E_1$) was more than 10% of its measured initial stiffness ($E_0$). This suggested that the flat plate system would have had a higher load carrying capacity if punching shear failure did not occur. For a comparison, the measured load-displacement curve for the flat slab system levelled off at a displacement of approximately 0.4 in. (10 mm), and after that the applied load was constant while the slab displacement increased to approximately 0.6 in. (15 mm). The flat slab ultimately failed in a flexural mode[57] (a so-called folding mechanism), as shown in Fig. 2-20 (b).

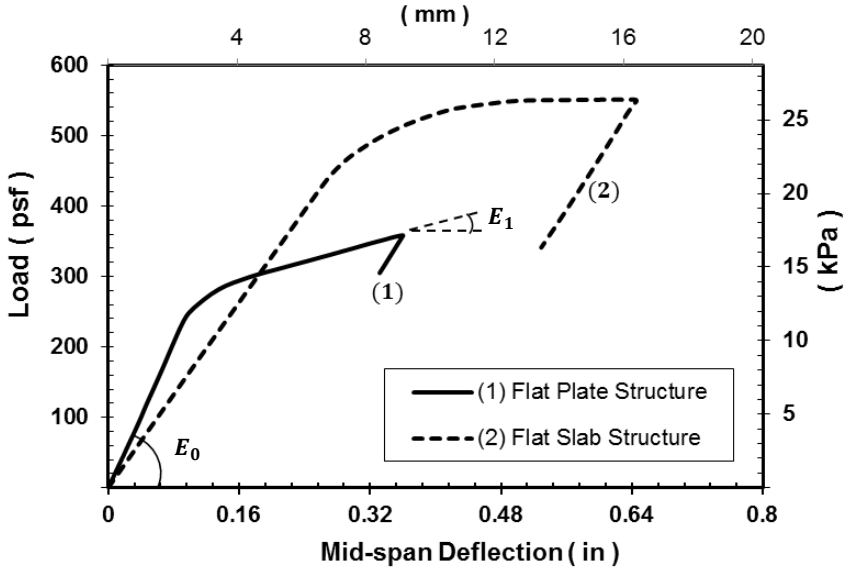


*Fig. 2-19:Load vs. displacement response for two slabs tested by Hatcher et al[57]*

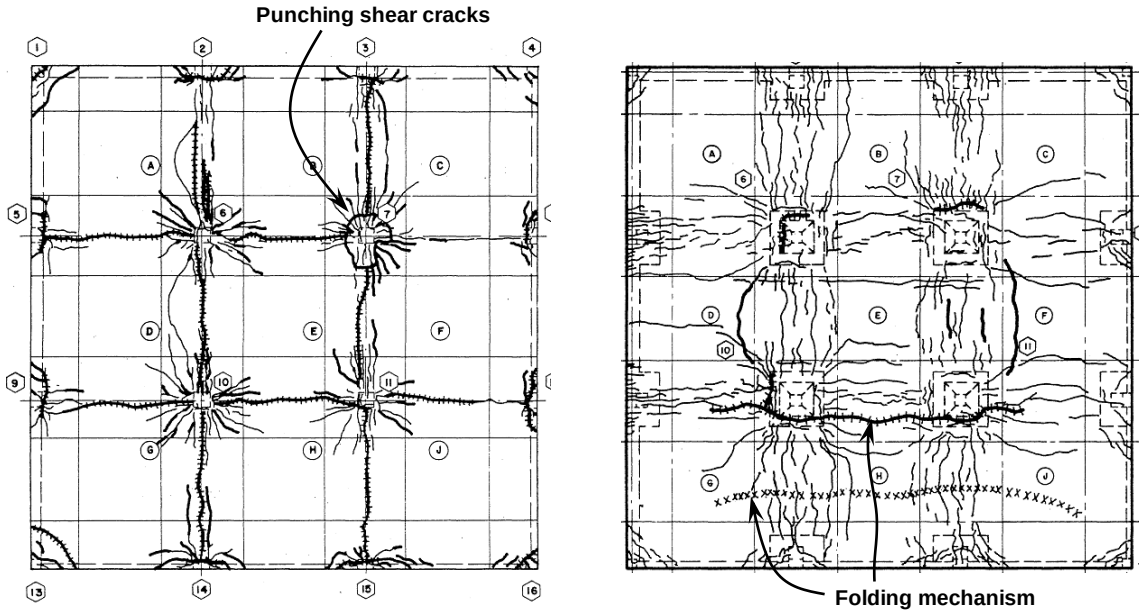


a) Flat plate system b) Flat slab system

*Fig. 2-20:Crack pattern on the top surface of the slabs after the failure tests of two slab systems by Hatcher et al[57]*

The test results also showed that the measured shear transfer at Column 7 near the failure of the flat plate system was 7.5 k (33.4 kN), and this measured shear strength was significantly smaller than the ACI Code[34] calculated shear strength (Eq. 6) of 10.95 k (48 kN)[57]. If

unbalanced moment was accounted in the calculation[57], the ultimate shear strength of the slab region near Column 7 was 8.1 k (36 kN), which was approximately 8% higher than the measured failure load[59].

For the flat plate system, measured strains in the top slab bars near Column 7 indicated that a significant yielding of slab flexural reinforcement developed before punching failure occurred at this column. This yielding of slab flexural reinforcement was also indicated by extensive number of radial cracks developed near Column 7, as shown in Fig. 2-20 (b). These radial cracks formed initially near the periphery of Column 7 and then extended radially away from it. At punching failure, these radial cracks were located in a region that was approximately bounded by a contra-flexure line around Column 7.

Although only one flat plate system was tested by Hatcher et al[57], test results from this study suggested that significant yielding of slab flexural reinforcement near the columns may have had a significant effect on the shear strength of the slab-column connection and the behavior of the slab system.

#### *2.4.2.2 Tests of three-quarter-scale flat plate system*

In 1963, test results of a flat plate system was reported by Guralnick and La Fraugh[58], and this report indicated that significant yielding of slab flexural reinforcement affected punching shear strength at slab-column connections. The test slab system was a three-quarter-scale model of the prototype system shown in Fig. 2-18 (a), which was designed for the quarter-scale slab systems tested by Hatcher et al[57]. In the Guralnick and La Fraugh[58] study, the slab was also loaded in a series of tests with service loads first, and then all panels of the slab were loaded uniformly to failure. Results from the failure test (Fig. 2-21) were found to be closely in agreement with that from the previous tests of smaller scale slabs by Hatcher et al[57]. Punching shear failure at Column 7 (Fig. 2-21a) caused the ultimate failure of the slab system, and the slab system still showed a considerable positive stiffness at failure (Fig. 2-21b). The measured shear strength for Column 7 was 25% smaller than the calculated shear strength given by the ACI Code[34]. Guralnick and La Fraugh[58] commented that the significant difference between the measured and calculated shear strengths might be related to the slab rotations induced by extensive yielding of the negative slab flexural reinforcement near the columns. These rotations

may have caused diagonal cracks to penetrate into the compression zone, thus precipitating the punching shear failure.

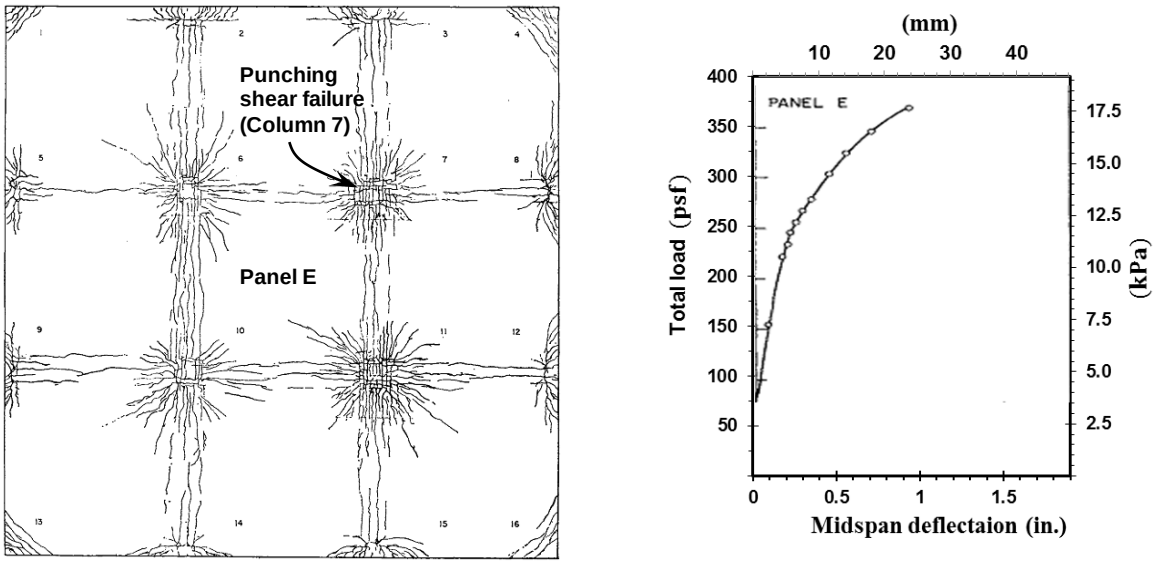


a) Crack pattern on the top of the slab b) Load versus deflection

*Fig. 2-21: Test results by Guralnick and La Fraugh[58]*

Test results of slab systems reported by Hatcher et al[57] and Guralnick and La Fraugh[58] showed that although the slabs were designed with the calculated shear strength of the slabs higher than their calculated flexural strength ($\phi_0(\text{system}) \geq 1$), punching shear failures still occurred before flexural mechanisms completely developed in the systems. The significant yielding of the slab flexural bars near the columns before punching failure suggested that the slab flexural reinforcement ratio should be considered in the ACI Code design specifications for two-way shear at slab-column connections.

## 2.5 EFFECT OF OTHER FACTORS ON PUNCHING SHEAR STRENGTH

The effects of shear stud layout and slab flexural reinforcement ratio were presented in the two previous sections. This section presents the effect of other factors on punching shear strength of slab-column connections. These factors are important in the design of experimental programs to study punching shear failure at slab-column connections.

### 2.5.1 Effect of Test Setup on Punching Shear Strength

Punching shear at slab-column connections has often been tested using a subassembly of a column and the adjacent slab regions, isolated from a flat plate system. It has been shown that the test boundary conditions and any in-plane confinement will affect the ultimate shear strength of the isolated slab-column specimens.

#### *2.5.1.1 Boundary Conditions*

The effect of boundary conditions on the ultimate shear strength of slab-column connections was reported by Sherif[59]. In his report, test results from Elstner and Hognestad[60] were reviewed. For these tests the specimens were built almost identically, but they were supported in three different conditions: continuous supports on four edges, continuous supports on two opposite edges, and point supports at four corners (Fig. 2-22). Measured shear strength of these specimens was computed for the critical perimeter at $d/2$ from the column faces. The results showed that the measured shear strength significantly increased as the number of supported slab edges increased.

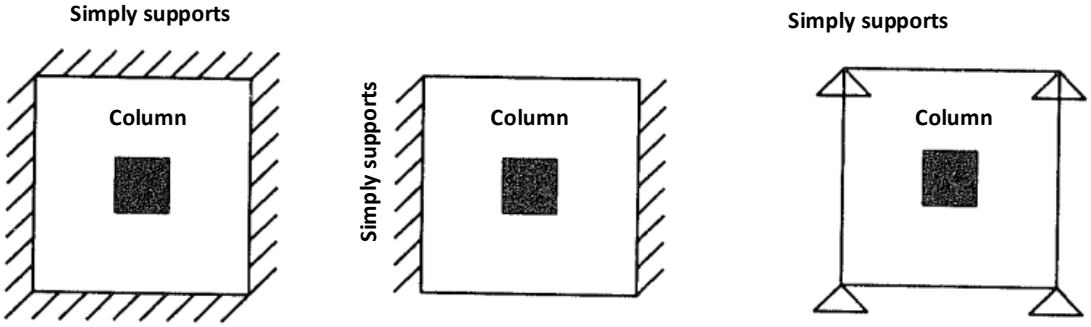


a) supports at 4 edges b) supports at 2 edges c) supports at 4 corners

*Fig. 2-22:Different boundary conditions tested by Elstner and Hognestad[60]*

*Typical test specimens for interior slab-column connections*—to minimize test setup complexity, a column and the slab region bounded by the contra-flexure line around it are usually isolated for testing. The contra-flexure line is located at approximately 20 percent of a span length ($L$) from the column (Fig. 2-23a), and thus, slabs for test specimens are ideally circles with a diameter of 0.4$L$. For construction convenience, regular octagons and squares are often used (Fig. 2-23b). Test specimens are often supported along the slab periphery and loaded at the columns, and they are sometime flipped over to reduce the complexity of support systems. The slabs can be supported continuously or discretely, for test convenience, along the slab edges. To be equivalent to continuous supports[61], discrete support systems should have at least eight discrete "points" that are uniformly distributed on a circle with a diameter of 0.4$L$.

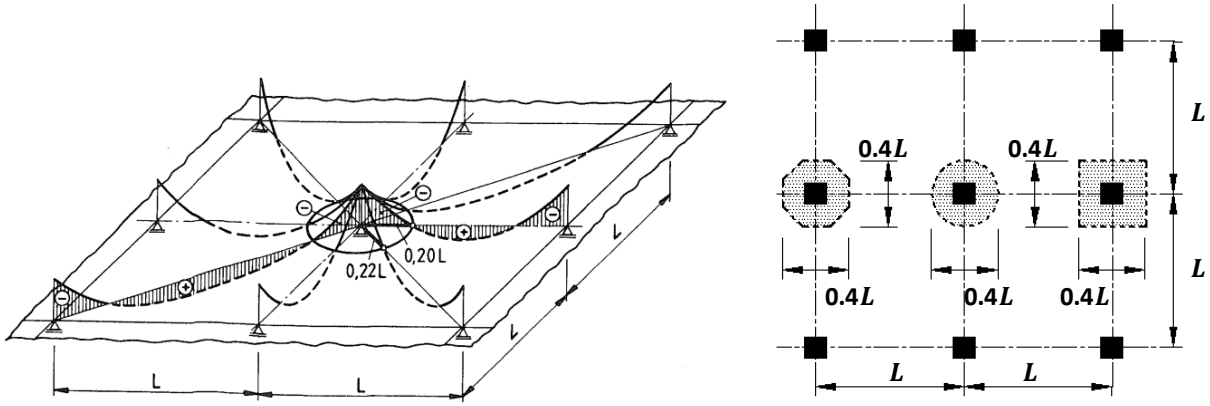


*a) Distribution radial bending moment*[20] *b) Portion of slab to be modeled*

*Fig. 2-23: Boundary of the slab in test specimens for interior slab-column connections*

### *2.5.1.2 In-plane Confinement*

In-plane confinement, a so-called compressive membrane action, will increase shear strength of slab-column connections. This confinement effect is self-generated if in-plane outward displacements, induced by yielding of slab reinforcement surrounding the column, are restrained[8]. This effect was evaluated through tests of seventeen slab-column specimens by Rankin and Long[62]. The slabs in these test specimens were squares with two different widths of 0.4$L$ and $L$ (Fig. 2-24), but they were all simply supported by a 0.4$L$ square steel frame. The smaller slabs were to represent a slab region bounded by a contra-flexure line, while the larger slabs were to represent a slab region from midspan to midspan between columns in a flat plate system. Test results indicated that the measured punching shear strength of specimens with the

slabs that extended beyond the support was higher than the measured shear strength of specimens with the smaller slabs. These results suggested that in-plane confinement increased shear strength of slab-column connections. However, values of in-plane confinement forces have not been measured. The effect of in-plane confinement is usually neglected in tests of typical isolated slab-column specimens, thus results from those tests are conservative.

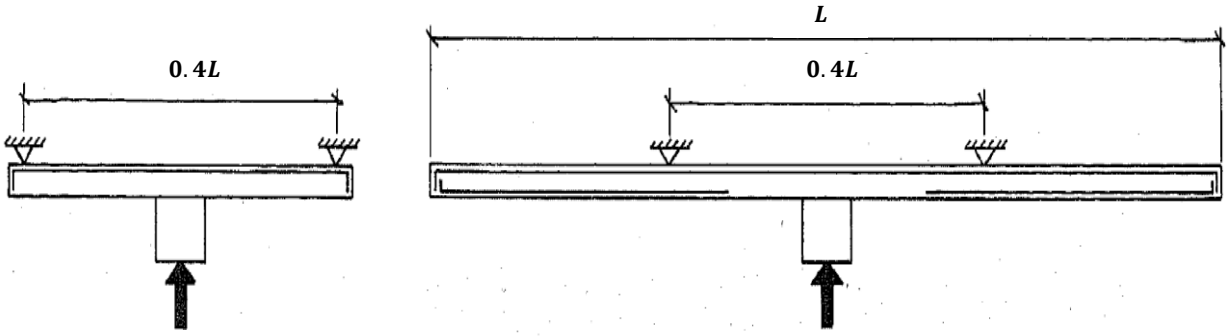


a) conventional specimens b) extending slab width specimens

*Fig. 2-24:Different slab widths tested by Rankin and Long[62]*

### 2.5.2 Concrete Compressive Strength

Shear strength of slab-column connections has been found to be proportional to the compressive strength of slab concrete ($f_c'$). A linearly proportional relationship between the ultimate shear strength of slabs and $f_c'$ was used until the 1963 ACI Code (Eq. 8), when Moe proposed that the ultimate shear strength should be represented by the square root of concrete compressive strength ($\sqrt[2]{f_c'}$). This square root relationship is used in most modern Building Codes, except the fib Model Code 90[63].

The fib Model Code 90[63] relates punching shear strength to the cubic root of concrete compressive strength ($\sqrt[3]{f_c'}$). Fig. 2-25 plots measured shear strength of slabs from different tests[60, 64, 65]versus the concrete compressive strength. In this figure, measured shear strengths were normalized by the cubic root of slab flexural reinforcement ratio ($v_u/\sqrt[3]{100\rho}$). Two relationships between punching shear strength versus $\sqrt[2]{f_c'}$ and $\sqrt[3]{f_c'}$ are also plotted in the figure. It can be seen from Fig. 2-25 that the cubic root curve presented the test data better than the square root curve.

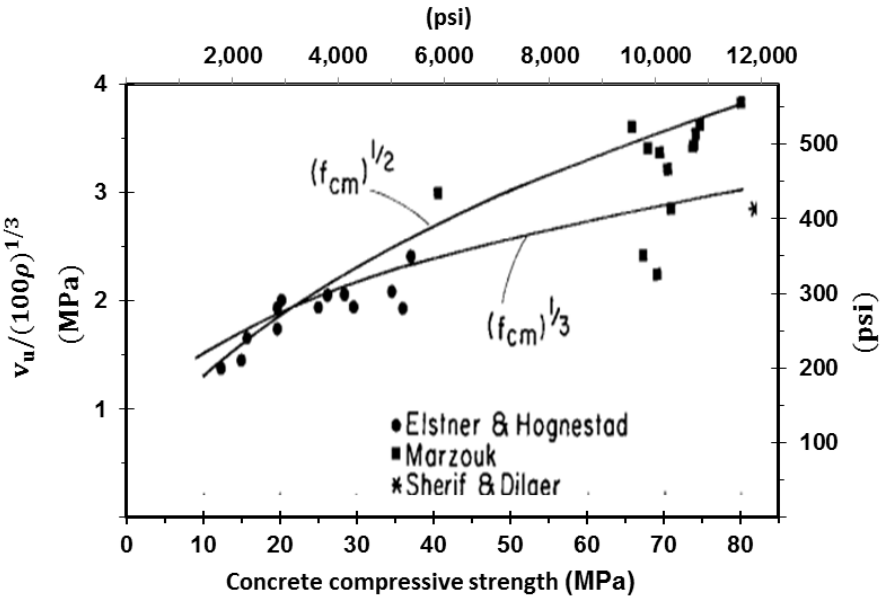


*Fig. 2-25: Effect of concrete strength and flexural reinforcement*[47]

### 2.5.3 Shear Stress Distribution at Column Perimeter

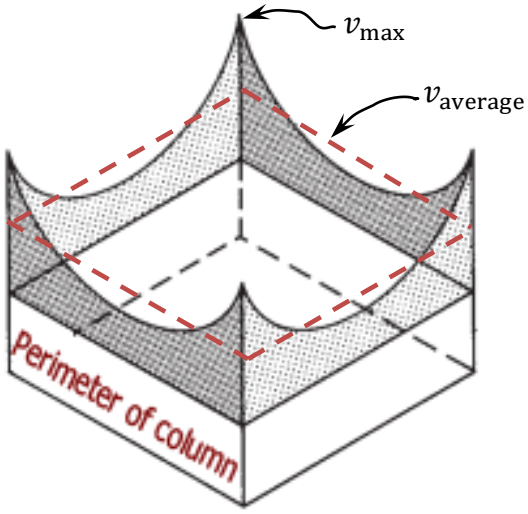


*Fig. 2-26: Shear stress distribution along the periphery of a column*[3]

Shear stress distribution along the periphery of a rectangular column is not uniform. As shown in Fig. 2-26, shear stresses highly concentrate at the corners of the column, and thus, punching shear failures more likely initiate near these locations. The punching shear strength of slabs, on the other hand, is normally evaluated using the average shear stress (a dashed line in Fig. 2-26). The difference between the average shear stress and the maximum shear stresses near the corners is significant when either the column cross section is long and narrow or column

dimensions are significantly larger than the slab flexural effective depth. For these cases, calculated punching shear strength given by Eq. (6) may overestimate shear strength of slab-column connections. For circular columns, shear stresses distribute more uniformly along column perimeters, so the measured shear strength for circular connections with a similar column area is usually higher than that for connections with rectangular columns.

#### *2.5.3.1 Aspect Ratio of Rectangular Columns*

Test results[8] have shown that measured shear strength of a slab-column connection reduces as the aspect ratio ($\beta$) of a rectangular column increases. $\beta$ is a ratio between the lengths of the long and short sizes of the column, and thus $\beta > 1$ for rectangular column and $\beta = 1$ for square columns. Measured shear strength from tests of slab-column specimens was plotted versus the ratio $\beta$ in Fig. 2-27[66]. The figure shows that measured shear strength of slab-column connection decreased as $\beta$ increased. Based on these results, the 1977 ACI Code[36] specified a new expression (Eq. 9) for shear strength of slabs. This expression is also plotted in Fig. 2-27. It can be seen that Eq. (9) governs over Eq. (8) if $\beta > 2$.

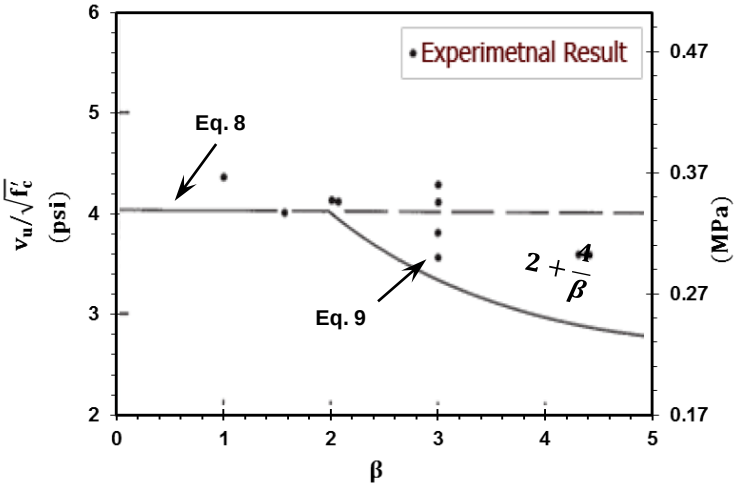


*Fig. 2-27: Effect of aspect ratio of rectangular columns[66]*

$$v_c = \left(2 + \frac{4}{\beta}\right)\lambda\sqrt{f'_c} \quad \text{(psi)} \qquad \textit{Eq. (9)}$$

$$v_c = 0.083\left(2 + \frac{4}{\beta}\right)\lambda\sqrt{f'_c} \quad \text{(MPa)} \qquad \textit{(9M)}$$

### *2.5.3.2 Critical Section Perimeter to Slab Depth Ratio*

Test results[38] have also shown that the punching shear strength of a slab-column connection is dependent on the ratio of $b_o/d$. In this ratio, $b_o$ is the perimeter of a critical section located at $d/2$ from the column faces, and $d$ is the slab effective flexural depth. Measured shear strength from tests[38] of slab-column specimens with different column shapes and sizes were plotted versus the ratio $b_o/d$ in Fig. 2-28. The figure shows that the shear strength of slab-column connections decreased as the ratio $b_o/d$ increased. Based on these results, the 1989 ACI Code[37] specified a new expression for two-way shear strength of slabs. This expression is given in Eq. (10) and also plotted in Fig. 2-28. In this expression, parameter $\alpha_s$ varies depending on the location of a column in slab systems, and it is set to 40, 30, and 20 for interior, edge, and corner columns, respectively. As shown in Fig. 2-28, for interior columns, Eq. (10) governs over Eq. (8) if $b_o/d > 20$.

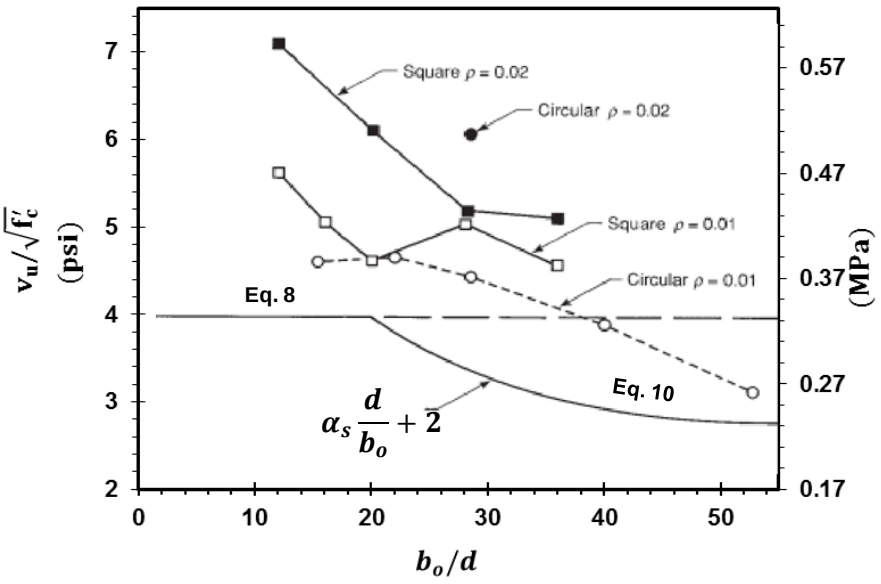


*Fig. 2-28: Effect of perimeter to depth ratio[66]*

$$v_c = \left(2 + \alpha_s \frac{d}{b_0}\right)\lambda\sqrt{f_c'} \quad \text{(psi)} \qquad \textit{Eq. (10)}$$

$$v_c = 0.083\left(2 + \alpha_s \frac{d}{b_0}\right)\lambda\sqrt{f_c'} \quad \text{(MPa)} \qquad \textit{(10M)}$$

### 2.5.4 Slab Thickness

Measured shear strengths of slab-column connections have been shown to decrease as the slab thickness increased (size effect). Test results reported by Guandalini and Muttoni[67] and Birkle and Dilger[61] showed that measured shear strengths of the slab-column specimens with a slab thickness of 11.8 and 19.7 in. (300 and 500 mm) were approximately 90% and 65% of the corresponding nominal shear strength given by the ACI Code, respectively. This size effect was also reported by other studies[68-70]. Based on these test results, Sherif and Dilger[70] suggested that the ACI Code should account for size effect if slab thickness is more than 12 in. (300 mm).

### 2.5.5 Concrete Cover

The effect of concrete cover on shear strength of slab-column specimens was evaluated by Alexander and Simmonds[71]. In their evaluation, Specimens P38S150 and P11S150 were identical except for the cover of the slab flexural tension reinforcement. The cover was 1.5 in. (38 mm) for Specimen P38S150 and 0.43 in. (11 mm) for Specimen P11S150. The slabs in these specimens were both 6 in. (150 mm) thick, and thus the effective depth of the slab in Specimen P38S150 was smaller than that in Specimen P11S150. According to the ACI Code[37], the calculated shear strength for Specimen P38S150 should have been 27% lower than that for Specimen P11S150. However, the measured shear strength for the two specimens were similar. These test results indicated that an increase in the concrete cover increased shear strength of the slab-column connections. Other studies[47, 72] also suggested that a total slab thickness, instead of an effective depth, should be used to calculate punching shear strength.

### 2.5.6 Test Specimen Slenderness

The slenderness of a slab-column specimen, or the shear span ratio[73, 74], is defined as a ratio of $l/2d$ ($l$ is the diameter of a circular slab or the width of a square slab, i.e. $l = 0.4L$). The effect of specimen slenderness on punching shear strength of slabs was studied by Einpaul et al[75]. In this study, three specimens, PP4, PP5, and PP6, were almost identical except for the slab widths. The slabs in these specimens were 10 in. (250 mm) thick squares, and the width of these slabs was 5.58, 7.55, and 12.8 ft (1.7, 2.3, and 3.9 m) for Specimen PP4, PP5, and PP6, respectively. Thus, the slenderness ratio for the three specimens increased from PP4, to PP5, and

to PP6. Test results of the three specimens (Fig. 2-29) showed that measured shear strength of these specimens decreased as the specimen slenderness increased.

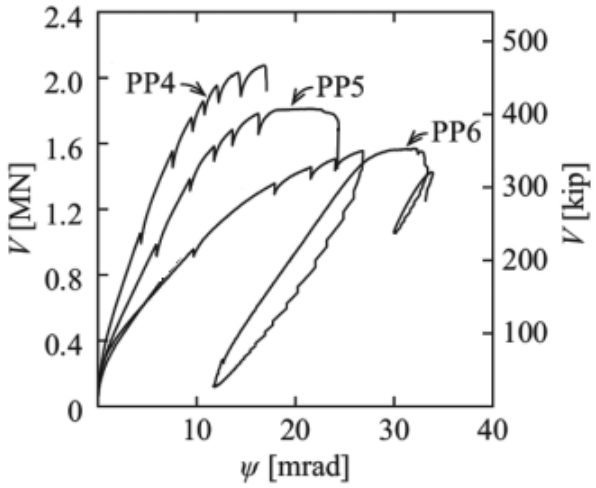


*Fig. 2-29: Effect of a specimen slenderness*[66]

## 2.6 FINITE ELEMENT MODELING OF SLAB-COLUMN CONNECTIONS

Since the first application of the finite element (F.E) method to the analysis of reinforced concrete beams was presented by Ngo and Scordelis[76] in 1967, the F.E. method has been used extensively to simulate the behavior of various reinforced concrete structures. This section presents a review of simulation studies using F.E. for reinforced concrete slab-column connections. These connections have often been simulated by either two- or three-dimensional models. Studies that used two-dimensional models are reviewed in Subsection 2.6.1, while studies that used three-dimensional models are reviewed in Subsection 2.6.2.

### 2.6.1 Two-Dimensional Models

A 2D nonlinear F.E. for reinforced concrete slabs was developed by Hueste and Wight[77] to study punching shear failures. This element behaved similarly to reinforced concrete beam elements prior to the prediction of punching shear failures. These failures were assumed to occur when the calculated rotations at the ends of the element exceeded the maximum allowable rotation based on test results of isolated slab-column specimens. The developed element was used to evaluate the behavior of a four story reinforced concrete building that experienced punching shear failures during the Northridge earthquake. The study results showed that the occurrence of punching shear failures in the building was successfully post-calculated by the model (Fig. 2-30).

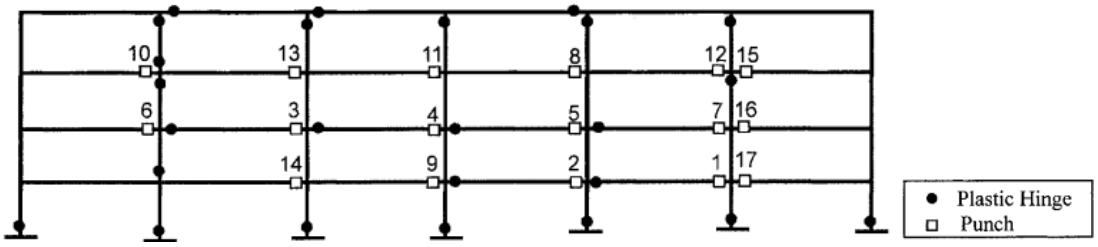


*Fig. 2-30: Prediction of punching failure and plastic hinges for a four stories building subjected to a ground motion[77]*

Tian[78] and others used a modeling approach similar to that used by Hueste and Wight[77]. Their results showed that beam-like elements were useful for studying the overall behavior of structures that experienced punching shear failures, but those models were not applicable for evaluating local behavior of slab regions near columns, e.g. crack propagation. To study such behavior, the use of other element types, such as four-node elements, is required.

A 2-D F.E. model using four-node quadrilateral elements was developed by Menetrey[79] to study punching shear failure at axisymmetric slab-column specimens. The model was used to simulate some circular slabs that were reinforced with ring reinforcement and tested by Kinnunen and Nylander[80]. As shown in Fig. 2-31, these slabs were modeled using four node quadrilateral axisymmetric elements (quad-axi), and the elements near the column were aligned to the direction of inclined cracks. The F.E. model accounted for the effects of radial and tangential cracks by relating the increment of crack opening to plastic strains, and it also considered the effect of three-dimensional stress conditions by using concrete failure criteria that were developed by Menetrey[81]. Results from this study showed that the ultimate loads given by the models agreed with the measured strengths from the tests, and inclined cracks near the column were also simulated (Fig. 2-31). The specimen stiffness given by the model, however, was significantly higher than the experimental results.

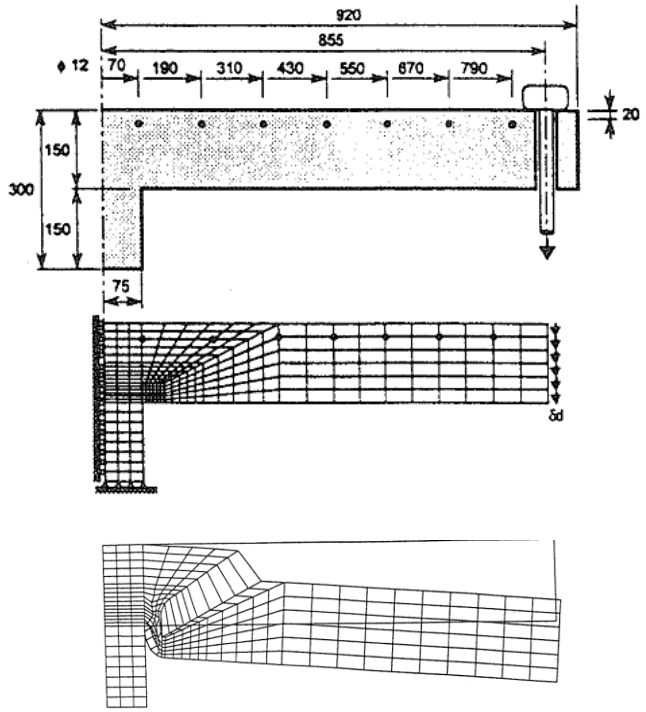


*Fig. 2-31: A 2D FE model for Kinnunen and Nylander[80] slabs by Menetrey[79]*

(*units shown are in mm, 1 in. = 25.4 mm*)

Using discretization approach similar to that used by Menetrey[79], other models were developed by De Borst and Nauta[82], Vidosa et al[83], Kheyroddin et al[84], and Hallgren and Bjerke[85]. Test results of these 2-D F.E. models demonstrated that these models were useful to

simulate axisymmetric slab-column specimens with ring reinforcement, but they were not applicable for general slab-column specimens that had columns with non-circle cross sections or slabs with orthogonal flexural reinforcement. To study these general slab-column connections, three-dimensional F.E. models are required.

## 2.6.2 Three-Dimensional Models

### *2.6.2.1 Shell Elements*

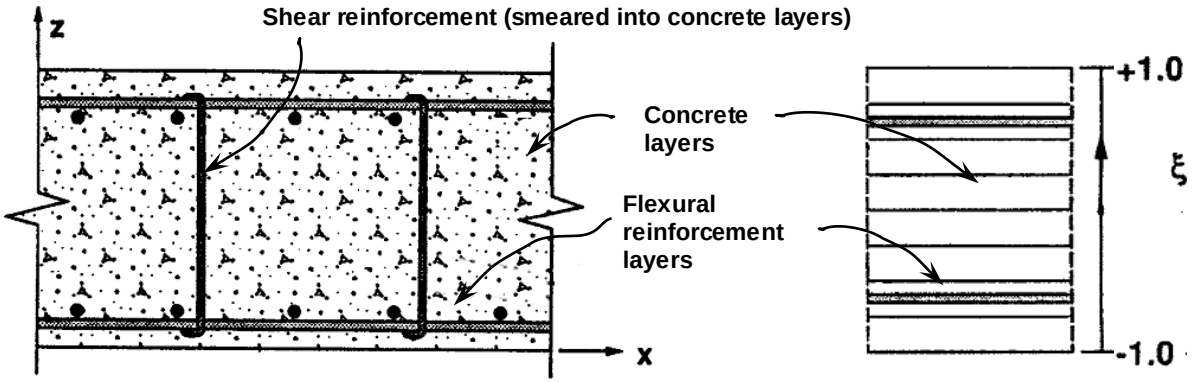


a) Reinforced concrete slabs with stirrups b) a layered shell element

*Fig. 2-32: A shell element for slabs by Polak[86]*

A 3-D F.E. model that consisted of layered shell elements was developed by Polak[86] to study shear behavior of reinforced concrete slabs. This F.E. model used the layered modeling approach (Fig. 2-32) that was often used to study the flexural behavior of slabs[87-93]. The significant feature of the shell elements used in this F.E. model was their ability to account for shear responses in the transverse direction of slabs. These shear responses were accounted for by incorporating into the shell elements the formation of a shear strain energy that was developed from Mindlin plate theory[94], so shear reinforcement in slabs could be modeled (smeared) as a property of the concrete layers (Fig. 2-32). Punching shear failures in the model were identified through either the failure of the concrete layers for slabs without shear reinforcement or a reduction in stiffness in the transverse direction of concrete layers for slabs with shear reinforcement. For verification, some slab-column specimens from other experimental studies[60, 95] were simulated using this F.E. model. The simulation results showed that the F.E. model was able to reproduce the ultimate loads and failure modes of the test specimens with good accuracy.

Using a layered modeling approach similar to Polak[86], other shell elements were also developed by Marzouk and Chen[96]. These shell element models of slabs were showed to be useful for global analyses of slab-column specimens and flat plate systems, but they were not suitable for analyses of local behavior at slab regions near the columns, e.g. the development of inclined cracks. To study such local behavior, slab-column connections need to be modeled using spatial 3-D continuum elements, e.g. 8-node cubical elements.

#### *2.6.2.2 Spatial 3-D Continuum Elements*

With a rapid and continuous development of computational technology, F.E. models with a large number of degrees of freedom and nonlinear material behavior have been able to be solved efficiently. This allows the use of three-dimensional continuum F.E. elements and more complicated material rules to model slab-column connections. In this subsection, a review of studies using spatial 3-D models to simulate slab-column specimens without or with shear reinforcement is presented.

##### *a) Specimens without shear reinforcement*

A 3-D F.E. model of slab-column specimens was presented by Xiao and O'Flaherty[97]. In this model, slabs were discretized and modeled by 3-D continuum elements (Solid65 in ANSYS), and the slab flexural reinforcement was defined (smeared) as material properties of the solid elements (Fig. 2-33). The model was used to simulate the behavior of a slab-column specimen tested by the authors. The simulation results showed a good agreement between the predicted and the measured failure load and deflection capacity. Because slab flexural reinforcement was smeared over the concrete elements, the effect of the interactions between slab flexural bars and concrete was not able to be considered by this and other similar models[98]. To model this interaction, flexural bars need to be modeled separately from the concrete elements.

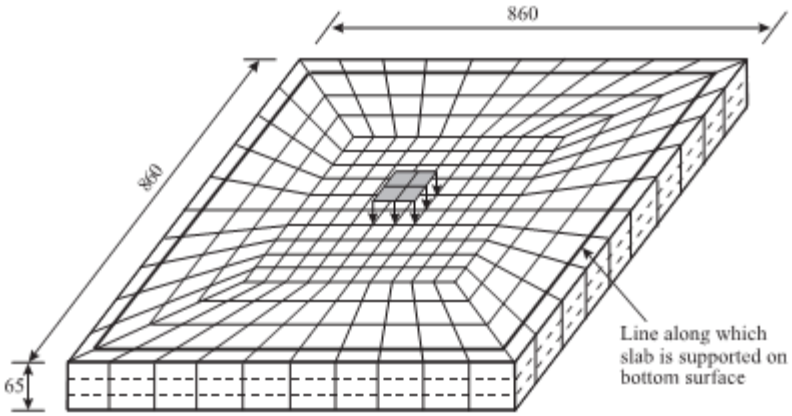


*Fig. 2-33: A 3-D F.E. model for slab-column specimens by Xiao and O'Flaherty[97]*

(units shown in mm, 1 in. = 25.4 mm)

A 3-D F.E. model, in which the concrete and flexural reinforcement were simulated separately, was presented by Winkler and Stangenberg[99]. In this model, as shown in Fig. 2-34, slab flexural reinforcement was not smeared over the cubical concrete elements, but modeled separately using 3-D truss elements. These truss elements were assumed to be perfectly bonded to the surrounding concrete elements by using an "embedded method" (in ABAQUS[19]). For the concrete elements, the behavior of concrete in three-dimensional stress stages was simulated by using the "concrete damaged plasticity" model[100, 101]. To define this concrete behavior, the uniaxial stress-strain relationships of concrete in compression and tension were adopted from the fib Model Code 2010[102] and Hordijk[103], respectively. For flexural reinforcement elements, a bilinear stress-strain relationship was used. The set of nonlinear equations from the F.E. model was solved using the "modified Riks method". This F.E. model was used to simulate a slab-column specimen tested by Li[104]. The simulation results (Fig. 2-35a) showed that predicted shear strength given by the model was similar (2% different) to the measured maximum load, but the F.E. model exhibited a significantly higher cracking strength and larger displacement capacity than the test results. Also, the predicted inclined cracks near the column (Fig. 2-35b) were steeper than the observed cracks. Using a similar discretization approach, other models were also developed by Xiao and Chin[105] using ANSYS and by Malvar[106] using ADINA. Results from these simulation studies showed that these 3-D F.E. models were very promising for studying the effects of various factors on the behavior of slab-column connections.

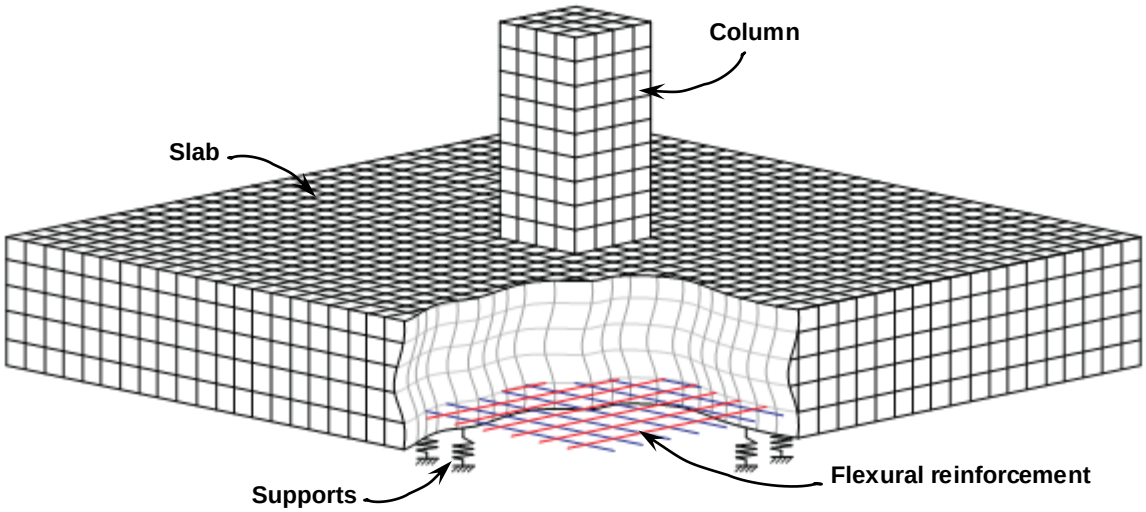


*Fig. 2-34: A 3-D F.E. model for slab-column specimens by Winkler and Stangenberg[99]*

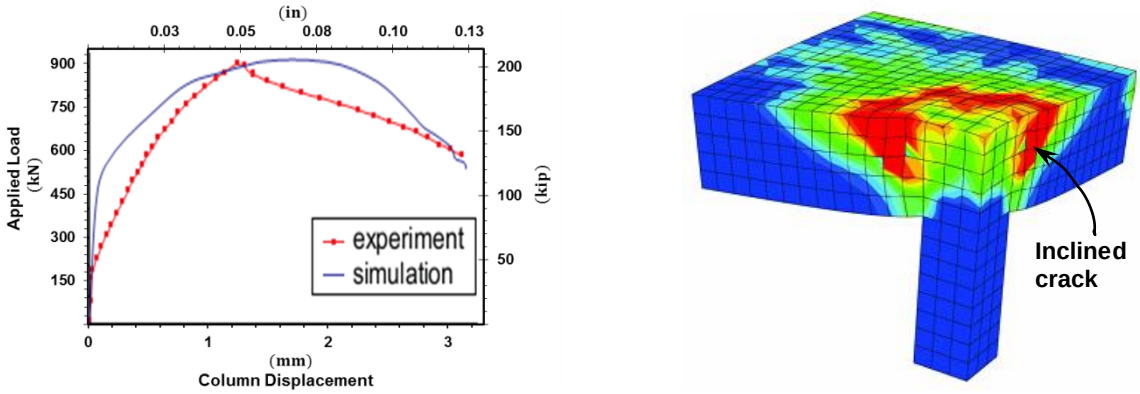


a) Load-column displacement relationship b) Crack pattern

*Fig. 2-35: Simulation results by Winkler and Stangenberg[99]*

The effects of two nonlinear material models for concrete on the simulation of slab-column specimens was reported by Wosatko et al[107] in 2014. In this study, "gradient-enhanced scalar damage" and "concrete damaged plasticity" models for the concrete elements were compared. A 3-D F.E. model similar to Winkler and Stangenberg[99] (Fig. 2-34) was used to simulate a slab-column specimen tested by Adetifa and Polak[108]. The simulation results (Fig. 2-36) showed that the two material models for concrete provided similar results, but cracking strength and the initial and post-cracking stiffness given by the two models were higher than the measured results. The overestimations of cracking strength and specimen post-cracking stiffness, however, were smaller for the model using "concrete damaged plasticity". In this study, predicted

strengths given by the F.E. models were found to be significantly dependent on a viscosity parameter (μ), which is used in "concrete damaged plasticity" model.

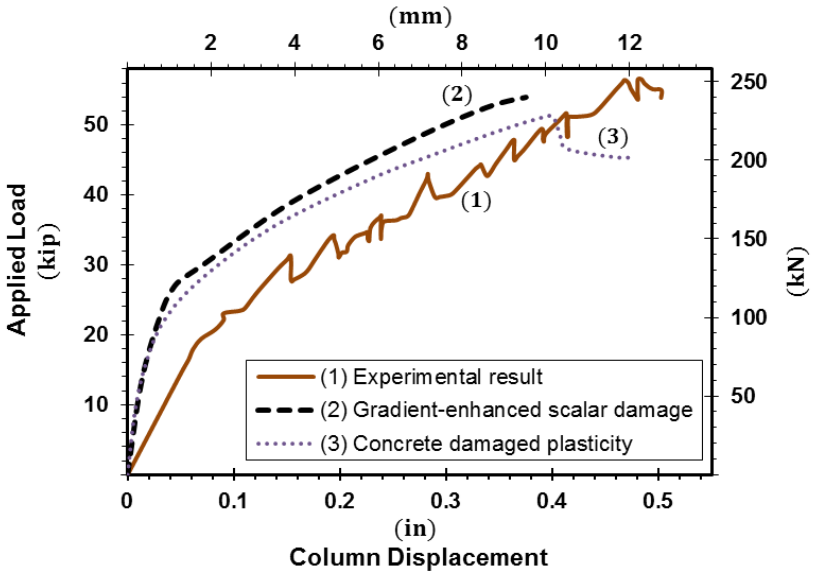


*Fig. 2-36: Simulation results by Wosatko et al[107]*

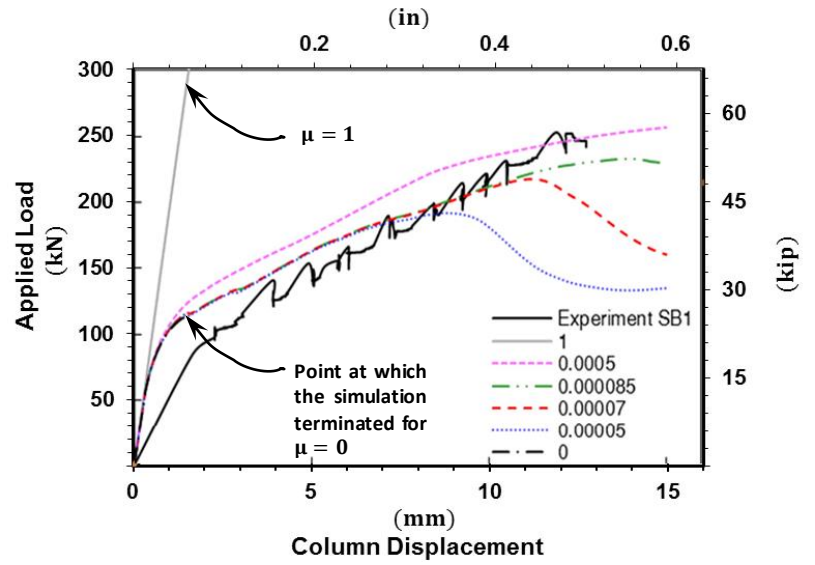


*Fig. 2-37: Effect of the viscosity parameter (μ) reported by Genikomsou and Polak[109]*

The effect of the viscosity parameter (μ) on the simulation of slab-column specimens was studied by Genikomsou and Polak[109, 110]. The viscosity parameter represents the relaxation time of the viscoplastic system, and it is used to regulate the singularity in the plastic multiplier by permitting stresses to be outside of the yield surface[101]. In this study, a 3-D F.E. model similar

to the Winkler and Stangenberg[99] model (Fig. 2-34) was used to simulate Specimen SB1 tested by Adetifa and Polak[108]. The model was analyzed using ABAQUS/Standard[19] (static analysis), and the value of the viscosity parameter varied from 0 (a default value in ABAQUS[19]) to 1. Results from this study (Fig. 2-37) showed that the analysis for $\mu = 0$ was aborted soon after the cracking point, but as $\mu$ increased the analyses could proceed further and resulted in higher ultimate strengths. For $\mu = 1$, the model response was similar to a linear elastic behavior. The simulation results also showed that the value of $\mu = 85$E-6 provided the best simulation results for Specimen SB1. In general, Lee and Fenves[101] suggested that $\mu$ should be set as small as possible, and 15 percent of the time increment step should be a sufficient value for $\mu$.

### *b) Specimens reinforced with shearhead reinforcement*

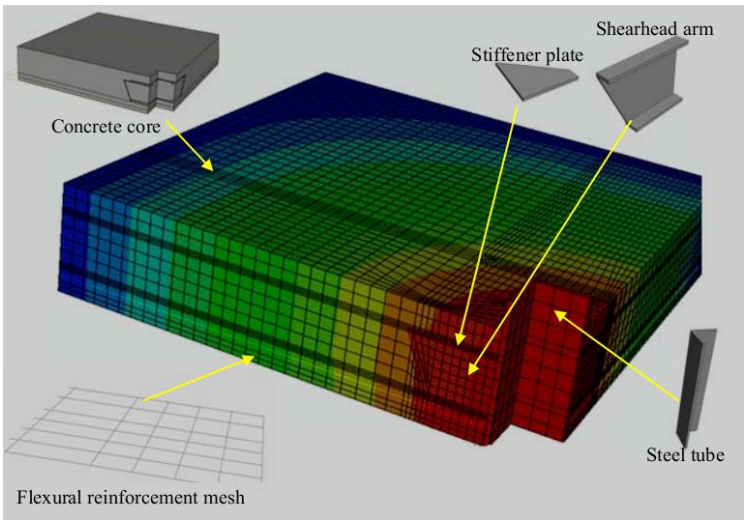


*Fig. 2-38: 3-D F.E. model for slab-column specimens by Yan[111]*

A 3-D F.E. model was developed by Yan[111] to study slab-column specimens reinforced with shearhead reinforcement, which were also tested by the author. In this model, the concrete and flexural reinforcement were discretized similarly to the Winkler and Stangenberg[99] model (Fig. 2-34), and the shearhead arms and stiffeners were modeled by using shell elements (Fig. 2-38). The shell elements for the shearhead arms were "embedded" in the surrounding concrete elements. The "concrete damaged plasticity" model was used for slab concrete elements, and a bi-linear stress-strain relationship was used for slab flexural and shearhead reinforcement. The simulation results for Specimen 2[111] (Fig. 2-39) showed that shear strength given by the model

was similar to the measured strength, but the initial stiffness and the cracking strength of the model were significantly higher than the experimental results.

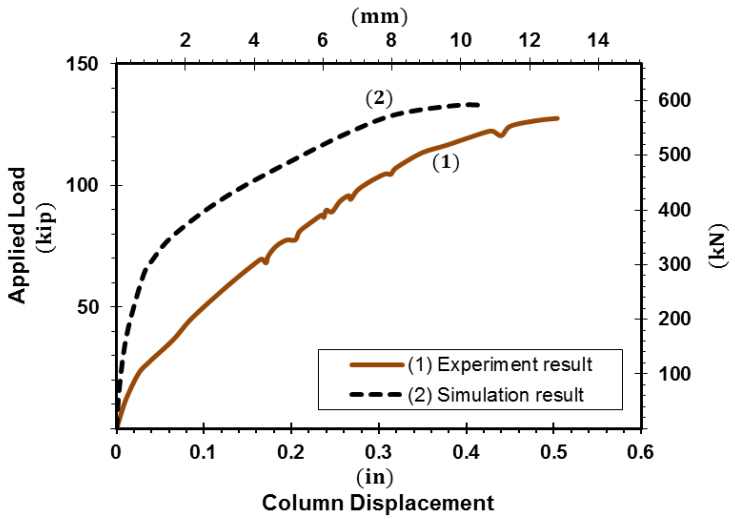


*Fig. 2-39: Simulation results by Yan[111]*

### *c) Specimens retrofitted with shear bolts*

Four approaches to model shear bolts that were used to retrofit slab-column specimens[108] were presented by Genikomsou et al[112]. These modeling approaches were studied with a 3-D F.E. model of slab-column specimens similar to Winkler and Stangenberg[99] (Fig. 2-34). In Approach 1, as shown in Fig. 2-40 (a), the modelling of each shear bolt consisted of a vertical truss element for the shank and two pairs of horizontal truss elements for the head and washer. These pairs of elements were then constrained to the top and bottom surface of concrete elements, and the initial prestressed forces in the shear bolts were neglected. In Approach 2, shear bolt regions were approximated as flange beams (Fig. 2-40b). Simulation results for Specimen SB2 tested by Adetifa and Polak[108] showed that the model behavior given by Approaches 1 and 2 were similar [lines (2) and (3) in Fig. 2-41], and the predicted shear strengths were significantly lower than the measured strength of Specimen SB2. These results indicated that there was no significant difference between the uses of truss or shell elements for shear bolts. In Approaches 3 and 4, the modeling of shear bolts was similar to Approach 1. The differences between Approach 1 and the last two approaches were that additional horizontal spring connections were added at the slab supports for Approach 3 (Fig. 2-40c), and the dilation angle (a parameter in "concrete damaged plasticity" model) was increased for Approach 4 (Fig. 2-40d). Simulation results for these two approaches [lines (4) and (5) in Fig. 2-41] showed that

the behavior and shear strength of the F.E. model were close to the experimental results. However, the value of the spring stiffness used in Approach 3 and the increase in dilation angle used in Approach 4 were not physically justified by the authors.

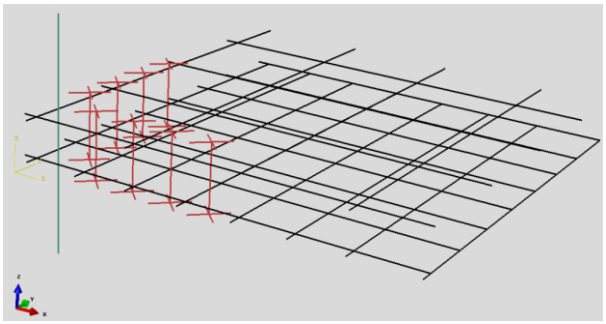

a) Modeling approach 1

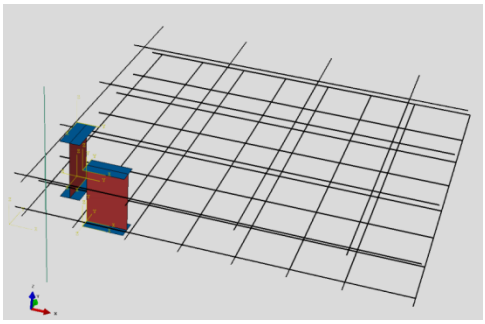

b) Modeling approach 2

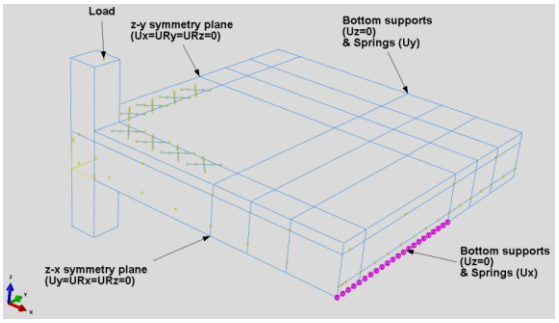


c) Modeling approach 3

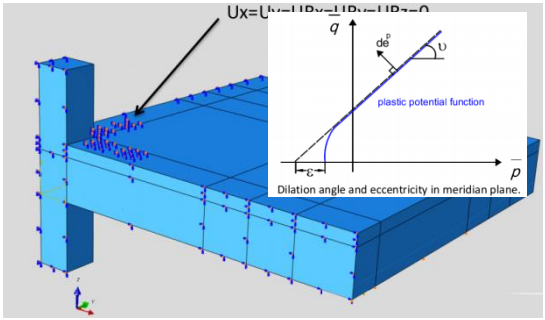


d) Modeling approach 4

*Fig. 2-40: Modeling approaches for shear bolts by Genikomsou et al[112]*

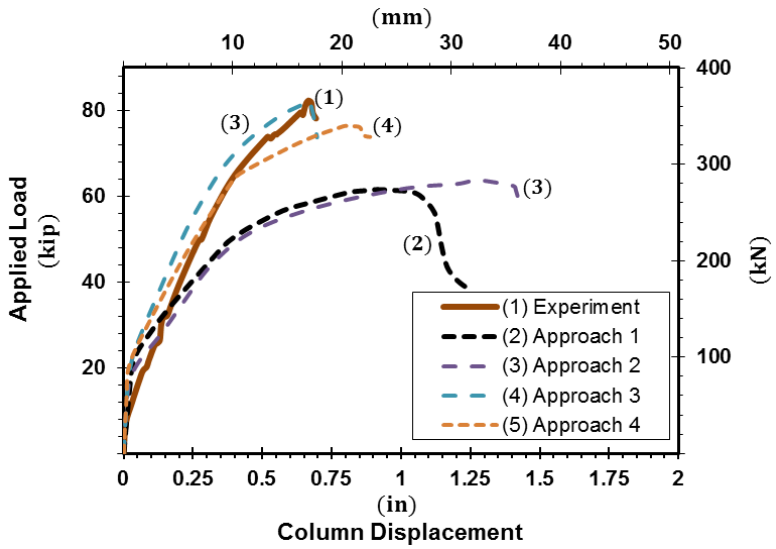


*Fig. 2-41: Simulation results by Genikomsou et al[112]*

### *d) Specimens reinforced with shear stud reinforcement*

This section has shown that the finite element method has been used to analyze many applications of slab-column connections, the failure of the connections reinforced with shear stud reinforcement or stirrups, however, has not been analyzed yet. To study the effect of a shear stud layout and other factors on the behavior of slab-column connections, these connections should be modeled using spatial 3-D F.E. models. The development of this 3-D finite element model is presented in Chapter 6.

# CHAPTER 3
# EXPERIMENTAL PROGRAM

The review of research investigations in Chapter 2 has shown that the behavior and shear strength of slab-column connections are significantly affected by the layout of headed shear studs and the slab flexural reinforcement ratio. A larger number of slab-column specimens built with a relatively low (typical) slab flexural reinforcement ratio and an orthogonal (popular) stud layout failed prematurely in punching shear. The measured shear strength for these specimens was considerably lower than the nominal shear strength given by the ACI Building Code. These test results have raised major concerns over the safety of flat plate systems that have been built with headed shear stud reinforcement in North America. For public safety, investigations of the effects of shear stud layout and slab flexural reinforcement ratio on the behavior and shear strength of slab-column connections are required.

This chapter presents an experimental program of five full-scale slab-column connections with different shear stud layouts and slab flexural tension reinforcement ratios. The sections in this chapter are as follows:

- Section 3.1 describes the five slab-column specimens,
- Section 3.2 elaborates on the design of the test specimens,
- Section 3.3 shows the construction of the test specimens,
- Section 3.4 provides the measured material properties for the test specimens, and
- Section 3.5 presents the test setup used in the program.

## 3.1 DESCRIPTION OF TEST SPECIMENS

The test specimens were designed to represent interior slab-column connections from a typical reinforced concrete flat plate system with 10 in. (254 mm) thick slabs supported by 12 in. by 12 in. columns (305 mm by 305 mm) approximately 25 ft (7620 mm) apart (Fig. 3-1). They all had the same geometry, in which the slab was 10 ft by 10 ft (3050 mm by 3050 mm) square, and the columns were located at the center of the slab. The specimens were rotated to be up-side down for testing convenience. For each test specimen, a vertical load was applied downward on top of the column and the slab were supported at eight different "points" that were uniformly distributed on a 10 ft. (3050 mm) diameter circle to represent the contra-flexure (inflection) line (Fig. 3-2). With this test specimen design, moments generated in the specimens were assumed to be similar to the moments in the flat plate system (refer to subsection 2.1.2).

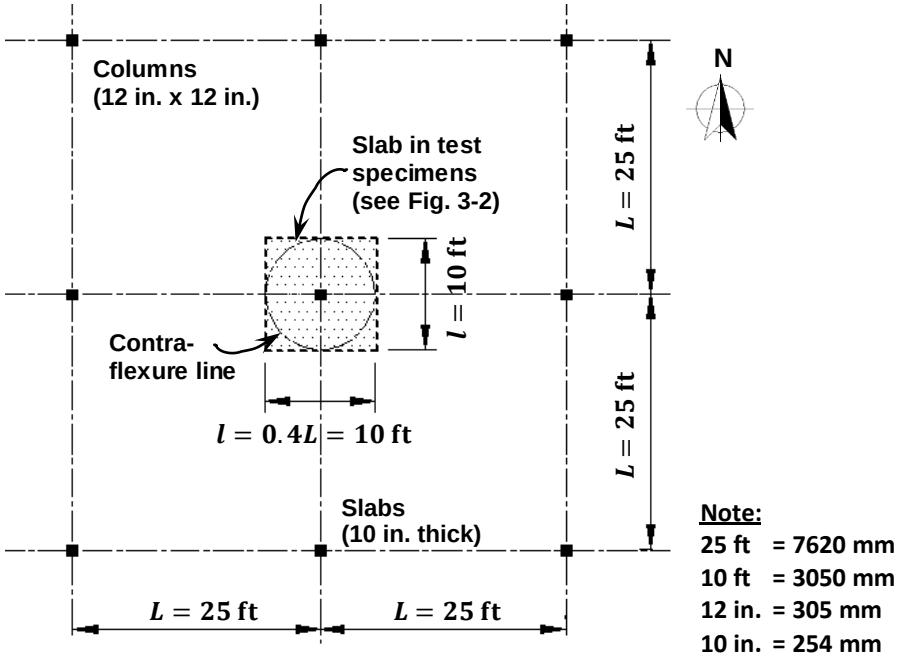


*Fig. 3-1: Size of test specimens*

One of the five test specimens (S08C) was built without shear reinforcement and served as a control specimen, while the remaining specimens were reinforced with the same amount of shear stud reinforcement. The target slab shear stress, calculated at a vertical section located at d/2 from the column periphery, was $4\sqrt{f_c'}$ psi ($0.33\sqrt{f_c'}$ MPa) for Specimen S08C and $6\sqrt{f_c'}$ psi ($0.50\sqrt{f_c'}$ MPa) for the other test specimens. The four specimens reinforced with shear studs

were divided into two groups with different slab flexural reinforcement ratios. These ratios were relatively low (0.87 %) for Group 1, Specimens S08O and S08R, and they were relatively high (1.25 %) for Group 2, Specimens S12O and S12R. In each group, the shear studs were arranged in either an orthogonal or radial layout for the two specimens. The descriptions of the test specimens are given in Table 3-1.

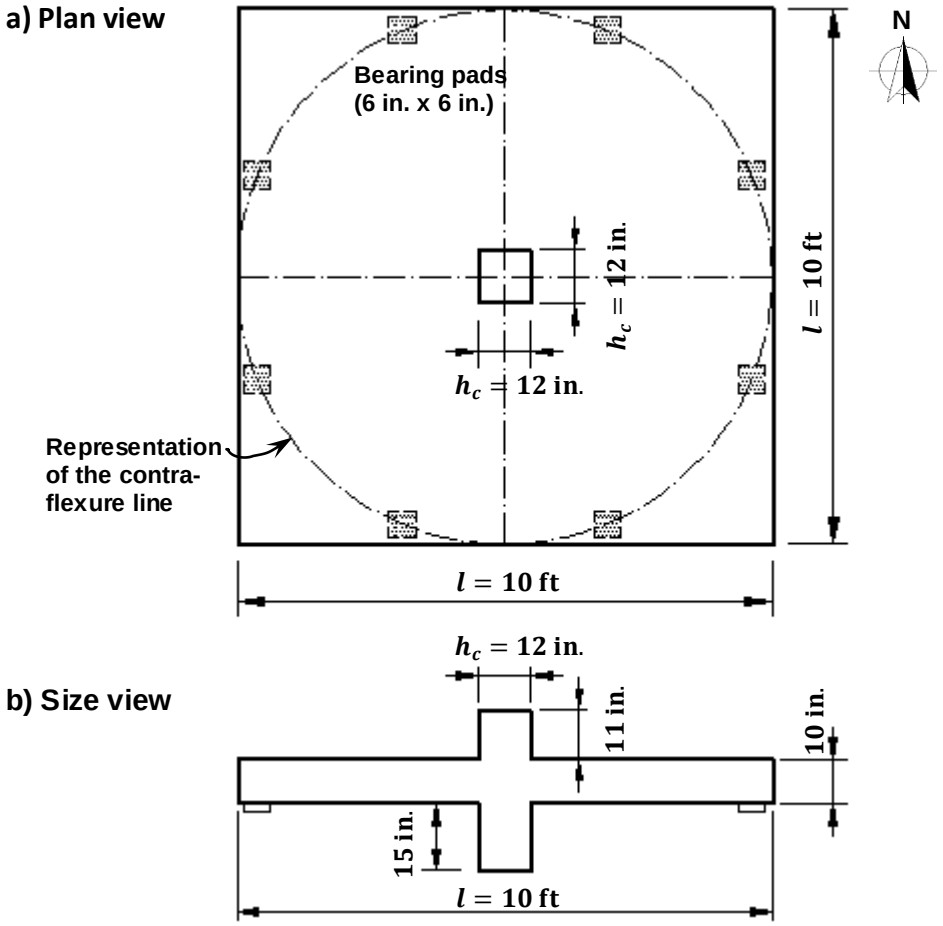


*Fig. 3-2: Test specimen dimensions*

*(units are in ft and in.; 1 ft = 305 mm, and 1 in. = 25.4 mm)*

*Labels of test specimens*—the letter S stands for "Specimen", and the numbers 08 and 12 represents the approximate slab flexural reinforcement ratio (0.87% and 1.25%). Specimen S08C was built without shear reinforcement and served as a Control specimen. The remaining four specimens were reinforced with the same number of shear studs configured in two different layouts. For Specimens S08O and S12O, stud rails were placed in an Othogonal layout, and for Specimens S08R and S12R, the stud rails were arranged in a Radial layout.

*Table 3-1: Test specimen descriptions*

| Specimen label | Slab flexural reinf. ratio, $\rho$ | Shear reinf. | Shear stud layout | Target shear stress psi (MPa) | Note |
|---|---|---|---|---|---|
| (1) | (2) | (3) | (4) | (5) | (6) |
| S08C | 0.87 % | NO | - | $4\sqrt{f'_c}$ ($0.33\sqrt{f'_c}$) | Control specimen |
| S08O | 0.87 % | YES | Orthogonal | $6\sqrt{f'_c}$ ($0.50\sqrt{f'_c}$) | Group 1 (relatively low $\rho$) |
| S08R | 0.87 % | YES | Radial | $6\sqrt{f'_c}$ ($0.50\sqrt{f'_c}$) | |
| S12O | 1.25 % | YES | Orthogonal | $6\sqrt{f'_c}$ ($0.50\sqrt{f'_c}$) | Group 2 (relatively high $\rho$) |
| S12R | 1.25 % | YES | Radial | $6\sqrt{f'_c}$ ($0.50\sqrt{f'_c}$) | |

## 3.2 DESIGN OF TEST SPECIMENS

Because the specimens, applied loads, and support systems were symmetric about the center of the columns, it was assumed that the resultant of the forces acting on the specimens passed through the center of the columns. And thus, no moments were transferred from the slabs to the columns. Also, flexural reinforcement was Grade 60 (ASTM A615[113], $f_y$ =60 ksi), shear stud reinforcement was Grade 1010-1020 (ASTM A29[114], $f_{yt}(\text{minimum}) = 51$ ksi[115]), and the specified concrete compressive strength, $f'_c$, was 4000 psi (27.6 MPa). The test specimens were designed in accordance with the 2014 ACI Building Code[5].

### 3.2.1 Shear Design

According to the ACI Code[5], nominal shear strength, given as a stress ($v_{shear} = V_{shear}/b_0 d$), of the test specimens was computed from Eq. (12),

$$v_{shear} = v_c + v_s \qquad \textit{Eq. (12)}$$

in which $v_c$ and $v_s$ were shear strength provided by the concrete and shear reinforcement, respectively. For Specimen S08C without shear reinforcement, $v_s = 0$, and $v_{shear} = v_c = 4\sqrt{f'_c}$ psi ($0.33\sqrt{f'_c}$ MPa). For the specimens with headed shear stud reinforcement, $v_c = 3\sqrt{f'_c}$ psi ($0.25\sqrt{f'_c}$ MPa), and $v_s$ was computed from Eq. (13),

$$v_s = \frac{A_v f_{yt}}{b_0 s} \qquad \textit{Eq. (13)}$$

where $A_v$ is the total stud area for each peripheral line of shear studs, $b_0$ is the perimeter of a critical section located at $d/2$ from the column periphery, and $s$ is the spacing between peripheral lines of shear studs (or distance between two adjacent studs on each stud rail). Stud rails were extended far enough from the column faces, so the shear stress computed at a critical section at $d/2$ outside the outermost shear studs would not exceed $2\sqrt{f_c'}$ psi ($0.17\sqrt{f_c'}$ MPa).

Specimen S08C was built without shear reinforcement, so the nominal shear strength of this specimen was $4\sqrt{f_c'}$ psi ($0.33\sqrt{f_c'}$ MPa). For the other test specimens, the target shear stresses were $6\sqrt{f_c'}$ psi ($0.50\sqrt{f_c'}$ MPa), and thus headed shear studs were designed to provide an additional shear strength of $v_s = 3\sqrt{f_c'}$ psi ($0.25\sqrt{f_c'}$ MPa). To obtain this value, twelve identical stud rails[14], conforming to ASTM A1044[115], were used for each specimen. Each stud rail had eight identical #3 ($\phi$10 mm) shear studs (Fig. 3-3), and they were welded at a uniform spacing ($s$) of 4-1/8 in. (105 mm) on an 1 in. wide and 3/16 in. thick steel plate (25.4 and 4.8 mm). The total height of the stud rails was 8.5 in. (215 mm) to satisfy the requirements in the ACI Code[5]. Shear design calculations for all test specimens is given in Appendix A.1.1.

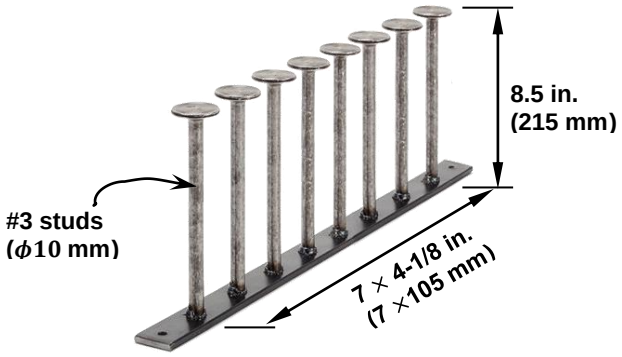


*Fig. 3-3: A typical stud rail used in the program[14]*

The stud rails were arranged in an orthogonal layout (Fig. 3-4a) for Specimens S08O and S12O, and in a radial layout (Fig. 3-4b) for Specimens S08R and S12R. The first studs were located at 3.75 in. (95 mm) away from the column faces or corners. The maximum peripheral spacing was smaller than $2d$ for the first three rows of shear studs in an orthogonal layout, and

for the first five rows in a radial layout (Fig. 3-4). Shear design descriptions for all test specimens are given in Table 3-1.

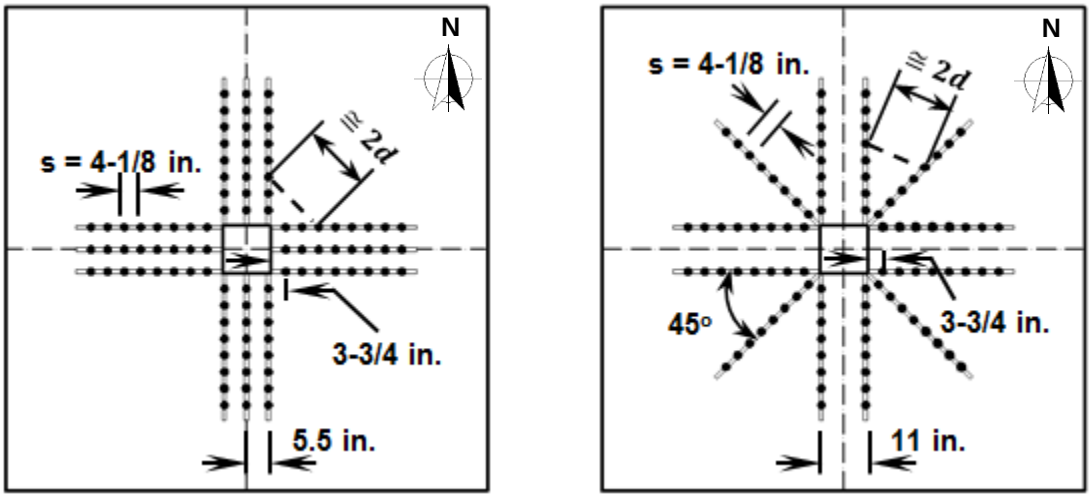


a) Orthogonal stud layout (S08O & S12O) b) Radial stud layout (S08R & S12R)

*Fig. 3-4: Shear stud layouts*

### 3.2.2 Flexural Design

Slab flexural reinforcement for the test specimens was designed so significant yielding of slab flexural reinforcement would take place (or flexural mechanisms would form) in some of the specimens before ultimate failure. Thus, the shear force required to develop a flexural mechanism in the test specimens ($V_{\text{flex}}$) was calculated. Yield line analysis[54] was used to calculate flexural strength of the test specimens ($V_{\text{flex}}$). Different possible flexural mechanisms for the test specimens were evaluated in Appendix A.1.2. The minimum value of $V_{\text{flex}}$ from those evaluations is given in the following expression,

$$V_{\text{flex}} = \frac{4\sqrt{2}}{cos(\frac{\pi}{8}) - \frac{h_c\sqrt{2}}{l}} m = 7.23m \qquad (18)$$

in which $h_c = 12$ in. (305 mm) was the column side dimension, $l = 10$ ft (7620 mm) was the specimen span length, and $m$ was the slab moment strength per unit width given in Eq. (19).

$$m \cong \left(1 - \frac{\rho f_y}{1.7 f_c'}\right) \rho f_y d^2 \qquad (19)$$

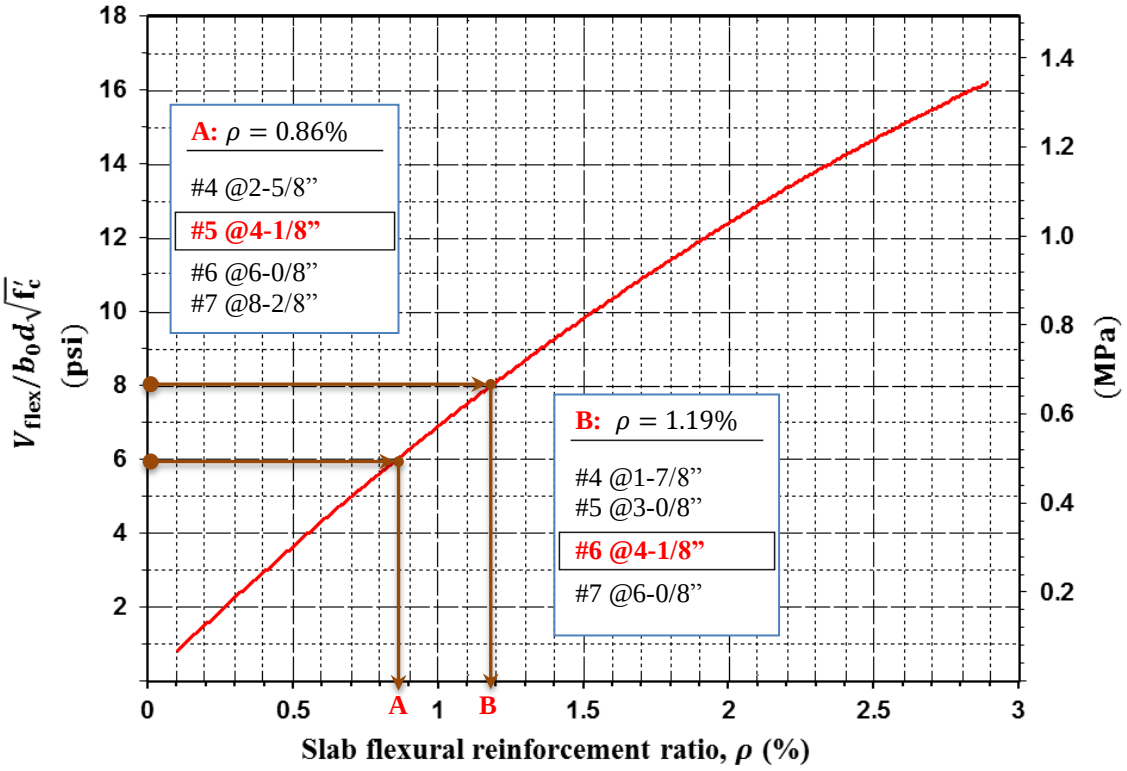


Fig. 3-5: Relationship between $v_{flex}$ and $\rho$

Equations (18) and (19) show that $V_{flex}$ was proportional to the slab flexural reinforcement ratio ($\rho$), and for the slab flexural effective depth ($d$) of 8.5 in. (216 mm), this relationship is plotted in Fig. 3-5. In this figure, the vertical axis presents the shear stress ($v_{flex}$) calculated at $d/2$ from the column faces, and $v_{flex}$ is given in the following equation.

$$v_{flex} = \frac{V_{flex}}{b_0 d} \qquad (20)$$

It is shown in Fig. 3-5 that slab flexure reinforcement ratios corresponding to $v_{flex}$ of $6\sqrt{f_c'}$ and $8\sqrt{f_c'}$ psi ($0.5\sqrt{f_c'}$ and $0.66\sqrt{f_c'}$ MPa) are approximately 0.86% and 1.19%, respectively. Different solutions of bar size and spacing for these values of $\rho$ are also shown in the figure. Two solutions of #5 bars for $\rho = 0.86\%$ and #6 bars for $\rho = 1.19\%$ were selected because they had the same spacing of 4-1/8 in. (105 mm). The selection of #5 bars was used for Specimens S08C, S08O,

and S08R, while the selection of #6 bars was used for the other two specimens, S12O and S12R. Because the specimens were tested up-side down, these bars, reffered to as tension reinforcement, were placed at the bottom of the slabs before casting the concrete. Assuming that the same spacing between slab flexural bars was used for two principle directions and the concrete cover was 3/4 in. (19 mm), the calculated average slab flexural reinforcement ratio was 0.87% for the S08 specimens and 1.25% for the S12 specimens.

The ACI Code[5] specifies two limits for slab flexural reinforcement. The first limit is the minimum area of slab flexural tension reinforcement per unit width of $0.0018t$, and for the test specimens $t = 10$ in. (254 mm). This leads to a minimum percentage of slab flexural reinforcement of approximately 0.21%. The second limit comes from the requirement that calculated strain in slab flexural reinforcement at nominal strength conditions must be at least 0.004. For the test specimens, this limit results in a maximum percentage of slab flexural reinforcement of approximately 2%. Thus, the two flexural reinforcement ratios of 0.87% and 1.25% for the test specimens satisfied the ACI Code limits for flexural design of two-way slabs.

Flexural reinforcement details for the test specimens are shown in Fig. 3-6. The compression (top) reinforcement in the slabs consisted of #4 bars ($\phi$13 mm) at a spacing of 6.5 in. (165 mm), with two bars passing through the column core (Fig. 3-6b) to satisfy the structural integrity requirement in the ACI Code[5]. The bars for the top and bottom layers were placed symmetrically about the center of the slabs. The column longitudinal reinforcement consisted of eight #8 bars, which were equally distributed around the column core. Ties were #3 bars ($\phi$10 mm) at a spacing of 3 in. (75 mm) along the entire column length. Because the specimens were tested up-side down, the stud rails were placed such that their base rails were above of the slab compression (Fig. 3-6b) reinforcement to represent their actual positions in practice.

Slab flexural reinforcement in Specimens S08O and S08R was expected to significantly yield before these specimens failed because the shear required to develop a flexural mechanism ($v_{\text{flex}}$) in the slabs was close to the nominal shear strength ($v_{\text{shear}}$) of these specimens ($6\sqrt{f_c'}$ psi or $0.5\sqrt{f_c'}$ MPa). For the other test specimens, punching shear failure was expected to govern their behavior.

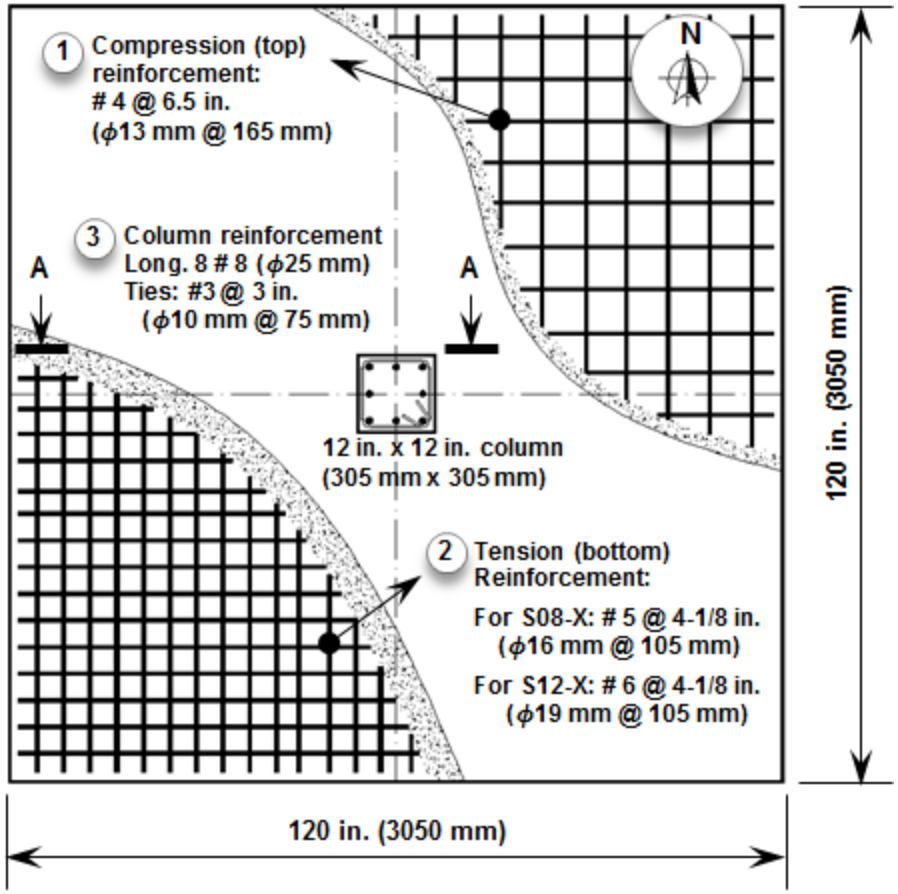


a) Top view

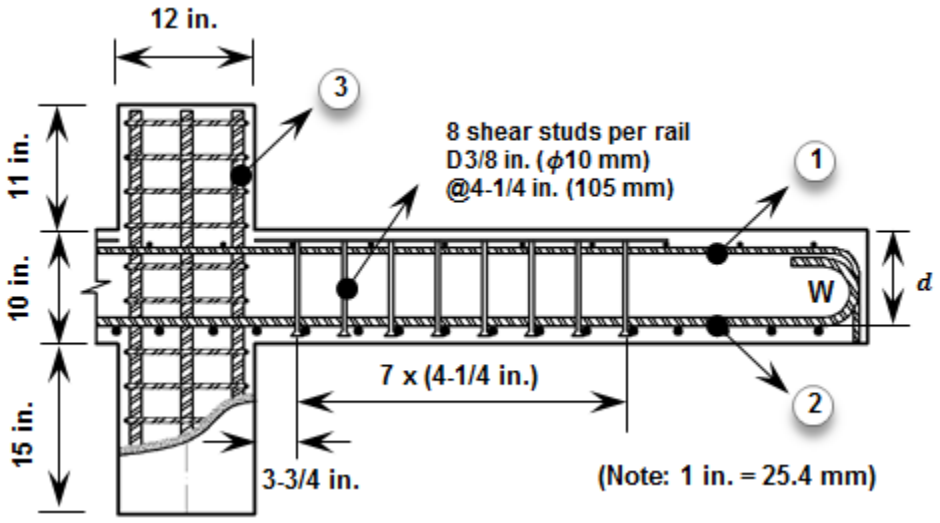


b) Section A-A in Fig. 3-6 (a)

*Fig. 3-6: Flexural reinforcement details*

## 3.3 CONSTRUCTION OF TEST SPECIMENS

All test specimens were constructed in the Structural Laboratory at the University of Michigan. This section presents construction of the test specimens, including attachment of strain gages to slab flexural bars and shear studs, installation of reinforcement, and concrete casting.

### 3.3.1 Strain Gages Attachment

*a. Surface preparation*

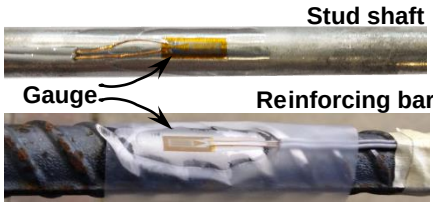


*b. Strain gauge attachment*


*c. M-Coat A coat*


*d. M-Coat B coat*


*e. Rubber-like tape*


*f. Waterproof liquid tape*

*Fig. 3-7: Strain gauge attachment steps*

To monitor strains in flexural and shear reinforcement during the tests, nearly 50 strain gauges, 0.2 in. (5 mm) long YFLA-5-5L gauges manufactured by Tokyo Sokki Kenkyujo Co., were attached at different locations on the slab reinforcing bars and shear studs for each test specimen. Each strain gauge was attached to the flexural bars or shear studs through the six steps shown in Fig. 3-7. First, a region of approximately 1 in. (25 mm) length (Fig. 3-7a) on the surface of the reinforcing bars or stud shafts was ground to remove bar ribs (if any), then smoothed by 220 to 260 grit sandpaper, and cleaned by a 6% phosphoric acid (M-PREP Conditioner A) and a neutralizer (M-PREP Neutralizer 5A). Second, the strain gauge was

aligned to the bar or stud longitudinal axis and glued to the surface (Fig. 3-7b) prepared in the previous step. When the glue dried completely, the surface and gauge were coated by a few layers of polyurethane and nitrile rubber coatings (M-COAT A and B), as shown in Fig. 3-7 (c) and (d). After the coatings were completely dry, this region was covered by a layer of electrical tape (rubber-like) to protect the gauge from damage in construction (Fig. 3-7e). Finally, regions around the rubber-like tape were covered by waterproof liquid tape (Fig. 3-7f).

### 3.3.2 Installation of Reinforcement

*a. Oil treatment for formwork*

*b. Slab bolsters placement*


*c. Top slab reinforcement installation*

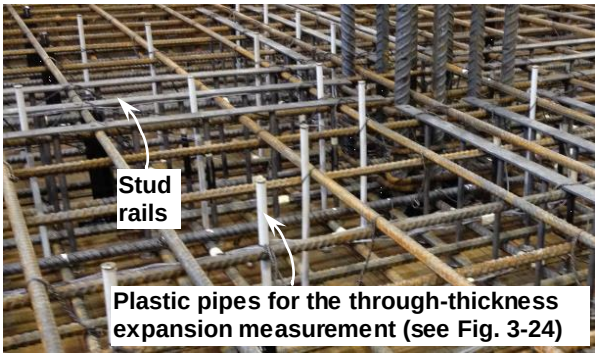


*d. Shear studs and plastic pipes configuration*

*Fig. 3-8: Installation of reinforcement*

The installation of flexural and shear reinforcement is shown in Fig. 3-8. After having the wooden formwork treated with concrete mold oil (Fig. 3-8a), slab bolsters of 3/4 in. (19 mm) height were placed on the formwork (Fig. 3-8b) to support the bottom slab reinforcing bars and provide a concrete cover layer. Then, the column and bottom slab reinforcement were installed and tied together using steel wires. After column stirrups through the depth of the slab were installed, the slab top reinforcing bars were placed using 8 in. (203 mm) high plastic rebar chairs

(Fig. 3-8c). Finally, the stud rails and plastic pipes (for the through-thickness strain measurement) were placed and tied to the slab reinforcing bars to avoid shifting during concrete casting (Fig. 3-8d).

### 3.3.3 Concrete Casting

*a. Pouring and vibrating*

*b. Concrete cylinders and beams making*

*c. Surface leveling*

*d. Concrete curing*

*Fig. 3-9: Concrete casting*

After the reinforcement was completely installed in the formwork, the slab and the bottom column stub were cast using normal weight ready-mix concrete supplied by a local concrete company, Doan Concrete Co.[116]. The concrete was delivered in one truck and poured into the formwork. A concrete vibrator was used to remove entrapped air and help consolidate the concrete (Fig. 3-9a). After concrete vibration, the top surface of the slab was leveled (Fig. 3-9c), and the specimen was covered for four weeks using a plastic sheet (Fig. 3-9d). Concrete cylinders (4 in. x 8 in. or 100 mm x 200 mm) and beams (6 in. x 6 in. x 30 in. or 150 mm x 150 mm x 760 mm), which were used to measure concrete compression and tension strength, were

also cast with the ready-mix concrete (Fig. 3-9b) and after three days they were demolded and submerged in a water tank for curing. After the slab concrete developed a sufficient strength, the top column stub was cast using concrete mixed in the laboratory. This same casting procedure was used for the five test specimens. In addition, blocks used to support the test specimens (refer to Subsection 3.5.1) were cast with the first two specimens using the ready-mix concrete (Fig. 3-10).

*Fig. 3-10: Cast concrete for supporting blocks.*

The ready-mix concrete was specified (Appendix A.2) to have a 28-days compressive strength of 4000 psi (27.6 MPa), a slump of 6 in. (150 mm), and a maximum aggregate size of 1/2 in. (13 mm). One mix design (Appendix A.2) was used for all test specimens and its weight proportion is shown in Table 3-2. The concrete mixed in the laboratory was also designed[117] to have a specified compressive strength of 4000 psi. The materials proportion for this concrete is shown in Table 3-3.

*Table 3-2: Material proportions per weight for the ready-mix concrete*

| Materials | Size / type | ASTM | Weight proportion |
|---|---|---|---|
| Cement | Type 1 | C-150 | 1.00 |
| Fly ash | Type F | C-618 | 0.37 |
| Water | Potable | C-94 | 0.74 |
| Fine aggregate | 2NS | C-33 | 5.05 |
| Coarse aggregate | 26-A | C-33 | 5.35 |

*Table 3-3: Material proportions per weight for the concrete mixed in the laboratory*

| Materials | Size / Type | ASTM | Weight proportion |
|---|---|---|---|
| Cement | Type 1 | C-150 | 1.00 |
| Water | Potable | C-94 | 0.44 |
| Fine aggregate | 2NS | C-33 | 2.32 |
| Coarse aggregate | 29-A | C-33 | 1.95 |

## 3.4 MATERIALS PROPERTIES

### 3.4.1 Concrete

Measured concrete properties of the slabs in all test specimens are given in Table 3-4. These concrete properties, including compressive strength, splitting strength, and modulus of rupture, are an average of results from uniaxial compression tests (Fig. 3-11), splitting tests (Fig. 3-12), and flexural strength tests (Fig. 3-13), respectively. In these tests, the concrete cylinders were 4 in. x 8 in. (100 mm x 200 mm) and the concrete beams were 6 in. x 6 in. x 30 in. (150 mm x 150 mm x 760 mm).Results from all of these tests are presented in Appendix B.1.

*Table 3-4: Measured properties of concrete at the testing days for all test specimens*

| Specimen | Compressive strength ($f_c'$), psi (MPa) | Splitting strength ($f_{ct}$) | | Modulus of rupture ($f_r$) | |
|---|---|---|---|---|---|
| | | psi (MPa) | $\sqrt{f_c'}$ psi ($\sqrt{f_c'}$ Mpa) | psi (MPa) | $\sqrt{f_c'}$ psi ($\sqrt{f_c'}$ Mpa) |
| S08C | 6100 (42.1) | 505 (3.48) | 6.47 (0.54) | 517 (3.57) | 6.62 (0.55) |
| S08O | 5050 (34.8) | 476 (3.28) | 6.70 (0.56) | 443 (3.06) | 6.23 (0.52) |
| S08R | 5360 (37.0) | 571 (3.94) | 7.80 (0.65) | 516 (3.52) | 7.05 (0.59) |
| S12O | 4510 (31.1) | 561 (3.87) | 8.35 (0.69) | * 658 (4.54) | * 9.80 (0.81) |
| S12R | 4790 (33.0) | 524 (3.61) | 7.58 (0.63) | 509 (3.51) | 7.35 (0.61) |

* Measurement on 33 days after the test date due to technical issues

*Fig. 3-11: Concrete compressive strength ($f_c'$) measurement (ASTM C39 [118])*

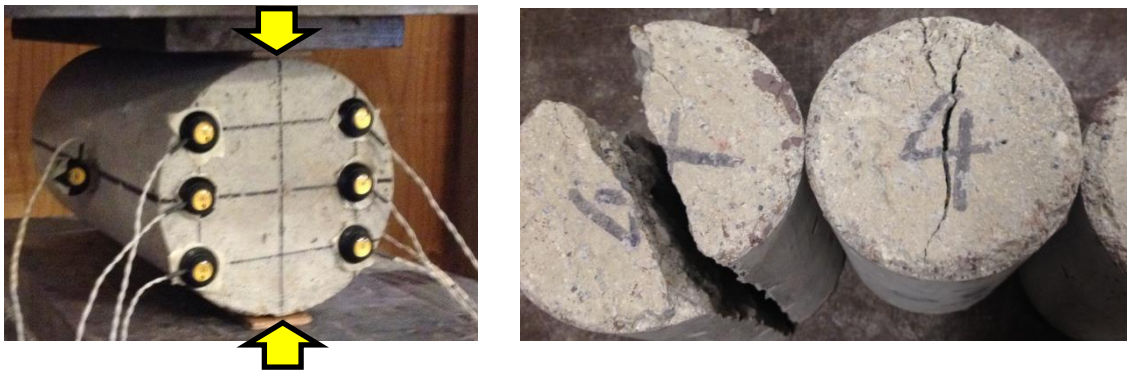

*Fig. 3-12: Concrete splitting strength ($f_{ct}$) measurement (ASTM C496 [119])*

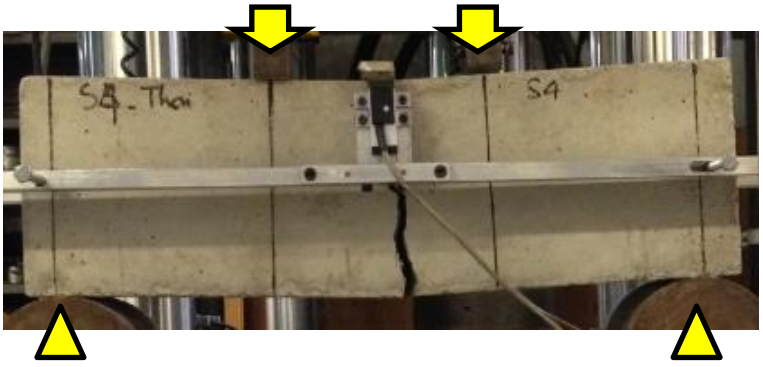

*Fig. 3-13: Concrete modulus of rupture ($f_r$) measurement (ASTM-C78 [120])*

### 3.4.2 Flexural Reinforcement

The reinforcing bars for all test specimens were cut, bent, and delivered by a local company, Barnsco Co.[121]. All of these bars were taken from one steel batch for each rebar size to ensure consistency between flexural reinforcement in the test specimens. For each bar size, at least three bars were randomly tested for tensile strength (Fig. 3-14a). The measured average yield strength, yield strain, and ultimate strength for each bar size are given in Table 3-5, and typical measured stress strain relationships are shown in Fig. 3-15.

*Table 3-5: Measured properties of flexural reinforcement*

| Bar size | Yield strength, $f_y$ ksi (MPa) | Yield strain, $\varepsilon_y$ | Ultimate strength, $f_u$ ksi (MPa) |
|---|---|---|---|
| #4 | 60.0 (415) | 0.00221 | 100 (670) |
| #5 | 66.5 (460) | 0.00226 | 107 (740) |
| #6 | 65.5 (450) | 0.00224 | 105 (730) |

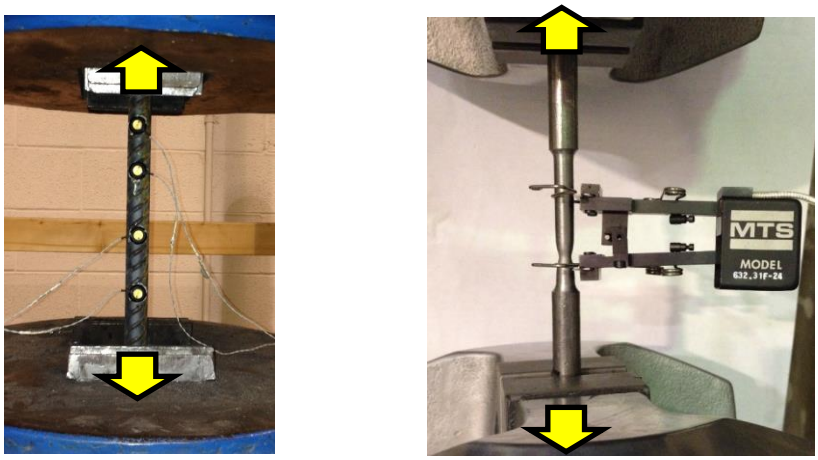


a) For reinforcing bars b) Shear Studs

*Fig. 3-14: Uniaxial tensile test (ASTM E8[122])*

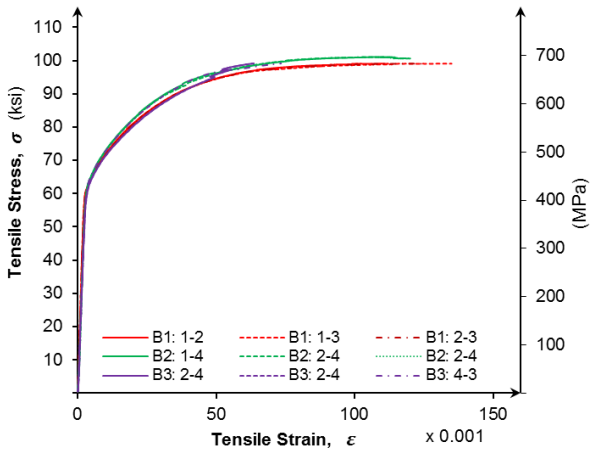


a) For #4 bars

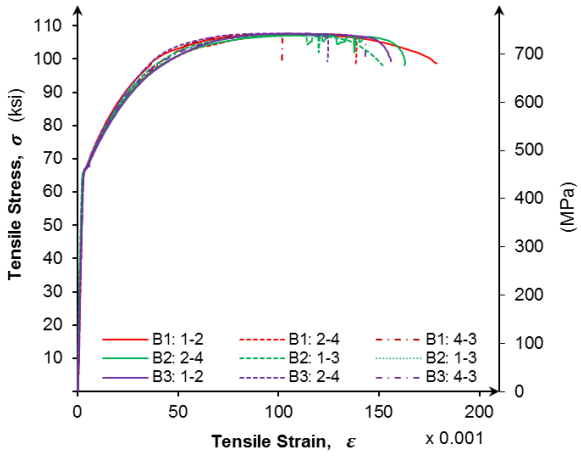


b) For #5 bars

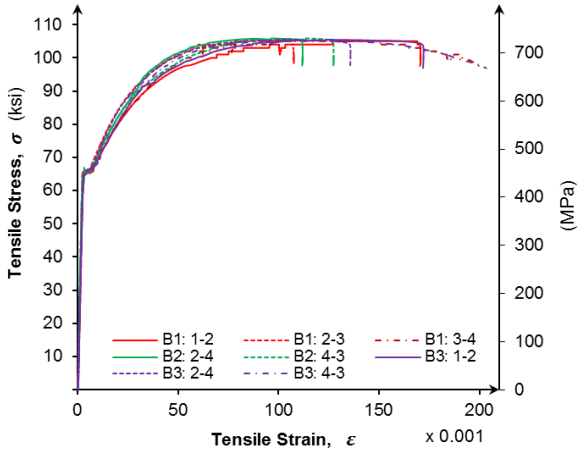


c) For #6 bars

*Fig. 3-15: Uniaxial Tensile Stress-Strain Relationship for reinforcing bars*

### 3.4.3 Shear Studs

The shear studs used in this investigation were provided by Decon USA[14]. They were manufactured in accordance with ASTM A1044[115], and their dimensions are shown in Fig. 3-16. Some of these studs were randomly selected and tested to measure their yield strength and stress-strain behavior (Fig. 3-14b). For the stud tests, a portion of 1.25 in. long (30 mm) at mid-length of the studs was machined so that the cross sectional diameter of this region was 0.25 in. (6.0 mm), and then they were loaded in uniaxial tension until failure. Measured stress-strain relationships of the studs are shown in Fig. 3-17. The average of the measured tensile yield strengths, computed by a 0.2% strain offset, was 71.1 ksi (490 MPa). In Fig. 3-17, a trilinear

stress-strain relationship given in Eq. (21) is also plotted. This relationship was used in a 3-D finite element model presented in Chapter 5.

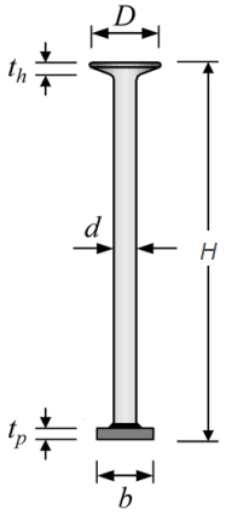


| Dimension | in. (mm) |
|---|---|
| Shank Diameter $d$ | 3/8 (9.5) |
| Head Diameter $D$ | 1.19 (30.1) |
| Head Thickness $t_h$ | 0.21 (5.3) |
| Rail Width $b_r$ | 1 (25.4) |
| Rail Thickness $t_p$ | 3/16 (4.8) |
| Total Height $H$ | 8.5 (216) |

*Fig. 3-16: Stud rail dimensions*[14]

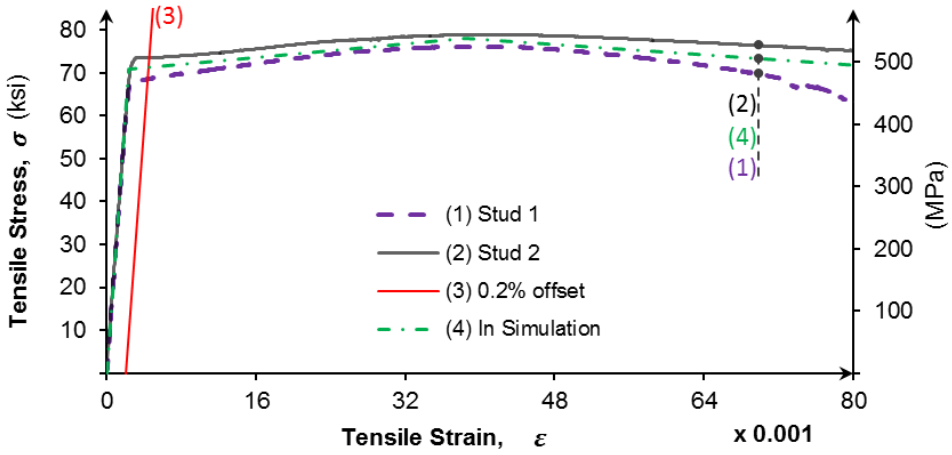


*Fig. 3-17: Uniaxial tensile stress-strain relation of shear studs (20 mm gages)*

$$\sigma = \begin{cases} 29500\varepsilon & if\ 0 \le \varepsilon < 0.0024 \\ 70.8 + 200(\varepsilon - 0.0024) & if\ 0.0024 \le \varepsilon < 0.0384 \\ 78.0 - 150(\varepsilon - 0.0384) & if\ \varepsilon \ge 0.0384 \end{cases} \quad (ksi) \qquad (21)$$

## 3.5 TEST SETUP

A typical test setup for all slab-column specimens in the program is shown in Fig. 3-18. The specimen was tested up-side down for testing convenience, and it was vertically supported by a system of eight discrete points distributed uniformly around the slab edge. A vertical downward load, generated by a 500 k (2.2 MN) hydraulic jack, was applied monotonically at the top of the column, and this load was measured by a load cell placed between the hydraulic jack and the reaction steel frame. Designs of supporting and loading systems are presented in Subsections 3.5.1 and 3.5.2, respectively. The testing instrumentations shown in Fig. 3-18, e.g. the Optotrak cameras and markers, are presented in Section 3.5.3.

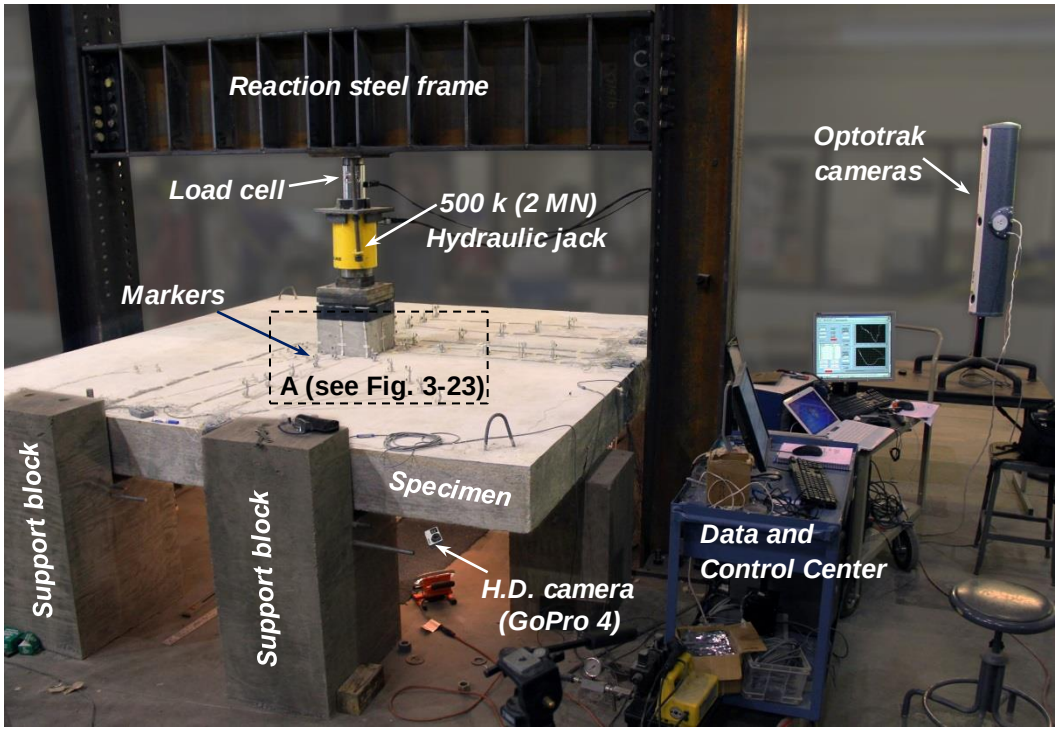


*Fig. 3-18: Test setup*

### 3.5.1 Support System

#### *3.5.1.1 Design of the support system*

The support system used in the program consisted of 8 concrete blocks, and these blocks were arranged uniformly around the slab periphery (Fig. 3-19). Eight bearing pads, each consisting of a 6 in. (150 mm) square steel plate and neoprene pad, were placed between the slab and the concrete blocks. The steel plates and neoprene pads were 1 in. and 5/8 in. (25.4 mm and

16 mm) thick, respectively. The bearing pad centers were uniformly distributed on a circle with a radius of 5 ft (1520 mm) to simulate contra-flexural lines in flat plate systems (refer to Section 2.1). When the specimens were in the testing position, the clear height to the slab from the laboratory floor was approximately 28 in. (720 mm), providing a sufficient space for working during test preparation and observing cracks during the test (Fig. 3-20).

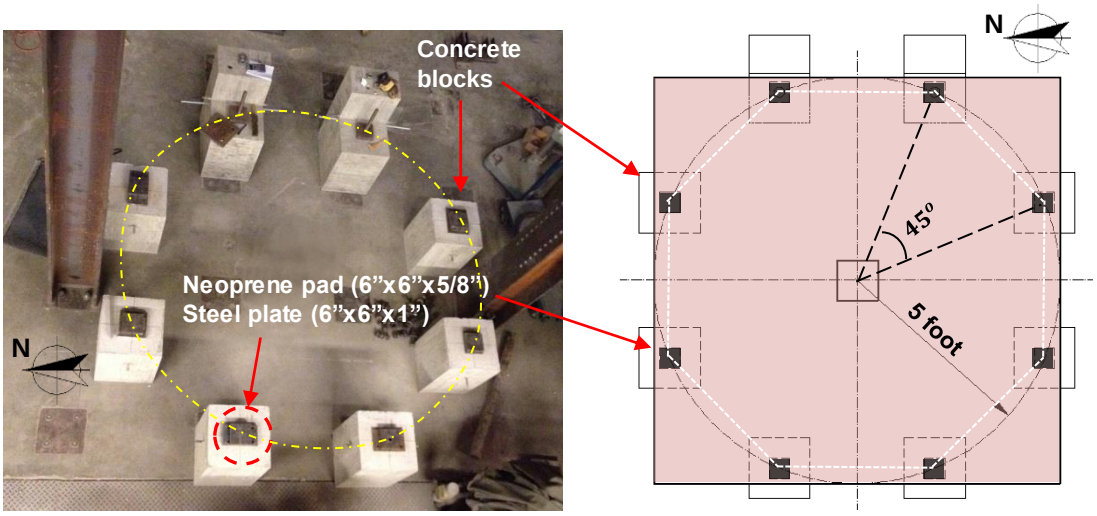


a) Concrete blocks and bearing pads b) Bearing pads arrangement

*Fig. 3-19: Supporting system*

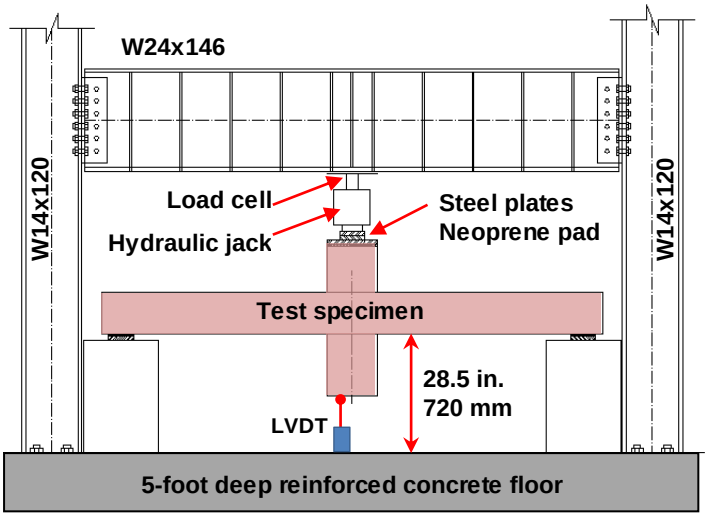


*Fig. 3-20: Loading and supporting systems (west view)*

### *3.5.1.2 Levelling of Supports and Specimens*

Because the slab bottom surface was not completely flat due to the imperfections and deformations of the wooden formwork, and because the eight supporting blocks were slightly different in height, the test specimen and support system needed to be leveled to ensure moment transfer was negligible. Two leveling methods were considered. The first method was to place wet non-shrink grout on top of all supporting blocks before the specimen was placed on them, and the grout was expected to fill possible gaps between the slab and the supports. This method would have been simple, but it may not have been reliable because an uneven placement process of the heavy specimen onto the eight support blocks could possibly squeeze out the wet grout at a few supporting blocks before the specimen was levelled off. The second method, on the other hand, was to use thin steel sheets and neoprene pads to fill possible gaps between the slab and the supports. This method was shown to be more reliable, but it required additional measurement and analysis as follows.

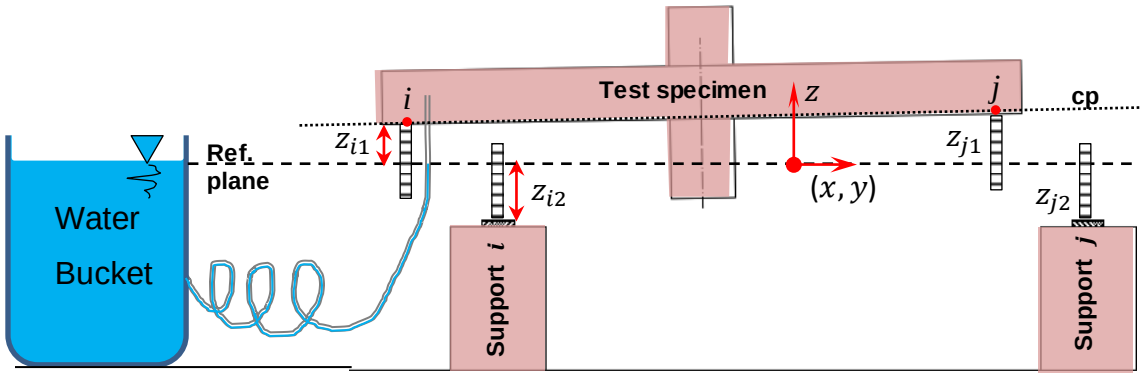


*Fig. 3-21: Leveling of test specimens and support system*

After removing the formwork, the specimen was placed on a temporary support system for a leveling process. First, a water level with an accuracy of 1/32 in. (0.8 mm) was used to measure the height ($z_{i1}$, $i = 1$ to 8) from a reference plane (Fig. 3-21) to the eight points on the slab bottom surface, at which the specimen was to be supported during the test. In a Cartesian coordinate system ($xyz$), these points were at different elevations ($z_{i1}$), but their projections on the horizontal plane ($xy$) were assumed to be the vertices of a regular octagon (Fig. 3-19b). Second, a least square analysis was used to find a plane that was closest to the eight points (plane "cp" in Fig. 3-21), and the distance from those points to the plane was then computed. Assuming the specimen is rotated so that this plane becomes a new horizontal reference plane, the

computed offsets from the least-square analysis become revised $z_{i1}$ ($i = 1$ to 8) values for new heights of the eight supported points. Third, the height from the reference plane of the eight bearing pads ($z_{i2}$, $i = 1$ to 8) was also measured. The gaps between these bearing pads and the slab bottom surface were given as $g_i = z_{i1} - z_{i2}$ ($i = 1$ to 8). Finally, the leveling process was completed by adding 6 in. square and 1/32 in. (150 and 0.8 mm) thick steel sheets to support blocks that had larger gaps ($g_i$) until all of the gaps were equal. After the specimen was completely placed on the support system, other checks were made by visually comparing the deformation of the neoprene pads. The specimen was assumed to be supported uniformly by eight support blocks if all neoprene pads deformed equally.

### 3.5.2 Loading System

The loading system consisted of a 500 kip (2.2 MN) hydraulic jack and a reaction steel frame (Fig. 3-18). The reaction frame was an assembly of a W24x146 beam and two W14x120 columns. The beam and columns were connected by bolts, and the two columns were also anchored to a 5-foot deep reinforced concrete structural floor (Fig. 3-20). The loading system was designed to resist a maximum force of 500 kip (2.2 MN) at midspan of the beam.

*Loading Method*—a load cell was placed between the hydraulic jack and the reaction steel frame to measure the applied load. An assembly of steel plates and neoprene pads was placed on top of the column to uniformly spread the load over the entire column section. Initial loading increments of 20 k (90 kN) were used until the load approached the predicted strength of the specimen. After each loading step, the applied load was held constant so the development of cracks in the slab could be recorded. Smaller load increments were used to capture the peak load resisted by the specimen. When the specimen started to fail, the column was continuously pushed downward until the load decreased below 60% of the peak specimen strength. The total testing time for each specimen was approximately 45 minutes.

### 3.5.3 Testing Instrumentations

#### *3.5.3.1 Displacement and Slab Through-Thickness Expansion Measurement*

*Displacement measurement*—displacements of the test specimen were measured using a Linear Variable Differential Transformer (LVDT) and an Optotrak Certus System[123]. The LVDT was used to monitor the column vertical displacement during the test (Fig. 3-20), while

the Optotrak Certus System, was used to measure the spatial displacements at different locations on the top column stub and the slab. This system used high-resolution infrared cameras to detect signals emitting from markers glued on the specimens (Fig. 3-18), and then it determined and recorded the local x, y, and z coordinates of each marker with an accuracy of 0.004 in. (0.1 mm) and at frequency of 10 Hz. A number of approximately 100 infrared-emitting markers were used for each test specimen, and their typical locations are shown in Fig. 3-22. These markers were grouped depending on the measurement purposes.

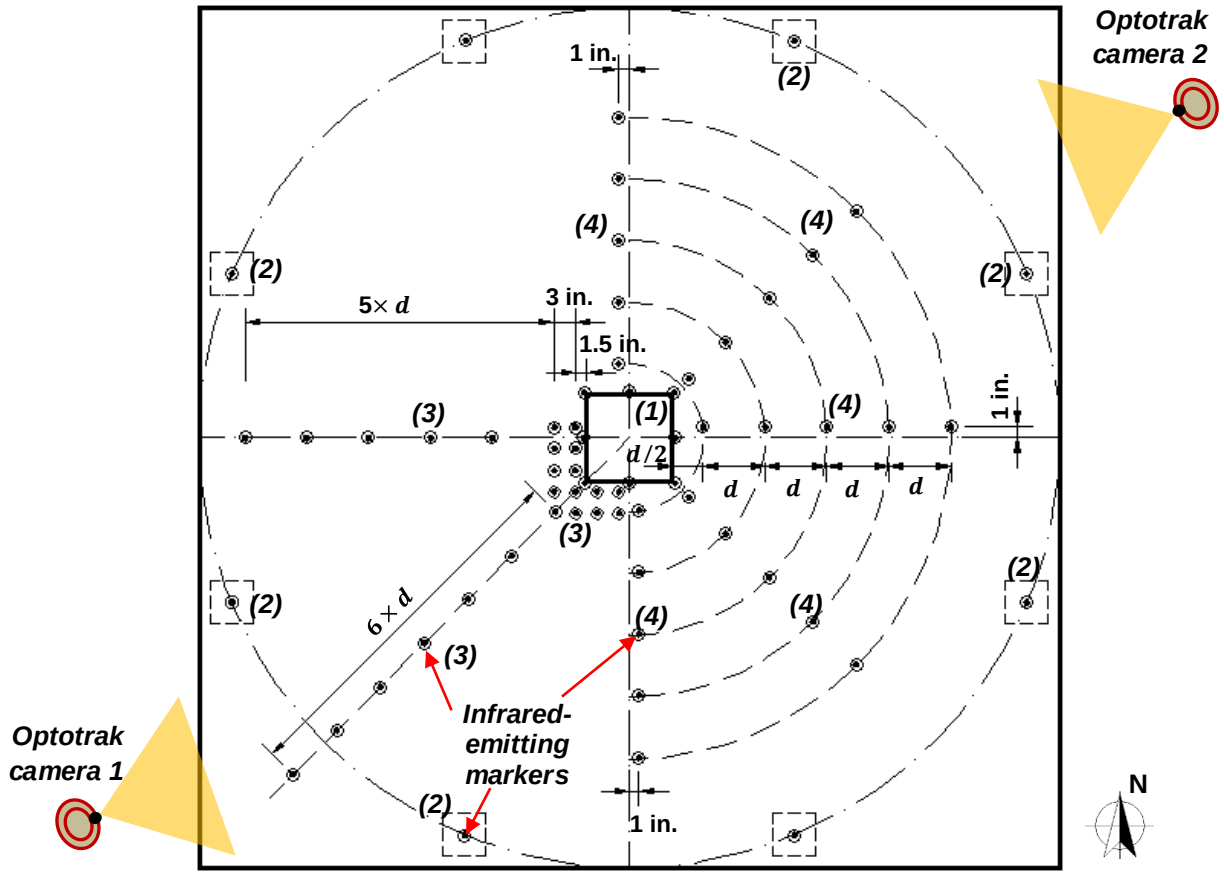


*Fig. 3-22: Infrared-emitting marker typical locations on the test specimens (top view)*

(units are in in., 1 in. = 25.4 mm)

Markers in the first group, labeled as "1" in Fig. 3-22, were located near the mid-sides and corners of the column perimeter. These markers were to measure displacements of the column (markers "1c" in Fig. 3-23) and the slab regions adjacent to the column faces (markers "1s" in Fig. 3-23). The markers "1c" were attached on the column faces, while the markers "1s" were glued on aluminum bars, which were attached to the slab region close to the column. The relative

displacements between these two markers (1s and 1c) in the column displacement direction ($z$) indicated the inititation of puncing shear failures.

The markers in the second group, labelled as "2" and "3" in Fig. 3-22, were glued on the top of the slab. The markers "2" were placed above the centers of the bearing pad to measure support deformation, while the markers "3" were placed at different locations on the slab to measure the slab displacement and concrete strains on the top slab surface. Some of markers "3" were placed at a spacing of 3 in. (76 mm) on two lines parallel to the column faces at the distances of 1.5 in and 4.5 in. (38 and 115 mm) from the column periphery. The others "3" markers were placed at a spacing of $d$ on two different radial lines extending from the column center to the West and the South-West (Fig. 3-22). To make sure the markers "2" and "3" were facing toward the Optotrak cameras, these markers were glued onto plastic triangular prisms, which were then glued on the slab surface (Fig. 3-22).

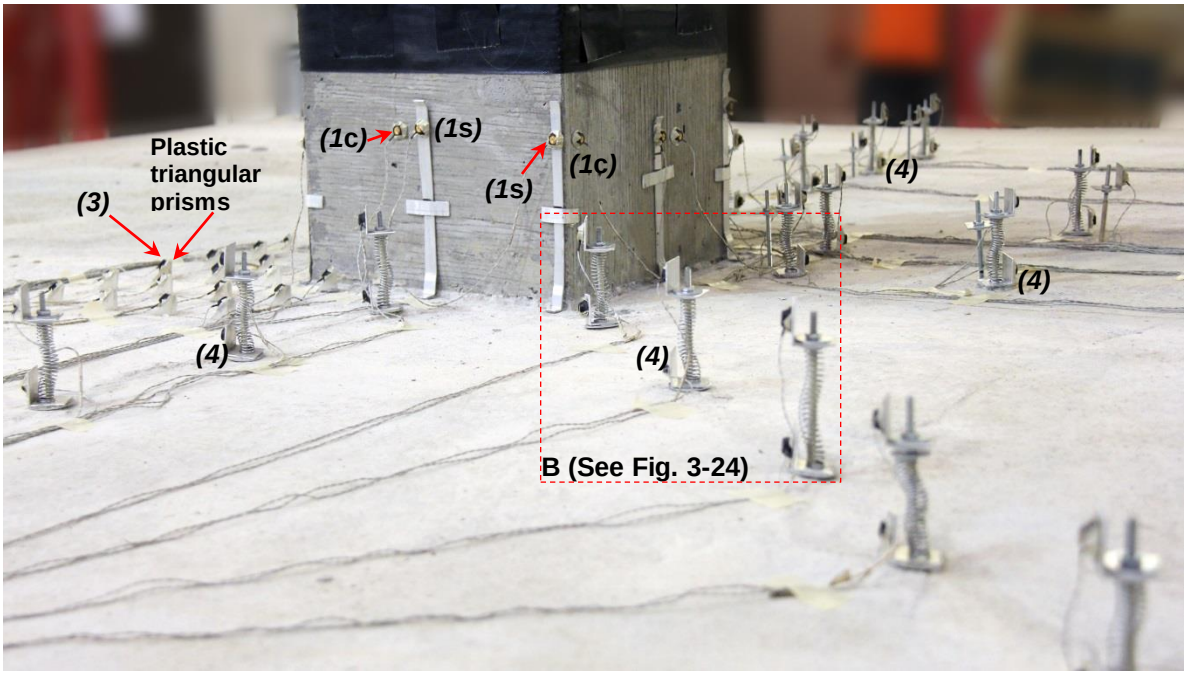


*Fig. 3-23: Infrared-emitting markers on the test sepecimens (region A in Fig. 3-18)*

*Slab through-thickness expansion measurement*—the last group of markers consisted of pairs of markers, labeled as "4" in Fig. 3-22 and Fig. 3-23. These pairs of markers were used to measure through-thickness (vertical) expansion of the slab at different locations along the five radial lines shown in Fig. 3-24 (b). These measurements were to study the development of inclined cracks and failure surfaces inside the slabs during the tests. For each pair of markers, as

shown in Fig. 3-24 (a), one marker was glued on the top surface of the slab and the other was attached to the top of a threaded rod. The steel rod extended vertically through the slab inside a 1/4 in. (6 mm) diameter plastic pipe (Fig. 3-8d) and the other end of the rod was attached to the bottom of the slab. A steel spring, preloaded in compression, was placed between the slab and the top of the threaded rod to stabilize the measurement unit. A relative displacement between the two markers indicated an expansion of the slab.

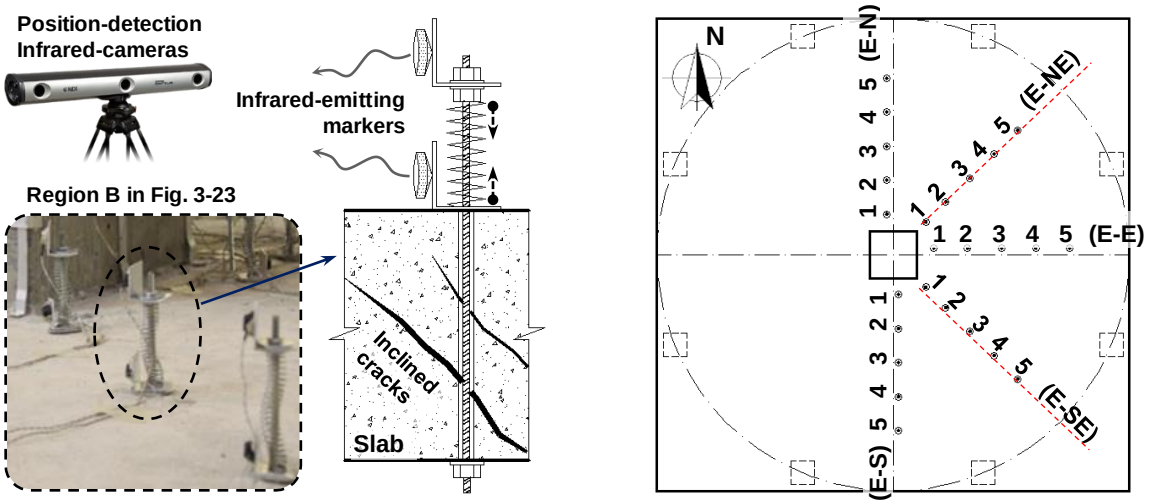


a) Expansion measurement method b) Labels (for locations see Fig. 3-22)

*Fig. 3-24: Measurement of through-thickness expansion of slabs*

### *3.5.3.2 Strain Gauge Locations*

Strains in the slab flexural tension reinforcing bars (bottom) and shear studs were measured using 0.2 in. (5 mm) long YFLA-5-5L gauges (Tokyo Sokki Kenkyujo Co.). The strain gauge attachment process was presented in Subsection 3.3.1. Thirty-six strain gauges were attached on the selected slab reinforcing bars for each test specimen, and the locations of these strain gauges are shown in Fig. 3-25. For shear stud reinforcement, strain gauge locations for Specimens S08O, S08R, S12O, and S12R are shown in Fig. 3-26.

### *3.5.3.3 Crack Observations*

Flexural cracks on the slab tension surface (bottom) were observed during the test using high-definition cameras placed below the specimen. These cameras recorded pictures of the slab bottom surface, and those pictures were transmitted to a digital screen at the Data and Control

Center (Fig. 3-18). Between load increments, the development of the flexural cracks was observed by moving the cameras underneath of the slab.

Shear cracks in the slab could not be observed during the test because they developed inside the slab. The development of these cracks, however, was studied from the measured through-thickness expansions of the slab (Fig. 3-24) and the measured strains in shear studs. After completion of a test, shear cracks and failure surfaces were studied by cutting the specimen and removing any loose concrete cover at the top of the slab.

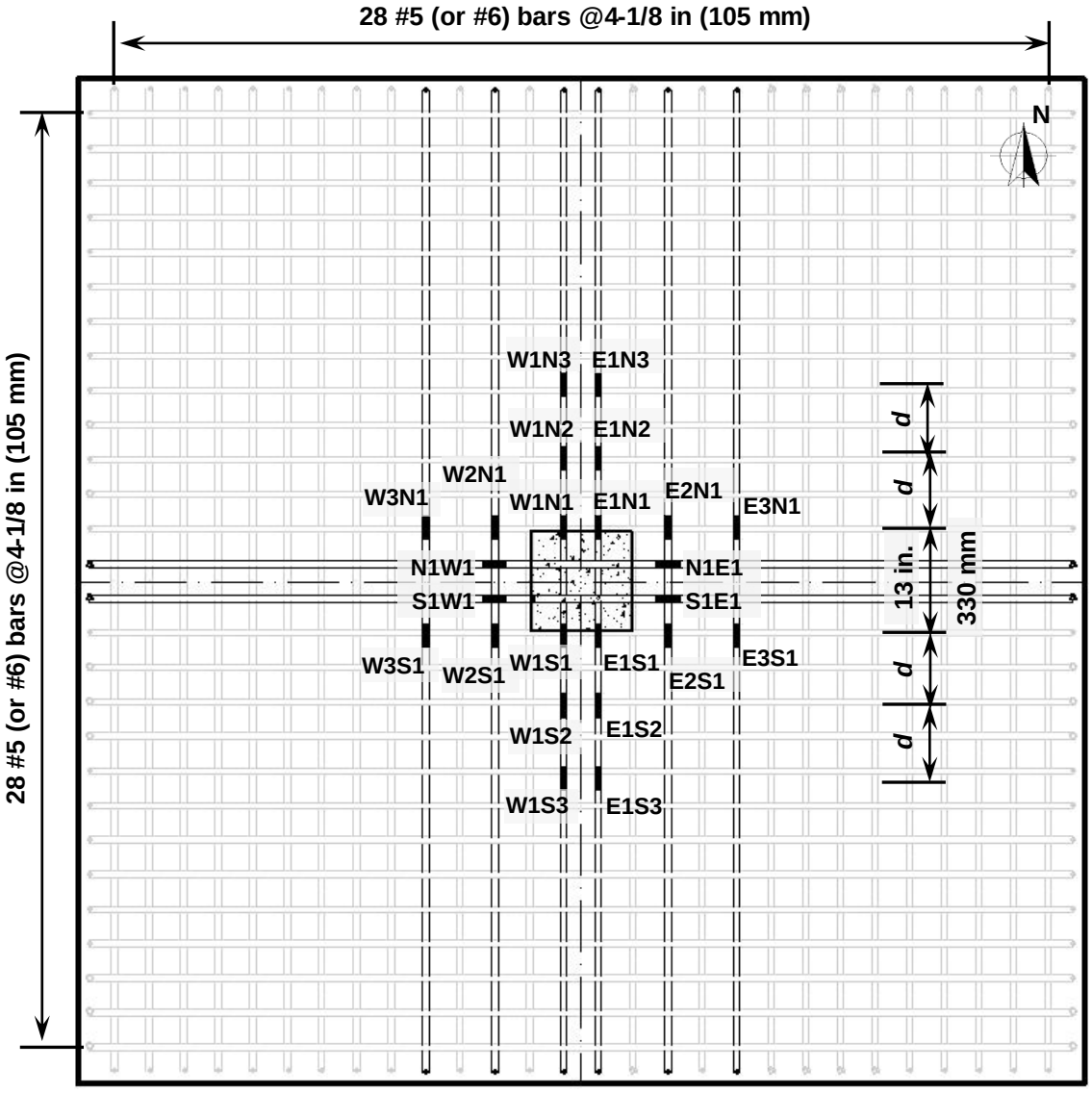


*Fig. 3-25: Typical strain gauge locations in slab flexural tension reinforcing bars (bottom)*

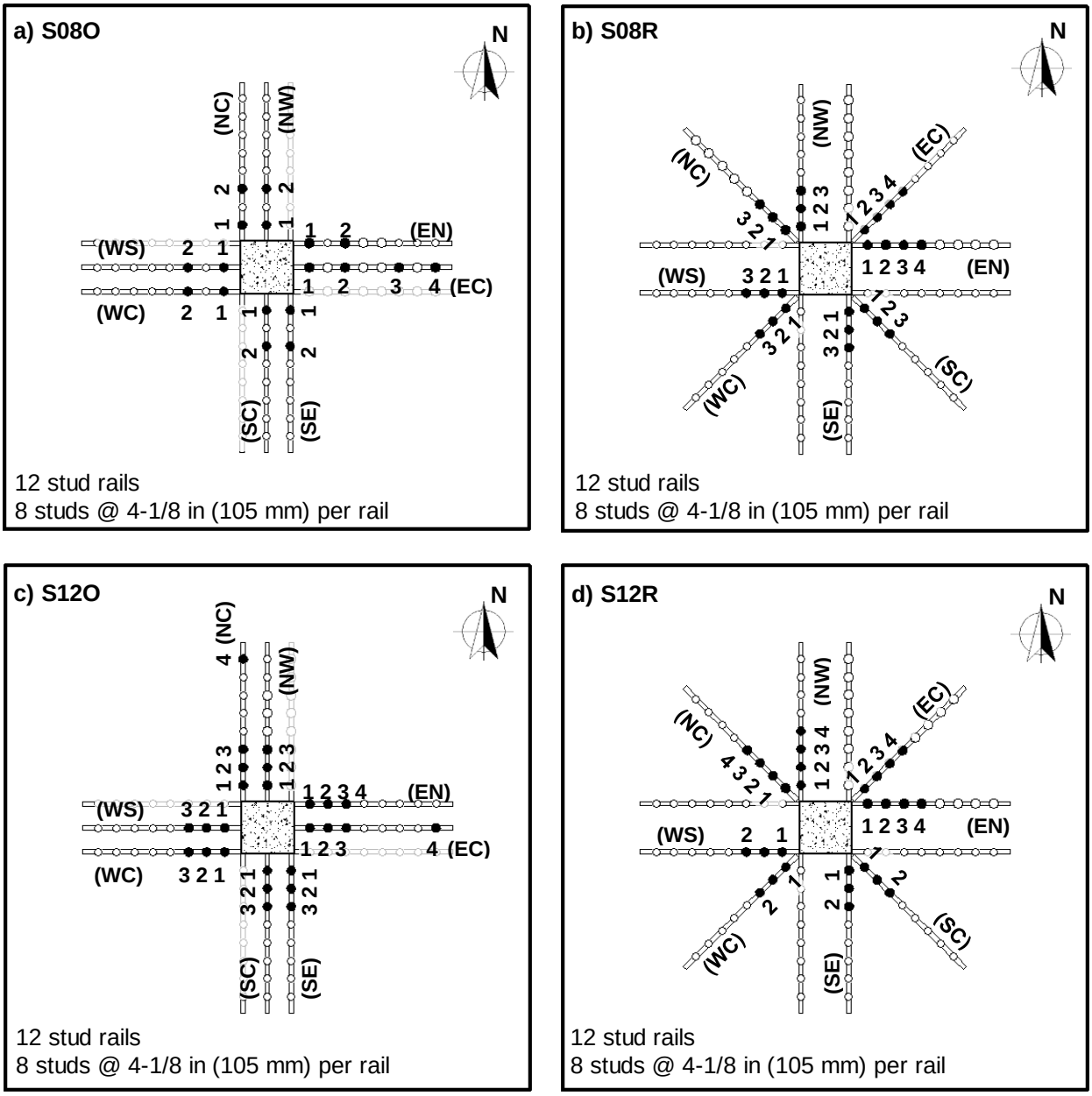


*Fig. 3-26: Strain gauge locations in shear stud reinforcement*

# CHAPTER 4
# EXPERIMENTAL RESULTS

This chapter presents test results from the experimental program described in Chapter 3. For each test specimen, test results consist of the measured data and observations on specimen behavior and crack development during the test, and the observations from post-test investigations of the crack pattern inside the slab. The results are presented and discussed in five sections as follows:

- Section 4.1 presents how the measured data were processed,
- Section 4.2 describes the overall behavior of all test specimens,
- Section 4.3 presents test results for each test specimen,
- Section 4.4 discusses the flexural behavior of the test specimens, and
- Section 4.5 discusses the shear behavior of the test specimens.

## 4.1 PROCESSING OF EXPERIMENTAL DATA

Measured data for each test specimen was stored in data tables. In these tables, the columns represent the measurements including the applied load, strains in flexural and shear reinforcement, and coordinates of the markers glued on the test specimen, while the rows (referred to as frames) show the values for these measurement at every tenth of a second during the test. This measured data needed to be processed to compute slab shear stresses, displacements, and slab through-thickness expansions.

### 4.1.1 Transformation of Coordinate Systems

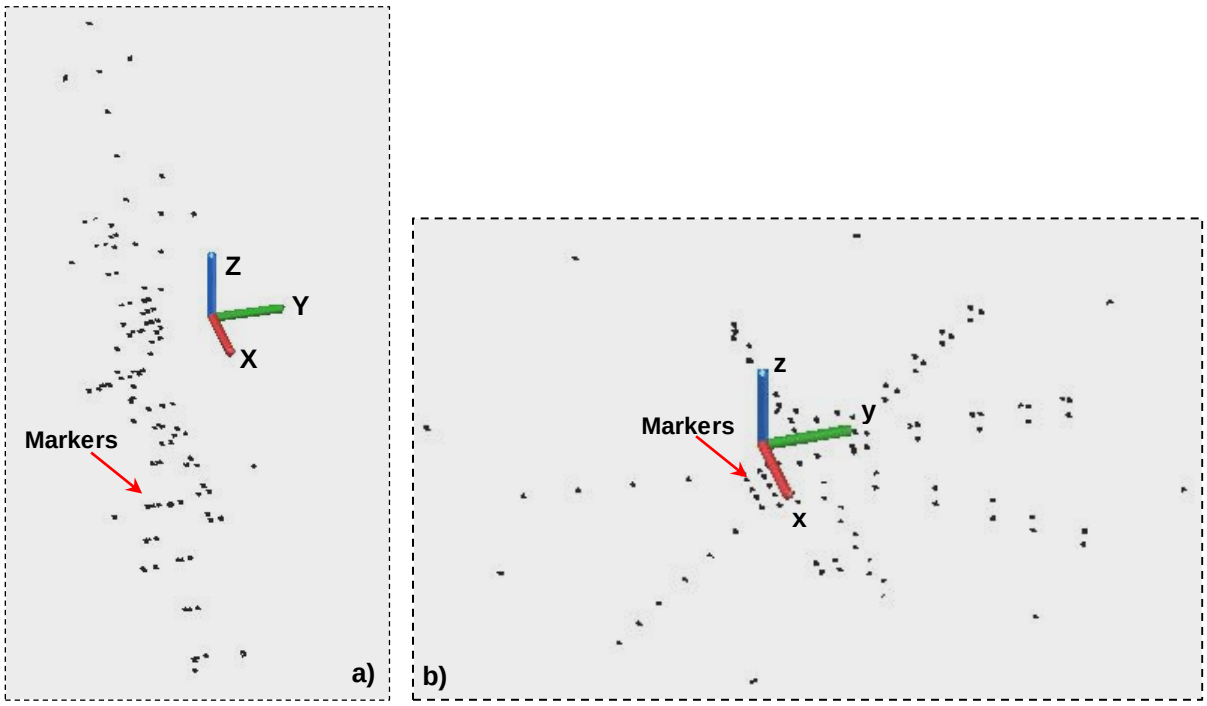


*Fig. 4-1: Transformation of coordinate systems*

a) The markers in the Optotrak coordinate system, *XYZ*

b) The markers in a new coordinate system, *xyz*

The Optotrak system determined and recorded the marker coordinates using its built-in Cartesian coordinate system, referred to as the *XYZ* system. This coordinate system was dependent on the location and position of the Optotrak cameras (Fig. 3-18 and Fig. 3-22), so it generally was not the same for all test specimens. Also, the axes *X*, *Y*, and *Z* usually did not align exactly with the slab dimensions or the applied load direction (Fig. 4-1a), so it was difficult to

use the *XYZ* system to study the displacements and deformations of the test specimen. In this program, the *XYZ* system was transformed to a new coordinate system *xyz* (Fig. 4-1b), as follows.

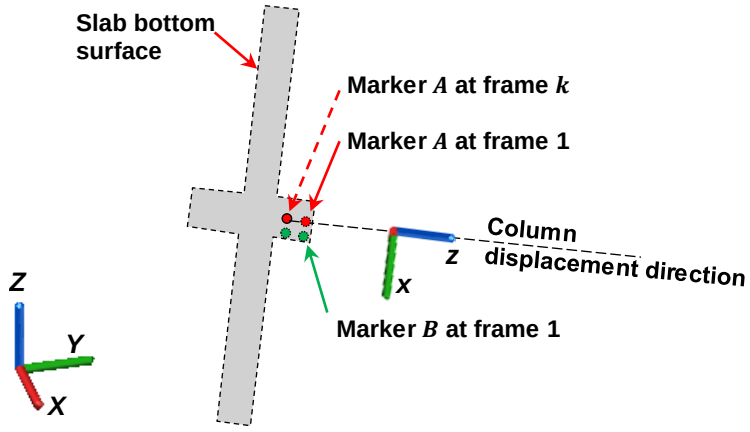


*Fig. 4-2: Definition of the xyz system in the XYZ system*

$$\boldsymbol{z}_A = \begin{bmatrix} X_A \\ Y_A \\ Z_A \end{bmatrix}_{\text{frame } k} - \begin{bmatrix} X_A \\ Y_A \\ Z_A \end{bmatrix}_{\text{frame 1}} \tag{22}$$

$$\boldsymbol{z} = -(\boldsymbol{z}_A + \boldsymbol{z}_B + \cdots) \tag{23}$$

The definition of the *xyz* in the *XYZ* system is shown in Fig. 4-2. The origin of the *xyz* system was positioned at the coordinates for one marker glued on the column faces, e.g., marker A (Fig. 4-2), measured at frame 1 (the beginning of the test). To define the *z* axis, two methods were considered. In the first method, the *z* axis was defined as the normal of a plane through three markers glued on the slab surface (Fig. 3-22). This plane, however, might not have represented the slab plane accurately because the markers were attached on the slab surface using plastic triangular prisms (Fig. 3-23) at different heights. In the second method, the *z* axis was defined as the applied load direction, which was computed from the positions of markers attached on the column at frame 1 (test beginning) and frame *k* (approximately 60% of the peak load). For each marker glued on the column faces, e.g. marker A, a vector $z_A$ representing the marker displacement direction from frames 1 to *k* is given in Eq. (22). The average orientation of all displacement vectors for markers attached on the column was assumed to represent the applied load direction, and it was used to define the *z* axis (Eq. 23). After that, the *xz* plane was defined as a plane through the z axis and marker B on the same column face with marker A (Fig.

4-2). Finally, the axis $y$ was defined as the direction normal to the plane $xz$. The $xyz$ system defined by this method had axes aligned with the test specimen dimensions, and the marker coordinates in this system were computed as follows.

Assuming $[\boldsymbol{e}_1 \quad \boldsymbol{e}_2 \quad \boldsymbol{e}_3]^{\mathrm{T}}$ were the unit vectors of the $xyz$ system in the $XYZ$ system, the coordinates of each marker presented in the $xyz$ coordinate system were computed using the following equation,

$$\begin{bmatrix} x \\ y \\ z \end{bmatrix}_{\text{frame } k} = \begin{bmatrix} \boldsymbol{e}_1 \cdot \boldsymbol{E}_1 & \boldsymbol{e}_1 \cdot \boldsymbol{E}_2 & \boldsymbol{e}_1 \cdot \boldsymbol{E}_3 \\ \boldsymbol{e}_2 \cdot \boldsymbol{E}_1 & \boldsymbol{e}_2 \cdot \boldsymbol{E}_2 & \boldsymbol{e}_2 \cdot \boldsymbol{E}_3 \\ \boldsymbol{e}_3 \cdot \boldsymbol{E}_1 & \boldsymbol{e}_3 \cdot \boldsymbol{E}_2 & \boldsymbol{e}_3 \cdot \boldsymbol{E}_3 \end{bmatrix} \left( \begin{bmatrix} X \\ Y \\ Z \end{bmatrix}_{\text{frame } k} - \begin{bmatrix} X_A \\ Y_A \\ Z_A \end{bmatrix}_{\text{frame } 1} \right) \tag{24}$$

in which, $k$ varied from 1 to the number of frames in the data tables, and vectors $\boldsymbol{E}_1$, $\boldsymbol{E}_2$, and $\boldsymbol{E}_3$ were the unit vectors of the $XYZ$ system, i.e. $\boldsymbol{E}_1 = [1 \quad 0 \quad 0]$, $\boldsymbol{E}_2 = [0 \quad 1 \quad 0]$, and $\boldsymbol{E}_3 = [0 \quad 0 \quad 1]$. The orginal system XYZ and transformed system $xyz$ for Specimen S12R are shown in Fig. 4-1 (a) and (b), respectively.

### 4.1.2 Specimen Displacements

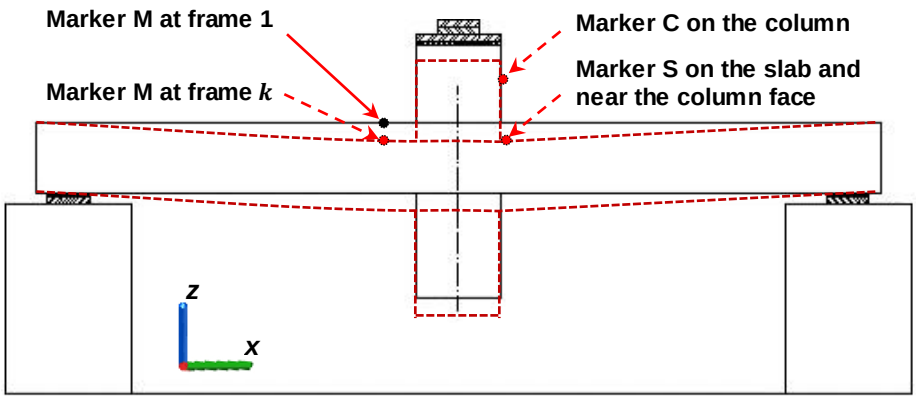


*Fig. 4-3: Specimen displacements for frame k*

The displacement of the test specimen was computed using the marker coordinates in the $xyz$ system (Fig. 4-3). The measured displacement for a marker M at frame $k$, $\Delta_{\text{M (frame k)}}$, was calculated using Eq. (25). The relative displacement between the column (marker C) and the adjacent slab regions (marker S), $\Delta_{\text{CS (frame k)}}$, was computed using Eq. (26), in which $V_{\text{(frame k)}}$ is the applied load at frame $k$, $(b_c)^2$ is a cross-sectional area of the column, and $E_c$ is the

concrete modulus approximated using Eq. (27). The third term in Eq. (26) represents the vertical deformation of the column region between makers C and S.

$$\Delta_{M\ (\text{frame } k)} = z_{M\ (\text{frame } 1)} - z_{M\ (\text{frame } k)} \tag{25}$$

$$\Delta_{CS\ (\text{frame } k)} = \Delta_{C\ (\text{frame } k)} - \Delta_{S\ (\text{frame } k)} - \frac{V_{(\text{frame } k)}}{(b_c)^2 \times E_c}\left(z_{C\ (\text{frame } 1)} - z_{S\ (\text{frame } 1)}\right) \tag{26}$$

$$E_c = 57000\sqrt{f_c'}\ \text{psi}\ (4730\sqrt{f_c'}\ \text{MPa}). \tag{27}$$

### 4.1.3 Through-thickness Expansion of Slabs

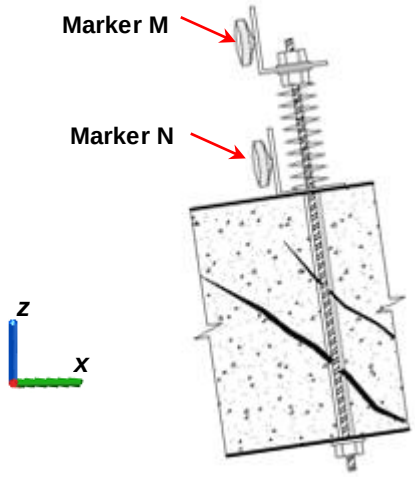


*Fig. 4-4: Through-thickness slab expansion calculation*

The though-thickness expansion of the slab measured using a pair of markers M and N (Fig. 4-4) at frame $k$ is given as follows,

$$\text{Expansion}_{MN(\text{frame } k)} = MN_{(\text{frame } 1)} - MN_{(\text{frame } k)} \tag{28}$$

in which MN is a distance between the two markers at frame $k$, as given in Eq. (29).

$$MN_{(\text{frame } k)} = \sqrt{[x_M(k) - x_N(k)]^2 + [y_M(k) - y_N(k)]^2 + [z_M(k) - z_N(k)]^2} \tag{29}$$

### 4.1.4 Slab Shear Stress

In this chapter, the term *slab shear stress* ($v$) is used to represent the average shear stress calculated at a vertical section located at $d/2$ from the column faces (the inner critical section

defined by the ACI Code[5]). At frame $k$, the *slab shear stress* was calculated from the applied load, $V$ (or shear transfer at the test specimen), using the following equation,

$$v_{(\text{frame } k)} = \frac{V_{(\text{frame } k)}}{b_0 d} = \frac{V_{(\text{frame } k)}}{4(h_c + d)d} \quad (30)$$

in which, $b_0 = 4(h_c + d)$, $h_c$ is the dimension of the square column, and $d$ is slab effective flexural depth. The slab shear stress was also presented in term of the square root of the concrete compressive strength (Eq. 31).

$$\frac{v_{(\text{frame } k)}}{\sqrt{f_c'}} = \frac{V_{(\text{frame } k)}}{b_0 d\sqrt{f_c'}} \quad (31)$$

Measured shear strength ($V_u$) of a specimen that failed due to shear failure was defined as the maximum applied load during the test.

$$V_u = max\left[V_{(\text{frame } k)}\right] \quad (k = 1 \text{ to the total number of frames}) \quad (32)$$

Measured shear strength of a test specimen may also be represented as slab shear stress ($v_u$), which was computed from $V_u$ using either Eq. (30) or Eq. (31).

### 4.1.5 Shear Stud Elongations

To study the development of cracks inside the slab of a test specimen, the elongations of the shear studs were calculated using the corresponding measured strains. Assuming a strain ($\varepsilon$) is uniformly distributed along the smooth stud shaft with a length of $l_{st} = 8$ in. (205 mm), the elongation of the stud was computed using Eq. (33).

$$\text{Stud elongation} = \varepsilon_{(\text{frame } k)} \times l_{st} \quad (33)$$

## 4.2 OVERALL TEST RESULTS

The five test specimens were loaded until failure, defined as when the applied load decreased below 60% of the maximum load. All of the test specimens failed in punching shear, and their measured load vs. column displacement behaviors are shown in Fig. 4-5. Control Specimen S08C (line 1), without shear reinforcement, experienced a typical punching shear failure at $V_u = 233$ k (1040 kN), which corresponded to a slab shear stress $v_u = 4.2\sqrt{f'_c}$ psi ($0.35\sqrt{f'_c}$ MPa). For the other specimens (lines 2 to 5), with shear studs, their measured strengths were 25% to 35% higher than that of Specimen S08C. These results show that the shear studs increased the shear strength for all of the slab-column connections with shear reinforcement. Measured shear strengths ($V_u$ and $v_u$) for the test specimens are given in Table 4-1.

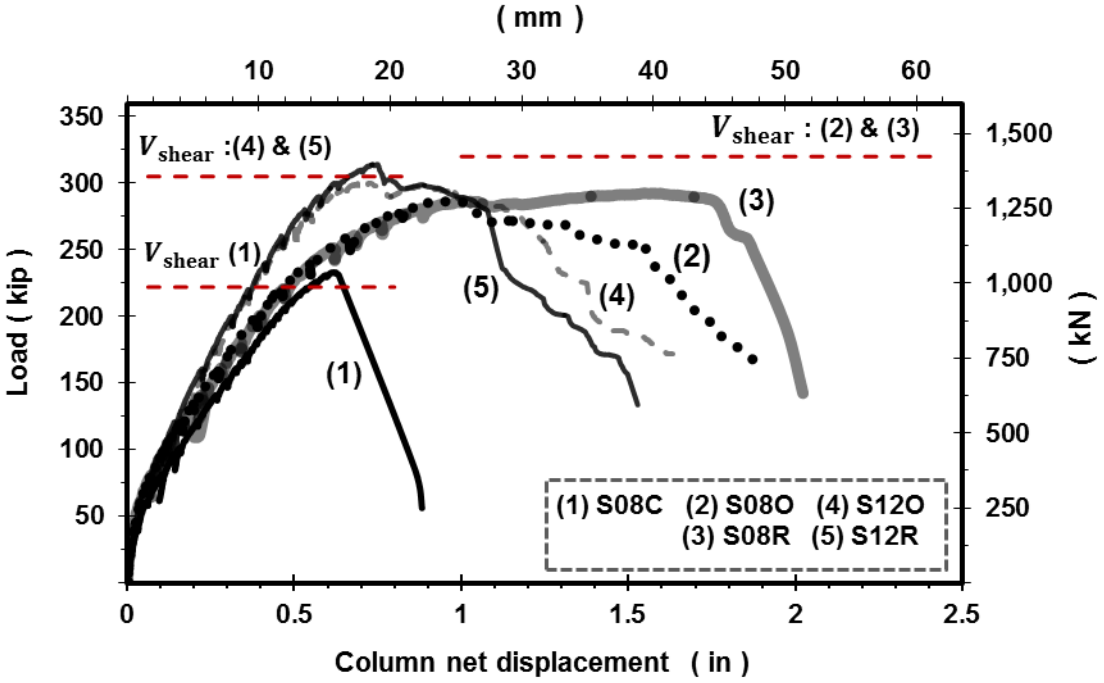


*Fig. 4-5: Load versus column displacement for all test specimens*

The horizontal dashed lines in Fig. 4-5 represent the nominal shear strength, $V_{shear}$, calculated using the ACI Code[5] (Eq. 12) with the measured material properties for each test specimen, and these calculated shear strengths are given in Table 4-1. Fig. 4-5 shows that the measured shear strengths ($V_u$) for Specimen S08C and the S12 specimens were greater than or equal to the corresponding calculated shear strength ($V_u \geq V_{shear}$), but for Specimens S08O and

S08R, $V_u$ values were approximately 10% lower than $V_{shear}$. This means that the ACI Code[5] equations for shear strength of slab-column connections overestimated the strength of Specimens S08O and S08R, which had a lower slab flexural reinforcement ratio, $\rho$.

*Table 4-1: Summary of test results for all test specimens*

| Specimen | $\rho$ % | $f'_c$ psi (MPa) | $f_y$ ksi (MPa) | $V_u$ k (kN) | $V_{shear}$ k (kN) | $V_{flex}$ k (kN) | $\frac{V_{shear}}{V_{flex}}$ | $\frac{V_u}{V_{shear}}$ | $\frac{V_u}{V_{flex}}$ | $v_u$ $\sqrt{f'_c}$ psi (MPa) | Failure mode |
|---|---|---|---|---|---|---|---|---|---|---|---|
| (1) | (2) | (3) | (4) | (5) | (6) | (7) | (8) | (9) | (10) | (11) | (12) |
| **S08C** | **0.87** | **6100** (42.1) | **66.5** (460) | **233** (1040) | **222** (990) | **285** (1270) | **0.78** | **1.05** | **0.82** | **4.2** (0.35) | **Punching shear** |
| **S08O** | **0.87** | **5050** (34.8) | **66.5** (460) | **287** (1280) | **317** (1410) | **285** (1270) | **1.11** | **0.91** | **1.01** | **5.67** (0.47) | **Punching shear*** |
| **S08R** | **0.87** | **5360** (37.0) | **66.5** (460) | **293** (1300) | **322** (1430) | **285** (1270) | **1.13** | **0.91** | **1.03** | **5.62** (0.47) | **punching shear*** |
| **S12O** | **1.25** | **4510** (31.1) | **65.0** (450) | **301** (1340) | **304** (1350) | **390** (1740) | **0.78** | **0.99** | **0.77** | **6.44** (0.53) | **Punching shear** |
| **S12R** | **1.25** | **4790** (33.0) | **65.0** (450) | **314** (1400) | **308** (1370) | **390** (1740) | **0.79** | **1.02** | **0.81** | **6.51** (0.54) | **Punching shear** |

*** Flexurally-triggered punching shear failure (see Section 4.4)**

Fig. 4-5 also shows that the S08 specimens (lines 1, 2, and 3), with a lower $\rho$, had a lower post-cracking stiffness than the S12 specimens (lines 4 and 5). For the specimens with shear studs, the failure sequence started with a slight drop in load carrying capacity at a column displacement of approximately 1 and 0.7 in. (25 and 18 mm) for the S08 and S12 specimens, respectively. After that, the behavior of the pairs of specimens in each group was different.

*Specimens S08O and S08R*—Fig. 4-5 shows that Specimens S08O (line 2) and S08R (line 3) behaved similarly up to an applied load of approximately 290 k (1290 kN), where both specimens suffered a slight drop in their load capacity. After this point, the behavior of Specimens S08O and S08R were significantly different. While the specimen with an orthogonal layout of shear studs, S08O, continuously lost strength (line 2), Specimen S08R, with a radial layout of shear studs, recovered strength and exhibited a more ductile behavior (line 3). These observations are similar to the test results reported by DaCosta and Parra-Montesinos,[18] and Broms.[17]

*Specimens S12O and S12R*— Fig. 4-5 shows that Specimens S12O (line 4) and S12R (line 5) behaved similarly until the applied load reached approximately 80 percent of their maximum load capacities. Beyond that point and up to the peak load, Specimen S12R retained slightly more stiffness than Specimen S12O. The two specimens reached their maximum load capacities at column displacement of approximately 0.7 in. (18 mm). After that, their load capacities dropped continuously as the column displacement increased. The measured strength of Specimen S12R (radial layout) was 314 k (1400 kN), which was similar (≅ 5% higher) to that of Specimen S12O (orthogonal layout). This finding was similar to the test results reported by Birkle and Dilger[15].

Although, in each pair, measured strengths for the two specimens with different layouts of shear studs were similar, the observed failure surface and measured strains in the shear studs for the specimens with an orthogonal layout of shear studs were very different from those for the specimens with a radial layout of shear studs. Results for each test specimen and a discussion of these differences are presented in the following sections.

## 4.3 TEST RESULTS FOR EACH TEST SPECIMEN

This section presents the measured relationships between the applied load versus slab and column displacements, measured strains in the slab flexural reinforcing bars and shear studs, and observations of the flexural cracks, shear cracks, and failure surfaces for each test specimen.

### 4.3.1 Specimen S08C ($\rho = 0.87\%$, without Shear Reinforcement)

#### *4.3.1.1 Load versus Displacement Relationships*

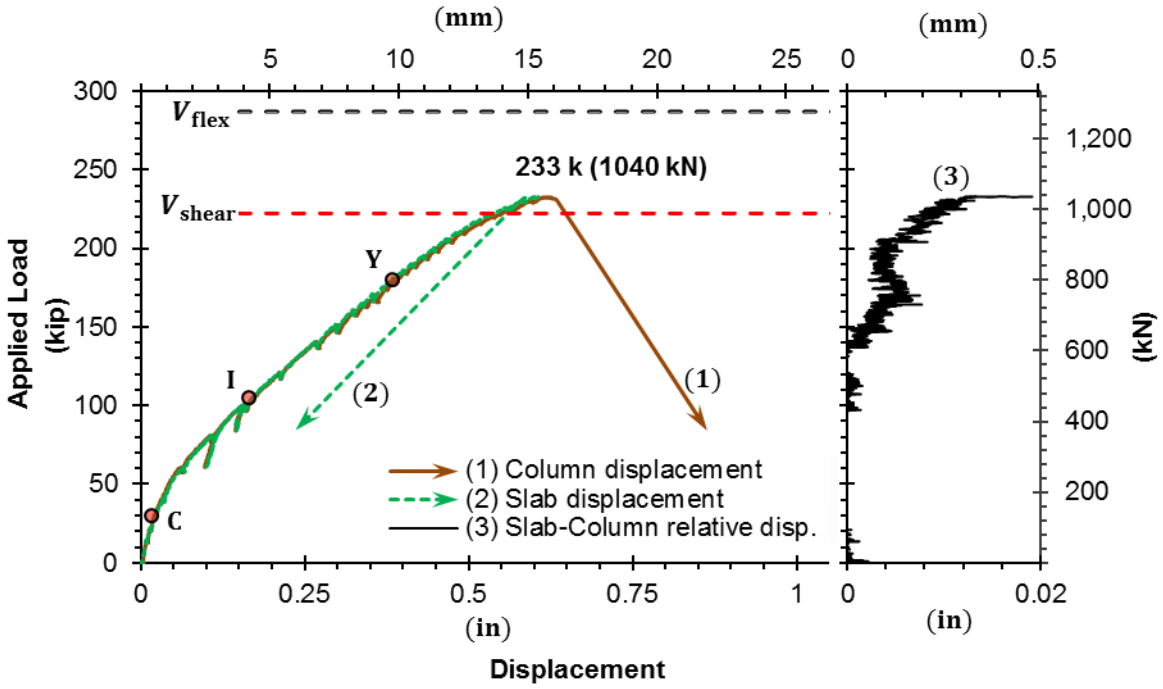


*Fig. 4-6: Load vs. displacement relationship for Specimen S08C*

The measured load versus displacement relationship for Specimen S08C is shown in Fig. 4-6. Line (1) in the figure represents the displacement of the column, line (2) represents the displacement of the slab measured at 1.25 in. (32 mm) from the west face of the column, and line (3) represents the difference between these displacements as the applied load increased to the maximum load. Fig. 4-6 shows that the column and slab displacements, lines (1) and (2), were almost identical as the applied load increased to approximately 150 k (670 kN), and then they started to separate, causing an increase in the relative displacement between the column and slab (line 3). When the applied load approached the maximum load, this relative displacement was approximately 0.02 in (0.5 mm). After that, as the load carrying capacity of the test specimen

suddenly dropped to 84 k (370 kN), the column displacement (line 1) increased to 0.9 in. (23 mm), but the slab displacement (line 2) rebounded to 0.2 in. (5 mm). This phenomenon indicated a punching shear failure, in which the column punched through the slab. Fig. 4-6 also shows that the measured shear strength of Specimen S08C ($V_u$ = 233 k or 1040 kN) was (5%) higher than its calculated shear strength ($V_{shear}$) given by the ACI Code[5], but (18%) lower than its calculated flexural strength ($V_{flex}$) (Table 4-1).

#### *4.3.1.2 Slab Displacement*

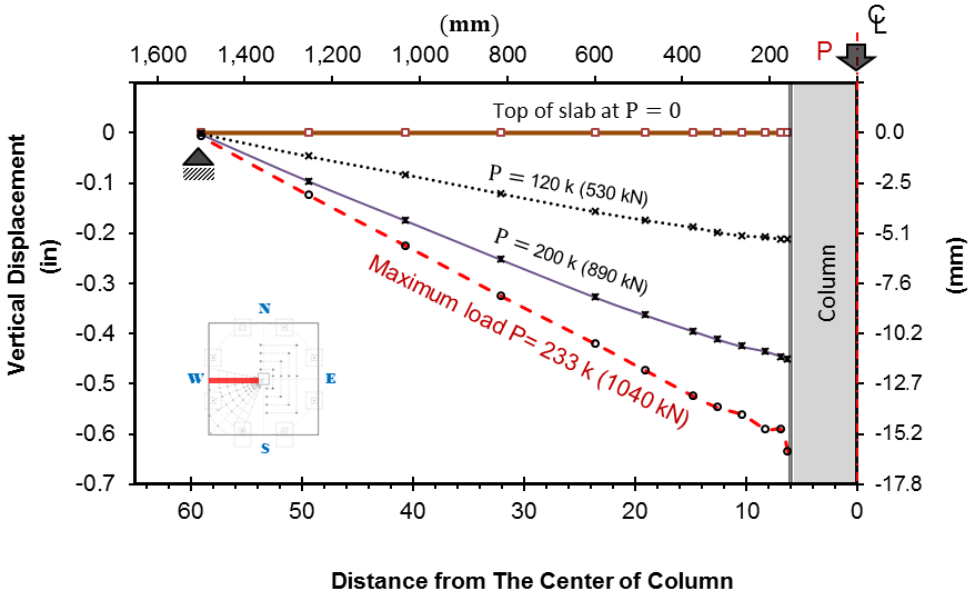


*Fig. 4-7: Measured displacements for the top of the slab in Specimen S08C*

Fig. 4-7 shows the measured displacements at different load stages for locations on the top of the slab along a line extending from the west column face to the supported edge of the slab. It shows that the top of the slab within a region extending approximately $d$ from the column face spalled off. The measured displacements for other regions of the slab were similar to Fig. 4-7, and they are shown in .

#### *4.3.1.3 Flexural Cracks in Concrete and Strains in Slab Flexural Reinforcing Bars*

Fig. 4-8 (a) shows the measured strains in slab tension reinforcing bars (bottom) when the applied load reached approximately 30 k (130 kN), or point C in Fig. 4-6. The measured strains near the north and south faces of the column were highest and exceeded the concrete cracking strain ($\varepsilon_{cr}$), which was approximated using the following equation.

$$\varepsilon_{cr} = \frac{f_r}{E_c} \cong \frac{7.5\sqrt{f_c'}\ psi}{57000\sqrt{f_c'}\ psi} = 1.3 \times 10^{-4} \qquad (34)$$

The strains in Fig. 4-8 (a) indicate that the first circumferential cracks initiated along the column periphery. After this load state, more flexural cracks formed near the column faces and propagated away from the column as the applied load increased. This development of flexural cracks resulted in a gradual decrease in the specimen stiffness after point C, as shown in Fig. 4-6. The crack patterns on the bottom surface of the slab after completion of the test are shown in Fig. B-1.

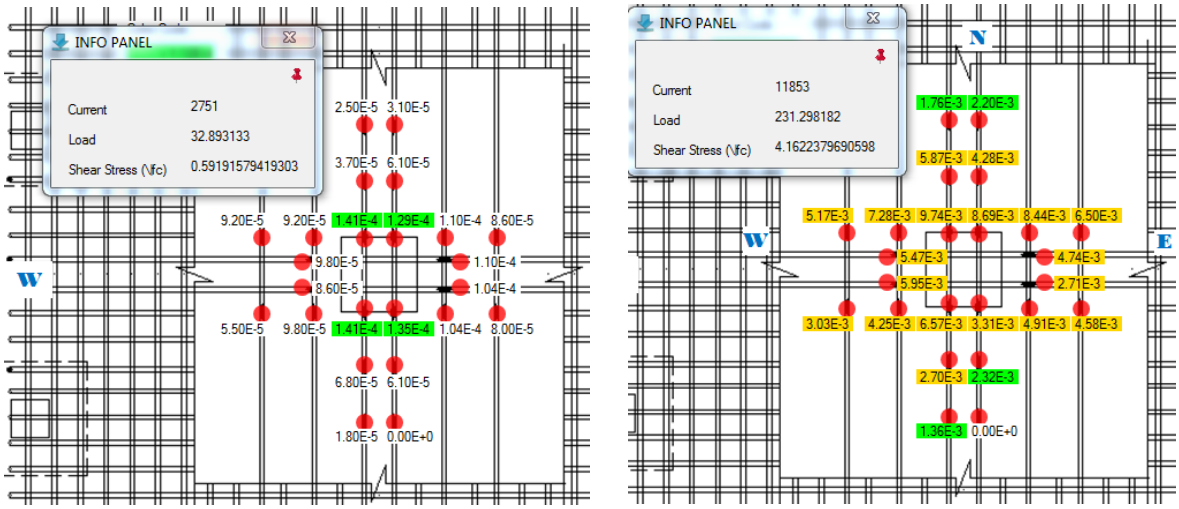


a) Near the occurrence of the first flexural crack b) Near the maximum applied load

*Fig. 4-8: Measured strains in slab flexural tension reinforcing bars (bottom)*

As the applied load increased, the measured strains in the slab reinforcing bars increased and they reached the yield strain ($\varepsilon_y = 0.0023$) at the applied load of approximately 180 kip (800 kN), which was corresponded to 75% of the maximum load ($V_u$) (point Y in Fig. 4-6). When the applied load reached $V_u$, the measured strains for most of the slab reinforcement strain gauges exceeded the yield strain (Fig. 4-8b).

#### *4.3.1.4 Shear Cracks and Failure Surfaces*

Shear (inclined) cracks were not observed during the test because they developed inside the slab. The development of inclined cracks, however, was studied using the measured through-thickness expansions of the slab. Fig. 4-9 shows the development of the measured slab

expansions at different locations along line E-NE (Fig. 3-24b), as the applied load, expressed as slab shear stress, increased. As shown in Fig. 4-9, the measured slab expansion at location E-NE1, approximately $d/2$ from column periphery, started to increase when the calculated slab shear stress reached $1.5\sqrt{f_c'}$ psi ($0.13\sqrt{f_c'}$ MPa), which corresponds to the applied load of approximately 45% of the maximum load (point I in Fig. 4-6). The increase in slab expansion at this load state indicates the initiation of inclined cracks. Fig. 4-9 also shows that the measured slab expansion at location E-NE2, approximately $1.5d$ from the column faces, started to increase at a later load stage as the calculated slab shear stress approached $2.6\sqrt{f_c'}$ psi ($0.22\sqrt{f_c'}$ MPa), implying the development of inclined cracks at this location. While the measured slab expansions for E-NE1 and E-NE2 significantly increased, the measured slab expansions at locations E-NE3 and E-NE4, $2.5d$ and $3.5d$ from the column faces, respectively, were almost unchanged as the applied load increased to the peak load. Before the punching shear failure, the maximum measured slab expansions (for E-NE1) were approximately 0.05 in. (1.3 mm). The measured slab expansions along other lines radiating out from the column were found to be similar to that in Fig. 4-9, as shown in Fig. B-3 and Fig. B-4.

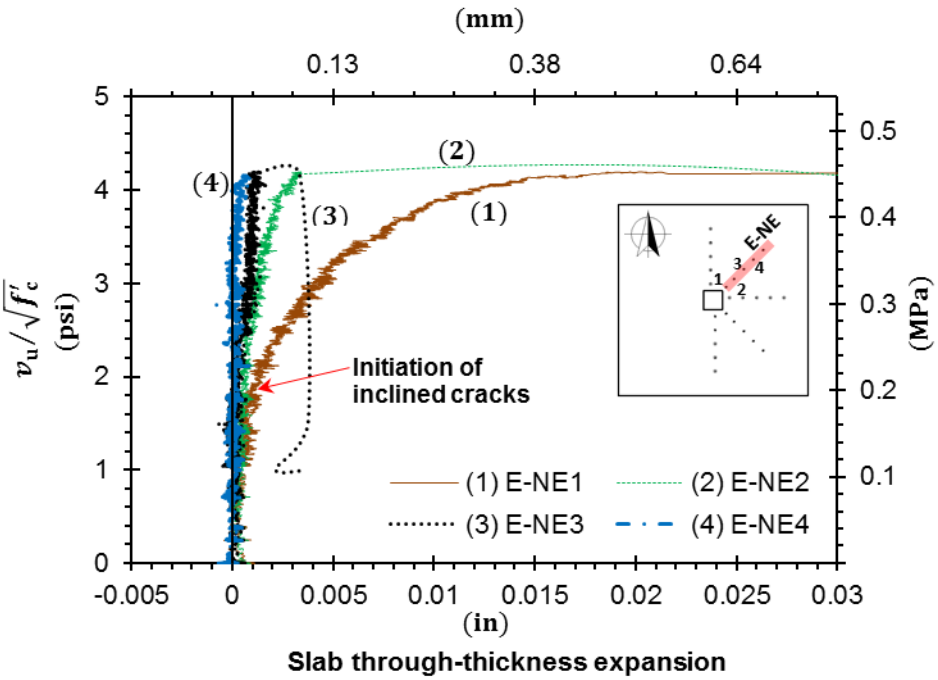


*Fig. 4-9: Measured slab through-thickness expansion along line E-EN (Fig. 3-24b)*

After completion of the test, the specimen was cut along a line close to the north face of the column to observe crack patterns in the slab. As shown in Fig. 4-10, the inclined cracks formed at approximately 30 degree to the horizontal, and they extended from the top of the slab near the column periphery to the bottom of the slab at approximately $1.5\,d$ from column faces. The observation of the crack patterns and the measured slab through-thickness expansions indicated that the inclined cracks formed near the mid-depth of the slab at $d/2$ from the column perimeter, and then propagated upward and downward to the bottom of the slab. At punching failure, these inclined cracks extended horizontally along the bottom slab reinforcing bars toward the edges of the slab due to dowel action (Fig. 4-10).

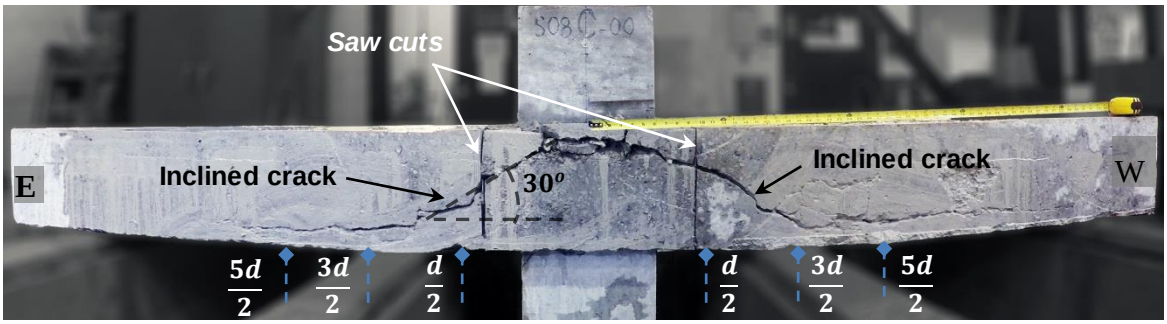


*Fig. 4-10: Cracks on a cut section close to the north face of the column for Specimen S08C (The cut location is shown in Fig. B-1)*

### 4.3.2 Specimen S08O ($\rho = 0.87\%$, Orthogonal Stud Layout)

#### *4.3.2.1 Load versus Displacement Relationship*

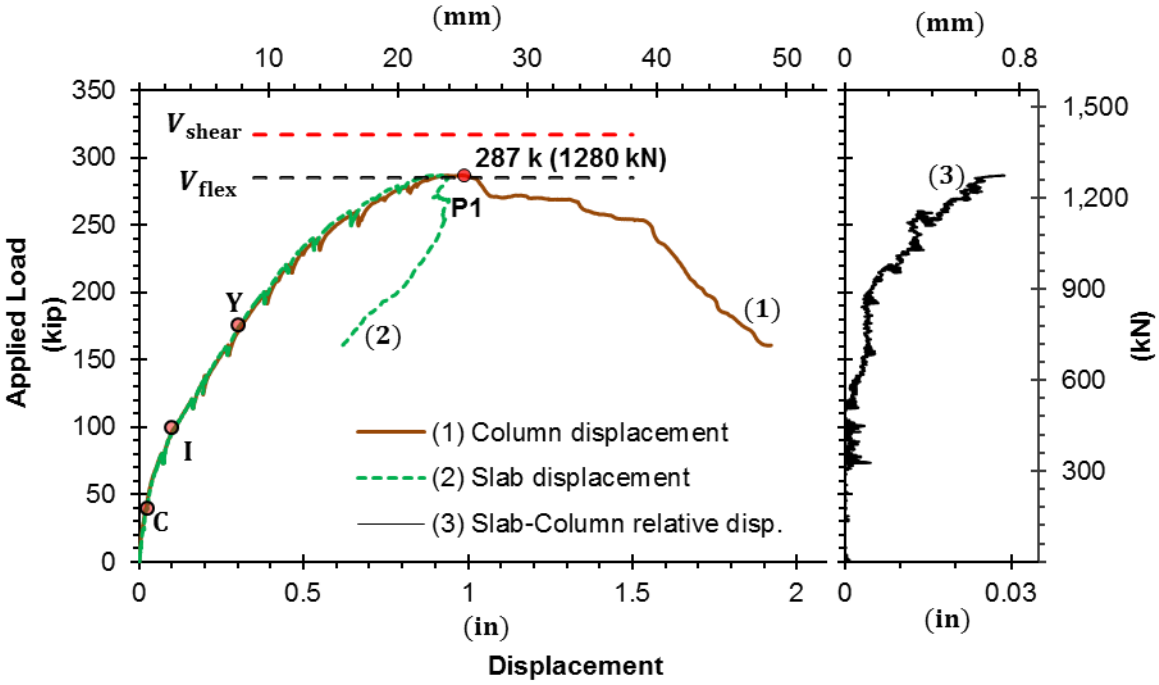


*Fig. 4-11: Load vs. displacement relationship for Specimen S08O*

The measured load versus displacement relationship for Specimen S08O is shown in Fig. 4-11. Line (1) in the figure represents the displacement of the column, line (2) represents the displacement of the slab measured at 1.25 in. (32 mm) from the west face of the column, and line (3) represents the difference between these displacements as the applied load increased to the maximum load. Fig. 4-11 shows that the two lines (1) and (2) were almost identical as the applied load increased to approximately 130 k (580 kN), and then they started to separate. At the applied load of approximately 200 k (890 kN), the relative displacement between the column and slab (line 3) increased at a faster rate. When the applied load reached maximum load, point P1, this relative displacement was approximately 0.03 in (0.8 mm). After this point, the displacements of the column and the slab split dramatically as the load carrying capacity of the test specimen decreased to 160 k (710 kN). While the column displacement increased to approximately 2 in. (50 mm), the slab displacement rebounded to 0.6 in. (15 mm). This phenomenon indicated a punching shear failure, in which the column punched through the slab. Fig. 4-11 also shows that the measured shear strength of Specimen S08O ($V_u = 287$ k or 1280

kN) was (10%) lower than its calculated shear strength ($V_{shear}$) given by the ACI Code[5], but it was equal to its calculated flexural strength ($V_{flex}$) (Table 4-1).

#### *4.3.2.2 Flexural Cracks and Strains in Slab Flexural Reinforcing Bars*

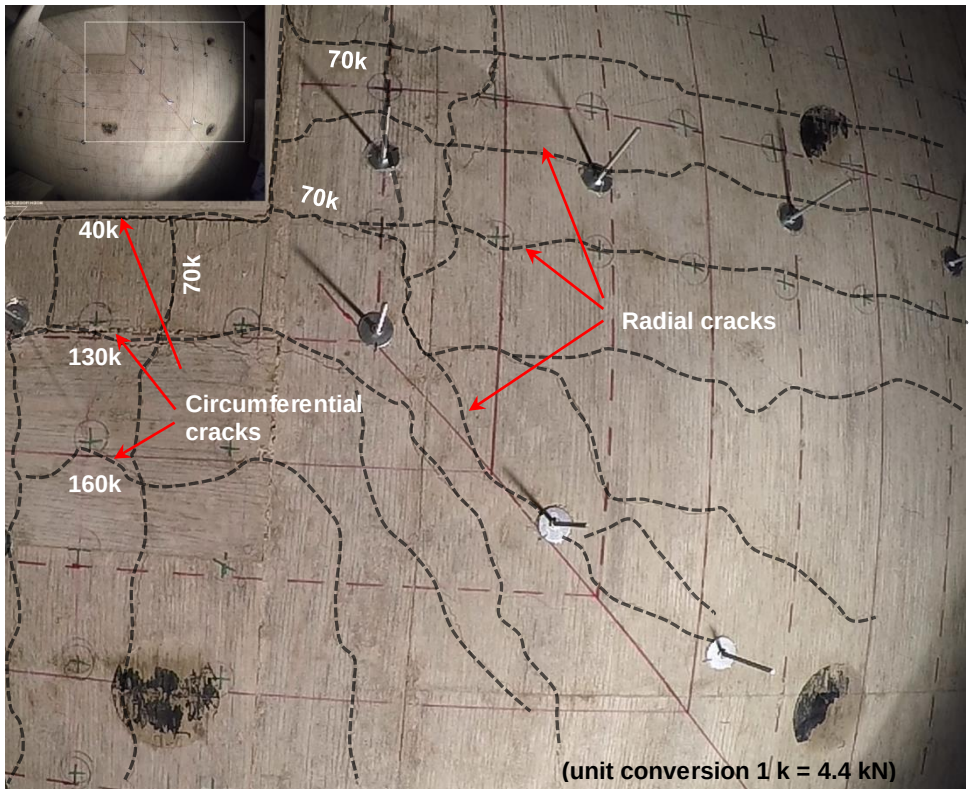


*Fig. 4-12: Crack patterns on the bottom of the slab of Specimen S08O near 280 k (1280 kN)*

The flexural cracks on the bottom of the slab before the punching shear failure of Specimen S08O are shown in Fig. 4-12. The first circumferential crack occurred along the column periphery at the applied load of approximately 40 k (180 kN) (point C in Fig. 4-11), when the measured strains in the slab flexural reinforcing bars reached the concrete cracking strain (Eq. 34). Other circumferential cracks were observed at 0.5$d$ and 1$d$ from the column faces when the applied load increased from 130 to 160 k (580 to 710 kN). The first radial cracks were observed near the column faces at the applied load of approximately 70 k (310 kN), and then they extended radially away from the column as the applied load increased. The development of the flexural cracks resulted in a continuous decrease in the stiffness of Specimen S08O after point C, as shown in Fig. 4-11. The crack patterns on the entire bottom surface of the slab after completion of the test is shown in Fig. B-6.

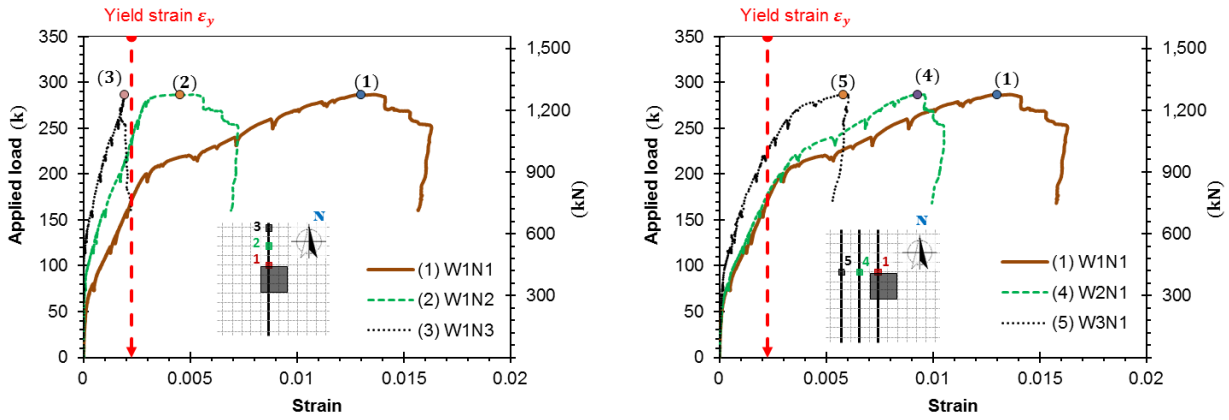


*Fig. 4-13: Measured strains in the slab flexural reinforcing bars of Specimen S08O (see Fig. 3-25 for strain gauge labels and locations)*

Typical results from the strain gauges attached on the slab flexural reinforcing bars (Fig. 3-25) are shown in Fig. 4-13. The measured value from Gauge 1, placed near the column faces, started to increase at the applied load of approximately 50 k (220kN), while the measured values from other gauges (2 to 5), placed further from the column, started to increase a later load stage. This observation was consistent with the development of the flexural cracks discussed previously. Fig. 4-13 also shows that the slab flexural reinforcing bars yielded when the applied load reached approximately 60 percent of the maximum load, which corresponds to point Y in Fig. 4-11. As the applied load increased to the maximum load, almost all of the measured strains exceeded the yield strain for the slab reinforcing bars (Fig. 4-13). Results from the other slab reinforcement strain gauges were similar and shown in Fig. B-7.

#### *4.3.2.3 Shear Cracks and Failure Surfaces*

Fig. 4-14 (a) shows the measured through-thickness expansion of the slab (slab expansion) along line E-E, which extends from the east face of the column. Fig. 4-14 (b) shows the measured strains in shear studs attached to a stud rail extending from the same column face. These figures show that the measured slab expansion at $d/2$ from the column face and the measured strain for the adjacent shear stud, lines (1) in Fig. 4-14 (a) and (b), respectively, almost simultaneously started to increase when the measured slab shear stress was approximately $2\sqrt{f_c'}$ psi ($0.17\sqrt{f_c'}$ MPa), and the corresponding applied load was approximately 35 percent of the peak load (point I in Fig. 4-11). The increases in these measurements indicated the formation of inclined cracks inside the slab. Fig. 4-14 also shows that when the measured slab shear stress

reached approximately $3\sqrt{f_c'}$ psi ($0.25\sqrt{f_c'}$ MPa), inclined cracks developed at $1.5d$ from the column faces, causing increases in the measured slab expansion and strains in the shear stud in these regions, lines (2) in Fig. 4-14 (a) and (b), respectively. The slab expansions were also measured at $2.5d$ (line 3) and $3.5d$ (line 4) from the column face, but no significant slab expansions were detected before the failure occurred. The measured slab expansions and strains in the shear studs in other slab regions, shown in Fig. B-9 and Fig. B-8, were found to be similar to those in Fig. 4-14.

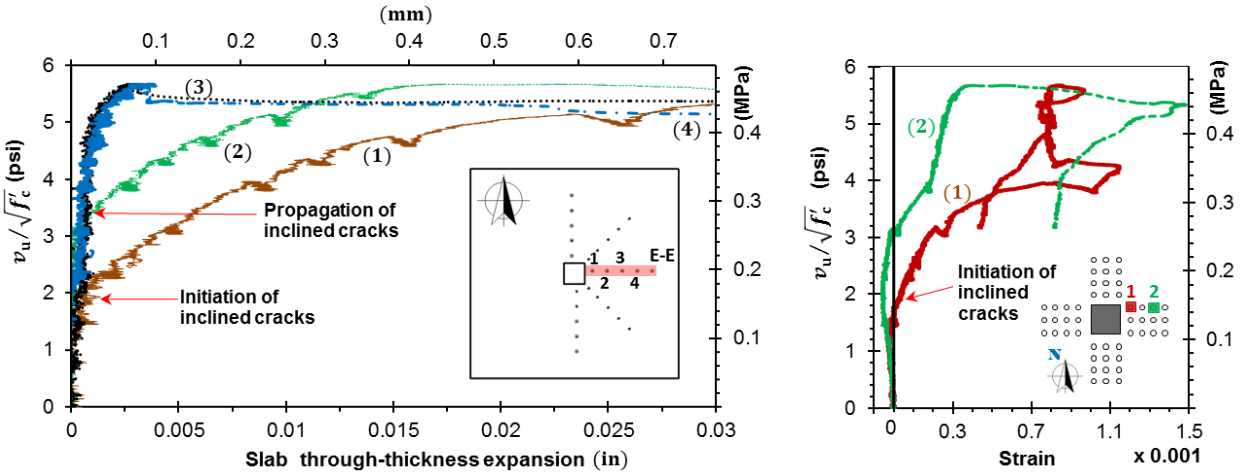


a) Slab through-thickness expansion b) Strains in shear studs

*Fig. 4-14: Measured slab expansions and strains in the shear studs of Specimen S08O*

*(see Fig. 3-24 to Fig. 3-26 for the instrument labels and locations)*

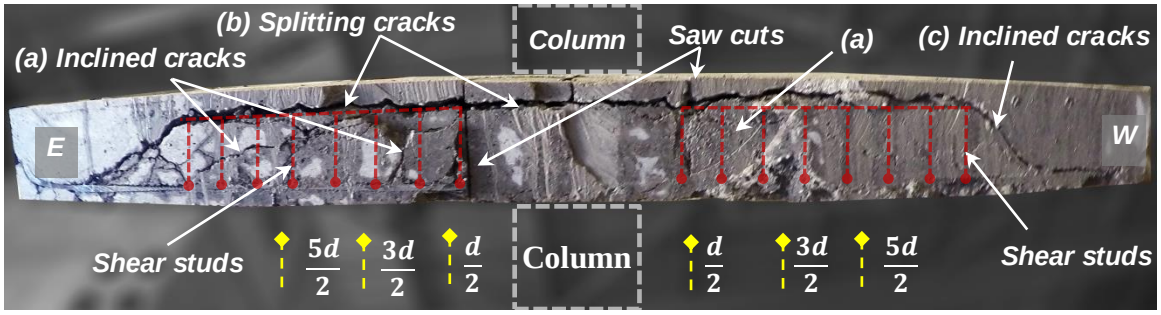


*Fig. 4-15: Cracks on a cut section close to the north face of the column for Specimen S08O*

*(The cut location is shown in Fig. B-6)*

After completion of the test, the specimen was cut along a line close to the north face of the column to observe crack patterns and failure surfaces in the slab. The cracks and failure surfaces

were different from those in Specimen S08C (Fig. 4-10). As shown in Fig. 4-15, some inclined cracks developed within shear stud regions, labeled as cracks (a). These inclined cracks engaged the shear studs and caused the increases in measured strains for these studs (Fig. 4-14). These inclined cracks, however, did not develop into failure surfaces. The failure surfaces for this specimen (S08O, with shear studs in an orthogonal layout) consisted of two segments: one developed horizontally above the stud rails, referred to as splitting cracks (b), and the other were the inclined cracks (c), which developed outside of the shear stud regions.

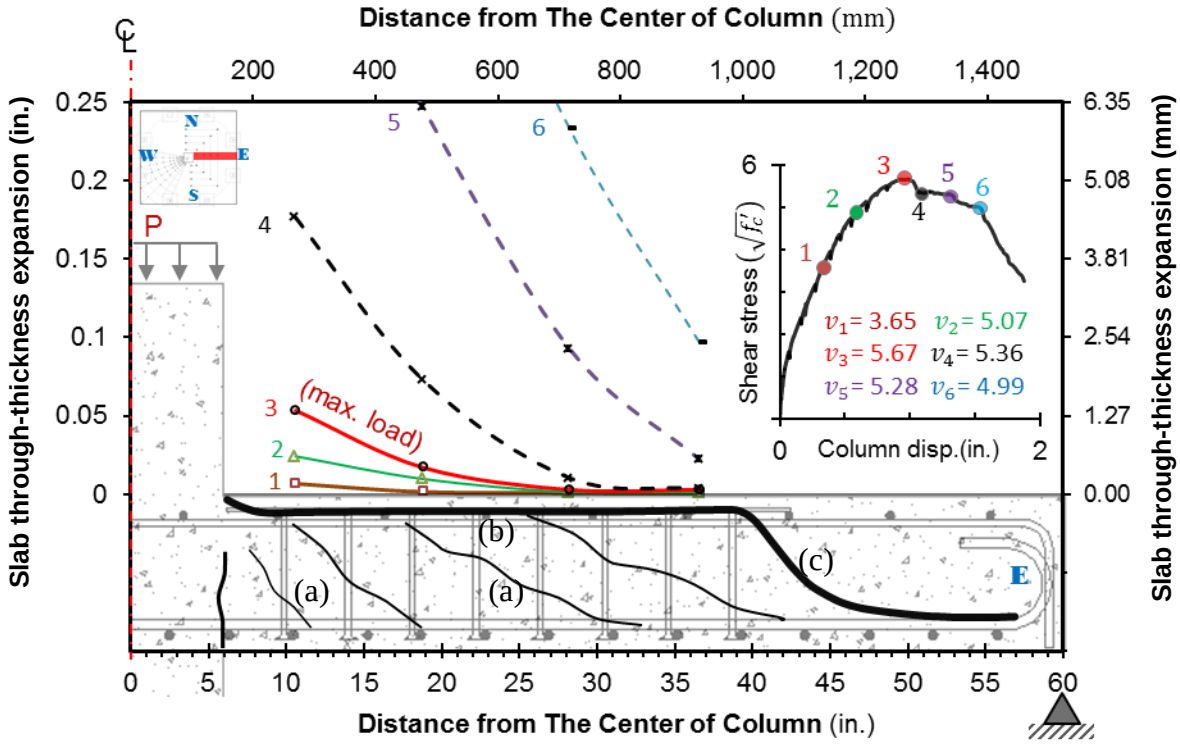


a. Inclined cracks b. Splitting cracks c. Flexural cracks

*Fig. 4-16: Slab through-thickness expansion along line E-E at different loads*

To study the development of the failure surfaces in Specimen S08O during the test, the measured slab through-thickness expansions (slab expansions) along line E-E (Fig. 4-14a) were plotted at the different measured slab shear stresses, as shown in Fig. 4-16. The distribution of the slab expansions measured at the maximum slab stress (line 3) shows that the cracks inside the slab were primarily developed within a regions extending $2d$ from the column face (within the 4$^{th}$ peripheral line of studs from the column). At stage 4 (line 4), after the load carring capacity of the specimen dropped slightly, the cracks in these regions grew twice as wide as they were in stage 3, while almost no significant slab expansions were measured in regions beyond the 5$^{th}$

stud row. The measured slab expansions near the outermost stud rows only started to increase from load stage 5 through 6. These results indicate that the failure surfaces would have formed in the regions near the column first (splitting cracks b). Then they propagated toward the ends of the stud rails, where they could extend downward to the bottom of the slab (inclined cracks c). The measured slab expansions in other directions were found to be similar to those shown in Fig. 4-16, and are shown in Fig. B-10.

### 4.3.3 Specimen S08R ($\rho$ = 0.87%, Radial Stud Layout)

#### *4.3.3.1 Load versus Displacement Relationship*

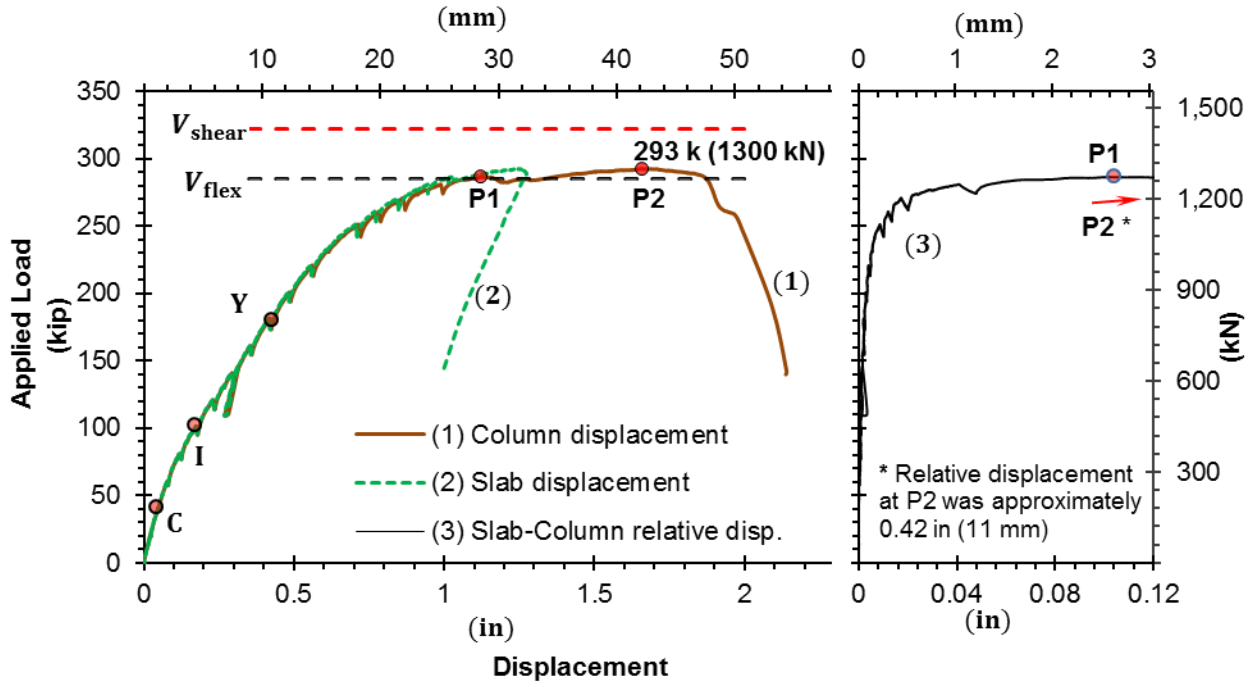


*Fig. 4-17: Load vs. displacement relationship for Specimen S08R*

The measured load versus displacement relationship for Specimen S08R is shown in Fig. 4-17. Line (1) in the figure represents the displacement of the column, line (2) represents the displacement of the slab regions adjacent to the column faces, and line (3) represents the difference between the slab and column displacements. Fig. 4-17 shows that the column and slab displacements were almost identical as the applied load increased to approximately 150 k (670 kN), and then they started to separate, as shown by the increase in the relative displacement between the column and the slab (line 3). This relative displacement increased at a faster rate as the applied load exceeded 250 k (1110 kN), and at the applied load of approximately 290 k (1290

kN), point P1, the difference between slab and column displacements was approximately 0.1 in (2.5 mm). After point P1, the specimen load carring capacity dropped slightly to 280 k (1250 kN), but quickly recovered. When the applied load reached the maximum load of 293 k (1300 kN), point P2, the relative displacement between the column and slab was approximately 0.42 in. (11 mm). After point P2, as the load decreased to 140 kip (620 kN), the column displacement (line 1) increased to approximately 2.1 in. (55 mm) while the slab displacement rebounded to approximately 1 in. (2.5 mm). This phenomenon indicated a punching shear failure. Fig. 4-17 also shows that the measured shear strength of Specimen S08R ($V_u = 293$ k or 1300 kN) was (10%) lower than its calculated shear strength ($V_{shear}$) given by the ACI Code[5], but similar to the calculated flexural strength ($V_{flex}$) (Table 4-1).

#### *4.3.3.2 Flexural Cracks and Strains in Slab Flexural Reinforcing Bars*

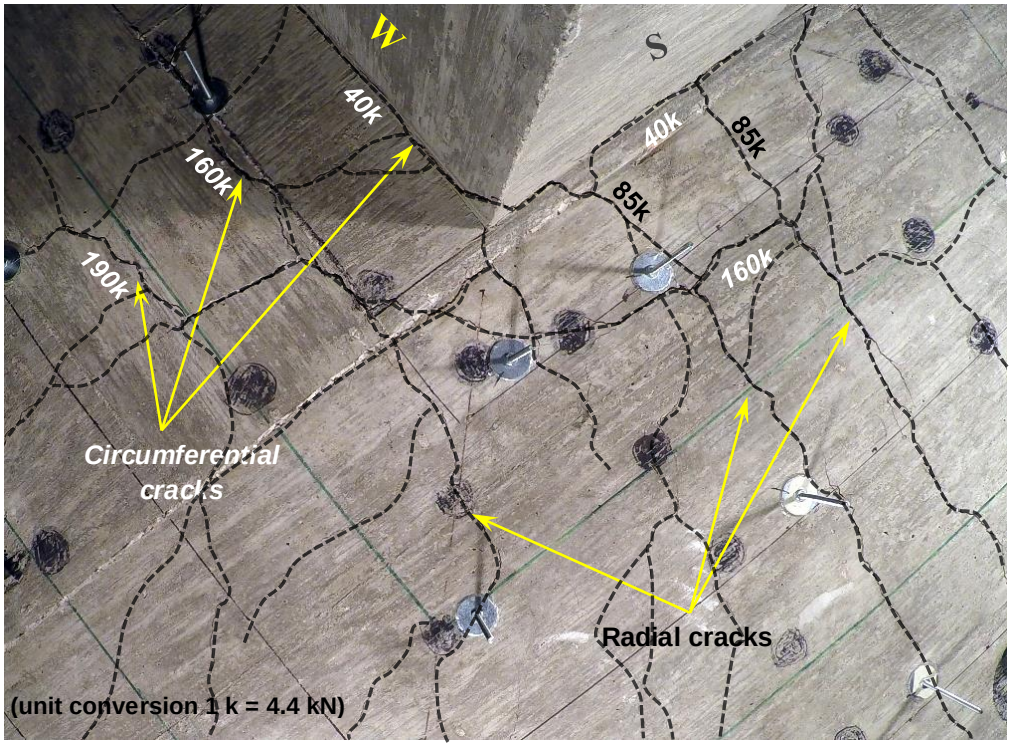


*Fig. 4-18: Crack patterns on the bottom of the slab in Specimen S08R near state P1 (Fig. 4-17)*

Fig. 4-18 shows the flexural cracks on the bottom of the slab in Specimen S08R when the applied load approached point P1 (Fig. 4-17). The first circumferential crack occurred along the column periphery at the applied load of approximately 40 k (180 kN) (point C in Fig. 4-17), when the measured strains in the slab flexural reinforcing bars reached the concrete cracking

strain (Eq. 34). Other circumferential cracks were observed at $0.5d$ and $1d$ from the column faces when the applied load increased from 160 to 190 k (710 to 850 kN). The first radial cracks were observed near the column faces at the applied load of approximately 85 k (380 kN), and they extended radially away from the column as the applied load increased. The development of the flexural cracks resulted in a continuous decrease in the stiffness of Specimen S08R after load state C, as shown in Fig. 4-17. The crack patterns on the entire bottom surface of the slab after completion of the test are shown in Fig. B-11.

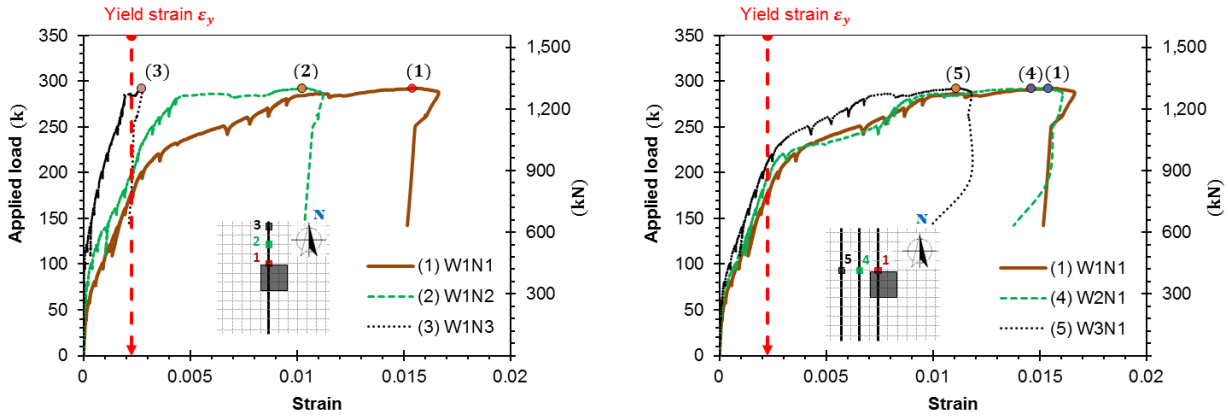


*Fig. 4-19: Measured strains in the slab flexural reinforcing bars of Specimen S08R (see Fig. 3-25 for strain gauge labels and locations)*

Typical results from the strain gauges attached to the slab flexural reinforcing bars (Fig. 3-25) are shown in Fig. 4-19. The strain value from Gauge 1, placed near the column faces, started to increase at the applied load of approximately 50 k (220kN), while the measured strains from other gauges (2 to 5), placed further from the column, started to increase at a later load stage. These measured strains were consistent with the development of the flexural cracks discussed previously. Fig. 4-19 also shows that the slab flexural reinforcing bars yielded when the applied load reached approximately 60 percent of the maximum measured load, which corresponds to point Y in Fig. 4-17. As the applied load increased to the maximum value, all of the measured strains exceeded the yield strain for the reinforcing bars (Fig. 4-19). The results from other strain gauges were found to be similar and are shown in Fig. B-12.

### 4.3.3.3 *Shear Cracks and Failure Surfaces*

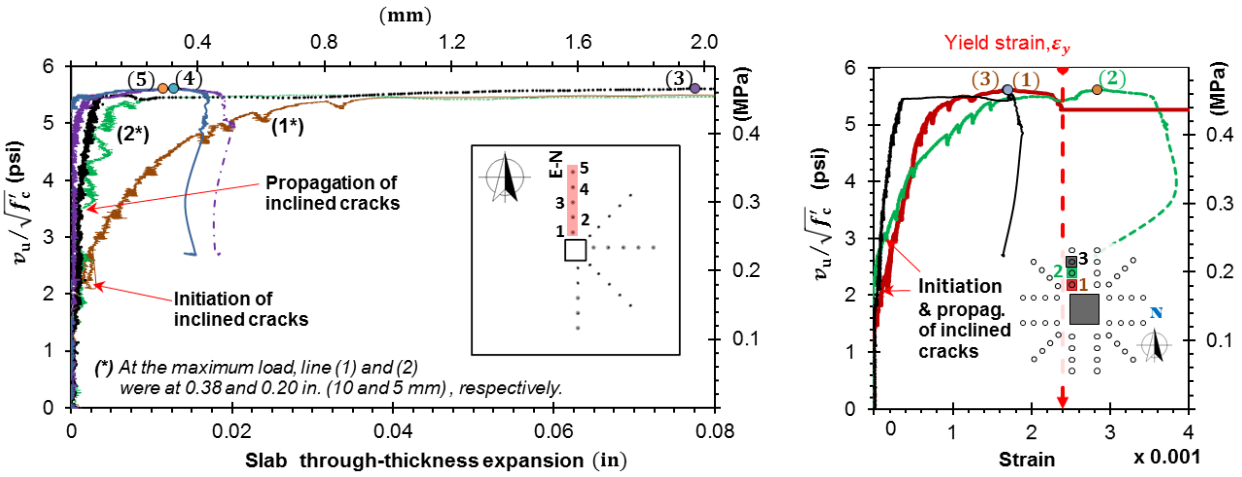


a) Slab through-thickness expansion

b) Strains in shear studs

*Fig. 4-20: Measured slab expansions and strains in the shear studs of Specimen S08R (see Fig. 3-24 to Fig. 3-26 for the instrument labels and locations)*

Fig. 4-20 (a) shows the measured through-thickness expansion of the slab (slab expansion) along line E-N, which extends from the north face of the column, and the measured strains in shear studs on a rail extending from this column face is shown in Fig. 4-20 (b). These figures shows that the measured slab expansion at $d/2$ from the column face and the measured strain for the adjacent shear stud, lines (1) in Fig. 4-20 (a) and (b), respectively, almost simultaneously started to increase when the measured slab shear stress was approximately $2\sqrt{f_c'}$ psi ($0.17\sqrt{f_c'}$ MPa), and the corresponding applied load was approximately 35 percent of the peak load (Point I in Fig. 4-17). The increases in these measurements indicated the formation of the inclined cracks inside the slab. Fig. 4-20 also shows that when the measured slab shear stress reached approximately $3\sqrt{f_c'}$ psi ($0.25\sqrt{f_c'}$ MPa), the inclined cracks propagated to the slab regions at $1.5d$ from the column faces, causing increases in the measured slab expansion and strain in the shear stud in these regions (lines (2) in Fig. 4-20 (a) and (b), respectively). The slab expansions were also measured at $2.5d$ (line 3), $3.5d$ (line 4), and $4.5d$ (line 5) from the column face, but the measured results for these locations were significantly smaller than the measured values at $0.5d$ and $1.5d$. At the maximum load (point P2 in Fig. 4-17), the measured slab expansions at $0.5d$ and $1.5d$. were approximately 0.38 and 0.2 in. (10 and 5 mm), respectively, while the expansions at locations $2.5d$ or futher from the column face were less than 5% the values at $0.5d$ and $1.5d$.

These results indicated that the cracks inside the slab developed primarily within the regions extending $1.5d$ from the column faces. The measured slab expansions and strains in the shear studs in other slab regions, shown in Fig. B-13 and Fig. B-14, were similar to those in Fig. 4-20.

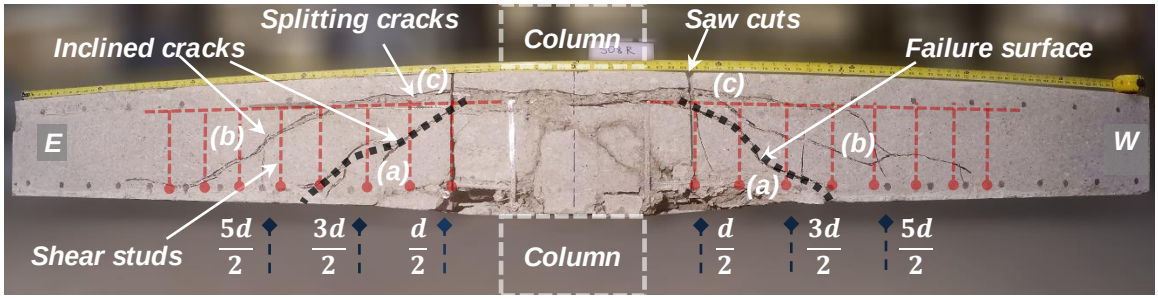


*Fig. 4-21: Cracks on a cut section close to the north face of the column for Specimen S08R (The cut location is shown in Fig. B-11)*

After completion of the test, the specimen was cut along a line close to the north face of the column to observe crack patterns and failure surfaces in the slab. As shown in Fig. 4-21, the inclined cracks, labeled as (a) and (b), developed in the shear stud regions and engaged the shear studs, causing increases in the measured strains for the studs (Fig. 4-20b). Fig. 4-21 also shows that splitting cracks (c) developed horizontally above the stud regions and then extended downward to the bottom of the slab, as inclined cracks (b). The development of splitting cracks and failure surfaces in this test specimen were different from those in Specimen S08O (with studs in an orthogonal layout). The splitting cracks did not extend to the outermost studs, and thus they were not a major part of the failure surface. The failure surface for this specimen (S08R, with studs in a radial layout) developed from inclined cracks (a) near the column and thus was similar to the failure surface in Specimen S08C (without shear reinforcement). This type of failure surface engaged the shear studs near the columns, eventually causing fracture of some shear studs near final failure of the test specimen. Comparisons between failure surfaces for Specimens S08O and S08R are presented in Section 4.5.4.

### 4.3.4 Specimen S12O ($\rho = 1.25\%$, Orthogonal Stud Layout)

#### *4.3.4.1 Load versus Displacement Relationship*

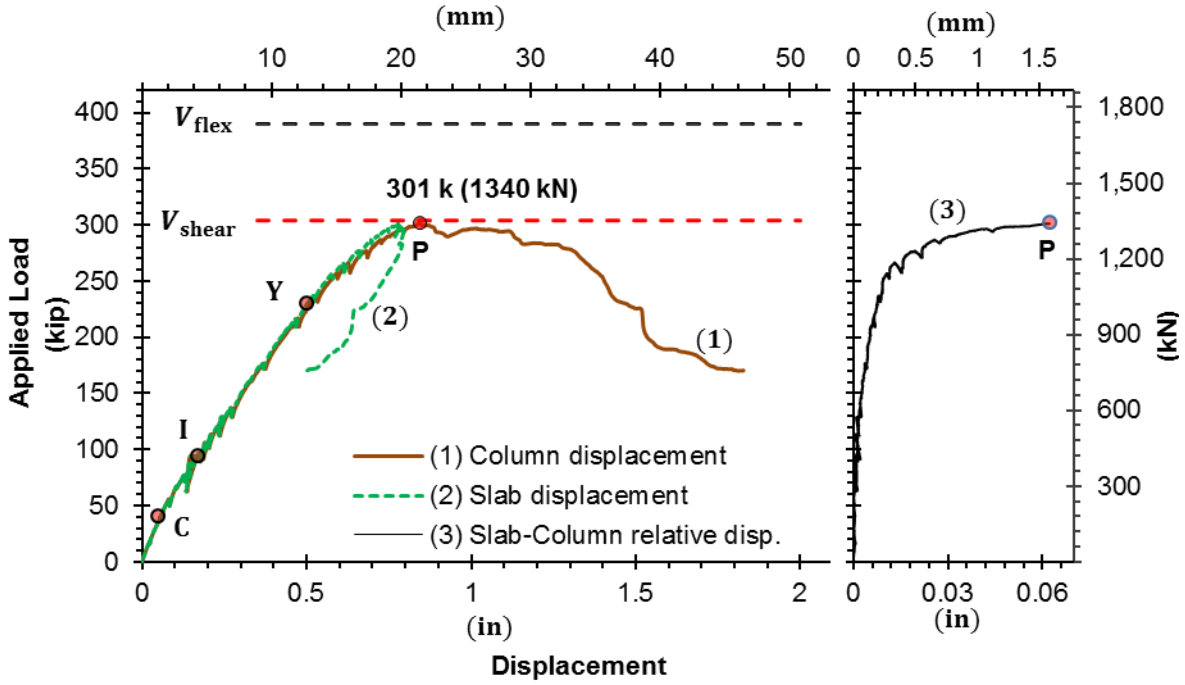


*Fig. 4-22: Load vs. displacement relationship for Specimen S12O*

The measured load versus displacement relationship for Specimen S12O is shown in Fig. 4-22. Line (1) in the figure represents the displacement of the column, line (2) represents the displacement of the slab regions adjacent to the column faces, and line (3) represents the difference between the slab and column displacements. Fig. 4-22 shows that the slab and column displacements were almost identical as the applied load increased to approximately 130 k (580 kN), and then they started to separate, causing an increase in the relative displacement between the column and slab (line 3). This relative displacement increased at a faster rate as the applied load exceeded approximately 250 k (1110 kN), and it was approximately 0.06 in. (1.5 mm) when the applied load reached the maximum value of 301 k (1340 kN), point P. After this point, as the specimen load carrying capacity decreased to 170 kip (750 kN), the column displacement (line 1) increased to approximately 1.9 in (48 mm), but the slab displacement rebounded to approximately 0.5 in. (13 mm). This phenomenon indicated a punching shear failure. Fig. 4-22 also shows that the measured shear strength of Specimen S12O ($V_u = 301$ k or 1340 kN) was

close to the calculated shear strength ($V_{shear}$) given by the ACI Code[5], and 25% lower than the calculated flexural strength ($V_{flex}$) (Table 4-1).

#### *4.3.4.2 Flexural Cracks and Strains in Slab Flexural Reinforcing Bars*

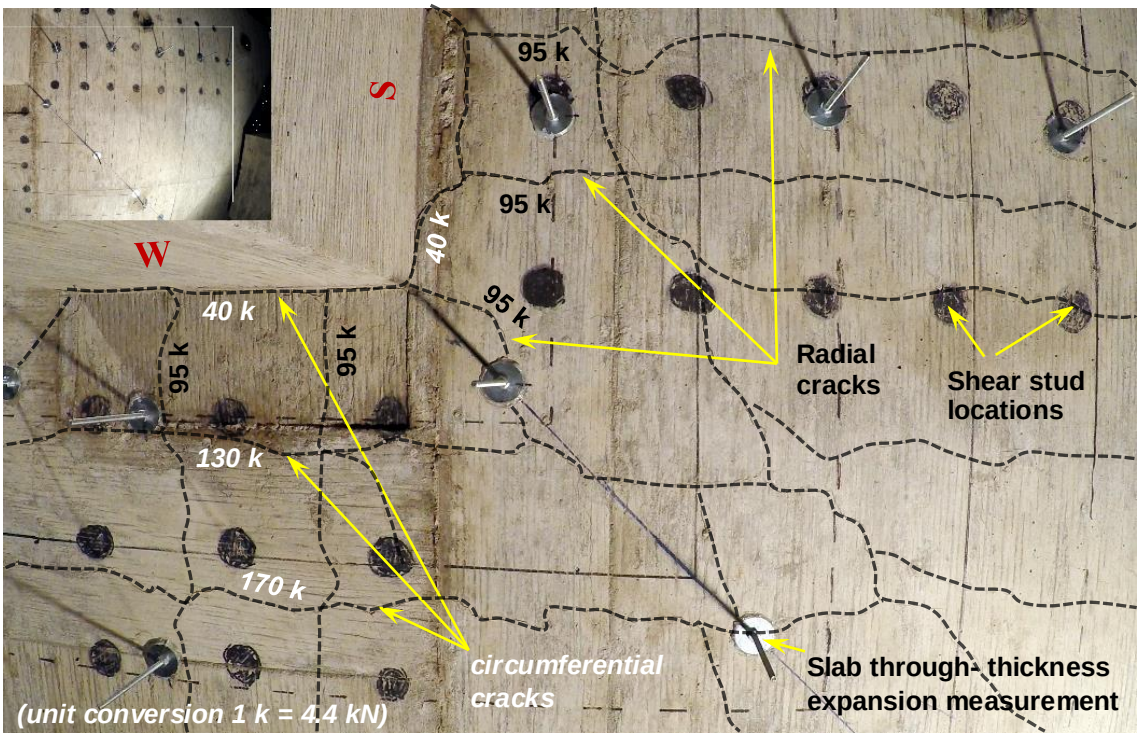


*Fig. 4-23: Crack patterns on the bottom of the slab of Specimen S12O near P (Fig. 4-22)*

The flexural cracks on the bottom of the slab before the punching shear failure of Specimen S12O are shown in Fig. 4-23. The first circumferential crack occurred along the column periphery at an applied load of approximately 40 k (180 kN) (point C in Fig. 4-22), when the measured strains in the slab flexural reinforcing bars reached the concrete cracking strain (Eq. 34). The other circumferential cracks were observed at 0.5$d$ and 1$d$ from the column faces when the applied load increased from 130 to 170 k (580 to 760 kN). The first radial cracks were observed near the column faces at an applied load of approximately 95 k (420 kN), and they extended radially away from the column as the applied load increased. The development of the flexural cracks resulted in a continuous decrease in the stiffness of Specimen S12O after point C, as shown in Fig. 4-22. The crack patterns on the entire bottom surface of the slab after completion of the test is shown in Fig. B-16.

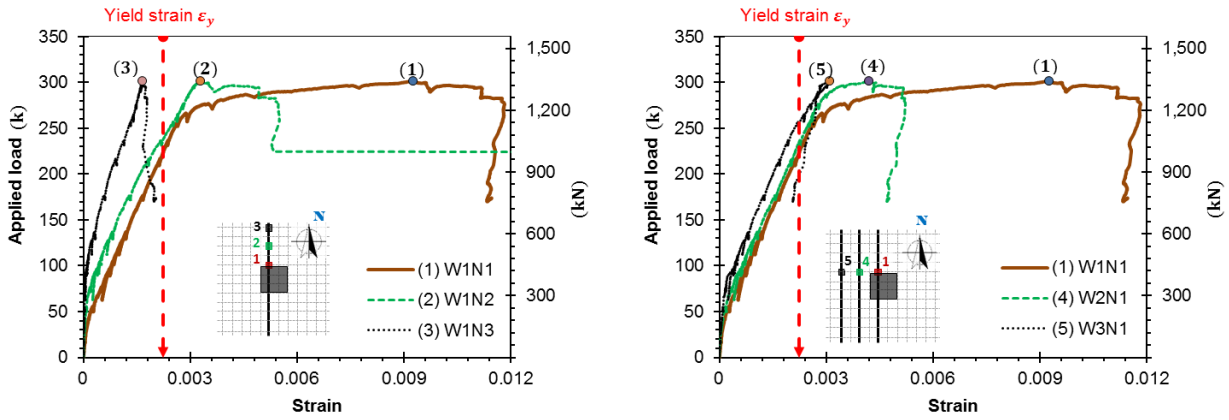


*Fig. 4-24: Measured strains in the slab flexural reinforcing bars of Specimen S12O*

*(see Fig. 3-25 for strain gauge labels and locations)*

The typical results from the strain gauges attached on the slab flexural reinforcing bars are shown in Fig. 4-24. The measured strain value from Gauge 1, placed near the column face, started to increase at the applied load of approximately 40 k (180kN), while the measured values from other gauges (2 to 5), placed further from the column, started to increase later as the applied load increased. These measured strains were consistent with the development of the flexural cracks discussed previously. Fig. 4-24 also shows that the slab flexural reinforcing bars yielded when the applied load reached approximately 75 percent of the maximum load, which corresponds to point Y in Fig. 4-22. As the applied load increased to the maximum load, almost all of the measured strains exceeded the yield strain for the reinforcing bars (Fig. 4-24). The results from other strain gauges were found to be similar and are shown in Fig. B-17.

### *4.3.4.3 Shear Cracks and Failure Surfaces*

Fig. 4-25 (a) shows the measured through-thickness expansion of the slab (slab expansion) along line E-E, which extends from the east face of the column, and Fig. 4-25 (b) shows the measured strains in shear studs located on a stud rail extending from this column face (Fig. 3-26). It is shown that the measured slab expansion at $d/2$ from the column face and the measured strain for the adjacent shear stud, lines (1) in Fig. 4-25 (a) and (b), respectively, almost simultaneously started to increase when the measured slab shear stress was approximately $2\sqrt{f_c'}$ psi ($0.17\sqrt{f_c'}$ MPa), and the corresponding applied load was approximately 30 percent of the peak load (point I in Fig. 4-22). Increases in these measurements indicated the formation of inclined cracks inside the slab. Fig. 4-25 shows that when the measured slab shear stress reached

approximately $3.5\sqrt{f_c'}$ psi ($0.29\sqrt{f_c'}$ MPa), inclined cracks developed at 1.5$d$ from the column faces, causing increases in the measured slab expansion and strains in the shear stud at this location, lines (2) in Fig. 4-25 (a) and (b), respectively. The slab expansions were also measured at 2.5$d$ (line 3), 3.5$d$ (line 4), and 4.5$d$ (line 5) from the column face, but slab expansion at these locations were almost zero before the failure occurred. These results indicated that the cracks inside the slab developed primarily within the regions extending 1.5d from the column faces. The measured slab expansions and strains in the shear studs in other slab regions adjacent to the column are shown in and Fig. B-19, and they were found to be similar to those in Fig. 4-25.

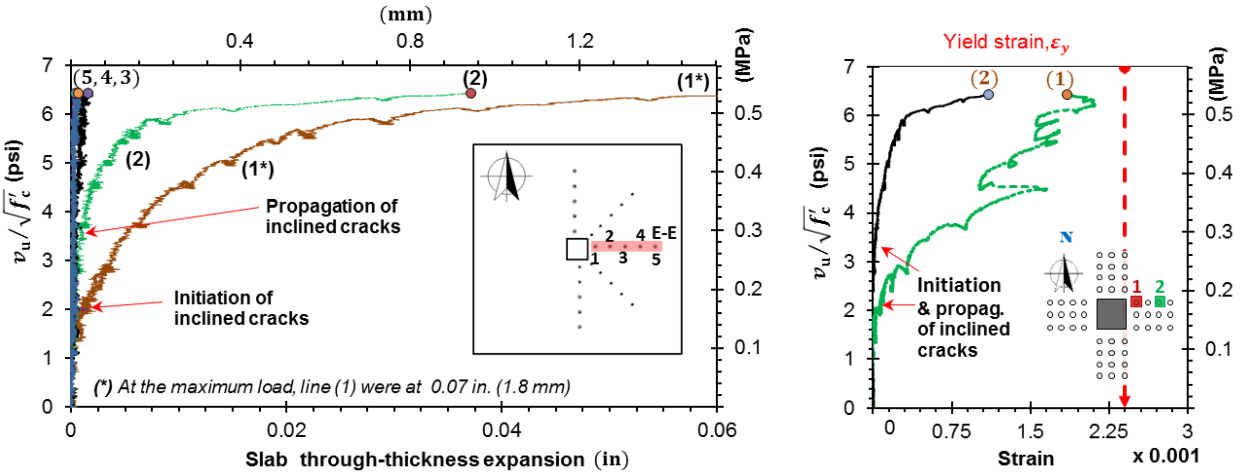


a) Slab through-thickness expansion

b) Strains in shear studs

*Fig. 4-25: Measured slab expansions and strains in the shear studs of Specimen S12O*

*(see Fig. 3-24 to Fig. 3-26 for the instrument labels and locations)*

After completion of the test, the specimen was cut along a line close to the north face of the column to observe cracks in the slab, as shown in Fig. 4-26. These cracks and failure surfaces were found to be similar to those for Specimen S08O. Some inclined cracks, labeled as cracks (a), developed within the shear stud regions. These cracks engaged the shear studs, causing increases in the measured strains in these studs (Fig. 4-25b). However, these inclined cracks did not become failure surfaces. Fig. 4-26 shows that the failure surfaces for this specimen (S12O) consisted of two segments: one that developed horizontally above the stud rails, referred to as splitting cracks (b), and the other were the inclined cracks (c), which developed outside the shear stud regions. Thus, the failure surface in this specimen (S12O with shear studs in an orthogonal layout) did not engage the shear studs. This type of failure surface was different from that in

Specimens S08C (Fig. 4-10) and S08R (Fig. 4-21), but it was similar to that in Specimen S08O (Fig. 4-15). Comparisons between failure surfaces for these specimens are presented in Section 4.5.4.

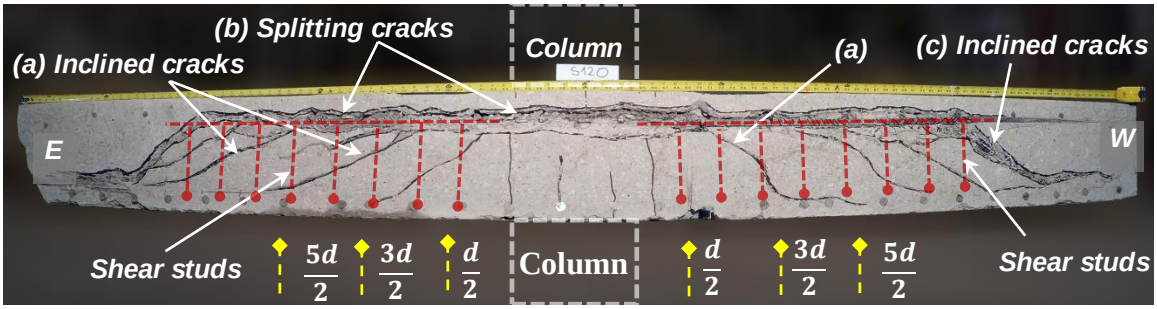


*Fig. 4-26: Cracks on a cut section close to the north face of the column for Specimen S12O (The cut location is shown in Fig. B-16)*

## 4.3.5 Specimen S12R ($\rho = 1.25\%$, Radial Stud Layout)

### *4.3.5.1 Load versus Displacement Relationship*

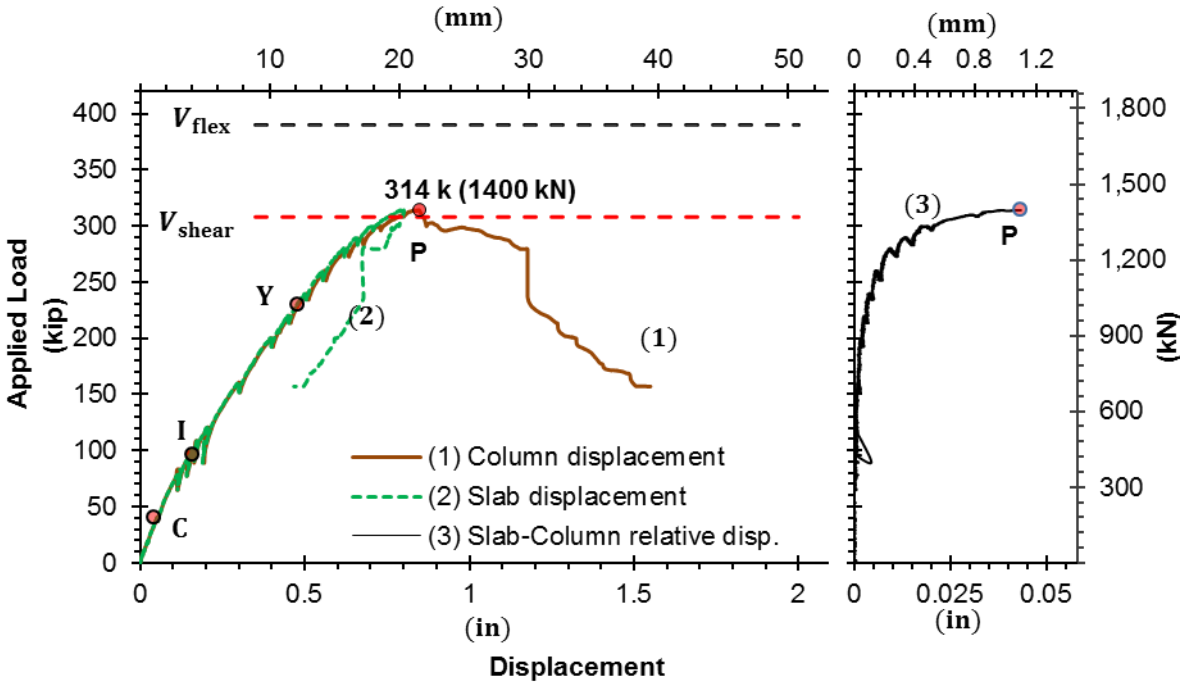


*Fig. 4-27: Load vs. displacement relationship for Specimen S12R*

The measured load versus displacement relationship for Specimen S12R is shown in Fig. 4-27. Line (1) in the figure represents the displacement of the column, line (2) represents the displacement of the slab regions adjacent to the column faces, and line (3) represents the

difference between the slab and column displacements. Fig. 4-27 shows that the column and slab displacements were almost identical as the applied load increased to approximately 170 k (760 kN). At higher loads, the relative displacement between the column and slab started to increase (line 3). Fig. 4-27 shows that this relative displacement increased at faster rate for loads above 280 k (1250 kN) and reached approximately 0.04 in. (1 mm) when the applied load approached the maximum value of 314 k (1400 kN), point P. After this point, as the specimen load carrying capacity decreased to 150 kip (750 kN), the column displacement (line 1) increased to approximately 1.6 in (41 mm), but the slab displacement rebounded to approximately 0.5 in. (13 mm). This phenomenon indicated a punching shear failure. Fig. 4-27 also shows that the measured shear strength of Specimen S12R ($V_{\mathrm{u}} = 314$ k or 1400 kN) was equal to the calculated shear strength ($V_{\mathrm{shear}}$) given by the ACI Code[5] and was 20% lower than the calculated flexural strength ($V_{\mathrm{flex}}$) (Table 4-1).

#### *4.3.5.2 Flexural Cracks and Strains in Slab Flexural Reinforcing Bars*

The flexural cracks on the bottom of the slab before the punching shear failure of Specimen S12O are shown in Fig. 4-28. The first circumferential crack occurred along the column periphery at the applied load of approximately 40 k (180 kN) (point C in Fig. 4-27), when the measured strains in the slab flexural reinforcing bars reached the concrete cracking strain (Eq. 34). Other circumferential cracks were observed at $0.75d$ and $1.25d$ from the column faces when the applied load increased from 160 to 190 k (710 to 850 kN). The first radial cracks were observed near the column faces at the applied load of approximately 120 k (530 kN), and they extended radially away from the column as the applied load increased. The development of the flexural cracks resulted in a continuous decrease in the stiffness of Specimen S12R after point C, as shown in Fig. 4-27. The crack pattern on the bottom surface of the slab after completion of the test is shown in Fig. B-20.

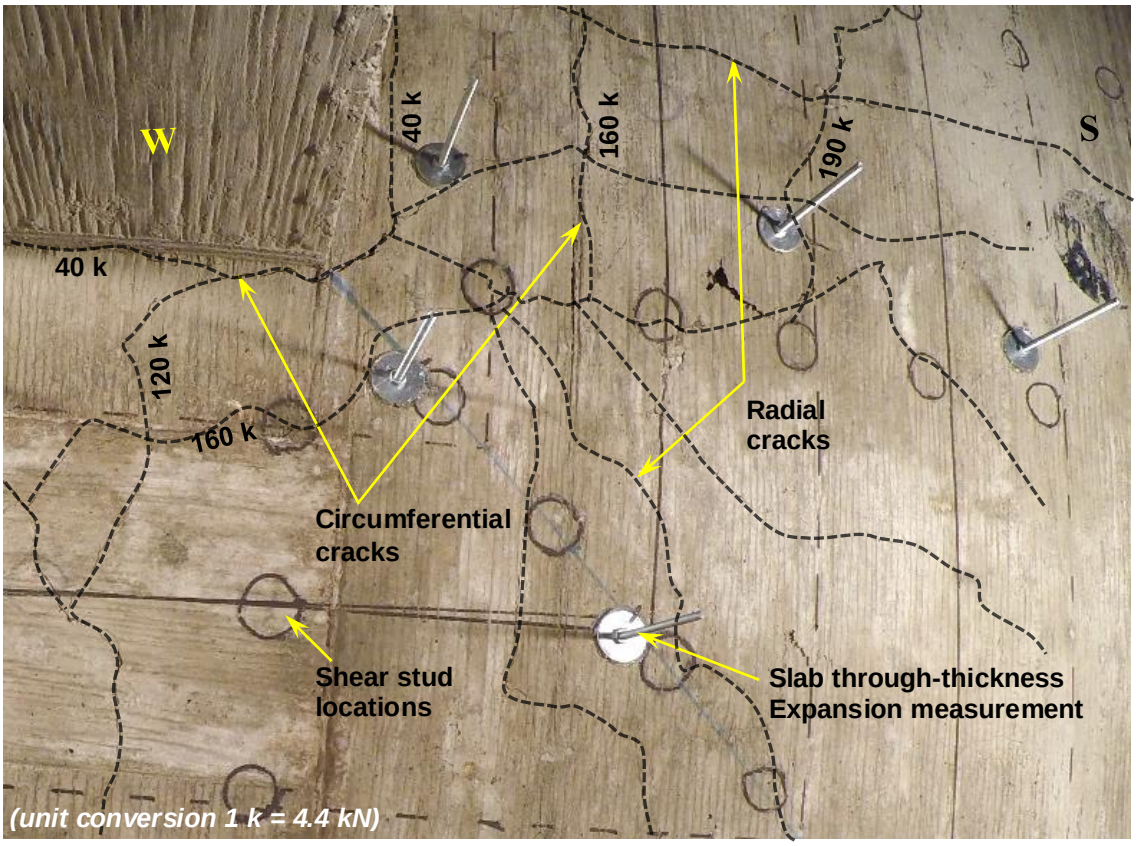


*Fig. 4-28: Crack patterns on the bottom of the slab of Specimen S12R near P (Fig. 4-22)*

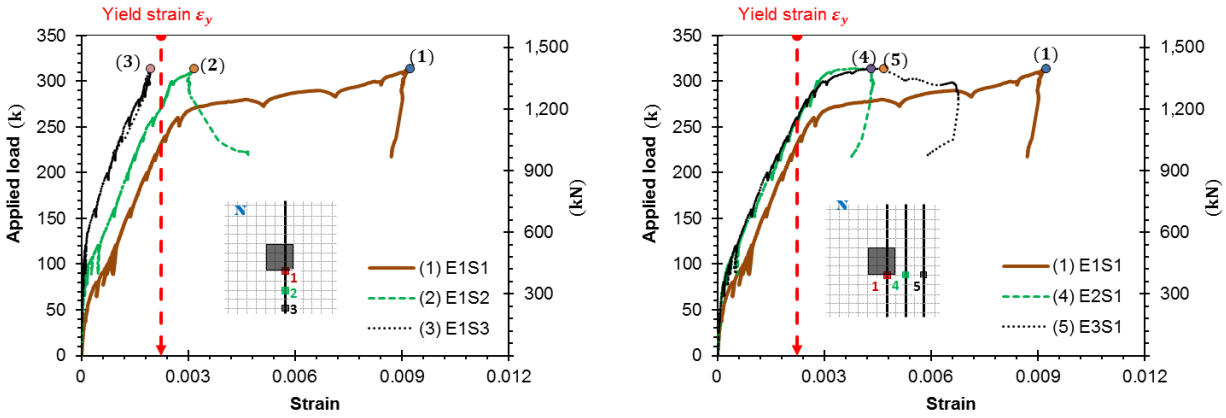


*Fig. 4-29: Measured strains in the slab flexural reinforcing bars of Specimen S12R*

*(see Fig. 3-25 for strain gauge labels and locations)*

Typical results from the strain gauges attached on the slab flexural reinforcing bars are shown in Fig. 4-29. The measured strain from Gauge 1, placed near the column face, started to increase first at the applied load of approximately 40 k (180kN), while the measured strains from other gauges (2 to 5), placed further from the column, started to increase later as the applied load

increased. These measured strains were consistent with the development of the flexural cracks discussed previously. Fig. 4-29 also shows that the slab flexural reinforcing bars yielded when the applied load reached approximately 70 percent of the maximum load, which corresponds to point Y in Fig. 4-27. As the applied load increased to the maximum load, almost all of the measured strains exceeded the yield strain for the slab reinforcing bars (Fig. 4-29). The results from other strain gauges were found to be similar and are shown in Fig. B-21.

#### *4.3.5.3 Shear Cracks and Failure Surfaces*

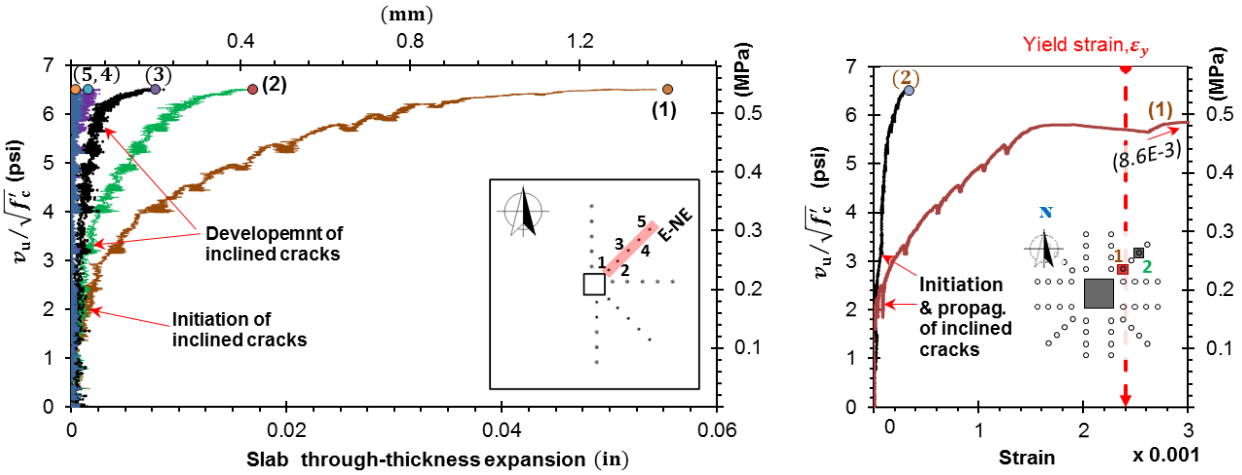


a) Slab through-thickness expansion b) Strains in shear studs

*Fig. 4-30: Measured slab expansions and strains in the shear studs of Specimen S12R*

*(see Fig. 3-24 to Fig. 3-26 for the instrument labels and locations)*

Fig. 4-30 (a) shows the measured through-thickness expansion of the slab (slab expansion) along the diagonal line E-NE, which extends from the north east corner of the column, and Fig. 4-30 (b) shows the measured strains in shear studs attached to a stud rail adjacent to this line (Fig. 3-26). The measured slab expansion at $d/2$ from the corner of the column and the measured strain for the adjacent shear stud, lines (1) in Fig. 4-30 (a) and (b), respectively, almost simultaneously started to increase when the measured slab shear stress was approximately $2\sqrt{f'_c}$ psi ($0.17\sqrt{f'_c}$ MPa), and the corresponding applied load was approximately 30 percent of the peak load (point I in Fig. 4-26). Increases in these measurements indicate the formation of inclined cracks inside the slab. It is also shown in Fig. 4-30 that when the measured slab shear stress reached approximately $3.5\sqrt{f'_c}$ psi ($0.29\sqrt{f'_c}$ MPa), inclined cracks developed at $1.5d$ from

the column periphery, causing increases in the measured slab expansion and strains in the shear stud in these regions, lines (2) in Fig. 4-30 (a) and (b), respectively. As the measured slab shear stress reached approximately $6\sqrt{f_c'}$ psi ($0.5\sqrt{f_c'}$ MPa), line (3) in Fig. 4-30 (a) shows a significant increase in the slab expansion, indicating the development of inclined cracks at the slab region 2.5 $d$ from the column faces. The slab expansions were also measured at 3.5$d$ (line 4) and 4.5$d$ (line 5) from the column periphery, but slab expansions at these locations were almost rezo before failure occurred. The measured slab expansions and strains in the shear studs in other slab regions are shown in Fig. B-22 and Fig. B-23, and they were found to be similar to those in Fig. 4-30.

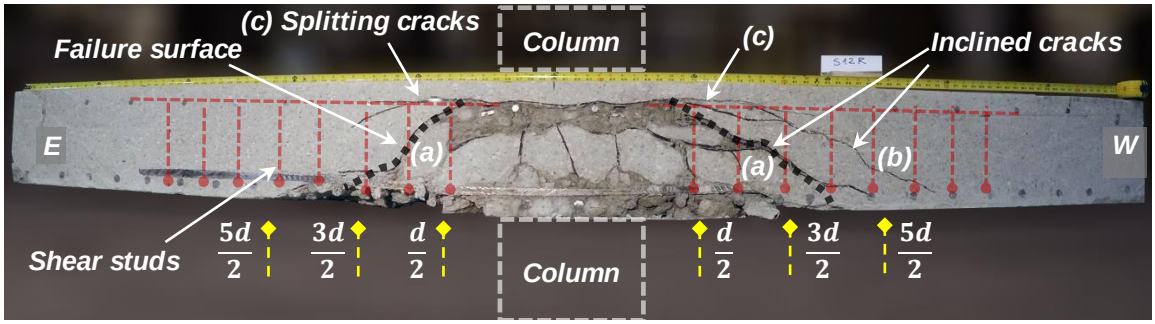


*Fig. 4-31: Cracks on a cut section close to the north face of the column for Specimen S12R*

*(The cut location is shown in Fig. B-20)*

After completion of the test, the specimen was cut along a line close to the north face of the column. The crack pattern and failure surfaces on the cut section are shown in Fig. 4-31, which was found to be similar to that for Specimen S08R (Fig. 4-21). Some inclined cracks, labeled as cracks (a) and (b), developed within the shear stud regions. These cracks engaged the shear studs and caused increases in the measured strains for these studs (Fig. 4-20). Fig. 4-31 also shows that splitting cracks (c) developed horizontally above the stud regions, but they did not extend to the outermost studs. Thus, they were not a significant part of the failure surfaces. The failure surfaces in this specimen (S12R) developed from the inclined cracks (a) near the column, resulting in a typical truncated pyramid failure surface around the column. This type of failure surface engaged the shear studs near the columns, causing fracture failure in some of the studs near the final failure of the test specimen. The crack patterns and failure surface for Specimens S12R S08R (with radial stud layout) were significantly different from those for Specimens S12O

and S08O (with orthogonal stud layout). Comparisons between failure surfaces for Specimens S08O and S08R are presented in Section 4.5.4.

## 4.4 FLEXURAL BEHAVIOR OF TEST SPECIMENS

### 4.4.1 Development of Flexural Cracks

Flexural cracks that were observed on the bottom of the test slabs consisted of circumferential (ring-shaped) and radial (fan-shaped) cracks. While the circumferential cracks formed around a column at various distances from the column faces, the latter extended radially (perpendicularly to the circumferential cracks) from the region close to the columns toward the edge of the slabs. The first circumferential crack occurred close to the column perimeter at an applied load of 30 to 40 k (130 to 180 kN). The second and third circumferential cracks formed later and at distances of approximately $0.5d$ and $1.25d$ from the column faces as the applied load increased from 120 to 160 k (530 to 710 kN) and 180 to 190 k (800 to 850 kN), respectively. The radial cracks occurred after the first circumferential crack. These cracks initiated in the region adjacent to the column faces when the applied load reached approximately 70 k (310 kN) for the S08 specimens and 90 k (400 kN) for the S12 specimens. While the radial cracks propagated all the way to the edges of the slabs in Specimens S08O and S08R (Fig. B-6 and Fig. B-11), they stopped at approximately $3d$ from the column faces in the S12 specimens (Fig. B-16 and Fig. B-20).

### 4.4.2 Development of Flexural Yielding

Measured strain distributions in slab flexural reinforcement at the maximum load for all specimens are shown in Fig. 4-32. The spread of the flexural yielding away from the south face of the column for one North-South bar near the center of the slab (gauges G1 to G3) is shown in Fig. 4-32 (a). The measured strains indicate that plastic hinging regions in the test specimens extended approximately to $0.15l$ to $0.25l$ ($l$ is the span length of specimens), or $2d$ to $3.5d$, from the center of the columns. In Fig. 4-32 (b), gauges G4 to G6, shows the spread of flexural yielding away from the west face of the column for three North-South bars. It can be seen that a slab flexural mechanism was more fully developed in Specimen S08R than in the other test specimens, which contributed to the higher ductility observed for Specimen S08R.

For all specimens, flexural reinforcement adjacent to the columns yielded. The strains in the slab flexural reinforcement were smallest in Specimen S08C, which failed in punching shear. The measured strains in slab flexural reinforcement in the S12 specimens were similar, but lower than the strains in the S08 specimens with shear reinforcement, which had a lower slab reinforcement ratio. Thus, a more complete flexural mechanism developed in the S08 specimens with shear reinforcement than in the S12 specimens.

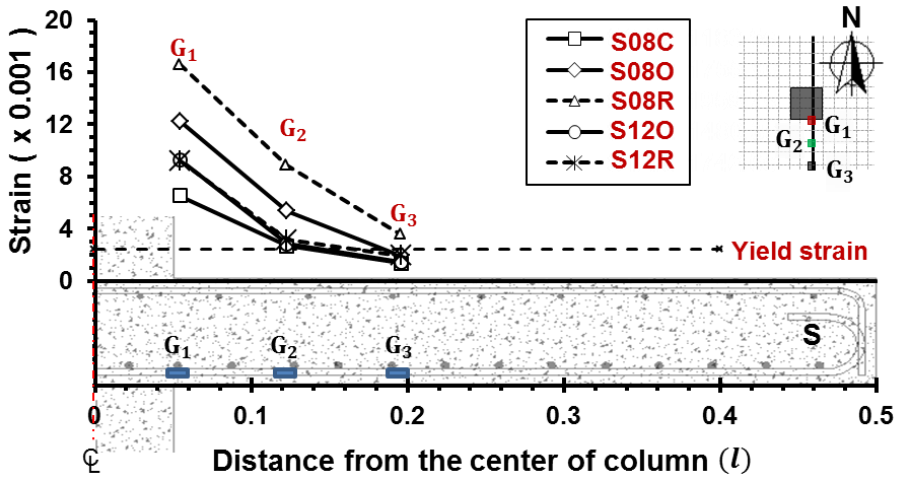


a) Gauges G1, G2, and G3 (or

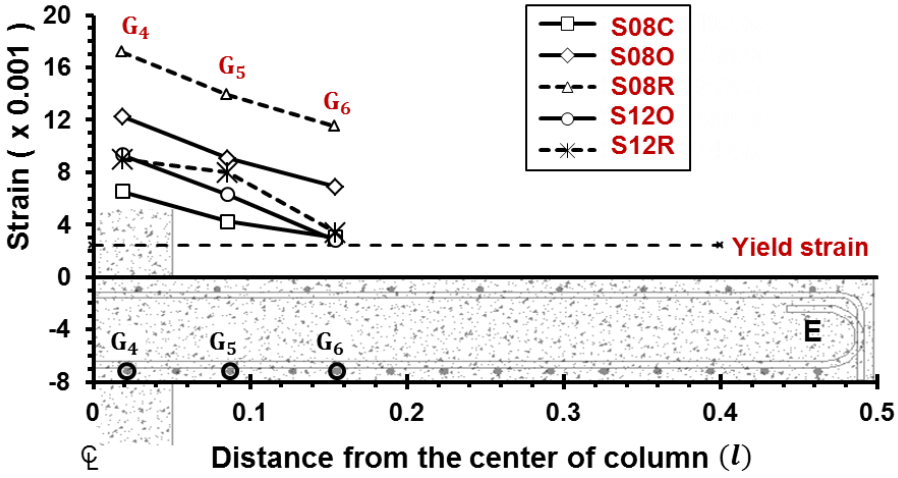


b) Gauges G4, G5, and G6

*Fig. 4-32: Strain distribution in flexural reinforcement at maximum loads*

It has been observed that yielding of slab flexural tension reinforcement near a column allows a wider opening of shear cracks close to the column, which reduces aggregate interlock along these cracks[8, 55, 80]. Significant yielding of slab flexural reinforcement near the columns in

Specimens S08O and S08R is believed to have been a primary cause for the lower shear strengths measured for those specimens, and their failure mode was thus called "flexurally-triggered punching shear" in Table 4-1.

The load required to develop a flexural mechanism in the slabs ($V_{\text{flex}}$) for the test specimens, calculated by yield-line analysis[3, 54, 124], is given in Eq. (18),

$$V_{\text{flex}} = \frac{4\sqrt{2}}{cos(\frac{\pi}{8}) - \frac{h_c\sqrt{2}}{l}} m \tag{18}$$

in which $h_c$ is the column side dimension, $l$ is the specimen span length, and $m$ is the slab moment strength per unit width given in Eq. (19).

$$m \cong \left(1 - \frac{\rho f_y}{1.7 f_c'}\right) \rho f_y d^2 \tag{19}$$

Calculated $V_{\text{flex}}$ for each test specimen is given in Table 4-1. For the S12 specimens, $V_{\text{flex}}$ was approximately 30% larger than the ACI Code nominal shear strength ($V_{\text{shear}}$); thus $V_{\text{shear}}$ governed the measured failure loads of those specimens. For Specimens S08O and S08R, however, $V_{\text{flex}}$ was approximately 10% smaller than the corresponding calculated shear strength $V_{\text{shear}}$, and the measured loads at "flexurally-trigger punching shear failure" for Specimens S08O and S08R (Table 4-1) were close to $V_{\text{flex}}$.

## 4.5 SHEAR BEHAVIOR OF TEST SPECIMENS

### 4.5.1 Strains in Shear Studs

Strains measured in the instrumented shear studs (Fig. 3-26) at six load stages, S1 to S6, during the tests of the S08 and S12 specimens are shown in Fig. 4-33 and Fig. 4-34, respectively. The dashed-lines in these figures represent averages of the measured strains. It can be seen that the average strains for all test specimens developed similarly until stage S2 (measured $v = 4.5\sqrt{f_c'}$ psi or $0.37\sqrt{f_c'}$ MPa). After that load stage, the strains in the shear studs in a radial layout (S08R and S12R) increased at a higher rate. At stage S3, when all of the specimens experienced a slight drop or leveling off in load capacity, strains in many of the shear studs in the radial layout reached or exceeded the yield strain (0.0024), but none of the shear studs in the specimens with an orthogonal layout of shear studs (S08O and S12O) yielded. For the radial layout of shear

studs, strains in shear studs increased rapidly beyond stage S3 (Fig. 4-33b), especially for the shear studs closest to the column. Some shear studs close to the column fractured near load stages S5 and S6 (Fig. 4-35). Strains in shear studs for the orthogonal layout, however, remained nearly constant and below the yield strain after load stage S3 (Fig. 4-33a and Fig. 4-34a). These strain measurements indicate that the final failure surfaces engaged the shear studs when the studs were arranged in a radial layout, but not when they were arranged in an orthogonal layout.

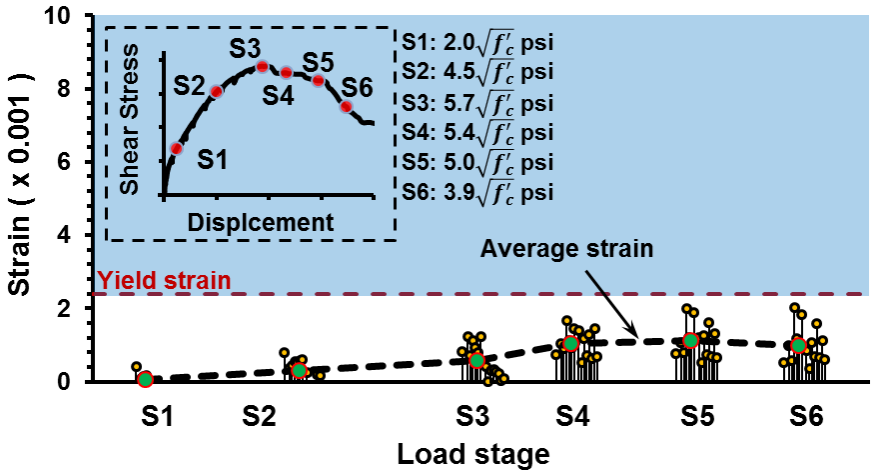


a) Specimen S08O, orthogonal layout

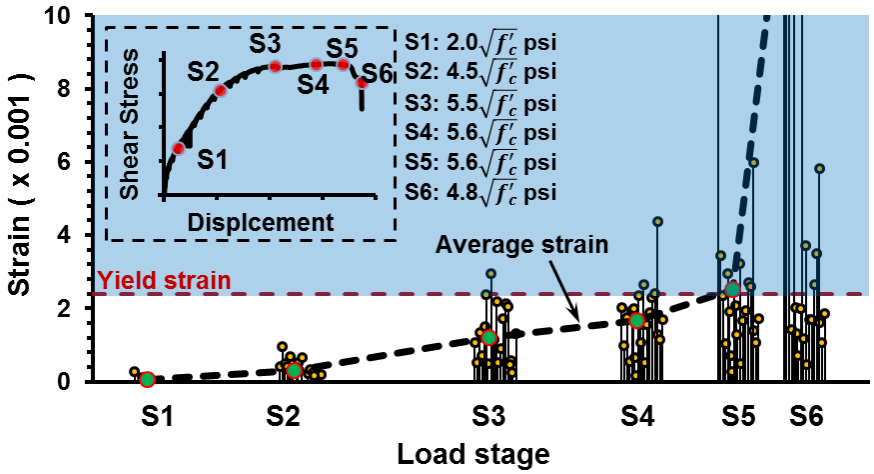


b) Specimen S08R, radial layout

*Fig. 4-33: Measured strains in shear studs for the S08 Specimens*

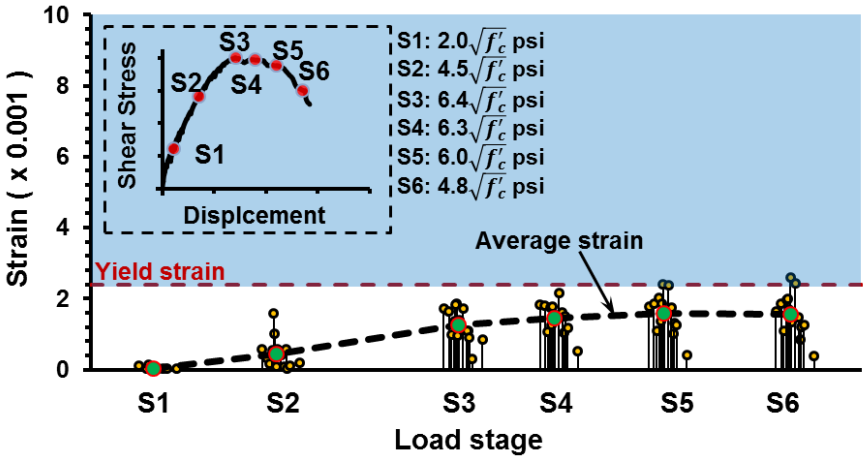


a) Specimen S12O, orthogonal layout

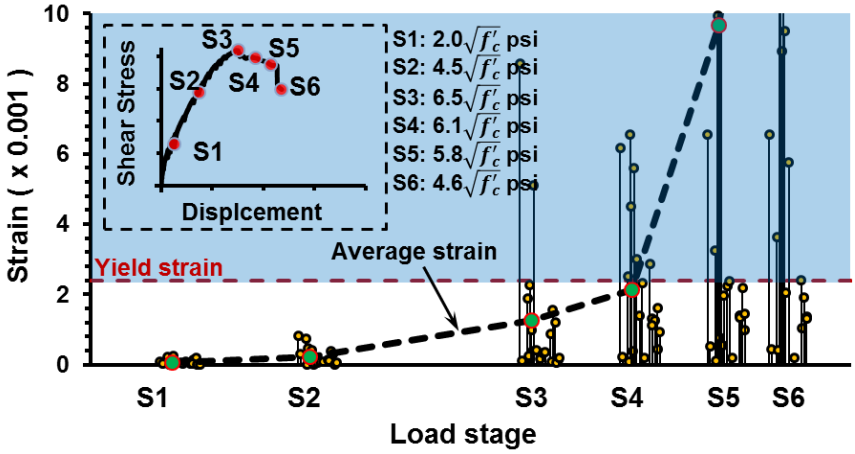


b) Specimen S12R, radial layout

*Fig. 4-34: Measured strains in shear studs for the S12 Specimens*

a) Specimen S08R b) Specimen S12R

*Fig. 4-35: Fracture of shear studs in the test specimens with a radial stud layout*

### 4.5.2 Shear Cracks

The developments of inclined cracks during the tests of all test specimens were studied using the measured through-thickness expansions of the slabs and strains in the shear studs. Inclined cracks initiated when slab shear stresses reached from $1.5\sqrt{f_c'}$ to $2.0\sqrt{f_c'}$ psi ($0.13\sqrt{f_c'}$ to $0.17\sqrt{f_c'}$ MPa). Because the circumferential flexural cracks, which could initiate flexural-shear cracking, had not yet been observed at this loading stage, the formation of the inclined cracks in the slabs was assumed to be similar to that of web-shear cracks in beams. Thus, these inclined cracks were likely initiated near the mid-depth of the slabs and then extended toward the top and bottom of the slabs.

After the tests were completed, the specimens were cut along a line close to the north face of the columns to observe crack patterns in the slabs. The cut surfaces for all test specimens are shown in Fig. 4-36. Specimen S08C, without shear reinforcement, had a single shear crack as seen in Fig. 4-36(a). For the other specimens, several inclined cracks can be observed within the regions reinforced with shear studs (Fig. 4-36b to Fig. 4-36e).

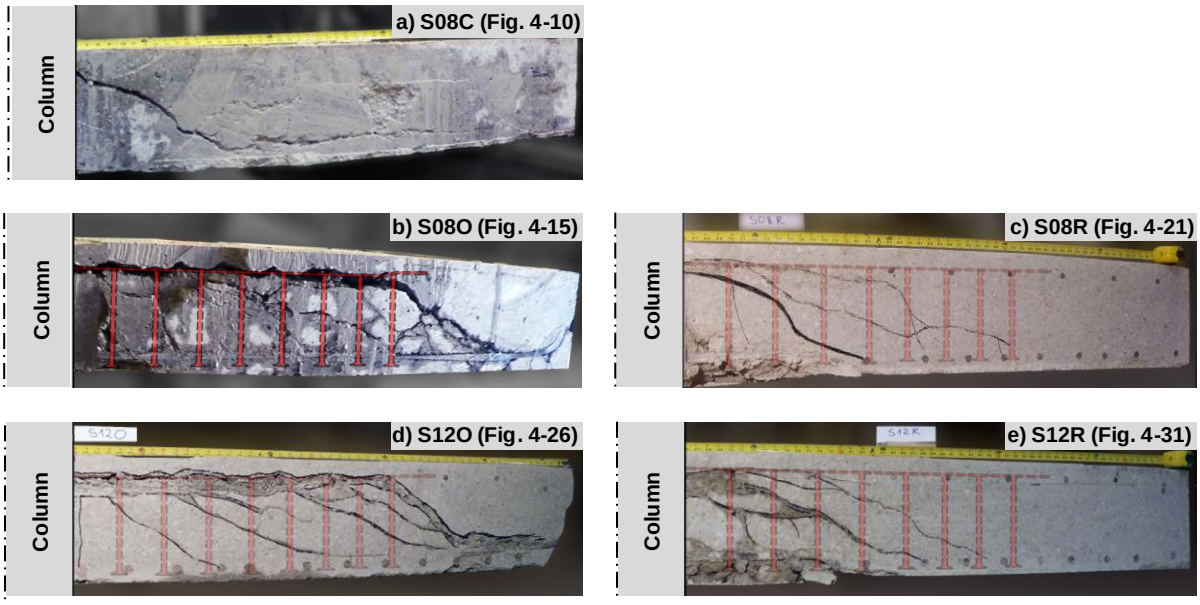


*Fig. 4-36: Inclined cracks and failure surfaces on cut sections*

### 4.5.3 Splitting Cracks

The cut surface for Specimen S08O (Fig. 4-36b) shows a horizontal splitting crack located above the shear studs, and this splitting crack did not become an inclined crack until it had extended beyond the outermost set of shear studs. A similar splitting crack can be seen in Specimen S12O (Fig. 4-36d). For Specimens S08R and S12R, with a radial layout of shear studs, horizontal splitting cracks appeared near the columns before joining with inclined cracks that extend through the second and third line of shear studs from the column (Fig. 4-36c and Fig. 4-36e). The splitting cracks in the shear-reinforced test specimens were not observed during the tests because the top of the slabs remained intact. Splitting cracks have been reported in different research investigations[17, 125-127] as the separations (or delamination) of concrete cover for the slab compression reinforcing bars, and they were usually assumed to be the consequence of punching failures. For the test specimens with shear studs in this program, the splitting cracks were found to form before the punching failures, and they were part of failure surfaces for test specimens with an orthogonal stud layout.

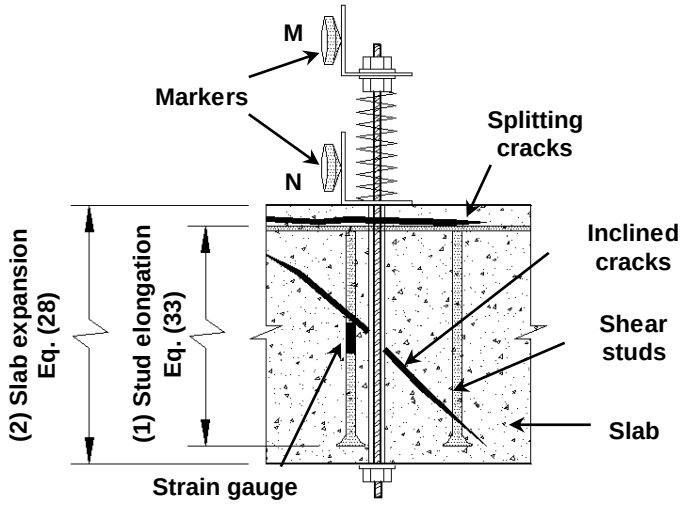


Fig. 4-37: Measurement of slab expansions and stud elongations

Fig. 4-37 shows the measurement of stud elongation (1) and slab through-thickness expansion (2) at one location in the slabs. The elongation of the stud was computed by assuming the measured strain on its shaft was constant along the length of the stud (Eq. 33),

$$\text{Stud elongation} = \varepsilon_{(\text{frame } k)} \times l_{\text{st}} \qquad (33)$$

while the slab expansion was measured using a pair of markers M and N attached to the top and bottom surface of the slab and placed adjacent to the stud (Eq. 28).

$$\text{Expansion}_{MN(\text{frame } k)} = MN_{(\text{frame } 1)} - MN_{(\text{frame } k)} \qquad (28)$$

Because the stud elongation indicated the growth of inclined cracks, and the slab expansion indicated the growth of all cracks including inclined and splitting cracks at this location (Fig. 4-37), the difference between these two measurements indicated the growth of splitting cracks.

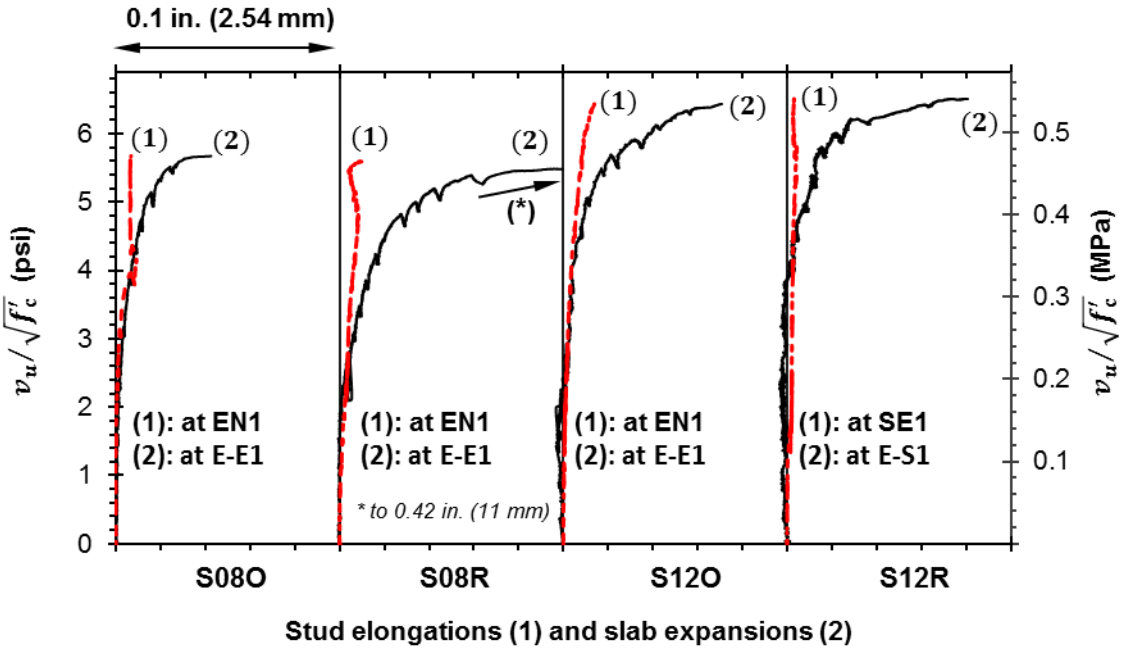


*Fig. 4-38: Measured slab shear stress versus slab expansions and stud elongations*

*(see Fig. 3-24 to Fig. 3-26 for the instrument labels and locations)*

Fig. 4-38 shows the calculated stud elongations (lines 1) and slab expansions (lines 2) at locations approximately $d/2$ from the column faces for all test specimens reinforced with shear studs, as the applied loads increased to the maximum loads. The results in Fig. 4-38 show that these displacement measurements for the test specimens started to vary significantly when the measured slab shear stresses reached approximately $3\sqrt{f'_c}$ to $4\sqrt{f'_c}$ psi ($0.25\sqrt{f'_c}$ to $0.33\sqrt{f'_c}$ MPa). At the maximum slab shear stresses, Fig. 4-38 indicates that the calculated stud elongations were smaller than 20 percent of the corresponding measured slab expansions, and thus approximately 80% of the slab expansions of the test specimens could be attributed to the

horizontal splitting cracks. This phenomenon indicated the initiation and growth of the splitting cracks above the shear studs before the punching shear failures developed.

### 4.5.4 Failure Behavior

Control Specimen S08C, without shear reinforcement, failed due to a typical punching shear failure (line 1 in Fig. 4-5). For the other specimens with shear studs, the failure sequence started with a slight drop in load carrying capacity (lines 2 to 5 in Fig. 4-5) at a column displacement of approximately 1 and 0.7 in. (25.4 and 18 mm) for S08 and S12 specimens, respectively. The formation and development of horizontal splitting cracks near the columns, as discussed in the previous subsection, is assumed to have caused these drops in load capacity. This state can also be considered as an initiation of punching failure, as the column and adjacent slab displacements started to deviate significantly. Beyond this stage, the development of the failure surfaces depended on the configuration of shear studs.

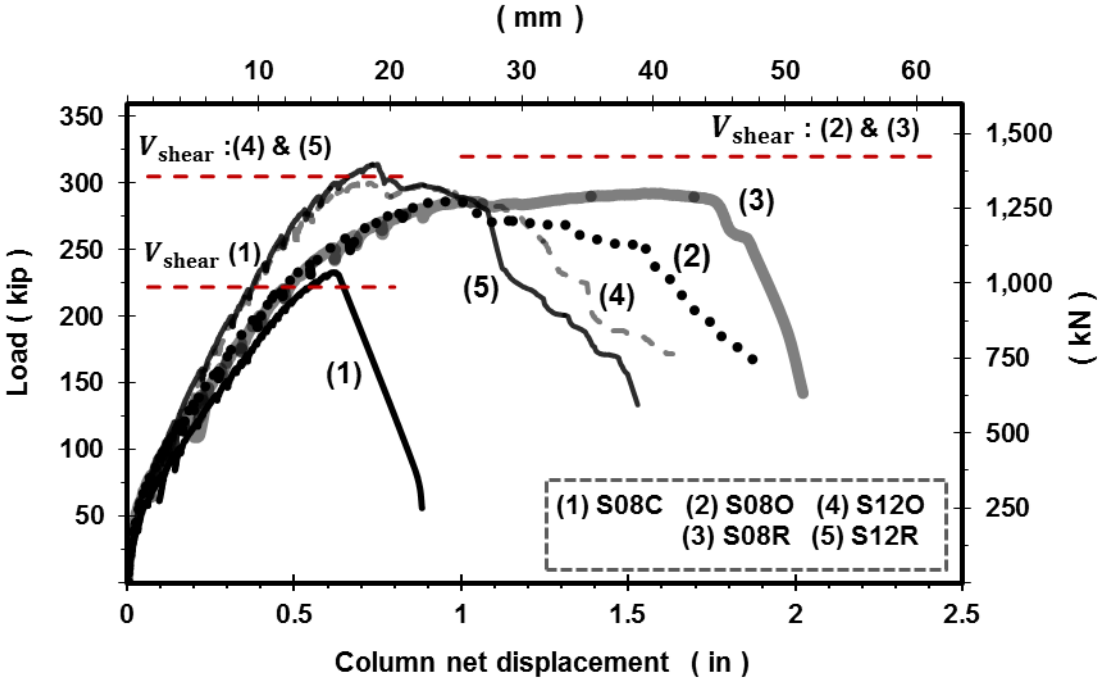


*Fig. 4-5: Load versus column displacement for all test specimens*

For Specimens S08O and S12O (orthogonal layout of shear studs), inclined cracks developed adjacent to the orthogonal stud rails and in the diagonal regions adjacent to the corners of the columns, shown as cracks (3) in Fig. 4-39 and Fig. 4-40 (a). These crack surfaces extended away from the column faces and remained parallel to the stud rails. The inclined cracks

adjacent to the stud rails and the splitting cracks (labeled as 1 in Fig. 4-39) over the top of the studs created failure surfaces that separated the shear studs from the slabs. It can be seen from Fig. 4-39 (b) that the propagation of the inclined failure surfaces (cracks 3) was not restrained because of the absence of shear reinforcement in the diagonal regions. Thus, these failure surfaces continuously extended away from the columns to the outermost shear studs, resulting in the nearly cruciform-shaped failure cones shown in Fig. 4-39(c). The base of the failure cones at the bottom surface of the slabs are shown in Fig. B-6 and Fig. B-16. During this development of these failure surfaces, the shear studs were not engaged by the failure surfaces and the strain in the studs remained constant up to failure (Fig. 4-33a). Extending the stud rails further away from the columns may not have improved the behavior and strength of these specimens.

For Specimens S08R and S12R (radial layout of shear studs), horizontal splitting cracks did develop above the stud rails in circular regions close to the column faces (Fig. 4-40b), but these cracks were not a significant part of the failure sequence for these specimens. The final failure in these specimens took place along a truncated-pyramid surface that engaged the shear studs near the columns (Fig. 4-40 (b) and Fig. 4-41). The failure cone bases at the bottom surfaces of the slabs are shown in Fig. B-11 and Fig. B-20. The shear studs in these specimens developed their yield strength, and thus, made a significant contribution to the measured strength of the test specimens.

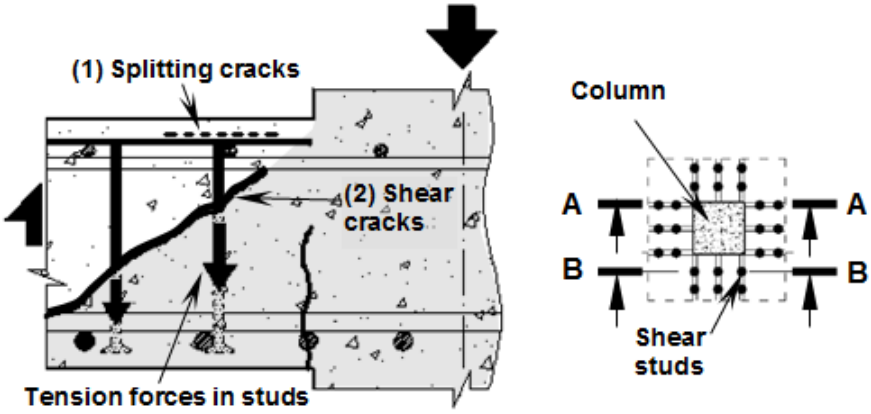


a) Cracks on section A-A

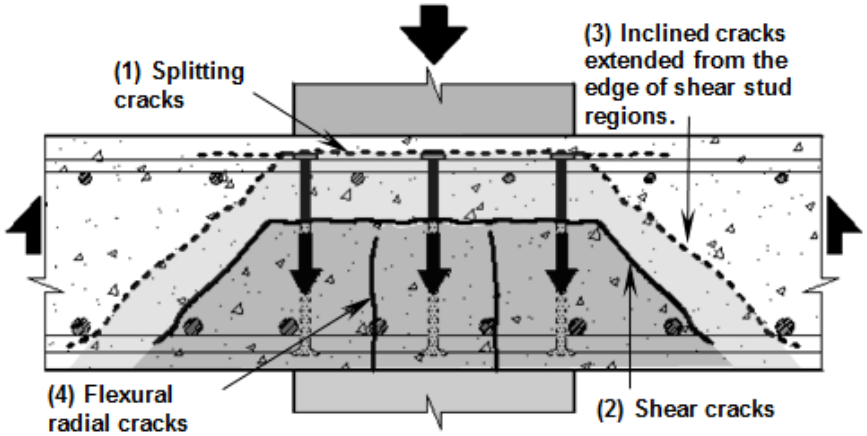


b) Cracks on section B-B

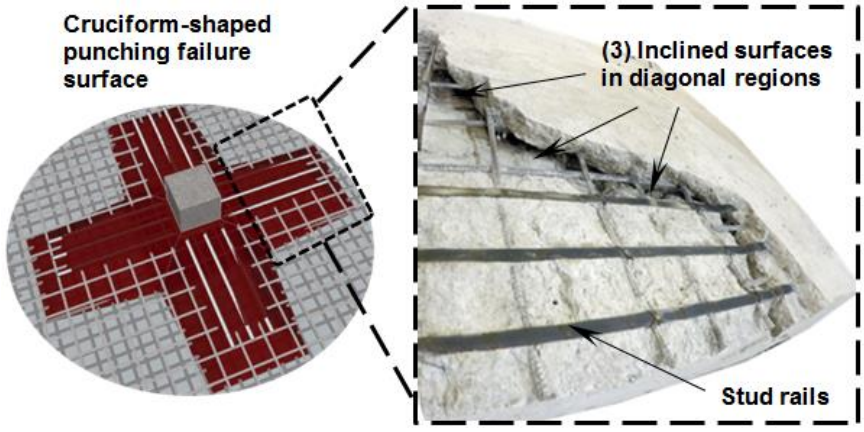


c) Cracking and failure surface in the specimens with an orthogonal layout

*Fig. 4-39: Failure surfaces in specimens with an orthogonal stud layout*

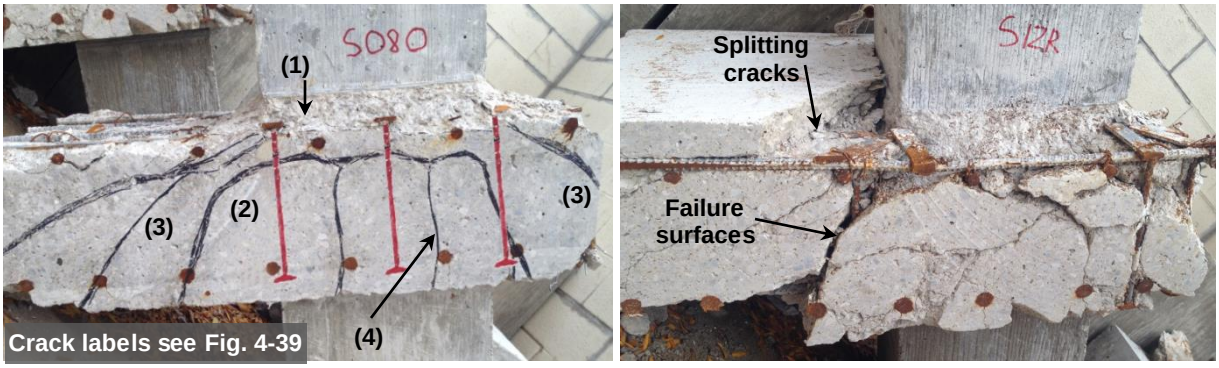


a) Orthogonal stud layout specmens b) Radial stud layout specimen

*Fig. 4-40: Cracks and failure surfaces near the columns*

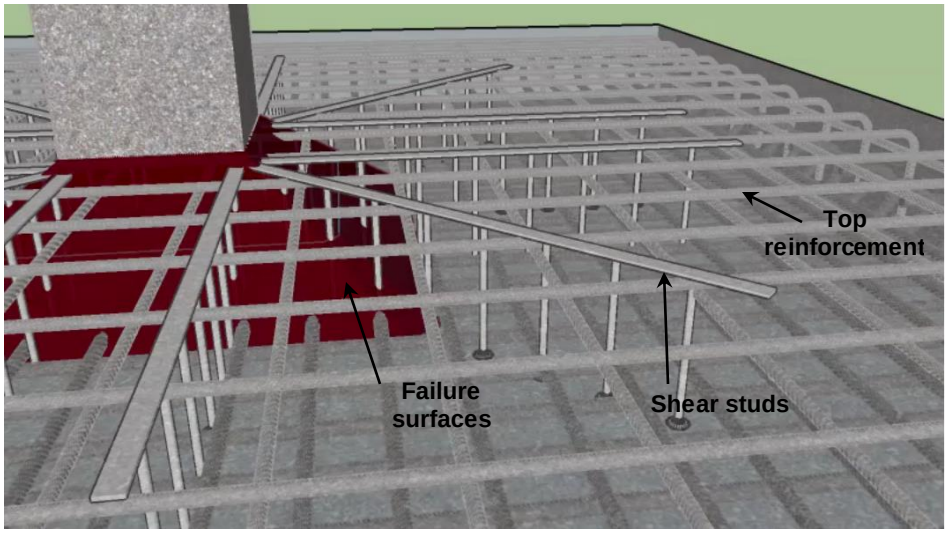


*Fig. 4-41: Failure surfaces in specimens with a radial stud layout*

# CHAPTER 5
# COMPARISONS WITH PRIOR RESEARCH INVESTIGATIONS AND DESIGN RECOMMENDATIONS

Test results for the five full-scale slab-column connections, presented in the previous chapter, showed that: 1) the layout of shear studs significantly affected the behavior of the test connections, and 2) the slab flexural reinforcement ratio affected the measured shear strength at failure of the test specimens. This chapter presents a study on these effects, using results from more than 60 tests of slab-column connections reinforced with shear stud reinforcement, and includes new design recommendations for shear strength of slab-column connections. The sections in this chapter are as follows:

- Section 5.1 presents the information and results from prior research investigations,
- Section 5.2 discusses effect of shear stud layouts and presents a design recommendation for these layouts,
- Section 5.3 discusses effect of slab flexural reinforcement ratio and presents a design recommendation for the minimum percentage of slab flexural reinforcement, and
- Section 5.4 discusses effect of punching failure surfaces on a lap splice length for integrity reinforcement in flat slab systems. A design recommendation for locations of those splices is also presented in this section.

## 5.1 PRIOR RESEARCH INVESTIGATION RESULTS

Specimen properties and results from 64 tests of slab-column specimens reinforced with shear studs, or stud-like shear reinforcement, including the test specimens in this program, are given in Tables 5-1 and 5-2. The test specimens are divided into the two tables based on the ratio of $V_{\text{flex}}/V_{\text{shear}}$, in which $V_{\text{flex}}$ is the calculated flexural strength of the test specimens[128], based on a yield line analysis in the region of the slab adjacent to the column, and $V_{\text{shear}}$ is the calculated shear strength from the ACI Code, Eq. (12). The eleven specimens in Table 5-1 have $V_{\text{flex}}/V_{\text{shear}} > 1$ (relatively high $\rho$), and the 53 specimens in Table 5-2 have $V_{\text{flex}}/V_{\text{shear}} \leq 1$ (relatively low $\rho$). The specimens in each table are divided into two groups: Group A consists of pairs of similar design specimens with the shear studs arranged in orthogonal and radial layouts and Group B consists of single specimens that are reinforced with either an orthogonal or radial layouts of shear studs. In the following sections, the effects of shear stud layout and slab flexural reinforcement ratio on the behavior and strength of slab-column connections in each of these groups are discussed.

*Table 5-1— Test Results from gravity-loaded slab-column connections reinforced with shear studs or stud-like shear reinforcement and with a relatively low ρ ($V_{flex}/V_{shear} \leq 1$)*

| Study | ID | $\rho$ % | $\beta = \frac{b_c}{L}$ | $\alpha = \frac{b_c}{d}$ | Layout | $\frac{V_{flex}}{V_{shear}}$ | $V_u$ (kip)* | $\frac{V_u}{V_{shear}}$ | $\frac{V_u}{V_{flex}}$ | $\mu$ |
|---|---|---|---|---|---|---|---|---|---|---|
| (1) | (2) | (3) | (4) | (5) | (6) | (7) | (8) | (9) | (10) | (11) |
| **Group A: Pairs of specimens with orthogonal and radial stud layouts** | | | | | | | | | | |
| This research | S08O | 0.87 | 0.04 | 1.39 | Ortho. | 0.90 | 287 | 0.92 | 1.01 | 2.8 |
| | S08R | 0.87 | 0.04 | 1.39 | Radial | 0.89 | 293 | 0.91 | 1.02 | 3.6 |
| Broms[17] | 18a | 1.29 | 0.05 | 2.16 | Ortho. | 0.93 | 193 | 0.84 | 0.90 | 2.4 |
| | 18b** | 1.21 | 0.05 | 2.16 | Radial | 0.92 | 218 | 0.87 | 0.95 | 3.4 |
| DaCosta and Parra-Montesinos[18] | M1 | 0.77 | 0.03 | 0.92 | Ortho. | 0.61 | 134 | 0.59 | 0.96 | 1.5 |
| | M9 | 0.80 | 0.03 | 0.96 | Radial | 0.75 | 136 | 0.75 | 1.00 | 4.1 |
| | M2 | 0.80 | 0.03 | 0.92 | Ortho. | 0.65 | 131 | 0.61 | 0.94 | 2.5 |
| | M12 | 0.80 | 0.03 | 0.96 | Radial | 0.77 | 151 | 0.83 | 1.07 | 4.0 |
| | M5 | 0.80 | 0.03 | 0.96 | Ortho. | 0.99 | 127 | 0.92 | 0.93 | 2.5 |
| | M10 | 0.80 | 0.03 | 0.96 | Radial | 0.98 | 149 | 1.06 | 1.08 | N/A |
| **Group B: Specimens with either orthogonal or radial stud layouts** | | | | | | | | | | |
| DaCosta and Parra-Montesinos[18] | M4 | 0.8 | 0.03 | 0.92 | Ortho. | 0.93 | 133 | 0.89 | 0.93 | 3.0 |

* 1 kip = 4.45 kN, ** stud spacing was larger than the limits specified in the ACI Code[5].

*Table 5-2— Test Results from gravity-loaded slab-column connections reinforced with shear studs or stud-like shear reinforcement and with a relatively high ρ ($V_{flex}/V_{shear} > 1$)*

| Study | ID | $\rho$ % | $\beta = \frac{b_c}{L}$ | $\alpha = \frac{b_c}{d}$ | Layout | $\frac{V_{flex}}{V_{shear}}$ | $V_u$ (kip)* | $\frac{V_u}{V_{shear}}$ | $\frac{V_u}{V_{flex}}$ | $\mu$ |
|---|---|---|---|---|---|---|---|---|---|---|
| (1) | (2) | (3) | (4) | (5) | (6) | (7) | (8) | (9) | (10) | (11) |
| **Group A: Pairs of specimens with orthogonal and radial stud layouts** | | | | | | | | | | |
| This research | S12O | 1.27 | 0.04 | 1.41 | Ortho. | 1.28 | 301 | 0.99 | 0.79 | 2.2 |
| | S12R | 1.27 | 0.04 | 1.41 | Radial | 1.27 | 314 | 1.02 | 0.82 | 2.2 |
| *(for comparison)* | S08C | 0.87 | 0.04 | 1.39 | — | 1.27 | 233 | 1.05 | 0.82 | 1.3 |
| DaCosta and Parra-Montesinos[18] | M8 | 1.3 | 0.03 | 0.98 | Ortho. | 1.05 | 166 | 0.90 | 0.85 | 1.7 |
| | M11 | 1.3 | 0.03 | 0.98 | Radial | 1.15 | 173 | 0.96 | 0.83 | 2.8 |
| Gomes and Regan[49] | 5 | 1.26 | 0.03 | 1.26 | Ortho. | 2.71 | 192 | 1.74 | 0.64 | 1.38 |
| | 6 | 1.26 | 0.03 | 1.26 | Radial | 2.68 | 234 | 2.08 | 0.78 | 1.32 |

* 1 kip = 4.45 kN

(Table is continued next page)

*Table 5-2— Test Results from gravity-loaded slab-column connections reinforced with shear studs or stud-like shear reinforcement and with a relatively high ρ ($V_{flex}/V_{shear} > 1$) (continued)*

| Study | ID | $\rho$ % | $\beta = \frac{b_c}{L}$ | $\alpha = \frac{b_c}{d}$ | Layout | $\frac{V_{flex}}{V_{shear}}$ | $V_u$ (kip)* | $\frac{V_u}{V_{shear}}$ | $\frac{V_u}{V_{flex}}$ | $\mu$ |
|---|---|---|---|---|---|---|---|---|---|---|
| (1) | (2) | (3) | (4) | (5) | (6) | (7) | (8) | (9) | (10) | (11) |
| **Group A: Pairs of specimens with orthogonal and radial stud layouts** | | | | | | | | | | |
| Birkle[15] | S2 | 1.51 | 0.05 | 2.02 | Ortho. | 1.32 | 129 | 1.03 | 0.78 | N/A |
| | S3 | 1.51 | 0.05 | 2.02 | Radial | 1.32 | 129 | 1.01 | 0.77 | 2.1 |
| | S5 | 1.51 | 0.05 | 2.02 | Ortho. | 1.19 | 140 | 1.01 | 0.85 | 2.5 |
| | S6 | 1.51 | 0.05 | 2.02 | Radial | 1.22 | 138 | 1.02 | 0.84 | 2.5 |
| Ferreira, Melo[16] | C4 | 1.52 | 0.06 | 2.28 | Ortho. | 1.22 | 252 | 1.21 | 0.99 | N/A |
| | C8 | 1.47 | 0.06 | 2.28 | Radial | 1.21 | 238 | 1.11 | 0.91 | N/A |
| **Group B: Specimens with either orthogonal or radial stud layouts** | | | | | | | | | | |
| DaCosta and Parra-Montesinos[18] | M6 | 1.3 | 0.03 | 0.98 | Ortho. | 1.41 | 151 | 1.09 | 0.77 | 1.8 |
| Birkle[129] | S4 | 1.51 | 0.05 | 2.02 | Orth. | 2.09 | 143 | 1.75 | 0.84 | 2.3 |
| | S8 | 1.29 | 0.04 | 1.58 | Orth. | 1.94 | 236 | 1.29 | 0.66 | 1.8 |
| | S9 | 1.29 | 0.04 | 1.58 | Orth. | 1.87 | 245 | 1.29 | 0.69 | 1.5 |
| | S11 | 1.1 | 0.04 | 1.35 | Orth. | 1.86 | 364 | 1.23 | 0.66 | 2.3 |
| | S12 | 1.1 | 0.04 | 1.35 | Orth. | 1.69 | 342 | 1.03 | 0.61 | 2.0 |
| Gomes and Regan[49] | 2 | 1.32 | 0.03 | 1.31 | Orth. | 4.65 | 156 | 2.51 | 0.54 | 1.2 |
| | 3 | 1.27 | 0.03 | 1.27 | Orth. | 4.35 | 174 | 2.51 | 0.58 | 1.2 |
| | 4 | 1.27 | 0.03 | 1.26 | Orth. | 3.69 | 192 | 2.40 | 0.65 | 1.3 |
| Ferreira, Melo[16] | C1 | 1.48 | 0.05 | 1.67 | Radial | 1.40 | 193 | 1.10 | 0.79 | 1.2 |
| | C2 | 1.52 | 0.06 | 2.28 | Radial | 1.44 | 215 | 1.20 | 0.83 | 1.2 |
| | C3 | 1.49 | 0.08 | 2.81 | Radial | 1.44 | 242 | 1.23 | 0.85 | 1.2 |
| | C5 | 2.0 | 0.06 | 2.28 | Radial | 1.79 | 251 | 1.36 | 0.76 | 1.2 |
| | C6 | 1.48 | 0.06 | 2.23 | Radial | 1.41 | 242 | 1.29 | 0.92 | 1.2 |
| | C7 | 1.47 | 0.06 | 2.22 | Radial | 1.46 | 250 | 1.37 | 0.93 | 1.2 |
| | S1 | 1.46 | 0.06 | 2.07 | Radial | 3.00 | 230 | 2.61 | 0.87 | 1.2 |
| | S2 | 1.48 | 0.06 | 2.10 | Radial | 1.93 | 254 | 1.88 | 0.97 | 1.2 |
| | S7 | 1.48 | 0.06 | 2.10 | Radial | 1.94 | 269 | 2.01 | 1.03 | 1.2 |

* 1 kip = 4.45 kN

(Table is continued next page)

*Table 5-2— Test Results from gravity-loaded slab-column connections reinforced with shear studs or stud-like shear reinforcement and with a relatively high ρ ($V_{flex}/V_{shear} > 1$) (continued)*

| Study | ID | $\rho$ % | $\beta = \frac{b_c}{L}$ | $\alpha = \frac{b_c}{d}$ | Layout | $\frac{V_{flex}}{V_{shear}}$ | $V_u$ (kip)* | $\frac{V_u}{V_{shear}}$ | $\frac{V_u}{V_{flex}}$ | $\mu$ |
|---|---|---|---|---|---|---|---|---|---|---|
| (1) | (2) | (3) | (4) | (5) | (6) | (7) | (8) | (9) | (10) | (11) |
| **Group B: Specimens with either orthogonal or radial stud layouts (continued)** | | | | | | | | | | |
| Gomes and Regan[49] | 7 | 1.27 | 0.03 | 1.26 | Radial | 2.54 | 252 | 2.15 | 0.84 | 1.6 |
| | 8 | 1.27 | 0.03 | 1.26 | Radial | 2.21 | 270 | 2.00 | 0.90 | 1.6 |
| | 9 | 1.27 | 0.03 | 1.26 | Radial | 1.51 | 276 | 1.36 | 0.90 | 1.8 |
| | 10 | 1.31 | 0.03 | 1.30 | Radial | 2.56 | 180 | 1.60 | 0.62 | 1.3 |
| | 11 | 1.31 | 0.03 | 1.30 | Radial | 2.51 | 204 | 1.78 | 0.71 | N/A |
| Ferreira, Melo[16] | C1 | 1.48 | 0.05 | 1.67 | Radial | 1.40 | 193 | 1.10 | 0.79 | 1.2 |
| | C2 | 1.52 | 0.06 | 2.28 | Radial | 1.44 | 215 | 1.20 | 0.83 | 1.2 |
| | C3 | 1.49 | 0.08 | 2.81 | Radial | 1.44 | 242 | 1.23 | 0.85 | 1.2 |
| | C5 | 2.0 | 0.06 | 2.28 | Radial | 1.79 | 251 | 1.36 | 0.76 | 1.2 |
| | C6 | 1.48 | 0.06 | 2.23 | Radial | 1.41 | 242 | 1.29 | 0.92 | 1.2 |
| | C7 | 1.47 | 0.06 | 2.22 | Radial | 1.46 | 250 | 1.37 | 0.93 | 1.2 |
| | S1 | 1.46 | 0.06 | 2.07 | Radial | 3.00 | 230 | 2.61 | 0.87 | 1.2 |
| | S2 | 1.48 | 0.06 | 2.10 | Radial | 1.93 | 254 | 1.88 | 0.97 | 1.2 |
| | S7 | 1.48 | 0.06 | 2.10 | Radial | 1.94 | 269 | 2.01 | 1.03 | 1.2 |
| Regan and Samadian[127] | R1 | 1.26 | 0.03 | 1.25 | Radial | 2.12 | 236 | 1.76 | 0.83 | N/A |
| | R2 | 1.26 | 0.03 | 1.25 | Radial | 2.12 | 214 | 1.56 | 0.74 | N/A |
| | R3 | 1.26 | 0.03 | 1.25 | Radial | 2.20 | 191 | 1.48 | 0.67 | N/A |
| | R4 | 1.26 | 0.03 | 1.25 | Radial | 2.01 | 214 | 1.47 | 0.73 | N/A |
| | A1 | 1.64 | 0.03 | 1.25 | Radial | 2.23 | 225 | 1.59 | 0.71 | N/A |
| | A2 | 1.64 | 0.03 | 1.25 | Radial | 2.19 | 214 | 1.45 | 0.66 | N/A |
| Beutel[130] | Z1 | 0.8 | 0.04 | 0.71 | Radial | 2.31 | 297 | 1.13 | 0.49 | N/A |
| | Z2 | 0.8 | 0.04 | 0.71 | Radial | 2.29 | 324 | 1.20 | 0.53 | N/A |
| | Z3 | 0.8 | 0.04 | 0.71 | Radial | 2.34 | 363 | 1.41 | 0.60 | N/A |
| | Z4 | 0.8 | 0.04 | 0.71 | Radial | 2.13 | 370 | 1.24 | 0.58 | N/A |
| | Z5 | 1.25 | 0.04 | 0.71 | Radial | 3.07 | 455 | 1.63 | 0.53 | N/A |
| | Z6 | 1.25 | 0.04 | 0.71 | Radial | 2.86 | 439 | 1.37 | 0.48 | N/A |

* 1 kip = 4.45 kN

(Table is continued next page)

*Table 5-2— Test Results from gravity-loaded slab-column connections reinforced with shear studs or stud-like shear reinforcement and with a relatively high ρ ($V_{flex}/V_{shear} > 1$) (continued)*

| Study | ID | $\rho$ % | $\beta = \frac{b_c}{L}$ | $\alpha = \frac{b_c}{d}$ | Layout | $\frac{V_{flex}}{V_{shear}}$ | $V_u$ (kip)* | $\frac{V_u}{V_{shear}}$ | $\frac{V_u}{V_{flex}}$ | $\mu$ |
|---|---|---|---|---|---|---|---|---|---|---|
| (1) | (2) | (3) | (4) | (5) | (6) | (7) | (8) | (9) | (10) | (11) |
| **Group B: Specimens with either orthogonal or radial stud layouts (continued)** | | | | | | | | | | |
| Lips et al[125] | PL6 | 1.59 | 0.02 | 0.66 | Radial | 1.94 | 306 | 1.31 | 0.67 | 1.4 |
| | PL7 | 1.59 | 0.04 | 1.31 | Radial | 1.51 | 399 | 1.23 | 0.81 | 1.8 |
| | PL8 | 1.57 | 0.07 | 2.60 | Radial | 1.13 | 507 | 0.98 | 0.87 | 2.2 |
| | PL9 | 1.59 | 0.05 | 1.28 | Radial | 1.66 | 704 | 1.26 | 0.78 | 1.8 |
| | PL10 | 1.55 | 0.06 | 1.28 | Radial | 1.71 | 1167 | 1.27 | 0.74 | 1.5 |
| | PL11 | 1.56 | 0.04 | 1.29 | Radial | 2.41 | 264 | 1.35 | 0.56 | 1.8 |
| | PL12 | 1.56 | 0.04 | 1.29 | Radial | 1.75 | 367 | 1.36 | 0.78 | 1.8 |
| Einpaul et al[75] | PP4 | 1.49 | 0.07 | 1.23 | Radial | 1.63 | 467 | 1.41 | 0.87 | 1.8 |
| | PP5 | 1.53 | 0.05 | 1.27 | Radial | 1.47 | 407 | 1.27 | 0.87 | 2.1 |
| | PP6 | 1.55 | 0.03 | 1.28 | Radial | 1.34 | 353 | 1.10 | 0.82 | 2.0 |

* 1 kip = 4.45 kN

## 5.2 EFFECT OF SHEAR STUD LAYOUTS

### 5.2.1 Punching Shear Strength

Table 5-2 shows that for the specimens with a relatively high $\rho$, even though the failure pattern may be different, an orthogonal layout and a radial layout of shear studs provided a similar shear strength. On the other hand, for the specimens with a relatively low $\rho$, Table 5-1, an orthogonal layout of shear studs provided a lower shear strength than a radial layout. The studies by DaCosta and Parra-Montesinos,[18] and Broms[17] showed that the measured strength of specimens with a radial layout of shear studs was approximately 10 percent to 15 percent higher than that of specimens with an orthogonal layout of shear studs.

### 5.2.2 Specimen Ductility

Recent investigations[17, 18, 124] have indicated that a radial layout of shear studs led to more ductile behavior than an orthogonal layout. To make a quantifiable comparison, displacement ductility, $\mu$, was calculated using Eq. (35),

$$\mu = \frac{\Delta_{\mathrm{f}}}{\Delta_{\mathrm{ym}}} \qquad (35)$$

where $\Delta_{\mathrm{f}}$ is the displacement when the applied load decreases to 90 percent of the maximum load, $V_{\mathrm{u}}$, and $\Delta_{\mathrm{ym}}$ is the displacement at the intersection point between the maximum load, $V_{\mathrm{u}}$, and a secant line from the origin through the point corresponding to an initial yielding of the flexural reinforcement $(\Delta_{\mathrm{y}}, V_{\mathrm{y}})$, as illustrated in Fig. 5-1. An approximation $V_{\mathrm{y}} \cong 2/3V_{\mathrm{u}}$ was used[131, 132] for tests in which information of an initial yielding point was not reported.

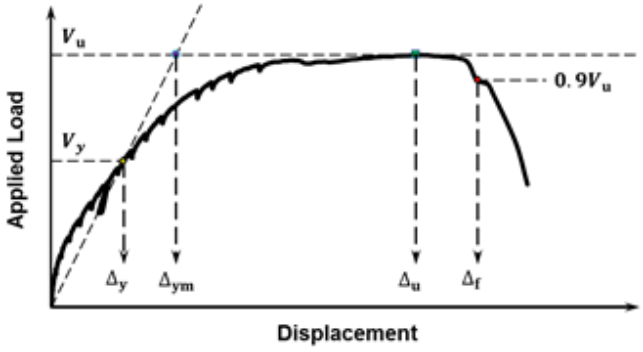


*Fig. 5-1: Definition of ductility*

Calculated ductility ($\mu$) for all test specimens in Table 5-1 and Table 5-2 is plotted versus the ratio $V_{\text{flex}}/V_{\text{shear}}$ in Fig. 5-2. It can be seen that for specimens with $V_{\text{flex}}/V_{\text{shear}} < 1$ (relatively low $\rho$), calculated ductility for a radial layout of shear studs was higher than that for an orthogonal layout. Also, the calculated ductility provided by a radial layout increased when the relative slab flexural reinforcement ratio $V_{\text{flex}}/V_{\text{shear}}$ decreased. The solid line in Fig. 5-2 presents a bilinear relationship (Eq. 36) between the calculated $V_{\text{flex}}/V_{\text{shear}}$ ratio and the measured ductility of slab-column specimens reinforced shear studs in a radial layout. For specimens with an orthogonal layout, however, the scattered test results indicate that there was no clear improvement in the measured ductility as the calculated ratio $V_{\text{flex}}/V_{\text{shear}}$ decreased.

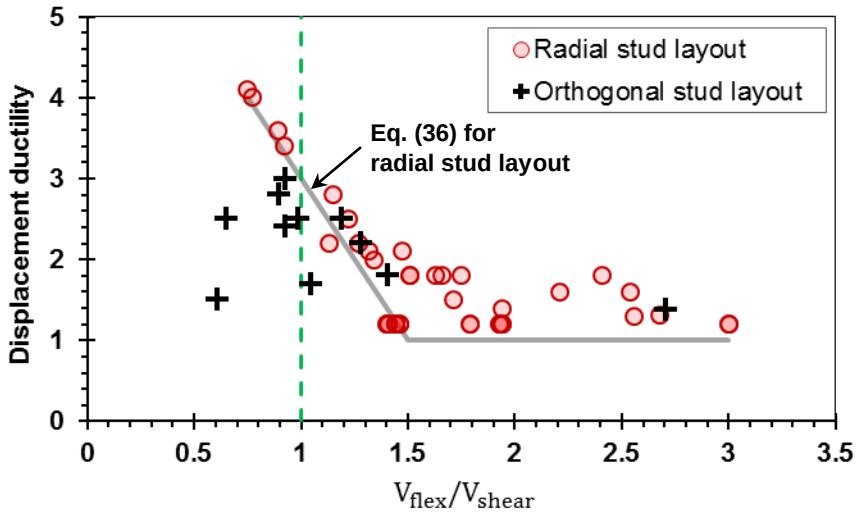


*Fig. 5-2: Ductility of test specimens reinforced with shear stud reinforcement*

$$\mu = \begin{cases} 7 - 4(V_{\text{flex}}/V_{\text{shear}}) & \text{if} \quad 1.5 > V_{\text{flex}}/V_{\text{shear}} > 0.7 \\ 1 & \text{if} \quad V_{\text{flex}}/V_{\text{shear}} \geq 1.5 \end{cases} \tag{36}$$

### 5.2.3 Recommendation for Shear Stud Layout

Results from more than 60 tests of slab-column connections reinforced with shear studs have indicated that a radial layout of shear studs is better than an orthogonal layout of shear studs in terms of shear strength and behavior of slab-column connections, especially for slab-column connections with relatively low slab reinforcement ratio. Based on these results, a radial layout of shear studs is recommended, especially in the locations where ductility is important (e.g. where redistribution of moments is accounted for in design).

## 5.3 EFFECT OF PERCENTAGE OF SLAB FLEXURAL REINFORCEMENT

### 5.3.1 Local Flexurally-Induced Shear Strength

It can be seen that the specimens in Table 5-2 (a relatively high $\rho$), had measured shear strengths higher than the corresponding shear strength calculated using the ACI Code[5]. However, for the specimens in Table 5-1 (a relatively low $\rho$), the measured loads at punching shear failure were substantially lower than the corresponding ACI Code calculated shear strengths. Similar observations have also been reported[55, 56, 128, 133, 134] for specimens without shear reinforcement and with a low $\rho$. Thus, the ACI Code provisions for punching shear strength may be unconservative for slab-column connections with a low percentage of slab flexural reinforcement. To determine the lower bound shear strength of a slab-column connection, design procedures should include an evaluation of the gravity shear required to develop a flexural mechanism that involves slab flexural yielding around the column. This will be referred to as a local flexurally-induced shear strength ($V_{\text{fn}}$).

For the test slab-column specimens, the local flexurally-induced shear strength ($V_{\text{fn}}$) can be taken as the flexural strength ($V_{\text{flex}}$), which is given in Eq. (18) and elsewhere[128] for different specimen shapes and test setups. For slab-column connections in an actual structure, the calculation of $V_{\text{fn}}$ needs to at least consider: 1) application of uniform loads on the slab, and 2) the shift of contra-flexural lines as plastic deformations take place. Considering these, a simple expression for $V_{\text{fn}}$ can be derived for interior slab-column connections with negligible moment transfer, equal spans in both principal directions, and circular, square or nearly square columns. A similar procedure may be applied to determine $V_{\text{fn}}$ for other design scenarios.

Consider a multi-span flat plate system supporting a uniform gravity load $q$ on all panels. If the columns in the system have a circular section with a diameter $d_{\text{c}}$ and are spaced equally at a distance $L$ in orthogonal directions, the line of contra-flexure (zero radial bending moment) around an interior column is approximately a circle with diameter $\gamma L$ (Fig. 5-3a). Shear force transferred from the slab to the column is

$$V \cong q\left(L^2 - \frac{\pi d_c^2}{4}\right) \qquad (37)$$

The free-body diagram of an interior slab-column connection isolated from the floor system by the contra-flexure line is shown in Fig. 5-3 (b). For no moment transfer, it is reasonable to assume that a vertical shear ($R/\pi\gamma L$) is distributed uniformly along the perimeter of the slab. The total shear force acting along the edge of the slab ($R$) can be calculated from equilibrium in the vertical direction and is given in Eq. (38).

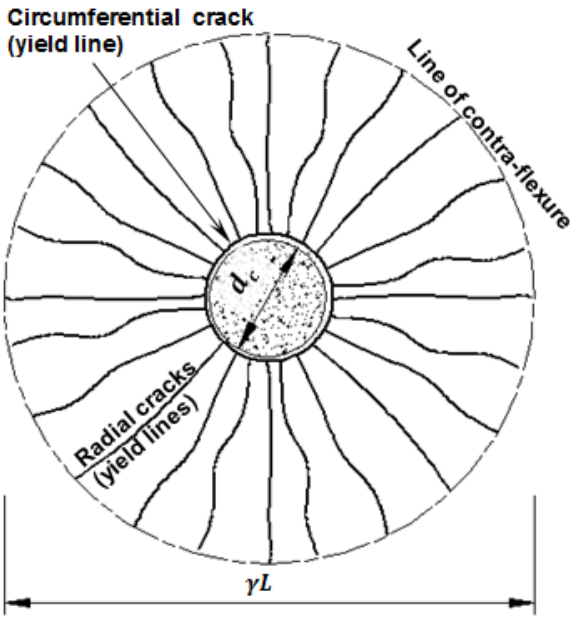


a) Top view

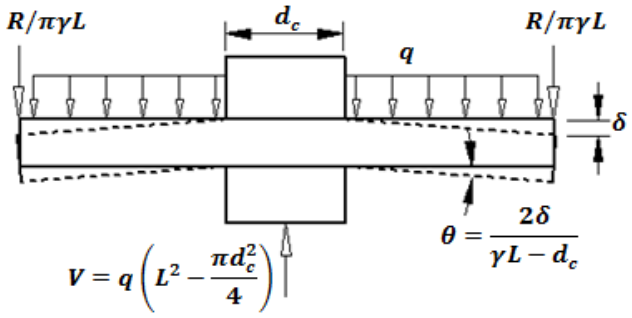


b) Free-body diagram and a virtual displacement

*Fig. 5-3: Interior slab-column connections*

$$R = q\left(L^2 - \frac{\pi(\gamma L)^2}{4}\right) \tag{38}$$

As the load $q$ increases, yielding of slab flexural reinforcement initiates near the column faces and then spreads away from the column. Yield line analysis[3, 54, 124] will be used to evaluate shear force transfer at the connection ($V_{\text{fn}}$), assuming that a punching shear failure will occur after yielding of slab flexural reinforcement adjacent to the column, but prior to the formation of positive moment yield lines. Thus, the yield line analysis presented herein only involves circumferential and radial negative yield lines, as shown in Fig. 5-3 (a). Applying a virtual displacement $\delta$ at the edge of the slab, the external (EW) and internal work (IW) are given as,

$$EW \cong q\frac{2}{3}\left[\frac{\pi(\gamma L)^2}{4}-\frac{\pi d_c^2}{4}\right]\delta + R\delta \tag{39}$$

$$IW = m\pi(\gamma L)\frac{2\delta}{\gamma L - d_c} \tag{40}$$

where $m$ is moment strength of the slab per unit width. Combining Eq. (38) through Eq. (40) and setting $V = V_{\text{fn}}$ in Eq. (37) leads to,

$$V_{\text{fn}} = 12m\frac{\pi\gamma\left[1-\left(\frac{\pi d_c^2}{4L^2}\right)\right]}{\left[\gamma/2-\left(\frac{\sqrt{\pi}d_c}{2L}\right)/\sqrt{\pi}\right]\left[12-8\left(\frac{\pi d_c^2}{4L^2}\right)-\pi\gamma^2\right]} \tag{41}$$

where $\gamma$ represents the location of the line of zero radial moment as a fraction of the span length $L$. Defining a parameter $\beta = \sqrt{A_{\text{c}}}/L$, where $A_{\text{c}}$ is the column cross sectional area, $V_{\text{fn}}$ for the case of circular columns can be expressed as,

$$V_{\text{fn}} = 12m\frac{\pi\gamma(1-\beta^2)}{(\gamma/2-\beta/\sqrt{\pi})(12-8\beta^2-\pi\gamma^2)} \tag{42}$$

For slab-column connections with noncircular column cross sections, $V_{\text{fn}}$ may be estimated from Eq. (42) by taking $\beta = \sqrt{A_{\text{c}}}/L$. Thus, for slab-column connections with square columns of side dimension $h_{\text{c}}$, $\beta = h_{\text{c}}/L$.

To account for the shifting of the contra-flexure line as slab flexural yielding develops around the column faces, $\gamma$ is assumed[3] to vary between 0.4 and 0.6. The ratio $\beta$ is assumed to vary from 0.03 to 0.1. The relationship between $V_{\text{fn}}$ and the parameters $\gamma$ and $\beta$ is shown in Fig. 5-4 (a). It can be seen that $V_{\text{fn}}$ increases as $\gamma$ or $\beta$ increases. From Fig. 5-4 (b), which shows the relationships between $V_{\text{fn}}$ and $\beta$ for $\gamma = 0.4$, 0.5, and 0.6, it can be seen that a shift of the contra-

flexure line has little effect on $V_{fn}$ for $\beta$ between 0.04 and approximately 0.07. As $\beta$ approaches 0.1, however, $V_{fn}$ decreases significantly because the contra-flexure line shifts away from the column. A linear expression (Eq. 43), plotted in Fig. 5-4 (b), represents a lower bound of $V_{fn}$ for typical values of $\beta$ between 0.04 and 0.1 and $\gamma$ between 0.4 and 0.6.

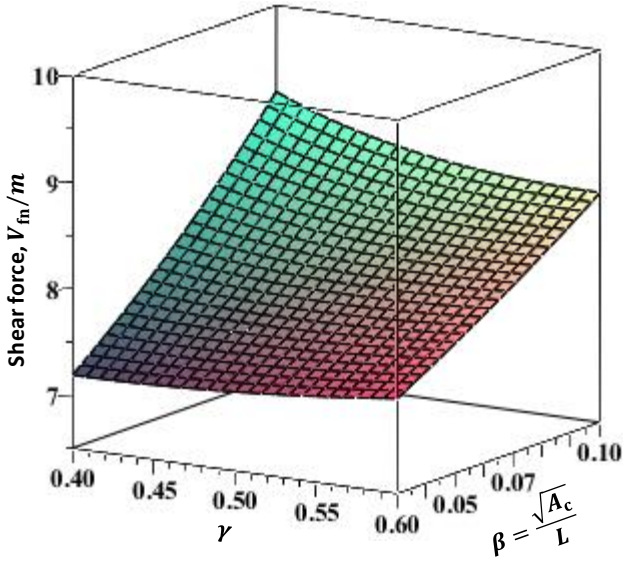


a) 3D plot of $V_{fn}$ as given in Eq. (42)

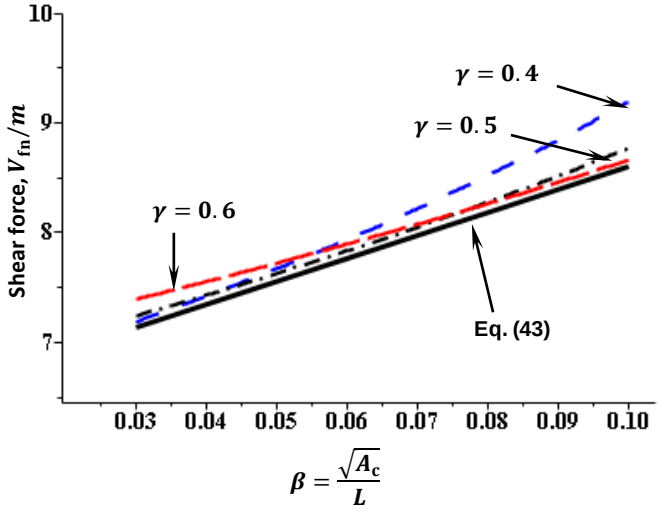


b) Comparison of $V_{fn}$ given in Eq. (42) at selected γ-planes and Eq. (43)

*Fig. 5-4: Shear force transferred at the connection*

$$V_{fn} \cong (6.5 + 20\beta)m \qquad (43)$$

This expression for $V_{fn}$ (Eq. 43) depends on the slab moment strength per unit width ($m$) and a parameter $\beta$ defined as $\sqrt{A_c}/L$, in which $A_c$ is the column cross sectional area, and $L$ is the slab span length. For square columns with side dimension $h_c$, $\beta = h_c/L$, which represents the column side dimension as a fraction of the span length.

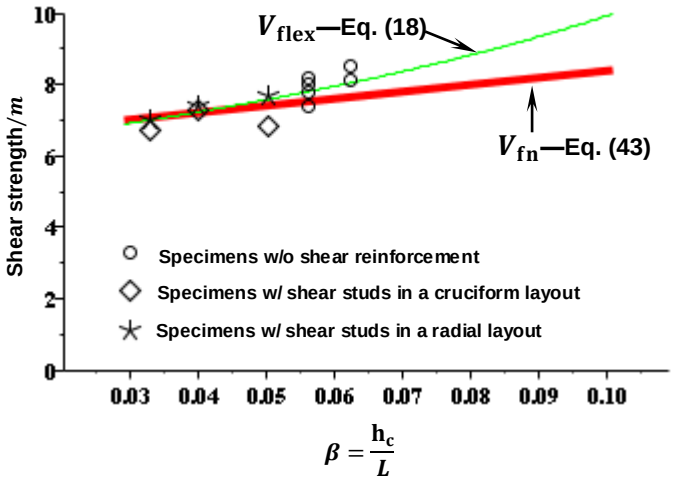


*Fig. 5-5: Punching failure loads for the specimens with a relatively low ρ*

Punching failure loads, expressed in terms of slab unit moment strength ($m$) for the specimens in Table 5-1 and other specimens[128] without shear reinforcement, but with a low $\rho$, are plotted in Fig. 5-5. These experimental results indicate that the measured shear strength of these specimens increases as $\beta$ increases. The calculated flexural strength of the test specimens ($V_{flex}$) using Eq. (18), assuming $l = 0.4L$, and the proposed $V_{fn}$ values from Eq. (43) are also plotted Fig. 5-5. It can be seen that $V_{flex} \approx V_{fn}$ if the column dimension is less than 5% of the slab span ($\beta < 0.05$), but $V_{flex}$ is significantly larger than the proposed $V_{fn}$ when the column size to span length ratio increases. This difference is partially due to the assumed location of the contra-flexural lines ($l = 0.4L$), which becomes less accurate as $\beta$ increases. It should be mentioned that, in practice, $\beta$ typically ranges from 0.04 to 0.1.

In practice, additional slab tension reinforcement is usually placed within a " transfer width", which includes the column width plus 1.5 times the slab thickness on each side of the column, so the slab moment strength per unit width ($m$) within the transfer width is typically higher than that it is in the remaining portions in the column strip. Because shear (inclined) cracks are shown to develop primarily in the regions within approximately $2d$ (e.g. Fig. 4-16)

from the column faces before the maximum load (e.g. Fig. 4-16), $m$ in Eq. (43) may be taken as the slab unit moment strength within the transfer width.

*Verification with tests of flat plate systems*—in the Hatcher et al[57] test of a flat plate system (presented in Section 2.4.2.1), the average moment strength per unit width for slab regions within the transfer width of the interior columns is 870 lb-ft./ft. (3870 N-m/m), and the ratio $\beta = h_c/L = 0.1$. The calculated local flexurally-induced shear strength (Eq. 43) for their Column 7 is 7.7 k (34.4 kN), which is close to the measured punching shear strength of 7.5 k (33.4 kN). For the other test of a flat plate system reported by Guralnick and La Fraugh[58] (Section 2.4.2.2), the calculated local flexurally-induced shear strength ($V_{fn}$) for the interior columns is 93.6 k (415 kN), which is also close to the measured punching shear strength of 95.9 k (425 kN). The calculations of these shear strengths for the two flat plate system tests are given in Appendix C. These results indicate that Eq. (43) can provide a good estimation for the local flexurally-induced shear strength ($V_{fn}$) at interior slab-column connections.

### 5.3.2 Proposed Minimum Slab Flexural Reinforcement

It has been shown that yielding of slab flexural reinforcement near the columns may substantially reduce the shear capacity of slab-column connections[8, 55, 80], and cause premature punching shear failures in flat plate systems[57, 58]. Thus, the maximal shear force that can be transferred at slab-column connections is limited by the local flexurally-induced shear strength ($V_{fn}$). For flat plate system, it is recommended that slab flexural reinforcement within the transfer width, which in the ACI Building Code is assumed to extend $1.5h$ ($h$ is slab thickness) on each side of the column, be designed such that the corresponding $V_{fn}$ is larger than the factored shear force, $V_u$, at the connection. Using $V_{fn}$ given in Eq. (43), the required unit moment strength ($m$) of the slab within the transfer width is given in Eq. (44),

$$m \geq \frac{V_u/\phi}{6.5 + 20\beta} \qquad (44)$$

where $V_{fn}$ is taken as equal to $V_u/\phi$. The strengh reduction factor, $\phi$, should be the value used for shear design (0.75) in the ACI Code. The unit moment strength of a slab ($m$) is a function of $\rho$, as given in Eq. (19), and it can be approximated as $m \cong 0.9\rho f_y d^2$. Using this approximation, Eq. (45) gives a minimum value ($\rho_{min}$) for the slab flexural reinforcement ratio in the transfer width.

$$m \cong \left(1 - \frac{\rho f_y}{1.7 f_c'}\right) \rho f_y d^2 \tag{19}$$

$$\rho_{\min} = \frac{V_u/\phi}{(5.85 + 18\beta) f_y d^2} \tag{45}$$

Assuming $f_y = 60{,}000$ psi, $f_c' = 5000$ psi, and $d \cong 0.9(L/33)$, the $\rho_{\min}$ from Eq. (45) required to transfer different levels of concentric slab shear stress ($v_u = V_u/b_0 d$) is shown in Fig. 5-6 for interior slab-column connections with square columns. These results indicate that $\rho_{\min}$ increases as either the design shear stress or the column size-to-span length ratio ($\beta$) increases.

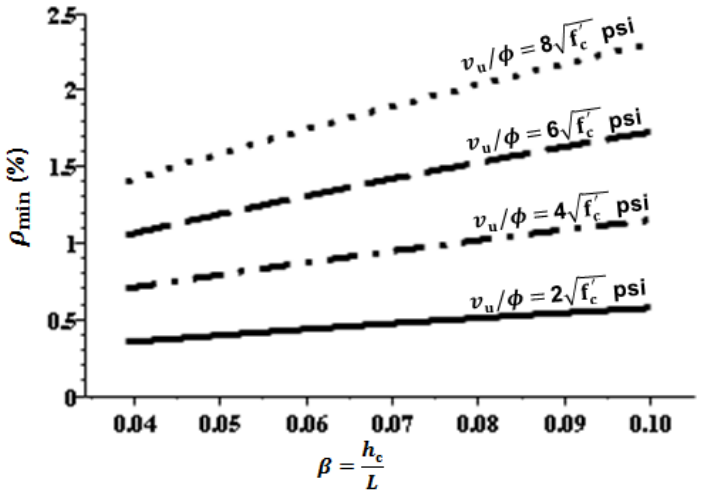


*Fig. 5-6: Minimum of slab flexural reinforcement $\rho_{min}$ ($1\sqrt{f_c'}$ psi = $0.083\sqrt{f_c'}$ MPa)*

For the five test specimens presented herein, the ratio $\beta$ was approximately 0.04. It can be seen from Fig. 5-6 that if the design slab shear stress for these specimens is $6\sqrt{f_c'}$ psi ($0.5\sqrt{f_c'}$ MPa), the minimum slab flexural reinforcement ($\rho_{\min}$) is approximated 1.1%. Because the S08 specimens in this test series had $\rho \cong 0.9\%$, the maximum slab shear stresses transferred in Specimens S08O and S08R did not reach $6\sqrt{f_c'}$ psi (see Table 4-1). For the S12 specimens, however, which had $\rho = 1.25\%$, the maximum measured slab shear stresses for these specimens were above of $6\sqrt{f_c'}$ psi. Fig. 5-6 also shows that for specimens without shear reinforcement ( $v_u/\phi \approx 4\sqrt{f_c'}$ psi ($0.33\sqrt{f_c'}$ MPa), a minimum slab flexural reinforcement ratio of approximately 1% would provide adequate flexural strength to develop the design shear strength for slab-column connections with typical values of $\beta$ (0.04 to 0.1).

## 5.4 EFFECT OF FAILURE SURFACES ON INTEGRITY REINFORCEMENT

### 5.4.1 Integrity Reinforcement for Flat Plate Systems

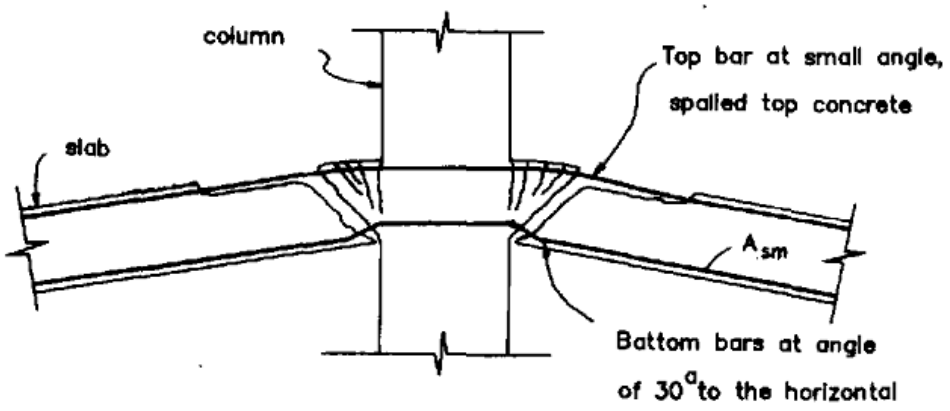


*Fig. 5-7: Conceptual model of a slab-column connection after punching failure[135]*

A conceptual model of slab-column connections after punching failure is shown in Fig. 5-7, in which the inclined failure surfaces near the column separate the slab from the column. The top (tension) reinforcing bars are often pulled out through the top of the slab as it drops, and thus, they are less effective in supporting the slab after punching failure[136]. The bottom slab flexural reinforcing bars that cross the column, however, are able to partially support the slab and prevent it from dropping to the floor below after punching failure[137]. The ACI Code[5] requires that: 1) at least two of the bottom slab bars in each direction must pass through the column core (Fig. 5-8), which is bounded by the longitudinal reinforcement of the column, and 2) these bars, referred to as integrity reinforcement, must be continuous or spliced at interior coonections with full mechanical, full welded, or Class B tension lap splices[5], and must be anchored at exterior connections. The splices for the integrity reinforcement are required to be placed within the shaded region in Fig. 5-8. After punching failure, if these integrity reinforcing bars are assumed to be at an angle of 30 degrees with respect to the horizontal[135], vertical force equilibrium for interior connections leads to the following minimum area of the integrity reinforcement in each principle direction,

$$A_{\text{sm}} \geq \frac{0.5 q_u l_1 l_2}{\phi f_y} \tag{46}$$

in which, $q_u$ is factored uniformly distributed load on the slab, $l_1$ and $l_2$ are center-to-center span lengths in each principle direction, and $\phi = 0.9$.

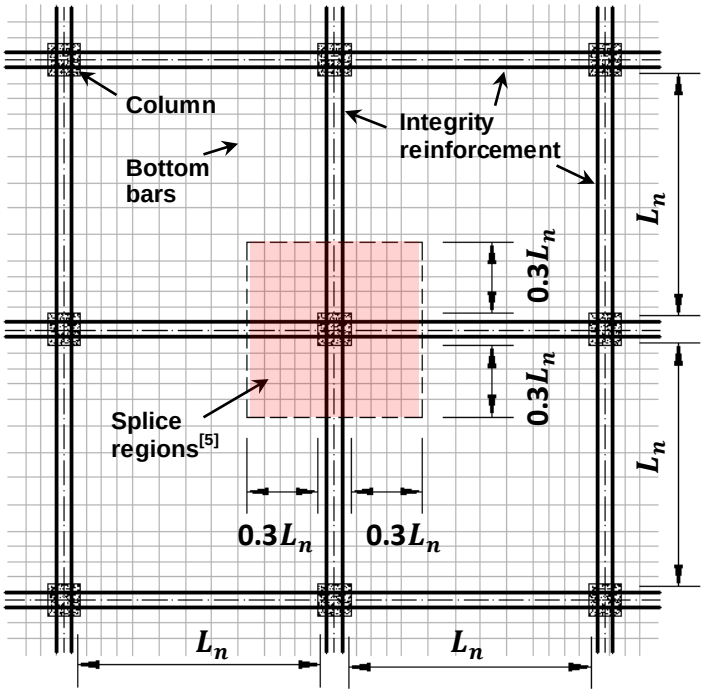


*Fig. 5-8: Integrity reinforcement (bottom) and its splice regions*

### 5.4.2 Punching Failure of Slab-Column Connections with Shear Studs

Results from tests of slab-column connections reinforced with shear stud reinforcement (Sections 4.5.3 and 4.5.4) show that failure surfaces may develop outside the shear stud regions, as shown in Fig. 5-9, which is a significantly different failure surface from that shown in Fig. 5-7. It can be seen from Fig. 5-9 that, after punching failure, as the slab separates from the punching cone that extends from the column faces to the outermost shear studs, the bottom bars, including integrity reinforcement, peel off the bottom concrete cover within the regions from the outermost shear studs to the column faces. The required area of the integrity reinforcing bars (Eq. 46) was calculated using the assumption that after punching failure these bars make an angle of 30 degrees with the horizontal. Thus, for the failure model in Fig. 5-9, the slab needs to drop a distance of $\Delta = r_{st} \times \tan(30)$ to reach the equilibrium state ($r_{st}$ is the distance from the outermost shear studs to the column periphery). However, a sudden slab displacement of this amount may produce a significant momentum for the slab, which could cause an overload for the integrity reinforcing bars. This effect is not considered in the derivations[136, 137] of Eq. (46), and

needs to be studied carefully considered for slab-column connections with shear stud reinformcement in an orthogonal layout.

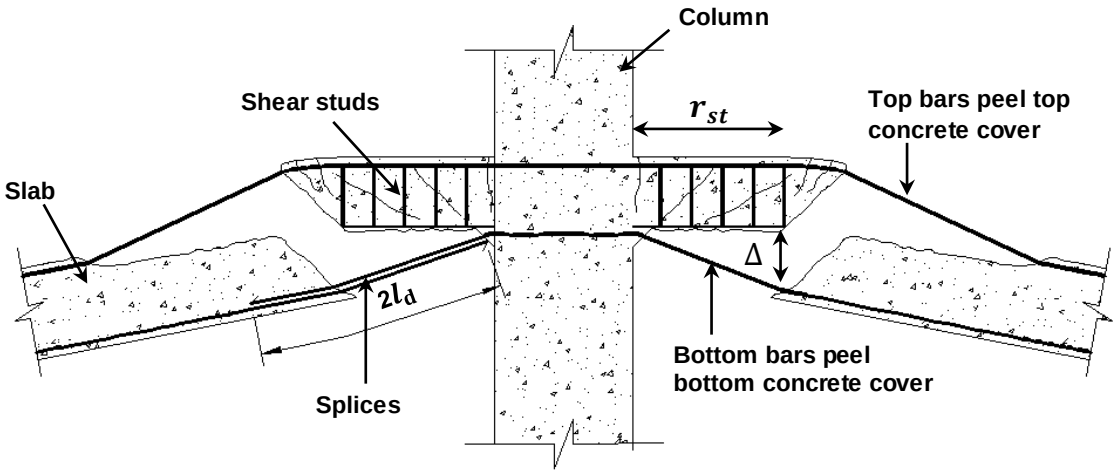


*Fig. 5-9: A possible punching failure of slab-column connections reinforced with shear studs*

### 5.4.3 Splice Location Recommendation

In order to be effective, integrity reinforcement for flat plate systems is required to be either continuous or spliced, and one of the permitted types of splices is a Class B tension lap-splice[5]. These splices are required to be placed within slab regions extending $0.3L_n$ from the column periphery, as shown in Fig. 5-8 ($L_n$ is the clear span). In practice, splices for integrity reinforcement are recommended[135] to be located:

1) outside a distance of $2l_d$ from the column faces with a minimum lap splice length of $l_d$,
2) within the column section with a minimum lap splice length of $l_d$, or
3) immediately outside the column periphery with a minimum lap splice length of $2l_d$, provided top reinforcement is also used in this region.

in which $l_d$ is the development length of a deformed bar in tension specified in the ACI Code[5].

In Fig. 5-9, a lap-splice that was designed following the third recommendation is shown on the left side of the column. Because the concrete cover under the shear stud regions may be split and peeled off during punching failure, the portion of the splice within these regions are essentially ineffective. Thus, the effective length of the lap splice is significantly reduced. This observation suggests that slab integrity reinforcement should not be spliced immediately outside of the column periphery, but outside of shear stud regions.

# CHAPTER 6
# NONLINEAR FINITE ELEMENT MODELING OF SLAB-COLUMN CONNECTIONS

This chapter presents the development of an analytical program for reinforced concrete slab-column connections. Finite element (F.E.) models were developed using Abaqus/Standard[19] to simulate the behavior and shear strength of the slab-column connection specimens that were presented in Chapters 3 to 5. In this chapter, after simulation results are developed, comparisions between the analytical results and the experiments are presented in terms of shear strength, strains in shear studs, flexural and shear crack developments, and failure surfaces. The sections in this chapter are as follows:

- Section 6.1: Introduction of Abaqus, a finite element analysis program,
- Section 6.2: Discusssion of three-dimensional F.E. models for the test specimens,
- Section 6.3: Presentation of mesh convergence and sensitivity analyses,
- Section 6.4: Simulation results from the F.E. models for the test specimens, and
- Section 6.5 Discussion of effect of shear stud layouts and slab flexural reinforcement ratio on shear strength and behavior of the analytical models of the test specimens.

## 6.1 ABAQUS FEA

In this analytical program, reinforced concrete slab-column connections were simulated using Abaqus FEA[19], a general finite element analysis application. This application has two packages: Abaqus/Standard and Abaqus/CAE. Abaqus/Standard is usually used to analyze static and low-speed dynamic systems, in which highly accurate stress and strain solutions are critical important. It supports many types of solid element with various material models, convenient simulation methods for defining interactions between elements, and efficient algorithms for solving nonlinear problems. The other package, Abaqus/CAE or Complete Abaqus Environment, is not only used to efficiently create models to input to Abaqus/Standard, but also to monitor and diagnose simulation processes in Abaqus/Standard, and visualize analysis results. In the following section, the development of a three-dimension finite element model of slab-column connections using Abaqus/CAE is presented.

## 6.2 THREE-DIMENTIONAL F.E. MODELS OF SLAB-COLUMN CONNECTIONS

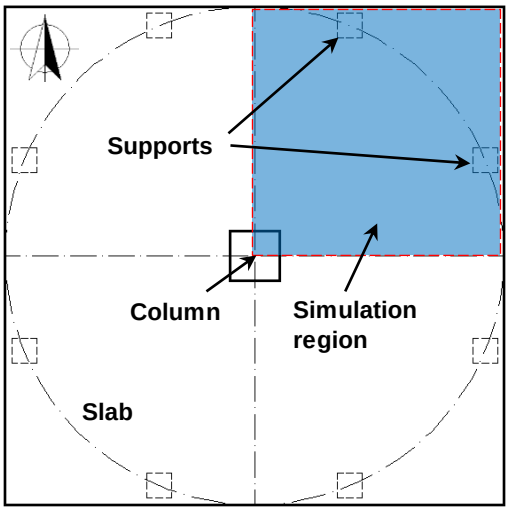


*Fig. 6-1: Simulation region for symmetric slab-column specimens*

In this section, models of symmetric interior slab-column specimens that are subjected to a concentric load at the column and axisymmetrically supported on the slab (Fig. 6-1) are developed. The slab-column specimens are symmetric about two principle axes, so only a quarter of a specimen is modeled to reduce computation time. Using the modeling methods presented in this section, models of slab-column connections that are not symmetric and/or subjected to eccentric loads can be developed.

### 6.2.1 Discretization Method

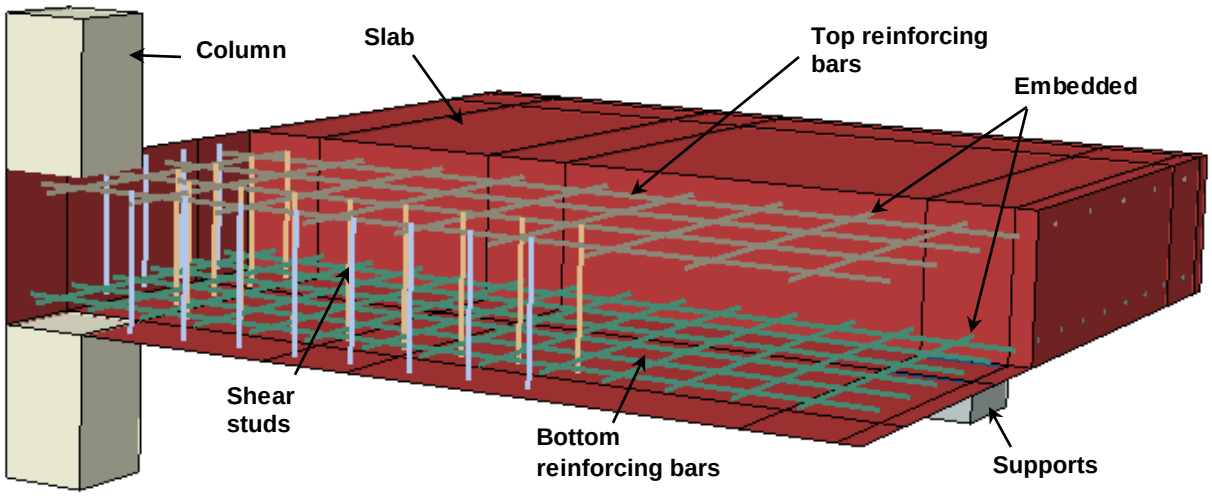


*Fig. 6-2: Discretization of slab-column model*

Models of reinforced concrete slab-column connections with shear studs were developed in this study using a discretization method that is similar to the Winkler and Stangenberg[99] model (Fig. 2-34). In these models, concrete, flexural reinforcing bars, and shear studs were modeled separately using different types of elements, as shown in Fig. 6-2. Concrete was modeled using solid elements, while flexural reinforcing bars and shear studs were modeled using three-dimensional truss elements. These reinforcement truss elements were embedded within the concrete solid elements to model interactions between concrete and reinforcement. This modelling approach allows the concrete behavior to be considered independently of the reinforecement. Effects of bond slip and dowel action are partially considered through some aspects of the concrete behavior such as "tension stiffening". The following sections discuss how finite element types for each material were selected, how these separate elements were assembled, and what material models were used.

### 6.2.2 Selection of Finite Elements

Abaqus/Standard[19] provides 24 continuum elements and four three-dimensional truss elements for stress and displacement analyses. These elements are different in their shapes, number of nodes, order of interpolation ($1^{st}$ or $2^{nd}$ -order), number of integration points (full or

reduced), and behavior (regular or hybrid). Thus, it is important to select the appropriate elements for concrete and reinforcement to study of punching failure at slab-column connections.

### *6.2.2.1 Concrete Elements*

Continuum elements that are available in Abaqus/Standard[19] have three different shapes: tetrahedron, triangular prism, and hexahedra. Although tetrahedron and triangular prism elements, which are geometrically versatile, are convenient to mesh a complex shape, hexahedra elements (or a so-called brick elements, Fig. 6-3) are highly recommended because they provide a better convergence rate, have no sensitivity to mesh orientation of regular meshes, and usually provide a solution of equivalent accuracy at less cost[19]. Thus, brick elements were selected for this study (Fig. 6-4).

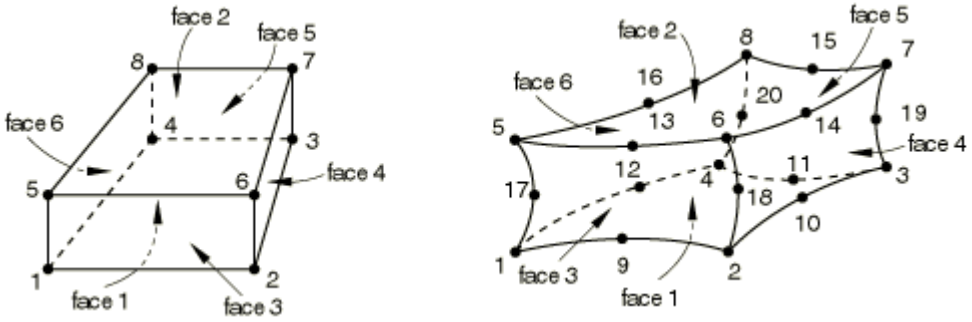


a) 8-node brick element (C3D8x) b) 20-node brick element (C3D20x)

*Fig. 6-3: Different hexahedra (brick) elements for concrete[19]*

Fig. 6-3 shows two different types of brick element, including a first-order element with eight nodes (Fig. 6-3a) and a second-order element with 20 nodes (Fig. 6-3b). The 20-node brick elements are used in simulations that have complex geometries, e.g. curved surfaces, and bending-dominated behaviors. For other simulations, the eight-node brick elements, with less integration points than the 20-node elements, are often used because they provide faster solutions with good accuracy. In this analytical study slabs have flat surfaces and shear-dominated behaviors, and thus the eight-node brick elements were considered.

Eight-node brick elements consist of six elements (C3D8x) that are different in the number of integration points and behavior. Elements with reduced number of integration points (C3D8R) reduce running time significantly but they can cause hourglassing problems[19]. In addition, hybrid elements (C3D8H) are intended primarily for use with incompressible and almost

incompressible material behavior (the Poisson's ratio is greater than 0.48). In this study, regular and full-integration 8-node brick elements (C3D8) were used for modeling concrete.

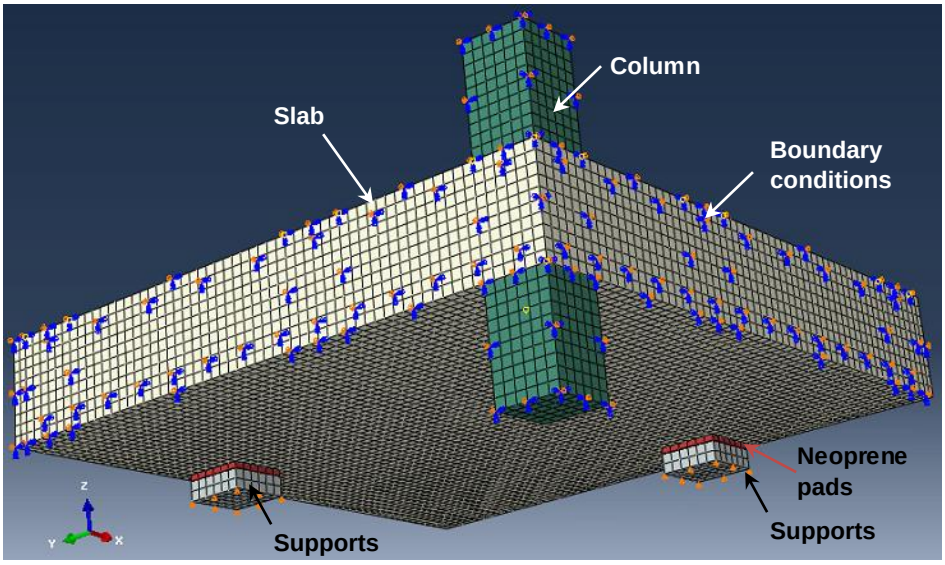


Fig. 6-4: Typical model of slab-column connections after mesh generation

### *6.2.2.2 Reinforcement Elements*

Abaqus/Standard[19] element library has four three-dimensional truss elements for stress and displacement analyses, and these elements are different in the number of nodes (Fig. 6-5) and behavior (regular or hybrid). Two-node straight elements have a constant stress and strain along the element, while three-node curved elements, which are used for modeling curved reinforcing cables, e.g. prestressed tendons in reinforced concrete structures, have stress and strain linearly distributed along the element. In addition, hybrid truss elements are used to represent rigid links that are much stiffer than the overall structural model. In this study, the regular and 2-node straight truss elements (T3D2) were used for modeling flexural reinforcing bars and shear studs.

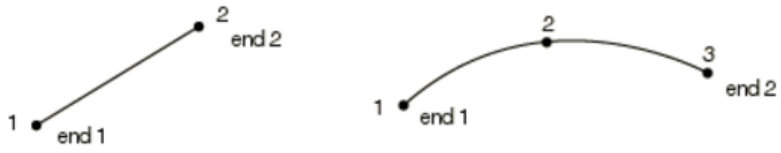


a) 2-node straight truss element b) 3-node curved truss element

*Fig. 6-5: Different three-dimensional truss elements for reinforcement*[19]

### 6.2.3 Model Assembly

#### *6.2.3.1 Embedded Elements*

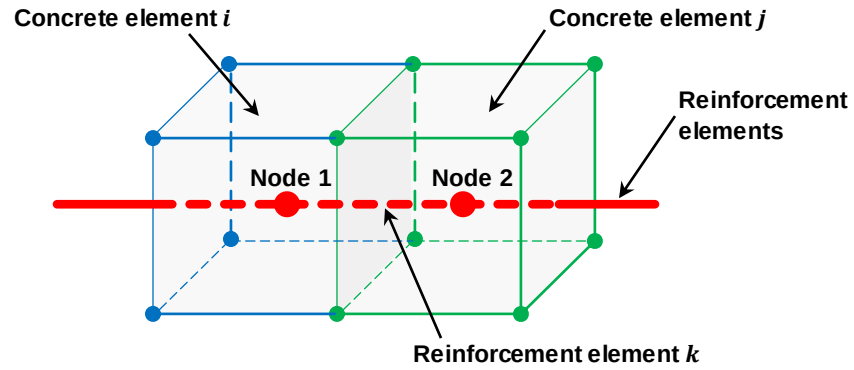


*Fig. 6-6: Embedded element technique in Abaqus/Standard*[19]

To model composite interaction between concrete and reinforcement, the nodes of a reinforcement element need to be incorporated into the nodes of adjacent concrete elements. These connections can be defined in Abaqus/Standard[19] using the embedded element technique, which is demonstrated in Fig. 6-6. Assuming reinforcement element $k$ is specified to be embedded in concrete elements (host) and its nodes (1 and 2) are located within concrete elements ($i$ and $j$, respectively), the translational degrees of freedom of each embedded node are automatically eliminated and then constrained to the interpolated values of the corresponding degrees of freedom of the host element, i.e. nodes 1 and 2 are constrained by concrete elements $i$ and $j$, respectively. Because the displacements of embedded nodes are computed from the displacements of the corresponding host elements, no relative displacement between each embedded node and its host element (or reinforcement slip) is permitted. Tension stiffening, or stiffness effect, of cracked concrete is accounted for by defining post-cracked strain-softening behavior for concrete elements. Fig. 6-7 shows the implementation of the embedded element technique for slab flexural reinforcement at the top and bottom in a model of slab-column connections.

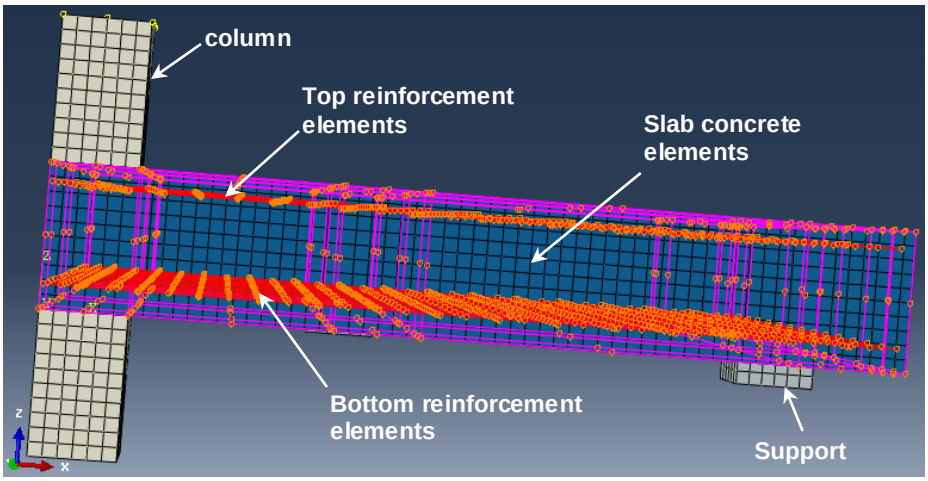


*Fig. 6-7: Embedded slab flexural reinforcement elements in slab concrete elements*

Connections between a shear stud element and nearby concrete are show in Fig. 6-8, in which the whole stud is represented by one three-dimensional truss element with the same length as the stud (Fig. 6-8b). The two nodes of this truss element were specified to be embedded in slab concrete elements. Stress and strain were uniform along this element, so this modeling of shear studs represents a regular shear stud with a smooth shaft. For modeling a shear stud with a deformed shaft, multiple embedded truss elements can be used instead of a single embedded truss element.

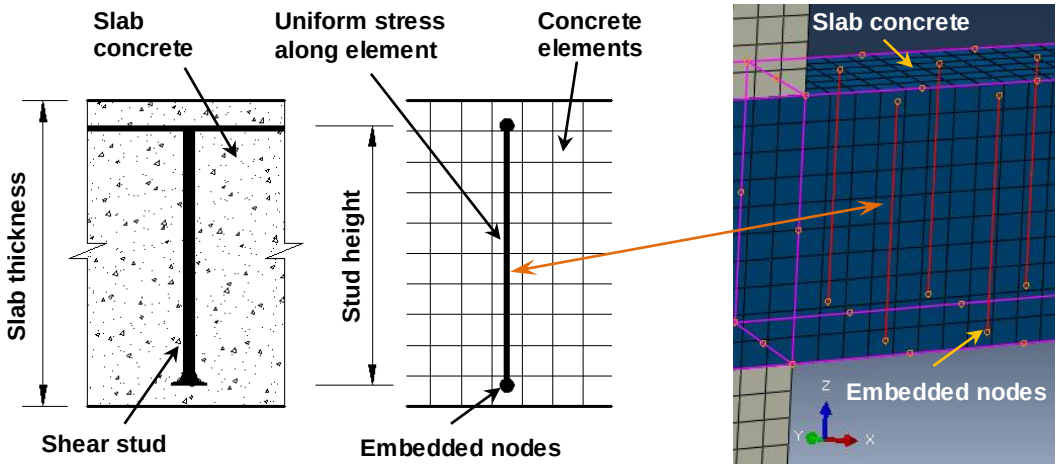


a) Shear stud b) Conceptual model c) Implementation in Abaqus

*Fig. 6-8: Modeling of headed shear studs with smooth shafts*

#### *6.2.3.2 Tie Constraints*

Columns and the slab are modeled using different parts (Fig. 6-4), and thus they need to be connected together in order to assembly a slab-column specimen. In this study, the connections between columns and slab were defined using tie constraints, in which the column contact surfaces (slave) are tied (constrained) to the corresponding slab surfaces (master). If nodes for the column and slab elements are coincident, the degrees of freedom of the nodes for column elements are identical to that of the corresponding nodes for slab elements. If support systems are discretized, tie constraints can also be used to connect their finite elements to the slab-column connection model (Fig. 6-4).

### 6.2.4 Support System Simulation

In the experimental program presented in Chapter 3, a support system with eight discrete "points" was used to support the specimens during the test. At each support point, one neoprene (rubber like) pad of 6 x 6 x 0.625 $in.^3$ (160 x 160 x 16 $mm^3$) was placed between the support and the test specimens. To simulate correctly the behavior of the slab-column specimens, the neoprene pads were included in the F.E. model, as shown in Fig. 6-4.

To measure the behavior of the neoprene pads, uniaxial compressive tests were conducted, as shown in Fig. 6-9 (a). Relationships between an average compressive stress calculated over the bearing area of the neoprene pads (6x6 $in.^2$ or 150x150 $mm^2$) and the corresponding average strain for the uniaxial tests are represented by the dashed lines in Fig. 6-10. These stress-strain relationships are nonlinear, and thus the neoprene pad elements in the F.E. model would require a nonlinear stress-strain relationship to simulate the actual support conditions. Because behavior of the neoprene pads was not an interest of this study and, moreover, such material nonlinearity for the neoprene pads would have added more unnecessary instability to the F.E. model of the slab-column specimens, the neoprene pads were approximately simulated using equivalent linear elasticity defined as follows.

A F.E. model for the uniaxial compressive tests (Fig. 6-9a) was developed using Abaqus, as shown in (Fig. 6-9b). Equivalent linear elasticity for the neoprene pads (Fig. 6-9b) was defined through two parameters: the Poisson's ratio and Young's modulus. The Poisson's ratio was assumed to be equal to 0.499 (rubber like material). The Young's modulus was selected so that

the calculated deformation of the neoprene pad was close to the measured deformations when a bearing stress varied from 800 to 1100 psi (5.5 to 7.6 MPa). This range of stress corresponds to a load range in which the punching failures of the test specimens occurred (Chapter 4). Based on this criterion, the Young's modulus was taken equal to 35 psi (240 kPa), and the corresponding simuation result is shown as the solid line in Fig. 6-10. It can be seen from Fig. 6-10 that the neoprene pad in the F.E. model is stiffer than the actual neoprene pads for low bearing stresses. The equivalent elastic properties for the neoprene pads used in this study are given in Table 6-1.

*Table 6-1— Neoprene pad properties*

| Young's modulus | Poisson's ratio |
|---|---|
| 35 psi (0.24 MPa) | 0.499 |

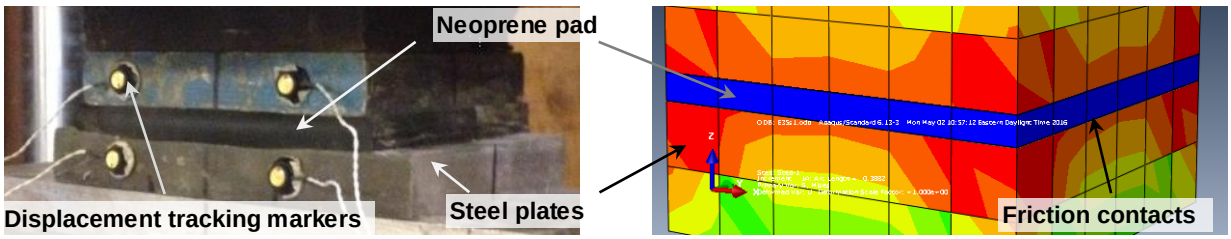


a) Uniaxial compressive test b) Simulation in Abaqus

*Fig. 6-9: Neoprene pad tests and simulations*

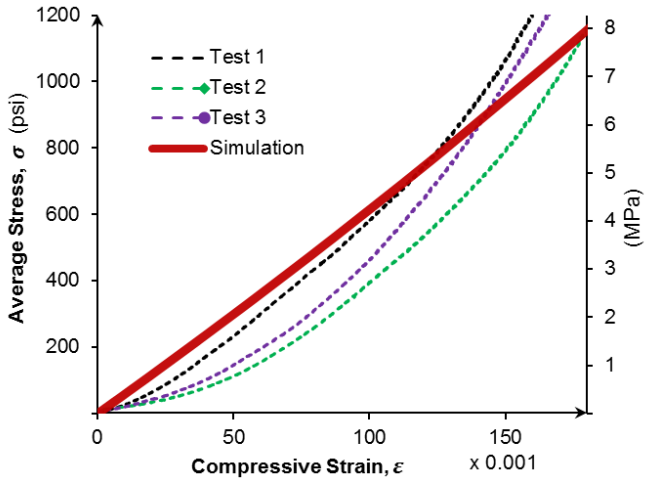


*Fig. 6-10: Test and simulation results for the neoprene pads*

### 6.2.5 Loading Method

In this study, the top surface of the column was imposed a vertical downward displacement instead of applying a concentric load. This displacement increased incrementally and Abaqus/Standard controls the rate of the displacement during the simulation.

### 6.2.6 Material Models

#### *6.2.6.1 Concrete*

Typical properties for normal weight concrete were used for concrete elements in the models. The concrete density ($\gamma_c$) and Poisson's ratio ($\nu$) are 145 pcf (2320 kG/m$^3$) and 0.2, respectively. The Young modulus is computed using Eq. (47),

$$E_c = 33\gamma_c^{1.5}\sqrt{f_c'} \quad \text{psi} \qquad (47)$$

$$E_c = 0.043\gamma_c^{1.5}\sqrt{f_c'} \quad \text{MPa} \qquad (47M)$$

in which $f_c'$ is the concrete compressive strength measured on the test day.

***a) Concrete Damaged Plasticity vs. Concrete Smeared Cracking Models***

To simulate behavior for concrete elements, inelastic models incorporated in Abaqus/Standard[19] including "Concrete Smeared Cracking" (CSC) and "Concrete Damaged Plasticity" (CDP) are often used. These two models consider effect of cracking on the behavior of concrete differently. In the CSC model, concrete is assumed to crack when stresses reach a so-called "crack detection surface", a simple Columnb line in the $\bar{p} - \bar{q}$ space ($\bar{p} = \bar{I}_1/3$ is the effective hyrostatic stress, $\bar{q} = \sqrt{3\bar{J}_2}$ is the effective Von-Misses stress, and $\bar{I}_1$ and $\bar{J}_2$ are two invariants of a stress tensor and stress deviator tensor, respectively). The direction of a crack ($\chi$) is taken as the direction of the maximum principle plastic strain increment at an integration point. Once a crack has occurred, it remains unchanged throughtout the rest of the simulation and the elastic stiffness coefficient $E_{\chi\chi\chi\chi}$, in the tensor ($\boldsymbol{E}$), that corresponds to the cracking direction ($\chi$) is replaced (damaged) by a stiffness computed from a user-defined stress-strain relationship in tension for concrete. The CSC model uses an associated flow rule and isotropic hardening to simulate plastic behavior of concrete. In the CDP model, the effect of cracking (and crushing) on concrete behavior is considered using a scalar damage variable ($0 \leq D \leq 1$) to reduce the elastic

stiffness (**E)** during the calculation (Eq. 48). The variable ($D$) is a function of a hardening variable ($\boldsymbol{\kappa}$), which is computed from plastic strains and stress conditions. Cracking directions are not determinded in the CDP model, but it can be studied through the evolution of a damage variable ($\kappa_{\mathrm{t}}$). The CDP model uses a non-associated flow rule to simulate plastic behavior of concrete.

$$\boldsymbol{E} = (1 - D)\boldsymbol{E}_0 \qquad (48)$$

Serveral concerns have been raised over the Concrete Smeared Cracking model (CSC). In this model, the associated flow assumption generally overestimates an inelastic volumn strain, and the simple yield surface, which consists of the two stress invariants ($\bar{p}$ and $\bar{q}$), does not accurately match experimental data[19]. The Concrete Damaged Plasticity model (CDP), on the other hand, uses a yield surface (Fig. 6-11 and Fig. 6-12) that has three stress variables (Eq. D18), including the two effective stress invariants ($\bar{p}$ and $\bar{q}$) and the algebraically maximum effective principle stress ($\bar{\sigma}_{max}$), and a non-associated flow rule to compute plastic strains (Fig. 6-13 and Fig. 6-14). Thus, the CDP model can predict the behavior of concrete in three-dimensional stress states more accurately. The CDP model is considered to be a better nonlinear plasticity concrete model for simulations of punching shear failure[99]. In this study, the Concrete Damage Plasticity model was used for the concrete elements and the model is described in Appendix D and elsewhere[19, 100, 138]. The following subsections present input for the CDP model used in Abaqus/Standard[19].

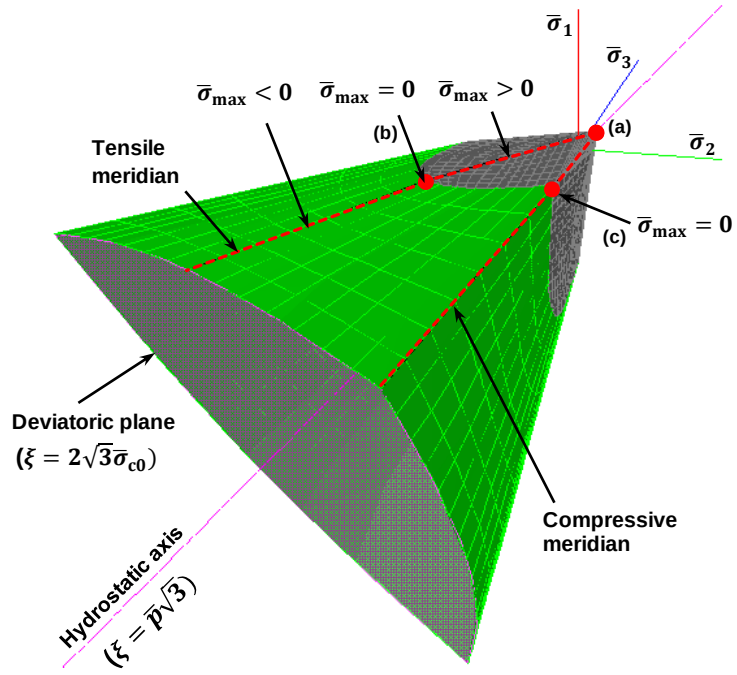


*Fig. 6-11: Yield surface for concrete used in the Concrete Damaged Plasticity model (Eq. D18)*

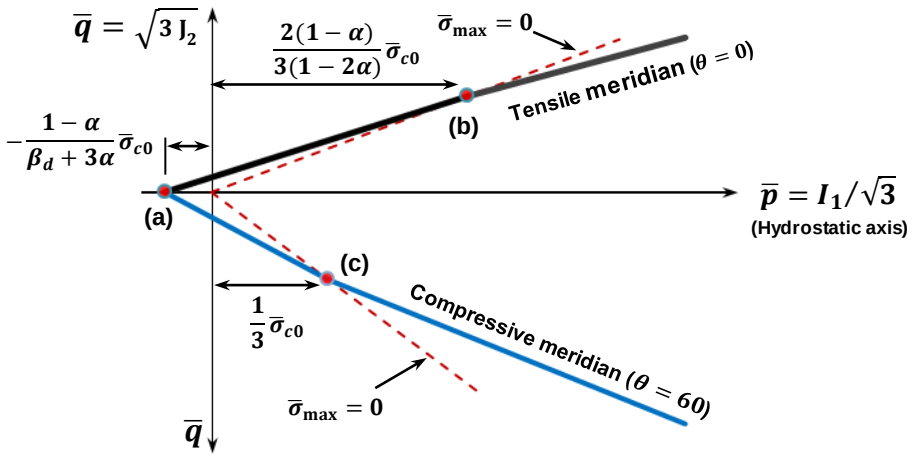


*Fig. 6-12: Tensile and compressive meridians for the yield surface in Fig. 6-11*

(Definitions of the parameters in this figure are given in Appendix D)

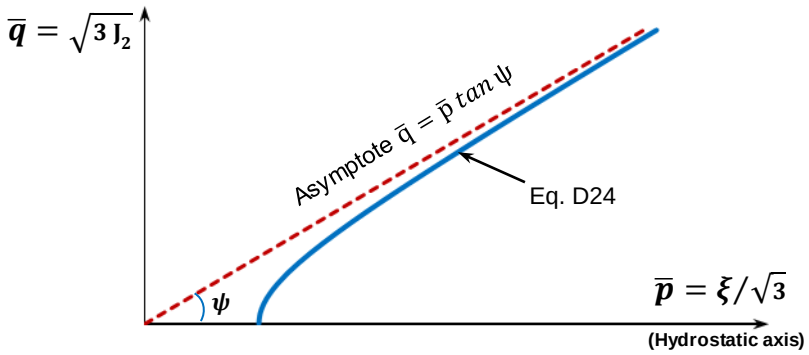


*Fig. 6-13: Non-associated plastic flows for the Concrete Damaged Plasticity model*

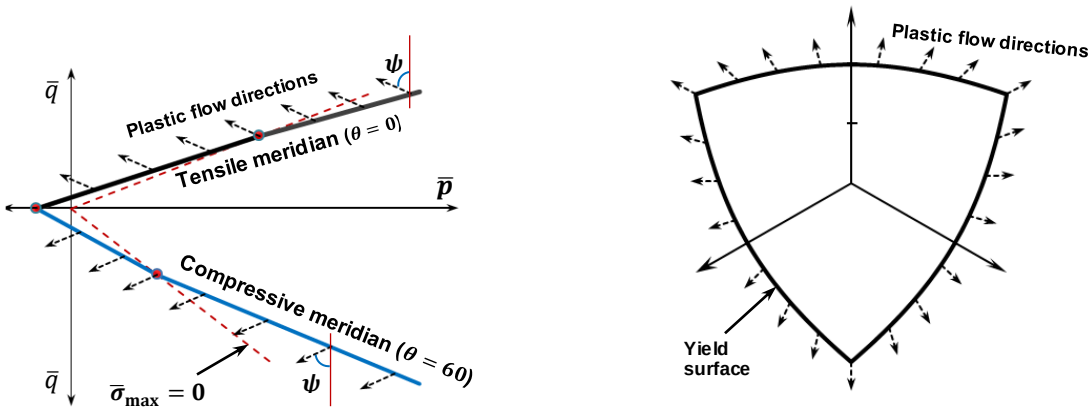


a) in p-q planes b) in a deviatoric plane

*Fig. 6-14: Plastic flow directions*

### *b) Uniaxial Compression Behavior of Concrete*

Behavior of concrete in a uniaxial compressive stress state was simulated using a tri-linear stress–strain relationship, as shown in Fig. 6-15 (a), which consists of three segments: elastic, harderning, and softenening. The concrete is assumed to behave elastically with the stiffness $E_c$, computed using Eq. (47), up to a compressive stress of 40 percent of the measured compressive strength of concrete ($f_c'$) on the test date, where concrete is assumed to start to yield, or loss stiffness, (Point Y in Fig. 6-15a). After that the hardening behavior of concrete is modeled using a line from point Y to point F (peak strength). The strain corresponding to point F is assumed to be 0.002.[3] The softening behavior of concrete is modelled linearly from point F to point U,

where the compressive stress is assumed to be 20 percent of $f'_c$ and the corresponding strain is assumed to be 0.004.

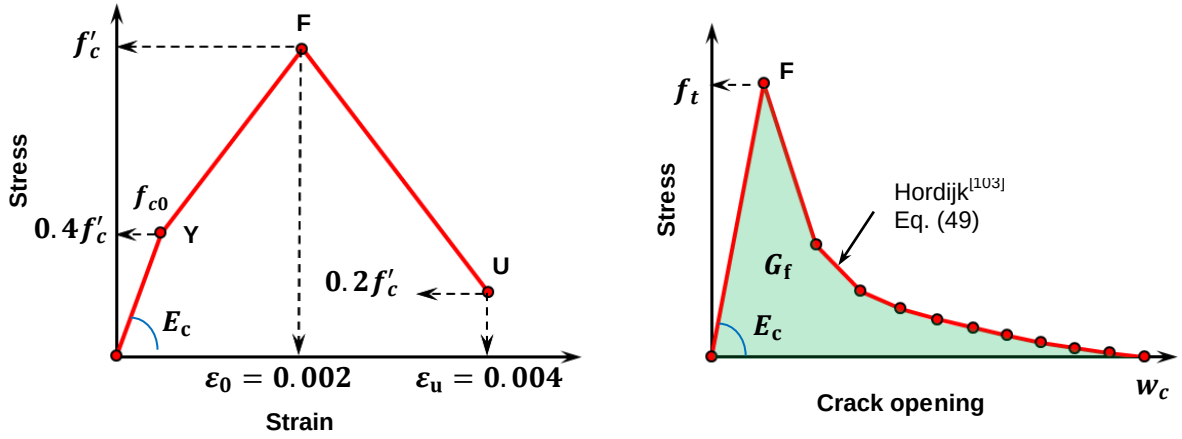


a) in compression b) in tension

*Fig. 6-15: Behavior of concrete in an uniaxial stress state*

### *c) Uniaxial Tension Behavior of Concrete*

Behavior of concrete in a uniaxial tensile stress state, in terms of stress-displacement relationship, consists of two parts: elastic and softening, as shown in Fig. 6-15 (b). The elastic behavior is assumed to be linear until tensile stress ($\sigma_t$) reaches the tensile strength of concrete ($f_t$, point F). The elastic stiffness ($E_c$) is computed using Eq. (47). The tensile strength of concrete was measured on the test date using splitting tests (Table 3-4). The softening behavior (or tension stiffening) of concrete is defined using the nonlinear stress–crack opening (displacement) relationship proposed by Hordijk[103], as given in Eq. (49) and presented in Fig. 6-15 (b). In Eq. (49), $w$ is a crack opening (displacement), $w_c$ is the critical crack opening (where $\sigma_t = 0$), and the parameters $c_1$ and $c_2$ are equal to 3 and 6.93, respectively. The critical crack opening is computed using a fracture energy cracking criterion[139], in which the energy required to open a unit area of crack, $G_f$, is the area under the stress-crack opening curve (shaded area in Fig. 6-15b), and given in Eq. (50). The fracture energy is often considered as a material property of concrete. In Eurocode 2[6], fracture energy is given as a function of the aggregate size and concrete compressive strength. In the Abaqus manual[19], $G_f$ is suggested to have a value from 0.22 to 0.67 lbf/in. (40 to 120 N/m) as the concrete compressive strength increases from 2850 to 5700 psi (20 to 40 MPa)[19]. Based on this suggestion, the fracture energy used in this study is

assumed to be a linear function of a concrete compressive strength ($f_c'$), as given in Eq. (51) and presented in Fig. 6-16. The use of stress-displacement relationship instead of stress-strain relationship helps reduce the mesh sentitivity of the numerical results (crack localization issues).

$$\frac{\sigma_t}{f_t} = \left[1 + \left(c_1 \frac{w}{w_c}\right)^3\right] e^{-c_2 \frac{w}{w_c}} - \frac{w}{w_c}(1 + c_1^3) e^{-c_2} \tag{49}$$

$$w_c = 5.14 \frac{G_f}{f_t} \tag{50}$$

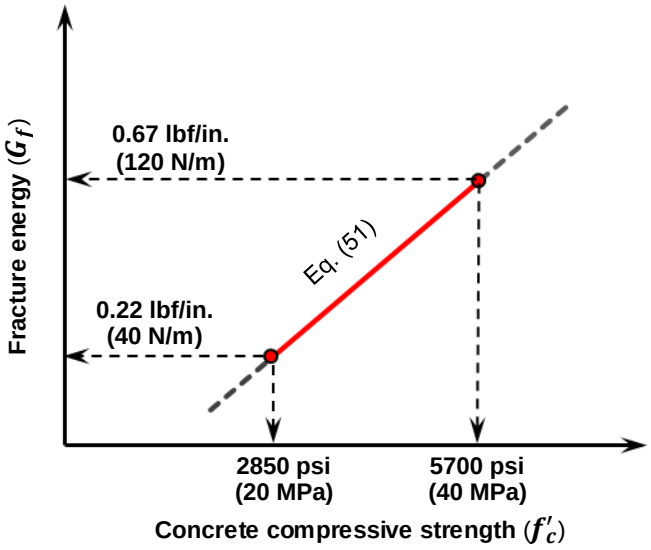


*Fig. 6-16: Fracture energy versus concrete compressive strength*

$$G_f = \frac{f_c'}{6330} - 0.23 \quad \text{(psi)} \tag{51}$$

$$G_f = 4 f_c' - 40 \quad \text{(MPa)} \tag{51M}$$

### *d) Damage Variables*

In the Concrete Damaged Plasticity model, a scalar damage variable $D$ is used to reduce the elastic stiffness due to cracking and crushing for unloading and reloading. This variable is computed from the stress state and two uniaxial damage variables $D_t$ and $D_c$ for tension and compression, respectively (see Appendix D). The two uniaxial damage variables are user-defined parameters as functions of inelastic displacements (cracking opening for $D_t$ and crushing

displacement for $D_c$), and then Abaqus converts these functions to relationships between $D_t$ and $D_c$ versus plastic strains (Appendix D). In addition, the evolution of the uniaxial damage variable in tension (DAMAGET, the output of $D_t$) is often used to study crack propagations in reinforced concrete structures[19]. In this study, even though the applied load is monotonic, the uniaxial damage variable in tension ($D_t$) was defined to investigate the development of flexural and punching shear cracks. The relationship between $D_t$ and a cracking opening was adopted from the Abaqus Example Problem Guide[19] (example 2.1.15), which is presented in Fig. 6-17.

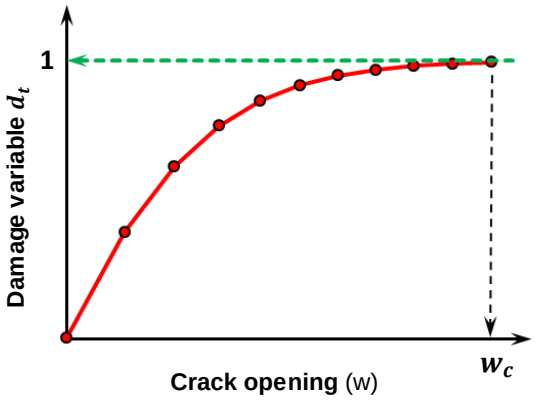


| $d_t$ | $w$ ($w_c$) |
|---|---|
| 0.00000 | 0.00000 |
| 0.38122 | 0.13727 |
| 0.61711 | 0.25481 |
| 0.76307 | 0.35968 |
| 0.85339 | 0.45667 |
| 0.90928 | 0.54902 |
| 0.94387 | 0.63897 |
| 0.96527 | 0.72807 |
| 0.97851 | 0.81743 |
| 0.98670 | 0.90787 |
| 0.99177 | 1.00000 |

*Fig. 6-17: Uniaxial tensile damage variable*

### *e) Other Parameters*

Besides the parameter presented in the previous subsections, the Concrete Damaged Plasticity requires some other parameters, including the dilation angle (ψ) measured in the $\bar{p} - \bar{q}$ space (Fig. 6-13), flow potential eccentricity (ϵ), stress ratio $f_{b0}/f_{c0}$, ratio between the second invariant stresses on the tensile and compressive meridians (K), and viscosity parameter (μ). The dilation angle is used to simulate the dilatance of concrete after cracking. For normal concrete this angle, which is measured in the principle effective stress space (Haigh-Wstergaard space[140]) is often taken between 13 degrees[141, 142] and 19 degrees[101, 138]. In the $\bar{p} - \bar{q}$ space, these values correspond to 26 degrees and 36 degrees, respectively. In this study, $\psi$ was set to 30 degrees. The flow potential eccentricity (ϵ) is used to define the rate at which the flow potential approaches its asymptote (Fig. 6-13 and Fig. D-4), and it was set at the default value of 0.1. The ratio of intial equibiaxial compressive yield stress ($f_{b0}$) to initial uniaxial compressive yield stress[143] ($f_{c0} = 0.4f_c'$, see Fig. 6-15a) was set as 1.16. The last parameter is the viscosity $\mu$,

which is used to define a visco-plastic regularization (a generalization of the Duvaut-Lions regularization) of the concrete consititutive equations. If the viscosity parameter is set to a non-zero possitive value, Abaqus permits stresses to be outside of the yield surface (Fig. D-5). Using this technique with a small value of the viscosity parameter (less than 15 percent of a time step[101]) helps improve the rate of convergence of the model in the softening regime without compromising results. The values used in this study for the parameters discussed in this subsection are given in Table 6-2.

*Table 6-2— Plasticity parameters for concrete*

| Dilation Angle ($\psi$) | Flow Potential Eccentricity ($\epsilon$) | Stress Ratio ($f_{b0}/f_{c0}$) | Yield surface shape factor $K_c$ | Viscosity Parameter ($\mu$) |
|---|---|---|---|---|
| **30 degrees** | **0.1** | **1.16** | **0.667** | **0 to 15% of time step** |

### *6.2.6.2 Flexural Reinforcement*

Trilinear stress-strain relationships were used for the slab flexural reinforcement elements, and these relationships are represented by the dashed and bold lines in Fig. 6-18. The thin lines in the figure represent the measured stress-strain curves. Fig. 6-18 (a) presents the stress-strain relationship for the #5 and #6 bars (tension bars) and Fig. 6-18 (b) presents the stress-strain relationship for the #4 bars (compression bars).

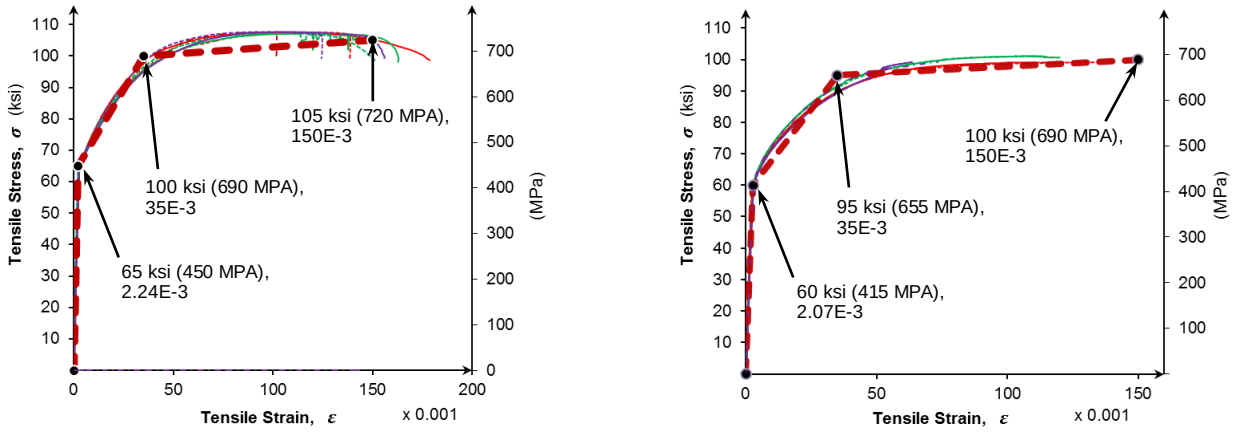


a) For #5 and #6 bars

b) For #4 bars

*Fig. 6-18: Uniaxial tensile stress-strain relationship of slab flexural reinforcement*

### *6.2.6.3 Headed Shear Studs*

A trilinear stress-strain relationship given in Eq. (21) was used to simulate the behavior of shear stud elements. This relation and the measured stress-strain curves are plotted in Fig. 3-17.

$$\sigma = \begin{cases} 29500\varepsilon & if\ 0 \le \varepsilon < 0.0024 \\ 70.8 + 200(\varepsilon - 0.0024) & if\ 0.0024 \le \varepsilon < 0.0384 \\ 78.0 - 150(\varepsilon - 0.0384) & if\ \varepsilon \ge 0.0384 \end{cases} \quad (ksi) \qquad (21)$$

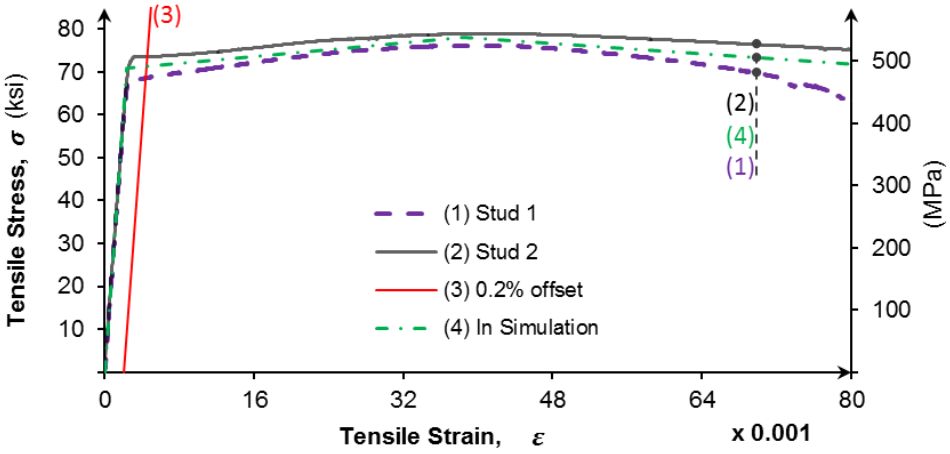


*Fig. 3-17: Uniaxial tensile stress-srain relationship of shear studs (20 mm gages)*

## 6.2.7 Modified Riks Method

In this study, the Modified Riks Method[19] was used to solve the nonlinear set of equations. The method uses the arc-length method[144] to measure the progress of the solution. These methods are effective for simulating unstable, geometrically nonlinear collapses of a structure.

## 6.3 MESH CONVERGENCE AND SENSITIVITY ANALYSES

Mesh convergence and sensitivity analyses were conducted to determine a suitable size of the finite concrete elements in the model and the effects of changes in various parameters including the concrete compressive and tensile strengths, dilation angle, and fracture enegy on the simulation results. For these studies, the finite element model described in the previous section was used to simulate a reinforced concrete slab-column connection, Specimen S1, tested by Birkle[129]. Information about Specmen S1 is given in Table 6-3. In the following subsections, results from the mesh convergence and sensitivity analyses are presented.

*Table 6-3—Speciemn S1[129] information*

| Parameter | Measured value |
|---|---|
| Slab dimensions | 6.5 ft (2000 mm) wide and 6.3 in. (160 mm) thick |
| Column dimensions | 250x250 $in^2$ (250x250 $mm^2$) |
| Shear reinforcement | No |
| Slab flexural reinforcement | #5 ($\phi$16 mm) @ 4.7 in. (120mm) |
| Flexural effective depth | 4.9 in. (124 mm) |
| Concrete compressive strength | 5250 psi (36.2 MPa), measured on test date |
| Flexural bar yield strength | 70.8 ksi (488 MPa) |

### 6.3.1 Mesh Convergence Analyses

For mesh convergence analyses, the size of the concrete cube elements varied from 0.5 in. to 3 in. (13 to 76 mm), and thus total number of the concrete elements decreased from 85722 to 402. The values of other parameters assumed for these analyses are given in Table 6-4.

*Table 6-4— Parameters for concrete in the mesh convergence analyses*

| Parameter | Assumed value |
|---|---|
| Dilation Angle ($\psi$) | 30 degrees |
| Concrete tensile strength ($f_t$) | $6.5\sqrt{f'_c}$ psi ($0.54\sqrt{f'_c}$ MPa) |
| Fracture energy ($G_f$) | 0.57 lbf/in. (100 N/m) |
| Flow Potential Eccentricity ($\epsilon$) | 0.1 |
| Stress Ratio ($f_{b0}/f_{c0}$) | 1.16 |
| Yield surface shape factor $K_c$ | 0.667 |
| Viscosity Parameter ($\mu$) | 0 |

Results from the convergence analyses are shown in Fig. 6-19. The load versus column displacement relationships for different sizes of the concrete elements (Fig. 6-19a) are very similar, except for the maximum displacement capacity. Calculated displacements corresponding to the maximum loads reduce approximately from 0.7 to 0.5 (17 to 13 mm) as the concrete element sizes decrease from 3 in. to 1.5 in. (38 to 76 mm), and then the calculated displacements increase as the element sizes decrease to 1 in. (25.4 mm). The maximum calculated load carrying capacity for each size of concrete elements is ploted versus the number of concrete elements in Fig. 6-19 (b). This figure shows the convergence of the calculated maximum load as the number of concrete elements increases. Fig. 6-19 (c), however, shows that as the number of the concrete

elements increase, the computational time (system time) used for the simulation increases. Based on these results, a concrete element size of 1 in. (25.4 mm) was selected because it provides a good simulation results and requires a reasonable computational time.

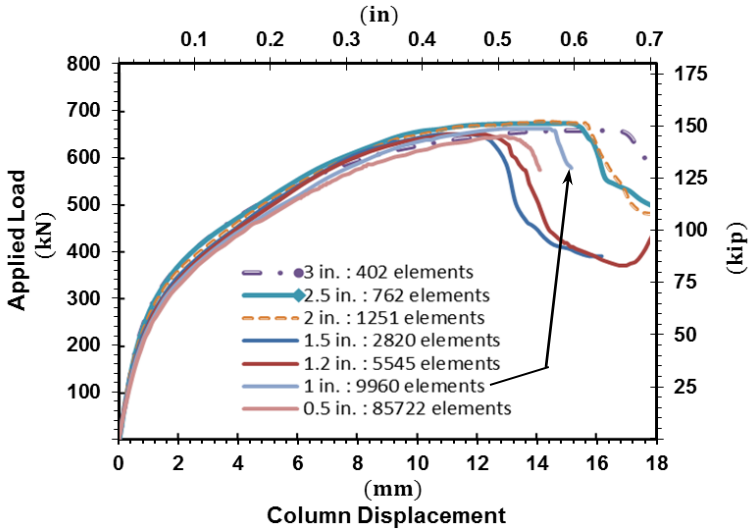


a) Load – displacement relationships

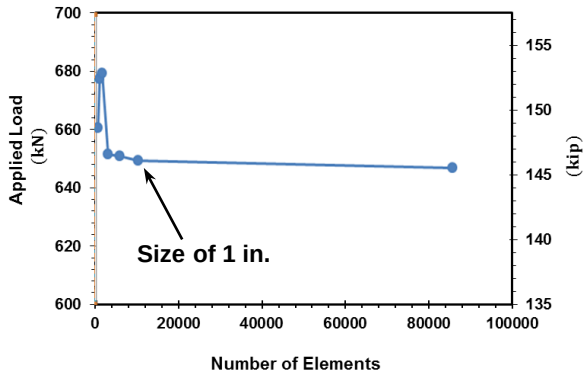


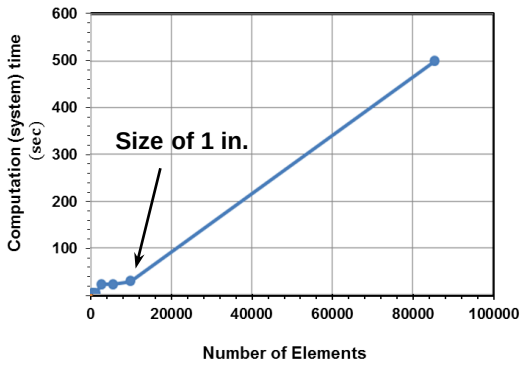


b) Strength vs. n.of concrete elements c) Computational time vs. n.of concrete elements

*Fig. 6-19: Mesh convergence analysis results*

### 6.3.2 Sensitivity Analyses

Sensitivity analyses were conducted to study the effects of changes in various parameters on the simulation of slab-column connections using the developed F.E. model. Using the concrete element size of 1 in. (25.4 mm), results from the sensitivity analyses showed that the concrete compressive and tensile strengths, dilation angle, and fracture enegy had significant effects on the simulation. Fig. 6-20 (a) shows that a decrease in the concrete compressive strength reduces

the calculated cracking and maximum loads. Fig. 6-20 (b), on the other hand, shows that an increase in the concrete compressive strength increases the cracking load, but reduce the maximum load capacity. Fig. 6-20 (c) and (d) present the effects of the dilation angle of concrete and the fractural energy. It can be seen that as the dilation angle increases from 20 degrees to 50 degrees or the fractural engery increases from 0.28 to 2.3 lbf/in. (50 to 400 N/m), the post cracking stiffness and maximum load carrying capacity both significantly increase.

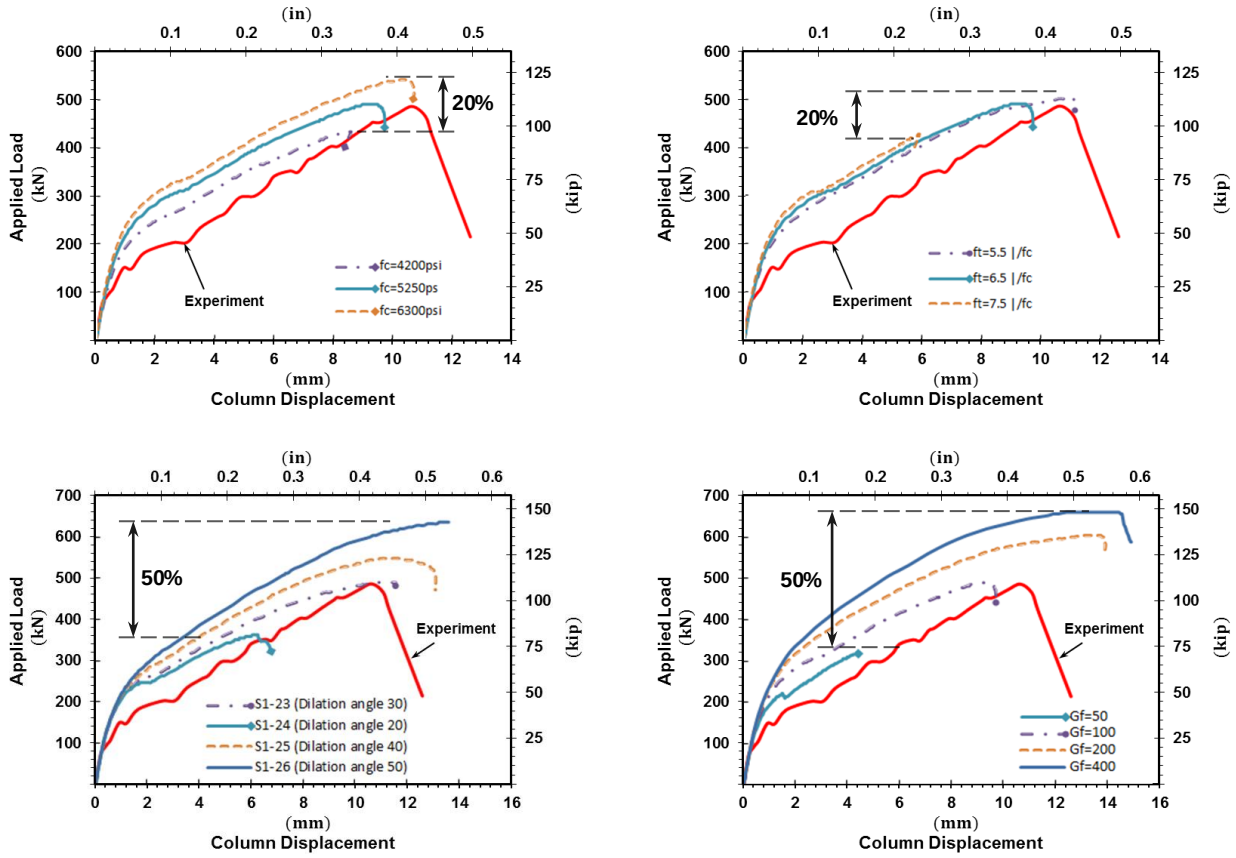


*Fig. 6-20: Sensitivity analysis results*

The measured load-dipsalcement for Specimen S1[129] is also shown in Fig. 6-20 (a) to (d), and the results from the sensitivity analyses were used to calibrate the parameters of the F.E. model for Specimen S1. The calibrated parameters are given in Table 6-5 and the corresponding simulation results are shown in Fig. 6-21. The results in Fig. 6-21 show that although the calculated cracking load was higher than the measured value, the F.E. model was able to reproduce the measured shear strength and displacement capacity of the slab-column connection.

*Table 6-5— Calibrated parameters the F.E. model*

| Parameter | Assumed value |
|---|---|
| Dilation Angle ($\psi$) | 30 degrees |
| Concrete compressive strength ($f'_c$) | measured from the Lab |
| Concrete tensile strength ($f_t$) | $6.5\sqrt{f'_c}$ or measured from the Lab |
| Fracture energy ($G_f$) | Eq. (51): 0.57 lbf/in. (100 N/m) |
| Flow Potential Eccentricity ($\epsilon$) | 0.1 (default in Abaqus) |
| Stress Ratio ($f_{b0}/f_{c0}$) | 1.16 (default in Abaqus) |
| Yield surface shape factor $K_c$ | 0.667 (default in Abaqus) |
| Viscosity Parameter ($\mu$) | 0 (default in Abaqus) |

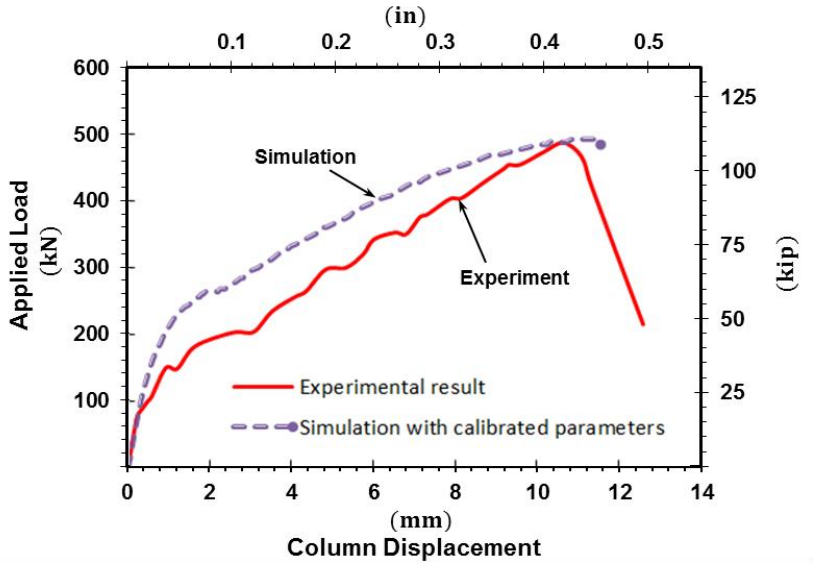


*Fig. 6-21: Experimental and caculated results for Specimen S1*[129]

## 6.4 SIMULATION RESULTS FOR THE TEST SPECIMENS

This section presents results from simulations of the test results described in Chapters 3 and 4 using the F.E. model developed in previous sections. Simulation results for Specimen S08C, without shear reinforcement, are presented in Subsection 6.4.1, results for Specimens S08O and S12O, with shear studs arranged in an orthogonal layout, are presented in Subsection 6.4.2, and results for Specimens S08R and S12R, with shear studs arranged in a radial layout, are presented in Subsection 6.4.3.

### 6.4.1 Specimen without Shear Reinforcement, S08C

#### *6.4.1.1 F.E. Model Information*

Based on the resuts from the mesh convergence study presented in Subsection 6.3.1, the concrete elements used for the model of Sepcimen S08C were 1 in.× 1 in.× 1 in. cubes (25.4×25.4× 25.4 $mm^3$). The maximum length of the slab flexural reinforcing bars was set equal to 0.5 in. (13 mm) to ensure each concrete cube crossed by reinforcing bars contained at least one node of the reinforcement elements. The parameter values used in the simulation of Specimen S08C are given in Table 6-6. The concrete strengths and yield strength of the slab reinforcement were equal to the corresponding measured values presented in Section 3.4. Other parameters were taken based on the calibrated values presented in Subsection 6.3.2.

*Table 6-6—Parameters for simulation of Specimen S08C*

| Parameter | Value |
|---|---|
| Concrete compressive strength ($f'_c$) | 6100 psi (42.1 MPa) |
| Concrete tensile strength ($f_t$) | 505 psi (3.48 MPa) |
| Fracture energy ($G_f$) | 0.73 lbf/in. (130 N/m) from Eq. (51) |
| Flow Potential Eccentricity ($\epsilon$) | 0.1 (default in Abaqus) |
| Stress Ratio ($f_{b0}/f_{c0}$) | 1.16 (default in Abaqus) |
| Yield surface shape factor $K_c$ | 0.667 (default in Abaqus) |
| Viscosity Parameter ($\mu$) | 0 (default in Abaqus) |
| Dilation Angle ($\psi$) | 30 degrees |
| Shear reinforcement | No |
| Slab flexural tension reinforcement | #5 ($\phi$16 mm) @ 4-1/8 in. (105 mm) |
| Flexural effective depth | 8-5/8 in. (220 mm) |
| Flexural bar yield strength (#5) | 66.5 ksi (460 MPa) |
| Slab flexural compression reinforcement | #4 ($\phi$13 mm) @ 6.5 in. (165 mm) |
| Flexural bar yield strength (#4) | 60 ksi (415 MPa) |

#### *6.4.1.2 Load-Displacement Behavior*

Load vesus displacement relationships from the test and simulation for Specimen S08C are represented by the solid and dashed lines in Fig. 6-22, respectively. As the applied load increased to approximately 50 k (220 kN), the stiffness of the model is slightly higher than the measured stiffness from the test. This difference may have been partially caused by the use of an

equivalent linear elasticity assumption for neoprene pads at the supports (Subsection 6.2.4). The calculated specimen stiffness starts to decrease significantly, due to concrete cracking, at an applied load of approximately 100 k (445 kN), which is approximate two times higher than the measured cracking load from the test. After cracking, the calculated stiffness was slightly lower than the measured value, and the maximum applied load given by the F.E. model is 220 k (980 kN), which is approximately 5% lower than the measured strength of Specimen S08C. The corresponding calculated column displacement was 0.51 in. (13 mm), which is lower than the measured value of approximately 0.61 in. (15 mm). The diffences in cracking and maximum loads, and displacement at failure may have been caused by variations in concrete material properties, particularly the concrete compressive and tensile strengths, and the fracture energy.

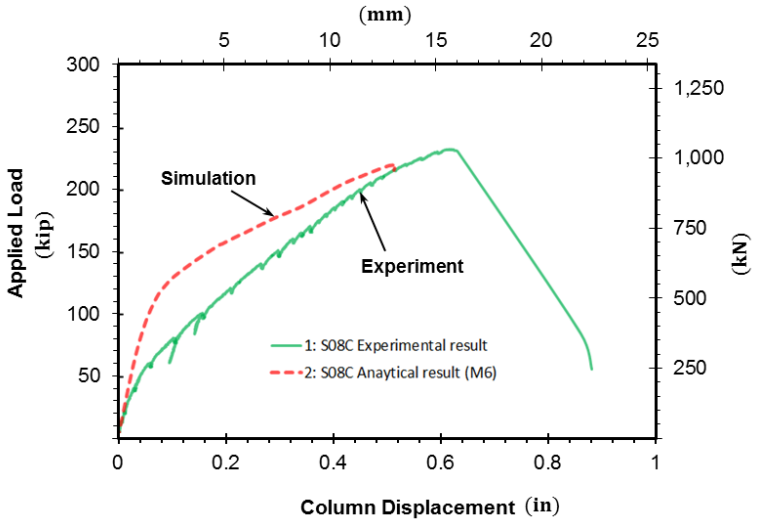


*Fig. 6-22: Experiment and simulation load-displacement results*

### *6.4.1.3 Flexural Cracks*

For the Concrete Damage Plasticity model, directions of cracks at an integration point are not computed, and thus crack development is often studied through the evolution of the tensile damage variable (Damaget) and/or maximum principle plastic strain (PE: Max. Principle)[19, 99, 110, 111]. In this study, the development of flexural cracks in the F.E. model of Specimen S08C is studied using the tensile damage variable and the results for different loads are shown in Fig. 6-23. The first flexural crack (circumferential crack) was found to form around the column periphery at a load of approximately 65 k (290 kN) (Fig. 6-23a). The first radial cracks formed perpendicular to the column faces and propagated toward the edge of the slab as the applied load

reached approximately 100 k (440 kN), as shown in Fig. 6-23 (b). At this load the neutral axis was near the mid-depth of the slab (side view in Fig. 6-23 (b)). As shown in Fig. 6-23 (c), the second circumpherential crack formed at a load of approximately 130 k (580 kN). The development of flexural cracks in the F.E. model of Specimen S08C is similar to the actual observations on flexural cracks discussed in Subsection 4.4.1. A comparison between the final flexural crack patterns from the simulation and the test are shown in Fig. 6-24. It can be seen that these two crack patterns were very similar.

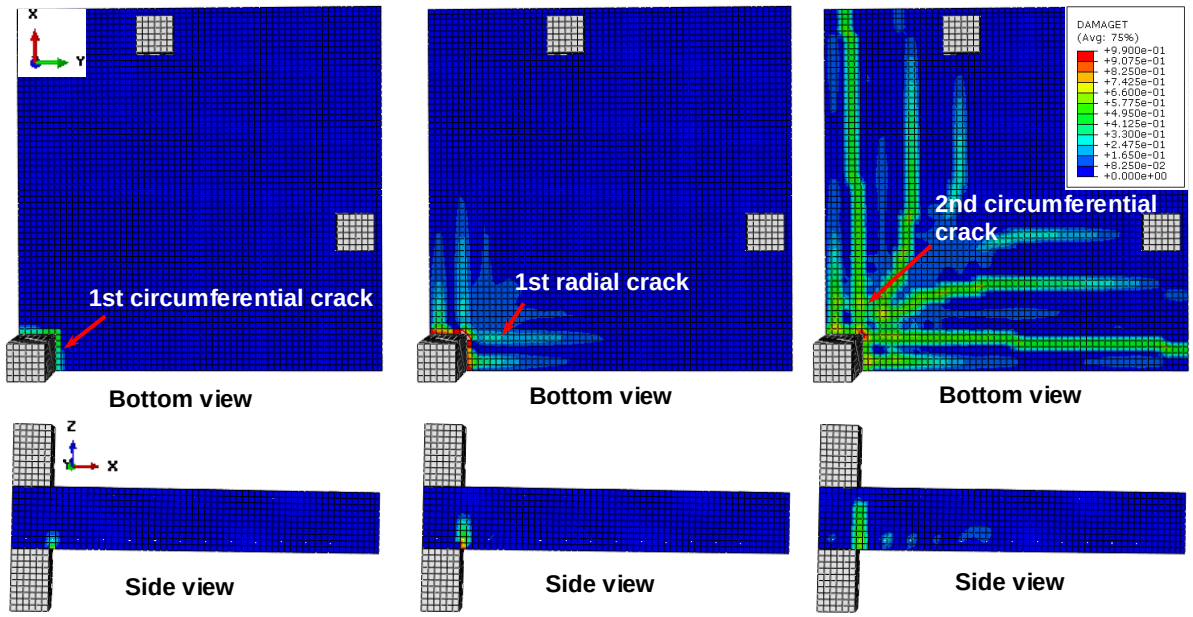


a) Near 65 k (290 kN) b) Near 100 k (440 kN) c) Near 130 k (580 kN)

*Fig. 6-23: Flexural crack development for the Specimen S08C simulation*

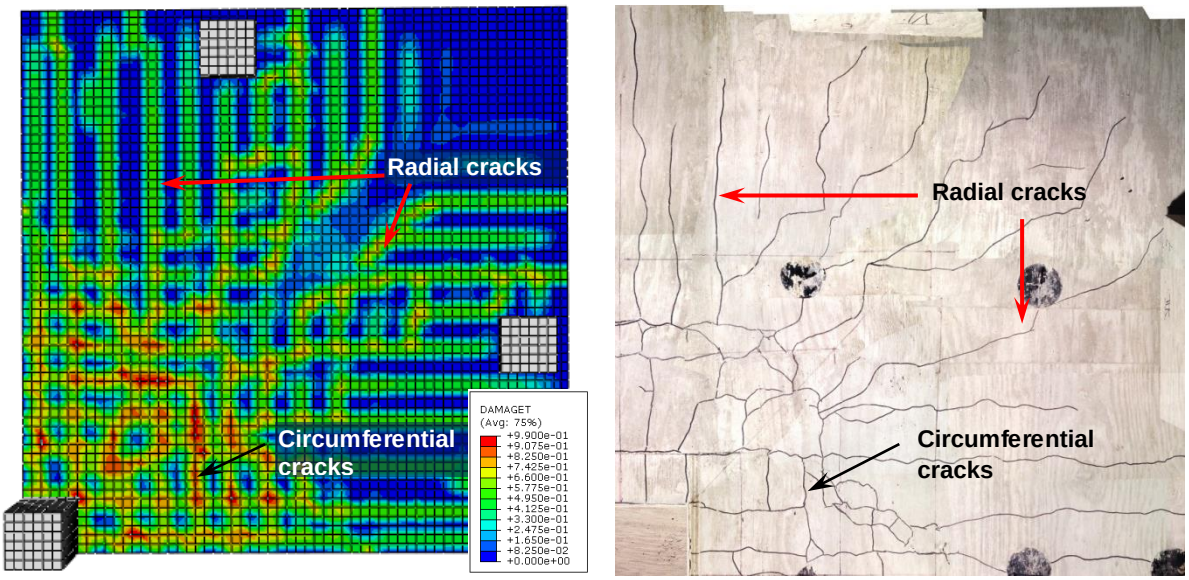


a) Simulation results b) Test results (Fig. B-1)

*Fig. 6-24: Test and simulation flexural crack patterns at failure for Specimen S08C*

#### *6.4.1.4 Shear Cracks and Failure Surfaces*

Studying the evolution of the damage variable (DAMAGET), inclined cracks were found to form at approximately $d/2$ from the column periphery when an applied load reached apprioximately 150 k (670 kN). At this load state, the tensile damage variable (Damaget) computed on two vertical sections are shown in Fig. 6-25. These two sections both cross the center of the column, but one section (Fig. 6-25a) extends perpendicular to the column face while the other section (Fig. 6-25b) extends along the diagonal direction toward the corner of the slab. Results presented in Fig. 6-25 indicate that the inclined cracks may have extended from the tips of the second set of circumferential cracks, located at approximate $d/2$ from the column, toward the top column. These results also show that the concrete near the coner of the column (Fig. 6-25b) was more damaged (higher DAMAGET values) than the concrete near the mid-sides of the column (Fig. 6-25a), indicating a high concentration of shear stress near the coners of the column.

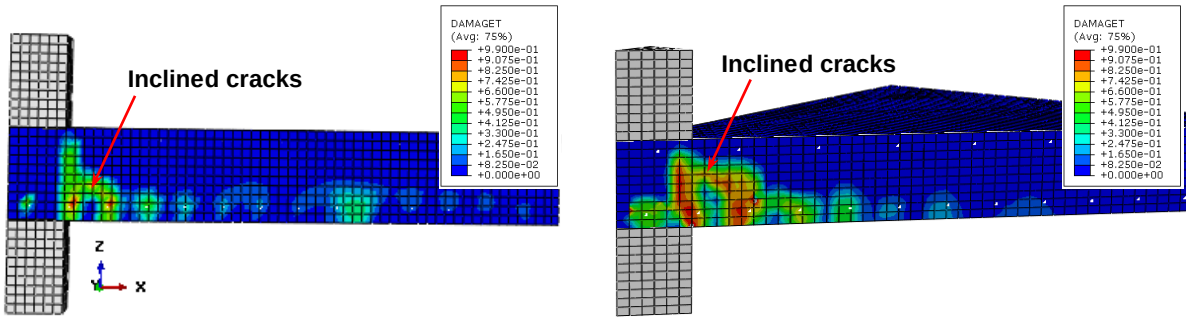


a) Section perpendicular to the column faces b) Section along a diagonal direction

*Fig. 6-25: Formation of shear cracks in the Specimen S08C model*

Failure surfaces in the Specimen S08C model and a photograph of the actual failure surface taken after the test are shown in Fig. 6-26 (a) and (b), respectively. It can be seen from Fig. 6-26 that although the simulated inclined cracks are steeper than the actual inclined cracks, the failure surfaces in the F.E. model have a similar shape to the actual failure surfaces.

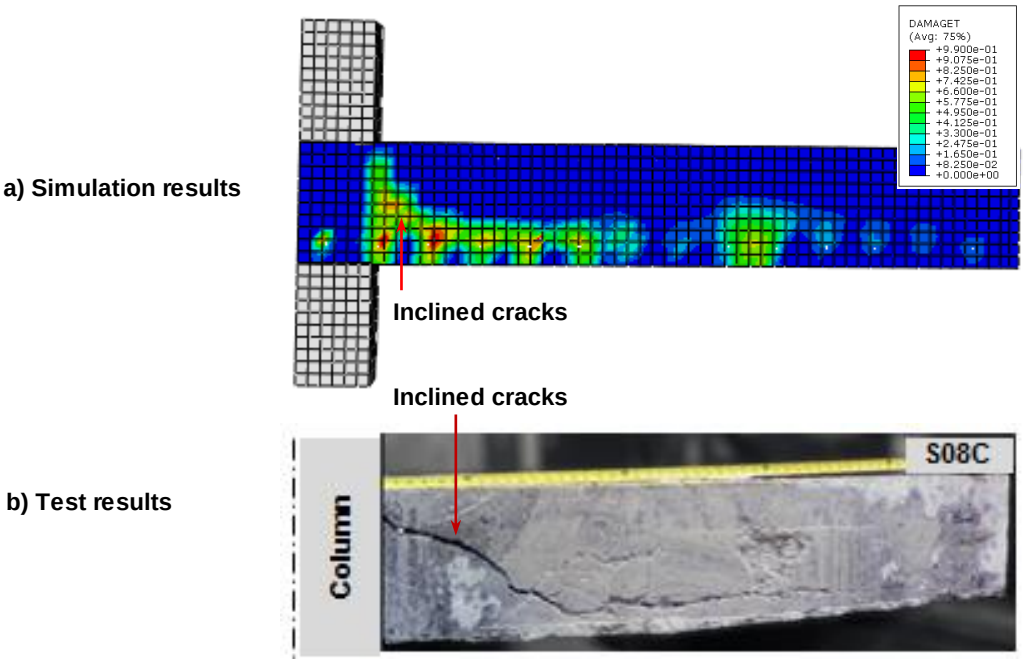


*Fig. 6-26: Shear crack patterns from the simulation (a) and test (b)*

### 6.4.2 Specimens with Shear Studs in an Orthogonal Layout, S08O and S12O

#### *6.4.2.1 F.E. Model Information*

As previously discussed, the concrete elements used for the model of Specimens S08O and S12O were 1 in.× 1 in.× 1 in. cubes (25.4×25.4× 25.4 $mm^3$). The parameter values used in the simulation for these two test specimens are given in Table 6-7. The concrete strengths and yield strength of the slab reinforcement were equal to the corresponding measured values presented in Section 3.4. Other parameters were taken based on the calibrated values presented in Subsection 6.3.2.

*Table 6-7—Parameters for simulation of Specimens with shear studs in an orthogonal layout*

| Parameter | Value (S08O / S12O) |
|---|---|
| Concrete compressive strength ($f'_c$) | 5050 psi (34.8 MPa) / 4510 psi (31.1 MPa) |
| Concrete tensile strength ($f_t$) | 476 psi (3.28 MPa) / 561 psi (3.87 MPa) |
| Fracture energy ($G_f$) | 0.57 lbf/in. (100 N/m) / 0.48 lbf/in. (85 N/m) |
| Flow Potential Eccentricity ($\epsilon$) | 0.1 (default in Abaqus) |
| Stress Ratio ($f_{bo}/f_{co}$) | 1.16 (default in Abaqus) |
| Yield surface shape factor ($K_c$) | 0.667 (default in Abaqus) |
| Viscosity Parameter ($\mu$) | 0 (default in Abaqus) |
| Dilation Angle ($\psi$) | 30 degrees |
| Shear reinforcement | 12 rails arranged in an orthogonal layout |
| Stud size and spacing | #3 @ 4-1/8 in. ($\phi$10 @ 105 mm) |
| Stud yield strength ($f_{yt}$) | 71.1 ksi (490 MPa) |
| Slab flexural tension reinforcement | #5 ($\phi$16 mm) @ 4-1/8 in. (105 mm) |
| Flexural effective depth ($d$) | 8-5/8 in. (220 mm) / 8.5 in. (115 mm) |
| Flexural bar yield strength (#5) | 66.5 ksi (460 MPa) |
| Slab flexural compression reinforcement | #4 ($\phi$13 mm) @ 6.5 in. (165 mm) |
| Flexural bar yield strength (#4) | 60 ksi (415 MPa) |

For Specimens S08O and S12O, four of the twelve stud rails used in each specimen were placed on the symmetrical planes (Fig. 6-1) that are used as boundaries for the F.E. model. Thus, the stud elements for these rails were placed near the edge of the F.E. model, and their cross section areas were set equal to a half of that of the actual studs (0.5x0.11 $in^2$ or 0.5x70 $mm^2$). Layout of shear studs in the F.E. model is shown in Fig. 6-27.

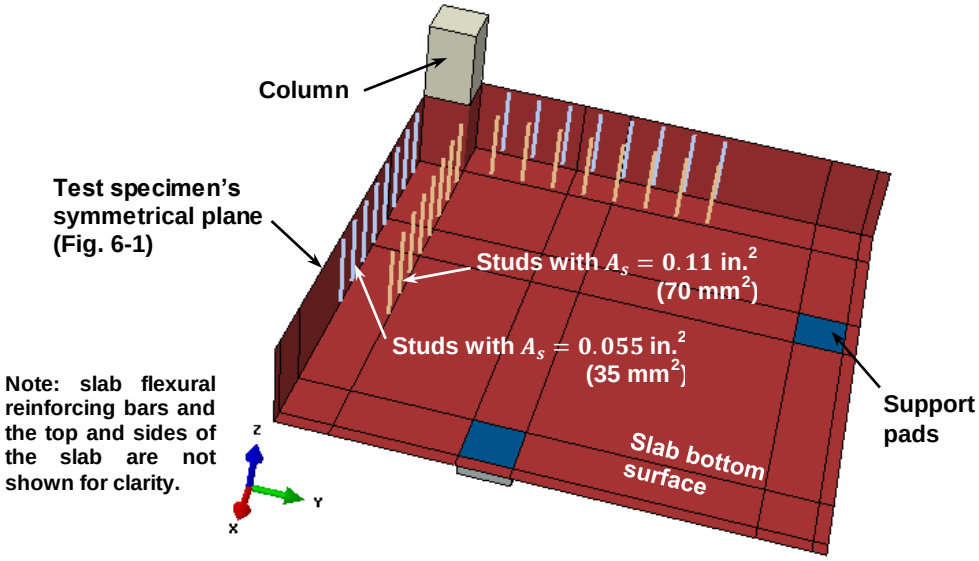


*Fig. 6-27: Simulation of shear studs in Specimens S08O and S12O*

### *6.4.2.2 Load-Displacement Behavior*

Load vesus displacement relationships from the test and the F.E. model for Specimens S08O and S12O are represented by the solid and dashed lines in Fig. 6-28, respectively. As noted in the prior section, the initial higher stiffnes of the models may have been partially caused by the use of an equivalent linear elasticity assumption for neoprene pads at the supports (Subsection 6.2.4). The calculated specimen stiffnesses started to significantly decrease, due to concrete cracking, at an applied load of approximately 100 k (445 kN). After cracking, the calculated specimen stiffness was lower than the measured value, and the maximum applied loads given by the F.E. models were 252 k (1120 kN) for Specimen S08O, approximately 10% lower than the measured strength, and 305 k (1360 kN) for Specimen S12O. The corresponding calculated column displacements were approximate 1.4 in. (35 mm) and 1.25 in. (30 mm), which are larger than the corresponding measured values. The diffences in cracking and maximum loads, post-cracking stiffness, and displacement at failure may have been caused by variations in concrete material properties, particularly the concrete compressive and tensile strengths, and the fracture energy.

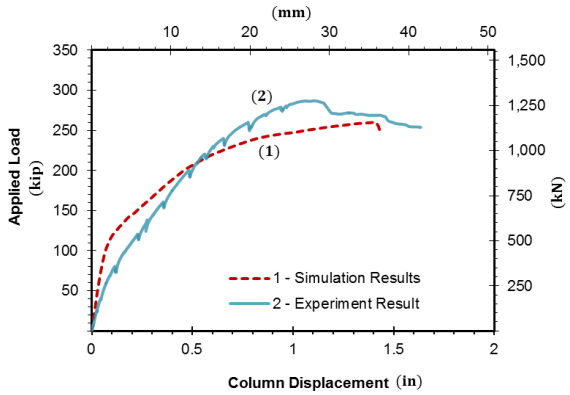


a) Specimen S08O

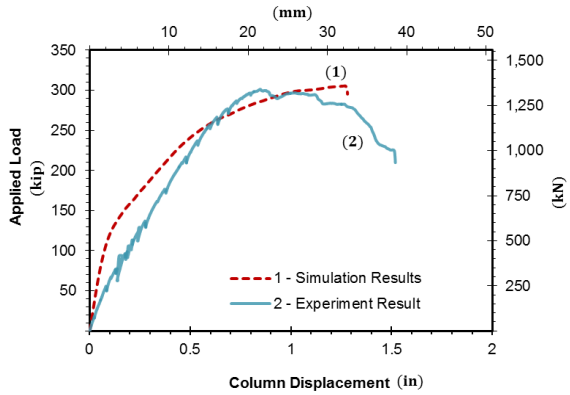


a) Specimen S12O

*Fig. 6-28: Simulation and test results for Specimens S08O and S12O*

#### *6.4.2.3 Flexural Cracks*

The development of flexural cracks on the bottom surfaces of the slabs in the F.E. model of Specimens S08O and S12O at different applied loads are shown in Fig. 6-29 and Fig. 6-30, respectively. In these figures, flexural cracks are indicated by positive values of the tensile damage variable (Damaget). The first flexural crack (circumferential crack) formed around the column perimeters at approximately 65 k (290 kN) for the two specimens, as shown in Fig. 6-29 (a) and Fig. 6-30 (b). The first radial cracks formed perpendicular to the column faces and propagated toward the edge of the slab when the applied load reached approximately 100 k (440 kN) for Specimen S08O (Fig. 6-29b) and 115 k (510 kN) for Specimen S12O (Fig. 6-30b). The second circumferential cracks formed at approximately a half of a slab depth from the column faces, at applied loads of approximately 130 k (580 kN) and 140 k (620 kN) for Specimens S08O and S12O, respective. The development of flexural cracks in the two specimens was similar to the observed flexural cracks discussed in Subsection 4.4.1. Flexural crack patterns at the terminations of the F.E. models for Specimens S08O and S12O are shown in Fig. 6-31 (a) and Fig. 6-32 (a), respectively, while the corresponding photographs of these specimens taken after the tests are shown in Fig. 6-31 (b) and Fig. 6-32 (b), respectively. It can be seen that the simulalated and actual crack patterns are very similar.

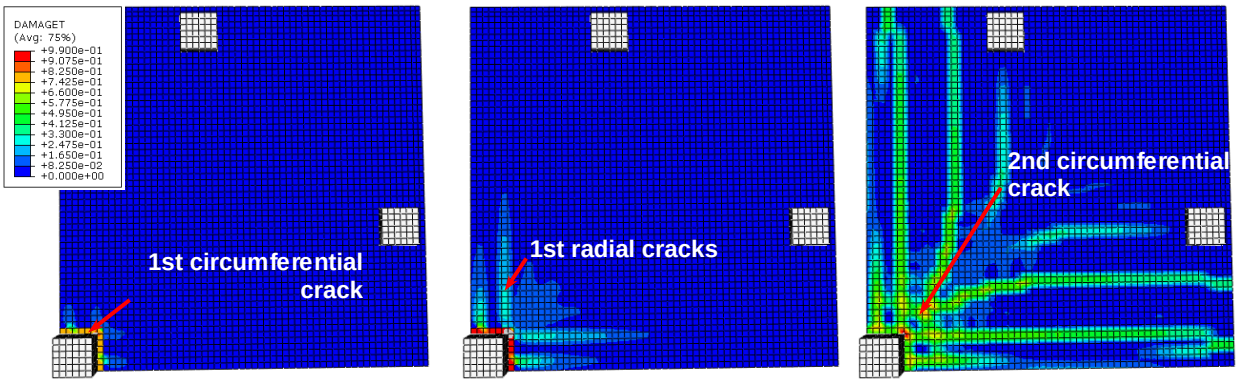


a) Near 65 k (290 kN) b) Near 100 k (440 kN) c) Near 130 k (580 kN)

*Fig. 6-29: Simulation flexural crack development for the Specimen S08O*

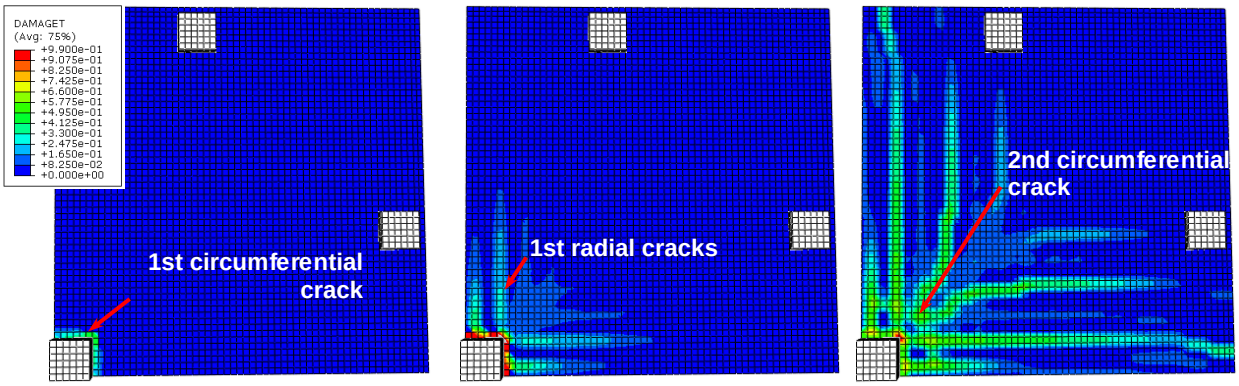


a) Near 65 k (290 kN) b) Near 115 k (510 kN) c) Near 140 k (620 kN)

*Fig. 6-30: Simulation flexural crack development for the Specimen S12O*

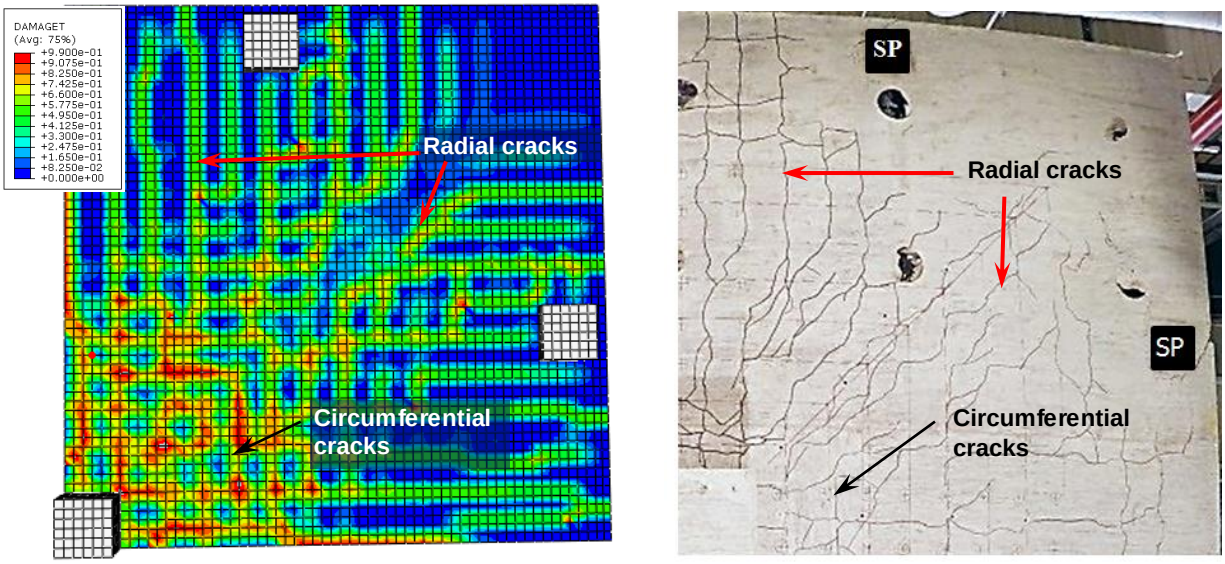


a) Simulation results b) Test results (Fig. B-6)

*Fig. 6-31: Test and simulation flexural crack patterns at failure for Specimen S08O*

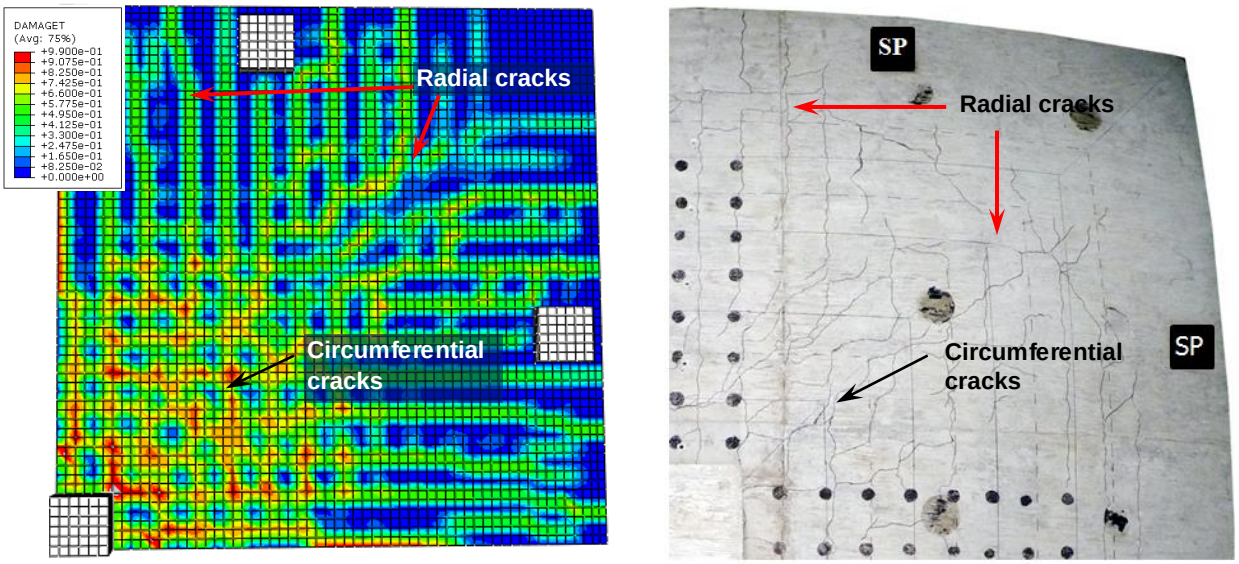


a) Simulation results b) Test results (Fig. B-16)

*Fig. 6-32: Test and simulation flexural crack patterns at failure for Specimen S12O*

#### *6.4.2.4 Shear and Splitting Cracks*

The development of shear (inclined) cracks in the F.E. models of Specimens S08O and S12O was studied using the evolution of the tensile damage variable (Damaget), and results are shown in Fig. 6-33 (a) and (b), respectively. The inclined cracks were found to form at approximately $d/2$ from the column periphery when the applied load reached apprioximately 150 k (670 kN) for Specimen S08O (Fig. 6-33a1) and 170 k (760 kN) for Specimen S12O (Fig. 6-33b1). These calculated loads are higher than the corresponding measured values from the tests (Fig. 4-11 and Fig. 4-22).

Splitting cracks were found to be initiated below the slab compression reinforcement and near the column perimeter, as shown in Fig. 6-33 (a2) and (b2), when the applied load reached approximately 210 k (930 kN) for Specimen S08O and 260 k (1060 kN) for Specimen S12O. These splitting cracks then extended horizontally away from the columns, as the applied load increased. The simulation results agree well with the discussions of splitting crack development presented in Subsection 4.5.3.

Shear and splitting crack patterns at failure (termination of the analysis) for the F.E. models for Specimens S08O and S12O are presented in Fig. 6-33 (a3) and (b3), respectively. It can be seen that the crack patterns in the F.E. models are quite similar to the corresponding actual crack

patterns from the tests, as shown in Fig. 6-33 (a4) and (b4), in terms of the location and direction of shear and splitting cracks. It can be also seen that the actual failure surfaces, which consisted of the splitting cracks and inclined cracks located beyond the outermost shear studs, were not observed in the corresponding simulation results, Fig. 6-33 (a3) and (b3). This difference between the simulated and observed test results is partially due to different load states at which those crack patterns were captured. While the actual crack patterns represent cracks at ultimate failure of the test specimens (the tests ended when the applied load dropped below 60% of the maximum load), the simulation crack patterns represent cracks when the F.E. simulation terminated (just beyond the peak load). In addition, the actual failure surfaces in Specimens S08O and S12O were shown to have formed after the peak loads (refer to Subsection 4.3.2.3), so to reproduce the actual failure surfaces the F.E. models must be able to undego post-failure progress. For implicit F.E. simulations, such as Abaqus/Standard, post-failure analyses of complex three-dimensional nonlinear problems, e.g., punching shear failure at reinforced concrete slab-column connections with shear reinforcement, are difficult to simulate.

#### *6.4.2.5 Strains in Shear Studs*

Computed strains in shear studs near the column from the F.E. models for Specimens S08O and S12O are shown as dashed lines in Fig. 6-34 (a) and (b), respectively, while the measured strains from shear studs in the first peripheral line of studs are shown as thin solid lines. It can be seen from the Fig. 6-34 that shear stud strains from the F.E. models start to increase when the applied loads reach approximately 150 k (670 kN), which is higher than the measured results. This observation agrees with the discussion of shear crack development in the previous subsection. The distribution of tensile stresses in shear studs for the F.E. model are presented in Fig. 6-35. This figure shows that the stress in studs decreased as a distance from the column increased. These simulation results are similar to the measured test results (Fig. B-8 and ).

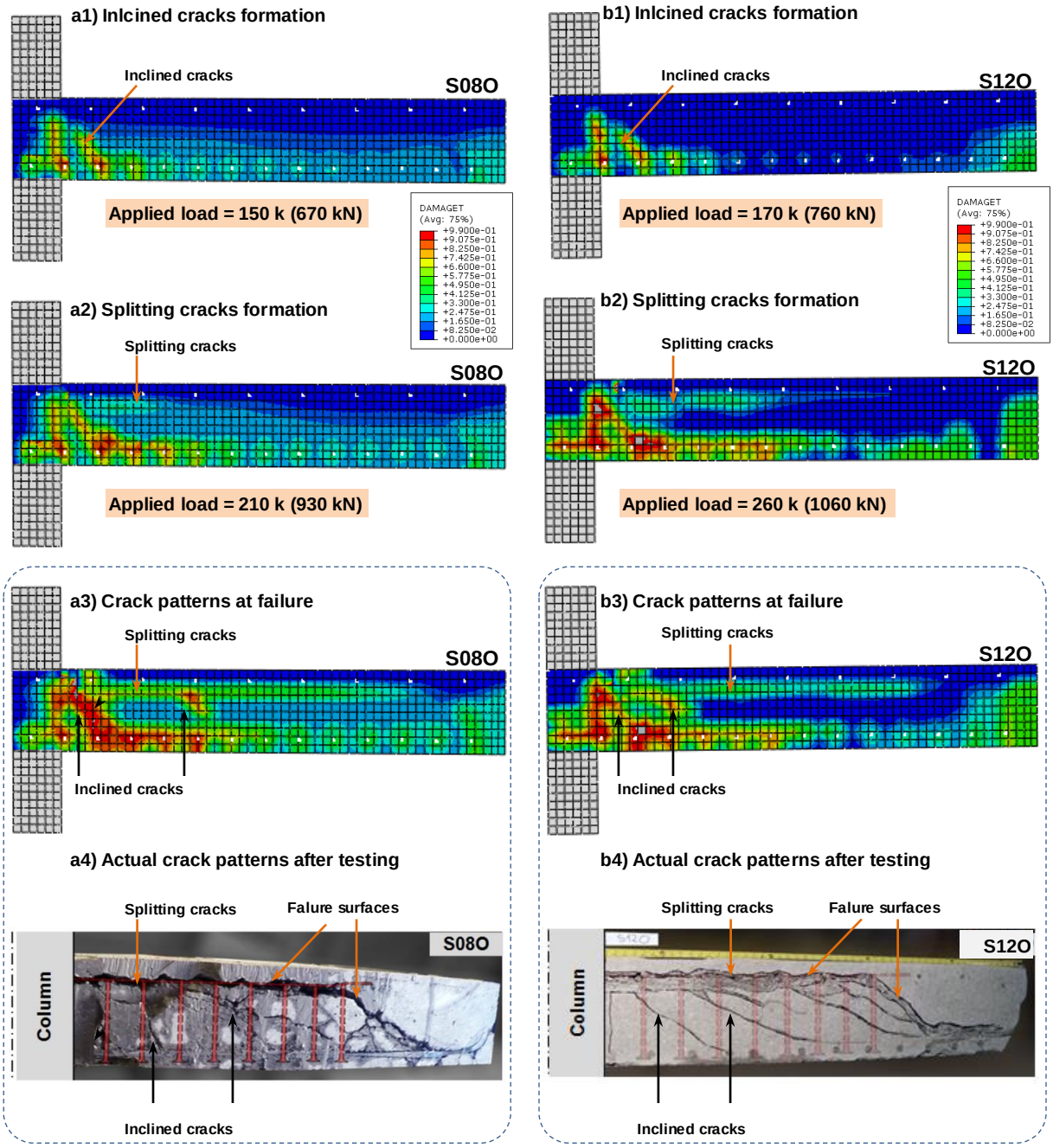


a) Specimen S08O b) Specimen S12O

*Fig. 6-33: Inclined and splitting crack development in Specimen S08O (a) and S12O (b)*

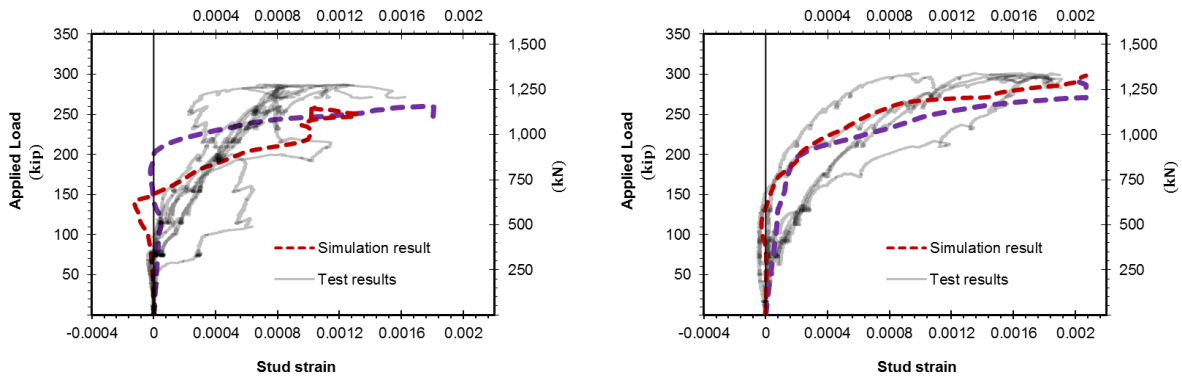


a) Specimen S08O b) Specimen S12O

*Fig. 6-34: Simulation and test results for Specimens S08O and S12O*

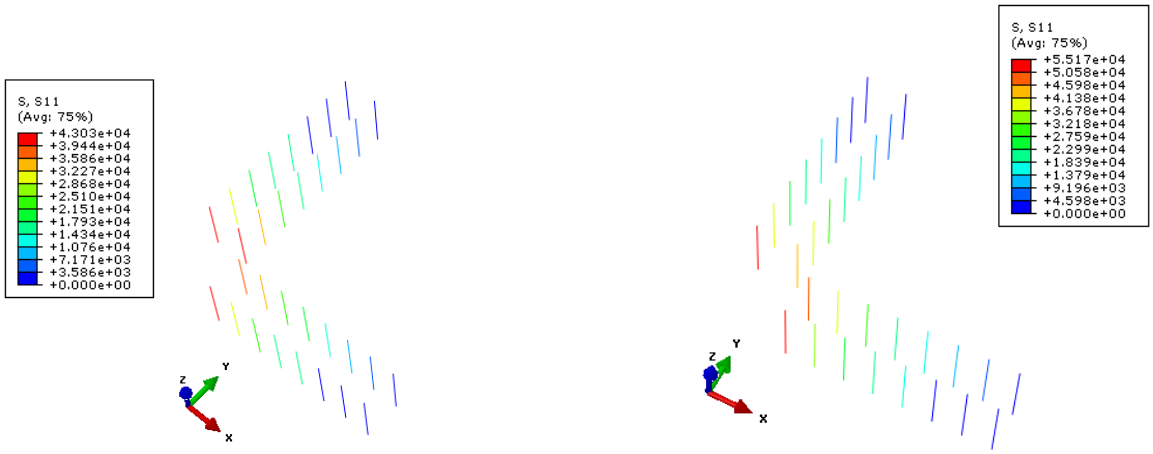


a) Specimen S08O b) Specimen S12O

*Fig. 6-35: Tensile stress in shear studs in the F.E. models of Specimen S08O and S12O*

## 6.4.3 Specimens with Shear Studs in a Radial Layout, S08R and S12R

### *6.4.3.1 F.E. Model Information*

The same mesh size and reinforcement details used for the prior models were used to simulate the behavior of Specimens S08R and S12R. The parameter values used in the simulation for these two test specimens are given in Table 6-8. The concrete strengths and yield strength of the slab reinforcement were equal to the corresponding measured values presented in Section 3.4. Other parameters were taken based on the calibrated values presented in Subsection 6.3.2. Stud elements in the F.E. models were placed as shown in Fig. 6-36 and their cross section areas were set equal to the actual value of 0.11 $in^2$ (70 $mm^2$).

*Table 6-8—Parameters for simulation of Specimens with shear studs in a radial layout*

| Parameter | Value (S08R / S12R) |
|---|---|
| Concrete compressive strength ($f'_c$) | 5360 psi (37.0 MPa) / 4790 psi (33.0 MPa) |
| Concrete tensile strength ($f_t$) | 571 psi (3.94 MPa) / 524 psi (3.61 MPa) |
| Fracture energy ($G_f$) | 0.62 lbf/in. (110 N/m) / 0.53 lbf/in. (95 N/m) |
| Flow Potential Eccentricity ($\epsilon$) | 0.1 (default in Abaqus) |
| Stress Ratio ($f_{bo}/f_{co}$) | 1.16 (default in Abaqus) |
| Yield surface shape factor ($K_c$) | 0.667 (default in Abaqus) |
| Viscosity Parameter ($\mu$) | 0.0005 / 0.0005 seconds |
| Dilation Angle ($\psi$) | 30 degrees |
| Shear reinforcement | 12 rails arranged in a radial layout |
| Stud size and spacing | #3 @ 4-1/8 in. ($\phi$10 @ 105 mm) |
| Stud yield strength ($f_{yt}$) | 71.1 ksi (490 MPa) |
| Slab flexural tension reinforcement | #5 ($\phi$16 mm) @ 4-1/8 in. (105 mm) |
| Flexural effective depth ($d$) | 8-5/8 in. (220 mm) / 8.5 in. (115 mm) |
| Flexural bar yield strength (#5) | 66.5 ksi (460 MPa) |
| Slab flexural compression reinforcement | #4 ($\phi$13 mm) @ 6.5 in. (165 mm) |
| Flexural bar yield strength (#4) | 60 ksi (415 MPa) |

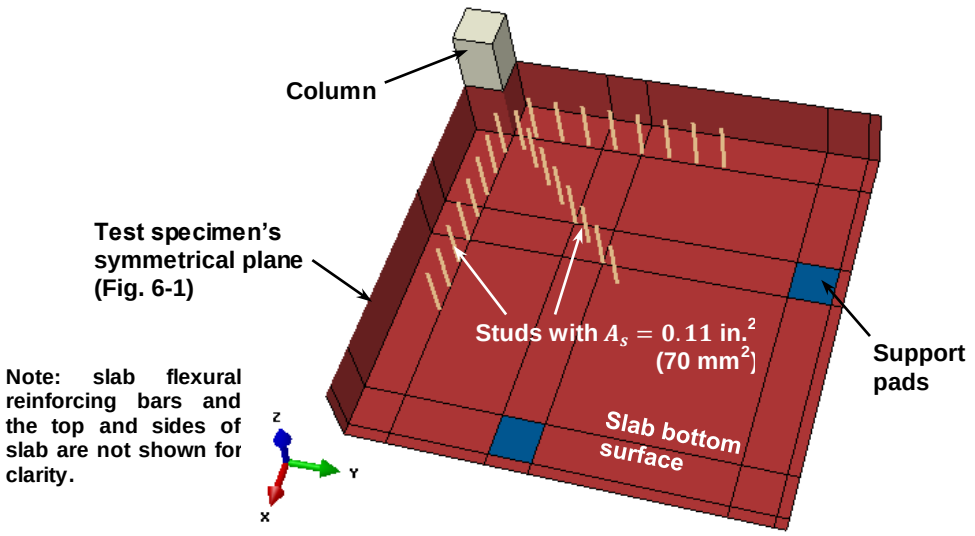


*Fig. 6-36: Simulation of shear studs for Specimens S08R and S12R*

### 6.4.3.2 *Load-Displacement Behavior*

Load vesus displacement relationships from the tests and the F.E. models for Specimens S08R and S12R are represented by the solid and dashed lines in Fig. 6-37, respectively. As the applied loads increase to approximately 130 k (580 kN), the stiffnesses of the F.E. models were higher than the measured stiffnesses from the tests. The calculated specimen stiffnesses started to decrease significantly, due to concrete cracking, as the applied loads increased. The calculated post-cracking stiffnesses from the F.E. models were lower than the measured values. The maximum applied loads given by the F.E. models were 280 k (1250 kN) for Specimen S08R, and 290 k (1290 kN) for Specimen S12R, which are approximately 10 percent smaller than the corresponding measured values (Fig. 6-37). The corresponding calculated column displacements were approximate 1.55 in. (40 mm) and 0.8 in. (20 mm), which are slightly smaller than the corresponding test results. The diffences in cracking and maximum loads, post-cracking stiffnesses, and displacement capacity may have been caused by variations in concrete material properties, particularly the concrete compressive and tensile strengths, and the fracture energy.

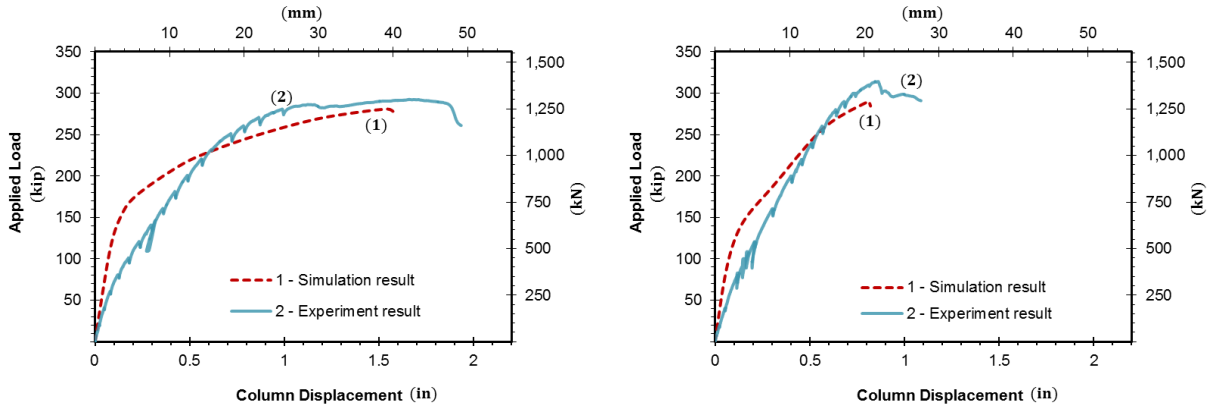


a) Specimen S08R




a) Specimen S12R

*Fig. 6-37: Simulation and test results for Specimens S08R and S12R*

### 6.4.3.3 *Flexural Cracks*

The development of flexural cracks on the bottom surfaces of the slabs in the F.E. model of Specimens S08R and S12R at different applied loads is shown in Fig. 6-38 and Fig. 6-39, respectively. In these figures, flexural cracks are indicated by positive values of the tensile damage variable (Damaget). The first flexural crack (circumferential crack) formed around the column perimeters at approximately 65 k (290 kN) for the two specimens, as shown in Fig.

6-38 (a) and Fig. 6-39 (b). The first radial cracks formed perpendicular to the column faces and propagated toward the edge of the slab when the applied load reached approximately 100 k (440 kN) for Specimen S08R (Fig. 6-38b) and 115 k (510 kN) for Specimen S12R (Fig. 6-39b). The second set of circumferential cracks formed at approximately a half of a slab depth from the column faces, as the applied loads reached approximately 140 k (620 kN) for both Specimens S08O and S12O. The development of flexural cracks in the two specimens is similar the observed flexural cracks discussed in Subsection 4.4.1.

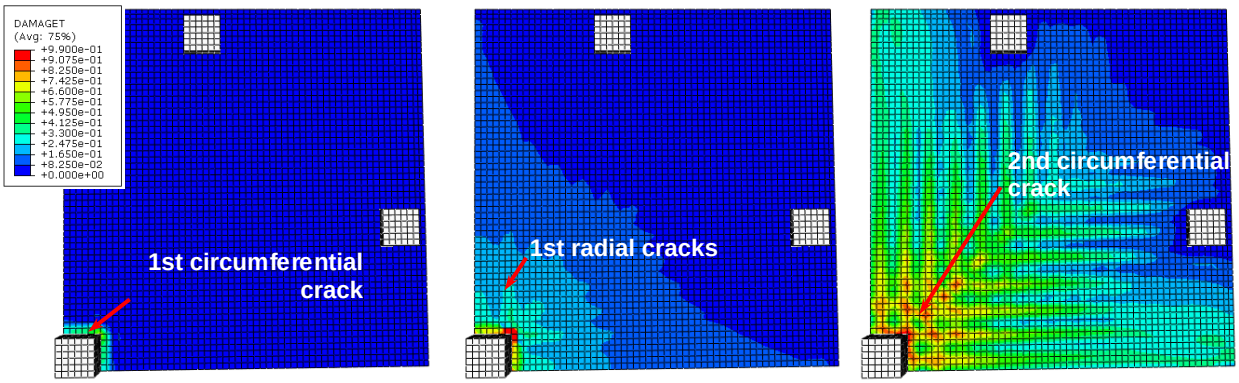


a) Near 65 k (290 kN) b) Near 100 k (440 kN) c) Near 140 k (620 kN)

*Fig. 6-38: Simulation flexural crack development for the Specimen S08R*

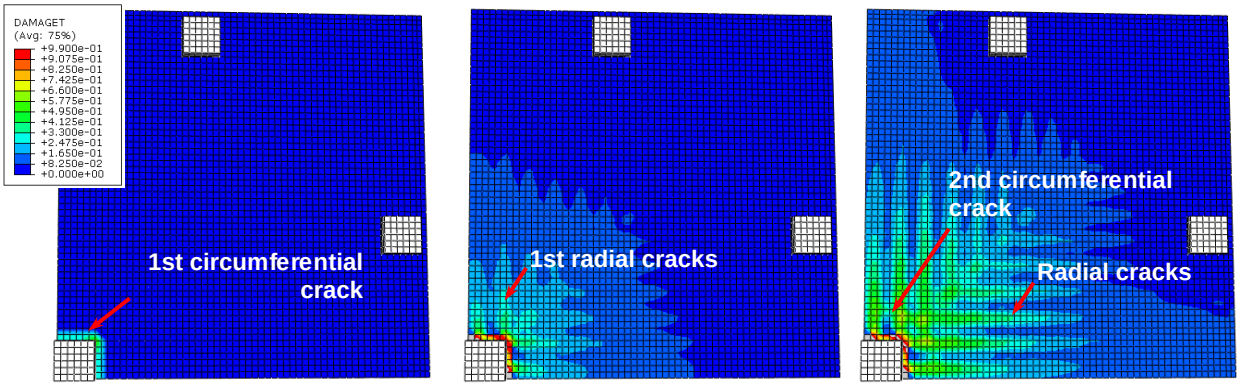


a) Near 65 k (290 kN) b) Near 115 k (510 kN) c) Near 140 k (620 kN)

*Fig. 6-39: Simulation flexural crack development for the Specimen S12R*

Crack patterns on the bottom of the slabs at the termination of the F.E. simulations for Specimens S08R and S12R are shown in Fig. 6-40 (a) and Fig. 6-41 (a), respectively, while the corresponding photographs of these specimens taken after the tests are shown in Fig. 6-40 (b) and Fig. 6-41 (b), respectively. It can be seen that region of cracking concrete near the punching cone bases shown in the photographs were also observed in the corresponding simulated results.

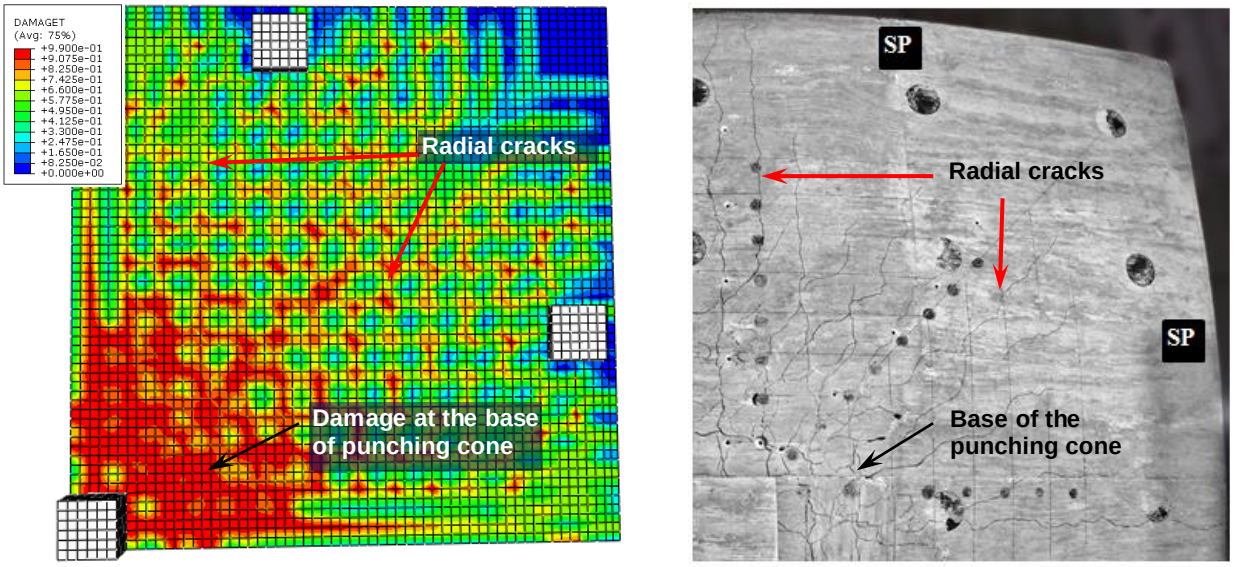


a) Simulation results b) Test results (Fig. B-11)

*Fig. 6-40: Test and simulation flexural crack patterns at failure for Specimen S08R*

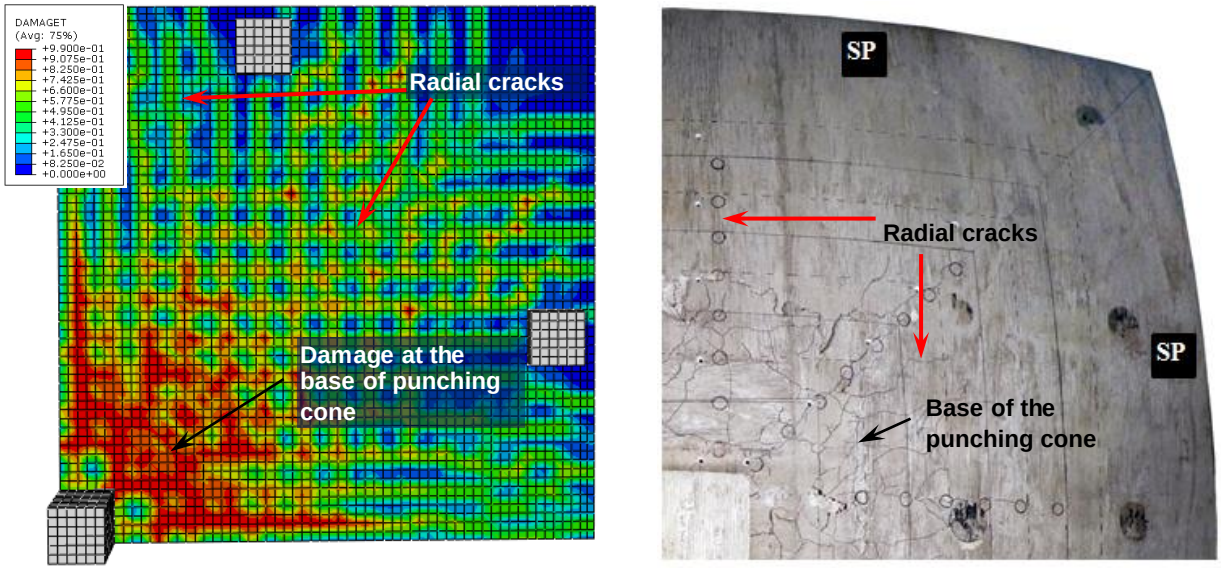


a) Simulation results b) Test results (Fig. B-20)

*Fig. 6-41: Test and simulation flexural crack patterns at failure for Specimen S12R*

### *6.4.3.4 Shear Crack Formation and Failure Surfaces*

The development of shear (inclined) cracks in the F.E. models of Specimens S08R and S12R is shown in Fig. 6-42 (a) and (b), respectively. The inclined cracks were found to form at approximately $d/2$ from the column periphery when the applied load reached apprioximately 150 k (670 kN) for Specimen S08R (Fig. 6-42a1) and 170 k (760 kN) for Specimen S12R (Fig. 6-42b1). These calculated loads are higher than the corresponding measured values from the tests (Points I in Fig. 4-17 and Fig. 4-27).

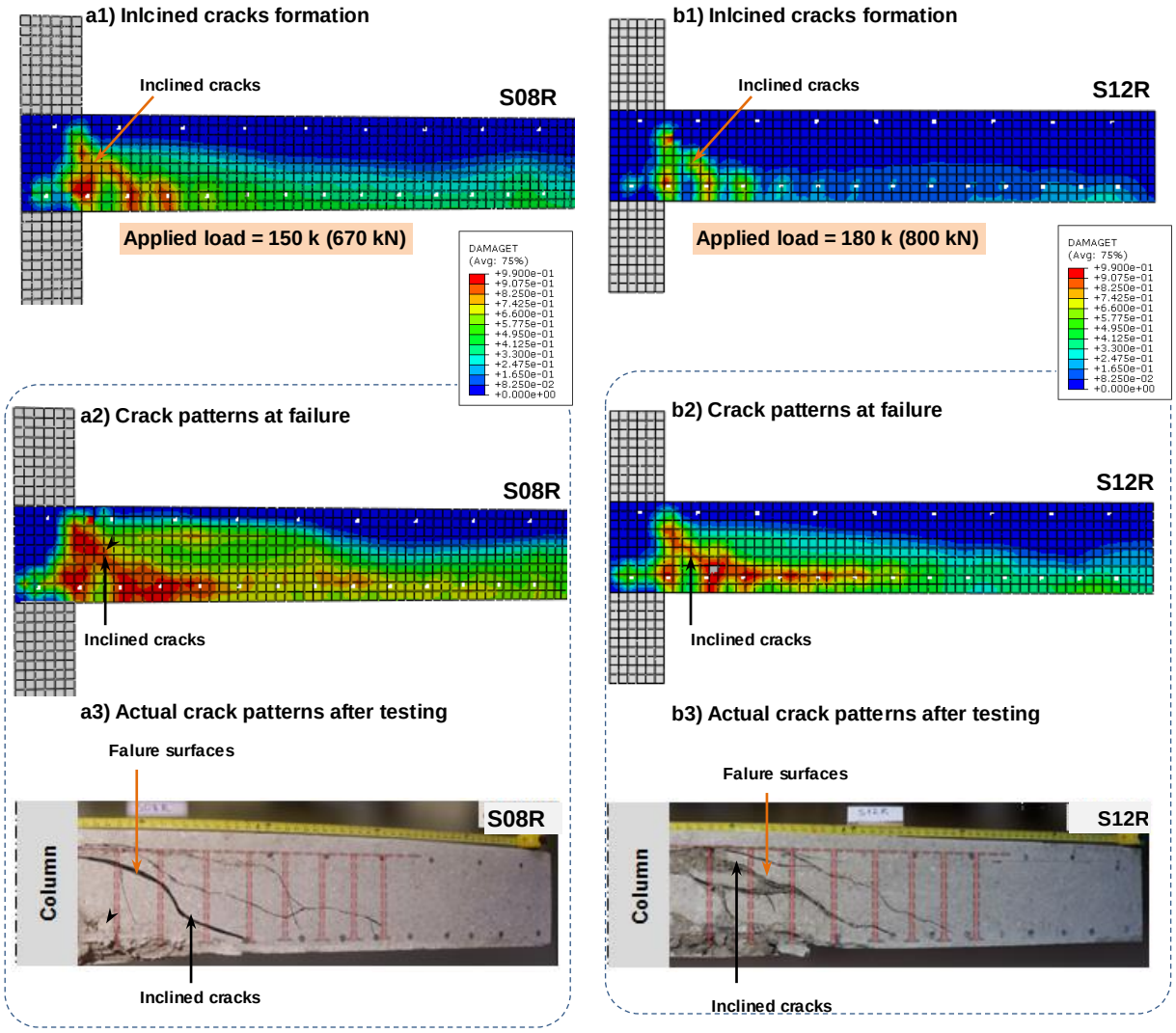


a) Specimen S08R b) Specimen S12R

*Fig. 6-42: Inclined and splitting crack development in Specimen S08R (a) and S12R (b)*

Shear crack patterns at failure (termination) of the F.E. simulations for Specimens S08R and S12R are presented in Fig. 6-42 (a2) and (b2), respectively. Unlike the F.E. models for Specimens S08O and S12O, splitting cracks, which formed below the slab compression reinforcement, were were not found in the models for the Specimens S08R and S12R. These results are consistant with the observed crack patterns after the tests for these specimens, as shown in Fig. 6-42 (a3) and (b3), respecitively. It can be seen that the observed failure surfaces, inclined cracks near the columns, were very similar to the simulated results.

### *6.4.3.5 Strains in Shear Studs*

Simulated strains in shear studs near the column from the F.E. models for Specimens S08S and S12S are shown as dashed lines in Fig. 6-43 (a) and (b), respectively, while the measured strains for some of the shear studs in the first peripheral line of studs from the columns are shown as thin solid lines. It can be seen from the Fig. 6-43 that shear stud strains from the F.E. models started to increase when the applied loads reached 150 to 200 k (670 to 890 kN), which are higher than the measured results. This observation agrees with the discussion of shear crack development in the previous subsection. The distribution of simulated tensile stresses in the shear studs for the Specimen S08R model (similar to the Specimen S12R model) is presented in Fig. 6-44. This figure shows that stress in the studs decreased as the distance from the column increased, which agrees with the measured results shown in Fig. B-13 and Fig. B-22.

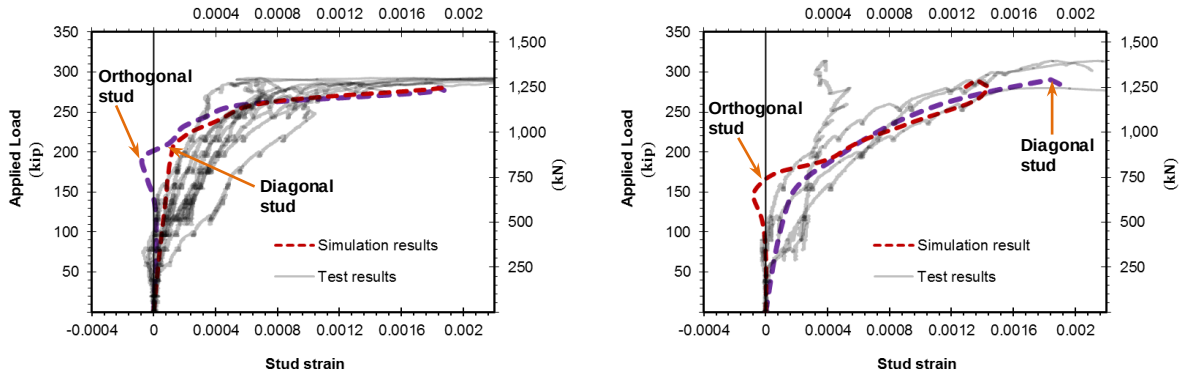


a) Specimen S08R b) Specimen S12R

*Fig. 6-43: Simulation and test results for Specimens S08R and S12R*

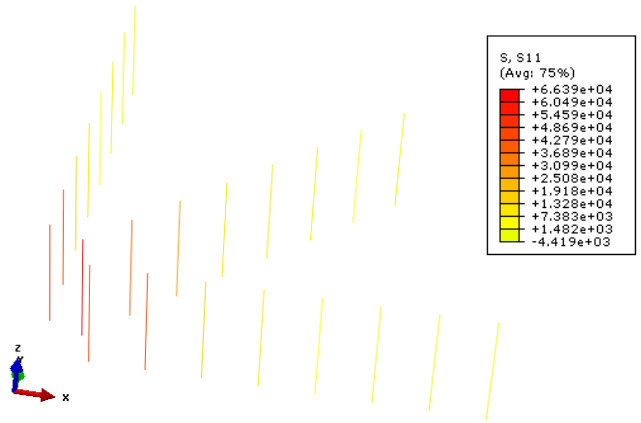


*Fig. 6-44: Tensile stress in shear studs in the Specimen S08R F.E. model*

## 6.5 EFFECTS OF SLAB FLEXURAL REINFORCEMENT RATIO AND SHEAR STUD LAYOUT

### 6.5.1 Effect of Slab Flexural Reinforcement Ratio

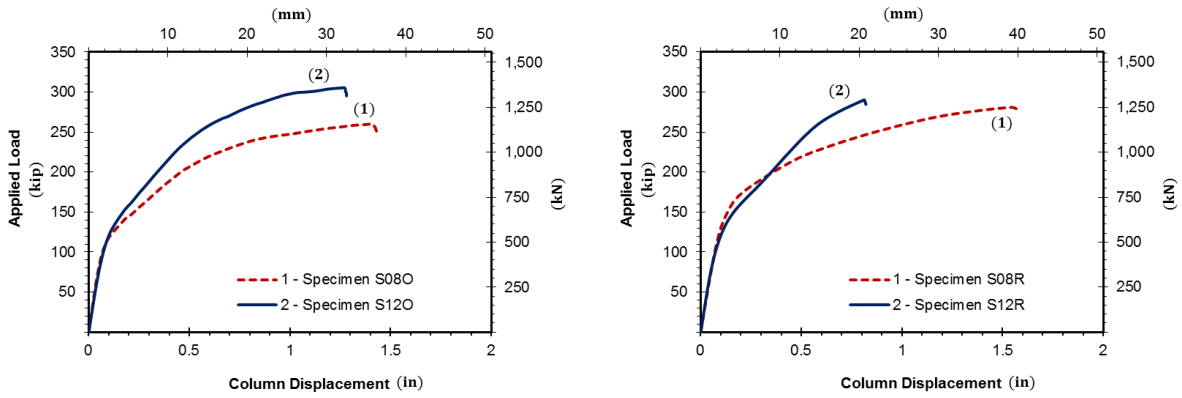


a) With an orthogonal layout of shear studs b) With a radial layout of shear studs

*Fig. 6-45: Effect of slab slab flexural tension reinforcement ratios from simulations*

Simulated load versus column displacement relationships for the test specimens reinforced with shear studs arranged in orthogonal and radial layouts are shown in Fig. 6-45 (a) and Fig. 6-45 (b), respectively. In each figure, it shows that the two specimens behaved similarly as applied loads reached approximately 120 k (530 kN). For higher loads the specimens with a higher slab reinforcement ratio of 1.2 percent (S12R and S12O) had a larger post-cracking stiffness and higher strength than the corresponding specimens with a lower reinforcement ratio of 0.8 percent (S08R and S08O). These simulated results agree well with the test results except that the cracking load for the model of SpecimenS08R was slightly higher than that for the model

of Specimen S12R, as shown in Fig. 6-45 (b). This difference in the simulated cracking loads for these two specimens may have been partially due to the higher values for concrete compressive and tensile strengths and fractural energy used in the model for Specimen S08R (Table 6-8).

### 6.5.2 Effect of Shear Stud Layout

Simulated load versus column displacement relationships for the test specimens reinforced with shear studs, which had slab reinforcement ratios of 0.8 percent and 1.2 percent, are shown in Fig. 6-46 (a) and Fig. 6-46 (b), respectively. These figures show that simulations for these specimens termintated soon after the applied loads reached the peak values, and did not include a post-peak evaluation. The termination stage for the simulations are thus assumed to correspond to a test stage when the shear-reinforced specimens experienced slight drops in their load carrying capacity (Points P1 or P in Fig. 4-11 Fig. 4-17, Fig. 4-22, and Fig. 4-27). Fig. 6-46 shows that orthogonal and radial layouts of shear studs had insignificant effects on the behavior of the test specimens up to the peak load, and this observation agrees well with the test results (Fig. 4-5).

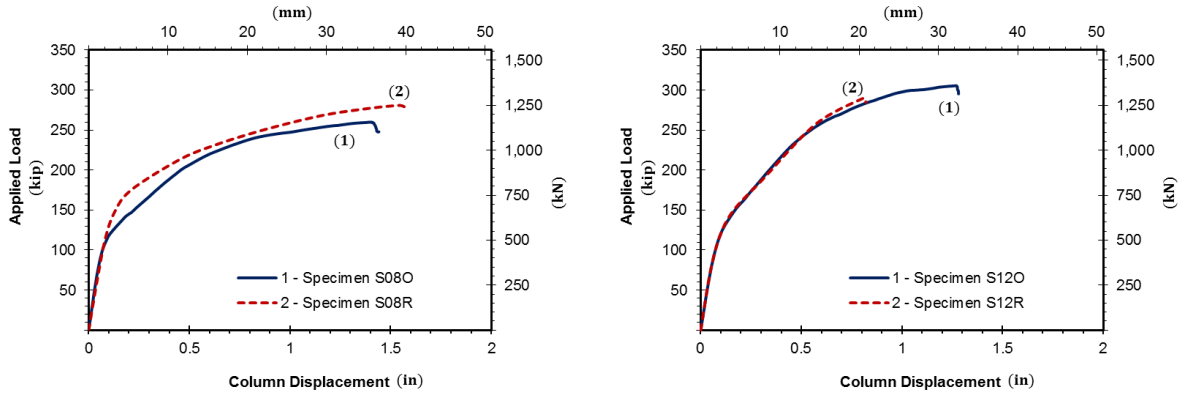


a) Speciemns with $\rho = 0.8\%$ b) Speciemns with $\rho = 1.2\%$

*Fig. 6-46: Effect of shear studs on shear strength from simulation results*

Simulated crack patterns for the test specimens reinforced with shear studs are shown in Fig. 6-47. Although the simulations did not include a post-failure evaluation (after the peak loads), Fig. 6-47 clearly shows the effect of the two different layouts of shear studs on the development of cracks in the models. A significant development of splitting cracks was observed in the F.E. models for test specimens with shear studs in an orthogonal layout (Fig. 6-47a and Fig. 6-47b). For the F.E. models of the test specimens with shear studs in a radial layout, significant splitting

cracks did not develop (Fig. 6-47c and Fig. 6-47d). These results agree very well with the observed crack patterns (Subsection 4.5.3).

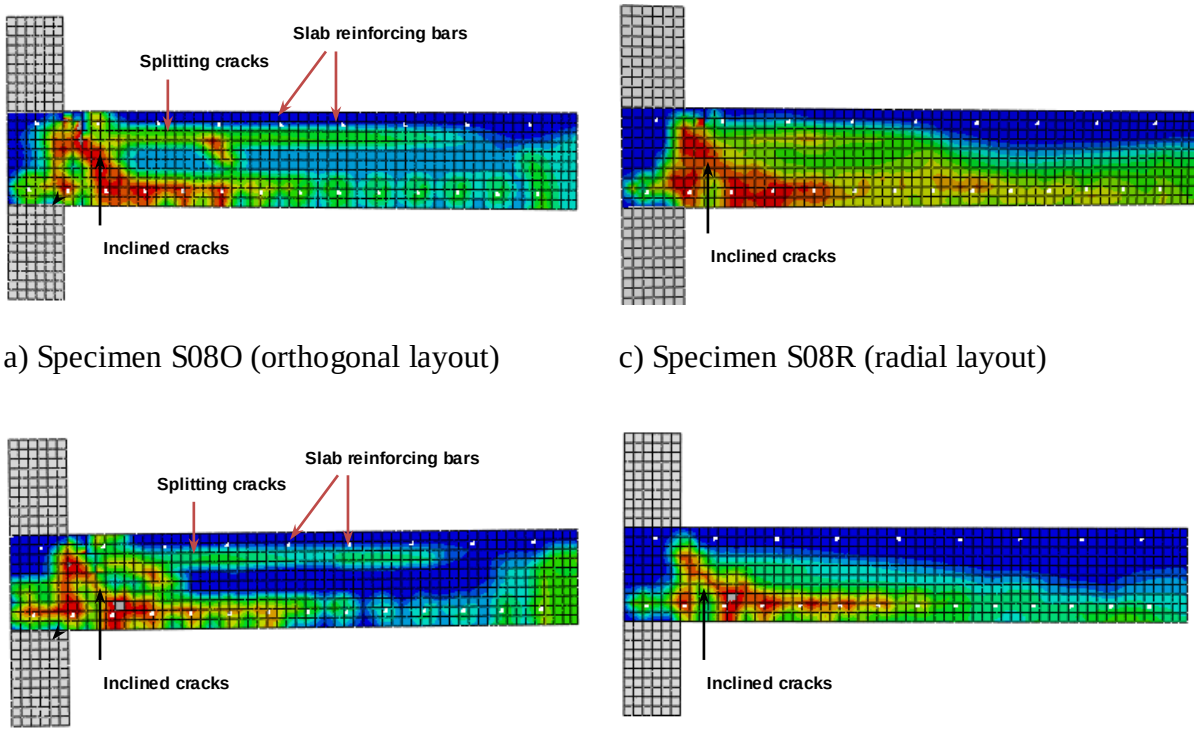


a) Specimen S08O (orthogonal layout)

c) Specimen S08R (radial layout)

b) Specimen S12O (orthogonal layout)

d) Specimen S12R (radial layout)

*Fig. 6-47: Crack patterns due to shear stud layouts from simulation results*

# CHAPTER 7
# CONCLUSIONS AND RECOMMENDATIONS

## 7.1 SUMMARY

Headed shear studs are a popular form of shear reinforcement used in two-way floor systems at slab-column connections, where either concentric shear or shear and moment are transferred from the slab to the column. Shear studs are often welded to a steel plate to form an assembly normally referred to as a stud rail. In North America, stud rails are typically placed perpendicular to column faces in a so-called orthogonal (or cruciform) layout to reduce interferences with slab flexural reinforcement. Results from prior research investigations have raised concerns over the effectiveness of shear studs on the behavior and shear strength of slab-column connections.

One potential issue with an orthogonal layout of shear studs is that large regions of the slab extending out from the corners of the columns are essentially unreinforced in shear. This issue can be addressed by placing stud rails that project radially out from the corners of the column, referred to herein as a radial layout. Some research investigations[15, 16, 45, 47] have indicated that stud layout (radial versus orthogonal) has no effect on shear strength of slab-column connections. However, other research investigations[17, 18, 49] have indicated that there may be a significant difference in the behavior and shear strength of slab-column connections with a radial versus an orthogonal layout of shear studs.

Another potential issue with slab-column connections reinforced with shear studs is that their punching shear strength may be significantly lower than the nominal strength given by the ACI Building Code[5] if slab flexural reinforcement ratios are relatively low. Significant yielding of slab flexural reinforcing bars near a column has been found to cause a premature punching shear failure at a slab-column connection[17, 18, 49]. The current design procedure for two-way shear strength of slabs in the ACI Code has been developed based on experimental results from slab-column specimens with relatively high slab reinforcement ratios, and thus the effect of the

percentage of flexural reinforcement in the slab near columns has not been consider thoroughly in the ACI Code.

The research investigation presented herein was organized to study issues related to the layout of shear stud reinforcement, radial vs. orthogonal, and the effect of a low flexural reinforcement ratio in the slab on the punching shear strength of a slab-column connection. Five full-scale interior slab-column connections were tested to failure under simulated gravity loading. The test specimens were simply supported along the edge of the slab to simulate moment and shear force conditions around a column in a flat plate system. The primary parameters for the tests were the average slab flexural reinforcement ratio (0.87% and 1.25%) and the layout of shear studs (radial or orthogonal). The main objectives of this experimental program were to evaluate: 1) the shear strength of gravity-loaded reinforced concrete slab-column connections with or without headed shear stud reinforcement, and 2) the effects of different layouts of headed shear studs and the percentage of slab flexural reinforcement on the behavior and shear strength of slab-column connections.

In addition to the experimental study, three-dimensional nonlinear finite element models were developed to simulate the observed behavior of reinforced concrete slab-column connections tested in this research investigation. In these models, concrete and reinforcement (flexural and shear reinforcement) were modeled separately using three-dimentional continuum solid elements and truss elements, respectively. The models were developed in Abaqus/Standard, an implicit simulation program. The reinforcement truss elements were connected to the adjacent concrete elements using the "embedded" method. Nonlinear plastic models were used for reinforcement truss elements and the "concrete damaged plasticity" model was used for concrete elements. Parameters for these nonlinear material models were calibrated using results from uniaxial tension tests for slab reinforcement and shear studs, and compression and splitting tests for concrete.

## 7.2 CONCLUSIONS

Based on the experimental and analytical results from the research investitgaion presented herein, as well as results from punching shear tests of slab-column specimens reported in the literature, the following conclusions are drawn:

(1) An orthogonal layout of shear studs provided similar strength as a radial layout for slab-column connections that had a large enough flexural reinforcement ratio to prevent the formation of a flexural mechanism before a punching shear failure developed.

(2) A radial layout of shear studs led to a higher shear strength (up to 13 percent) than an orthogonal layout for slab-column connections that exhibited significant slab flexural yielding prior to punching.

(3) The observed failure surfaces crossed the shear studs when they were arranged in a radial layout, but did not cross them when an orthogonal layout was used.

(4) A radial layout of shear studs permitted the development of a ductile flexural mechanism in the test specimens that had a lower reinforcement ratio (less than 1 percent). Thus, a radial layout is recommended in locations where ductility is important (e.g. where redistribution of moments is accounted for in design).

(5) The ACI Building Code nominal strength equations for punching shear at slab-column connections overestimate shear strength of slab-column connections when slabs have a low flexural reinforcement ratio. For such cases the shear required to develop a plastic flexural mechanism in the region of the slab around the column should be used as an upper bound for the shear strength of a slab-column connection.

(6) For slab-column connections with circular or approximately square columns that are part of a floor system with equal span lengths, the flexural tension reinforcement ratio within a slab transfer width, which extends 1.5h ($h$ is slab thickness) on each side of the column, should be greater than or equal to the proposed minimum value given in Eq. (45).

(7) For the test specimens with an orthogonal layout of shear studs, splitting cracks in the concrete cover were observed to extend horizontally away from the column faces. Thus, lap splices of structural integrity reinforcing bars should not be located inside the shear stud reinforced regions near a column.

(8) The three-dimensional finite element models developed in Abaqus/Standard were able to simulate with reasonably accuracy the behavior and shear strength of the tested slab-column connections.

(9) The finite element models were able to accurately reproduce the flexural, shear, and splitting cracks observed in the test specimens.

## 7.3 RECOMMENDATIONS FOR FUTURE RESEARCH

In this study, slab-column connections reinforced with headed shear studs subjected to simulated gravity loads were studied. Further experimental and analytical investigations are recommended in the following areas:

(1) Effect of shear stud layouts on the behavior and shear strength of slab-column connections under other load applications, e.g. gravity loads with unbalanced moments and lateral cyclic loads,

(2) Effectiveness of slab structural integrity reinforcement in flat slab systems reinforced with shear studs.

(3) Finite element simulation of post-punching behavior for slab-column connections reinforced with shear studs.

(4) Finite element simulation of slab-column connections reinforced with other shear reinforcement systems.

# APPENDIX A

# DESIGN OF EXPERIMENTAL PROGRAM

## A.1: DESIGN OF TEST SPECIMENS

### A.1.1 Shear Design

**CONNECTION GEOMETRY**

Slab thickness $t := 10in$ Slab Square Size $l := 120in$

Column Square Section $h_c := 12in$

**MATERIALS PROPERTIES**

Concrete $f_c := 4000psi$ $\lambda := 1$

Flexural Reinforcement $f_y := 60ksi$

Headed Studs $f_{yt} := 51ksi$

**SHEAR DESIGN**

Assume slab flexural effective depth $d := 8.5in$

Target shear strength $v_n := 6 \cdot \lambda \sqrt{\frac{f_c}{psi}} \cdot psi = 379\,psi$

Shear strength provided by concrete $v_c := 3 \cdot \lambda \sqrt{\frac{f_c}{psi}} \cdot psi = 190\,psi$

Shear strength provided by shear studs $v_s := v_n - v_c = 190\,psi$

Assuming 12 rails of #3 shear studs were used.

$n_{rail} := 12$

$A_v := n_{rail} \cdot 0.11in^2 = 1.32\,in^2$

Perimeter of the inner critical section $b_0 := 4 \cdot (h_c + d) = 82 \cdot in$

Required spacing between studs $s_{req} := \frac{A_v \cdot f_{yt}}{v_s \cdot b_0} = 4.33\,in$

Maximum spacing suggested by the ACI Code

$s_{max} := \frac{d}{2} = 4.25\,in$

Assume using 8 studs per rail, and spaced at

$$s := \left(4 + \frac{1}{8}\right)\text{in} = 4.125\,\text{in}$$

The first shear studs was placed at $s_0 := \left(3 + \frac{3}{4}\right)\text{in} = 3.75\,\text{in}$

*Check for shear strength at outer critical section for orthogonal layout*

Perimeter of outer critical section $b_{0out} := 260\text{in}$

Shear stress $v_{out} := \frac{v_n \cdot b_0}{b_{0out}} = 120\,\text{psi} < 2 \cdot \lambda \sqrt{\frac{f_c}{\text{psi}}} \cdot \text{psi} = 126\,\text{psi}$ OK

*Check for shear strength at outer critical section for radial layout*

Perimeter of outer critical section $b_{0out} := 276\text{in}$

Shear stress $v_{out} := \frac{v_n \cdot b_0}{b_{0out}} = 113\,\text{psi} < 2 \cdot \lambda \sqrt{\frac{f_c}{\text{psi}}} \cdot \text{psi} = 126\,\text{psi}$ OK

## A.1.2 Flexural Design

Yield line analysis[3, 54, 145] was used to estimate the flexural strength of the test specimens. These specimens were loaded vertical at the columns and simply supported by eight "points" uniformly distributed on the incircles of the slab perimeters. Assuming slab flexural tension reinforcement ratio was m, possible flexural mechanisms and the corresponding flexural strength for the test specimens were presented as follows.

### *1. Failure Mechanism 1*

One possible failure mechanism was shown in Fig. A-1. A slab was divided into two segments by the yield lines extending away from the columns and perpendicularly to slab edges. The external ($EW$) and internal energy ($IW$) were calculated as follows:

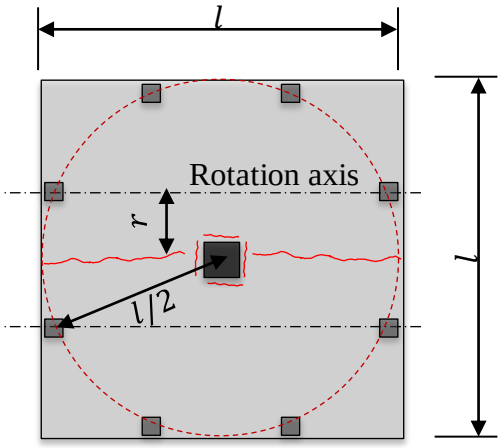


Fig. A-1: Failure mechanism #1

$$EW = V_{\text{flex}} \times \delta$$

$$IW = 2(m \times l)\frac{\delta}{\text{r}} = 2m\frac{l}{\frac{l}{2}\sin(\frac{\pi}{8})} \times \delta = \frac{4}{\sin(\frac{\pi}{8})} m \times \delta$$

The energy conservation theorem, $EW = IW$, gave:

$$V_{\text{flex}} = \frac{4}{\sin(\frac{\pi}{8})} m = 10.5m$$

### 2. *Failure Mechanism 2*

$$EW = V_{\text{flex}} \times \delta$$

$$IW = 4\left(m \times \frac{l\sqrt{2}}{2}\right)\frac{\delta}{\text{r}}$$

$$= 2\sqrt{2}m \frac{l}{\frac{l}{2}\cos\left(\frac{\pi}{8}\right) - \frac{b_c\sqrt{2}}{2}} \times \delta$$

$$= \frac{4\sqrt{2}}{cos(\frac{\pi}{8}) - \frac{b_c\sqrt{2}}{l}} m \times \delta$$

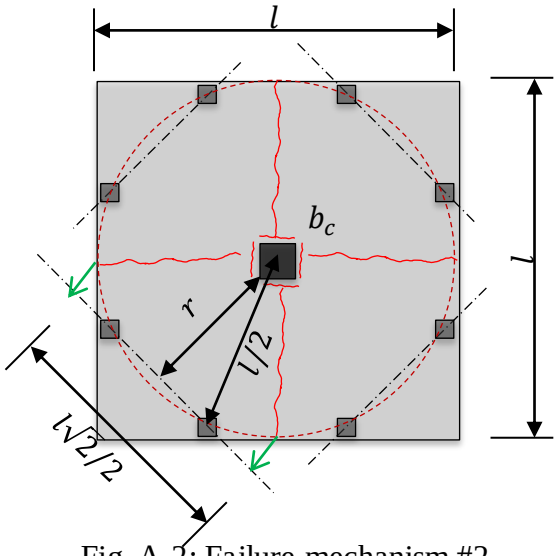


Fig. A-2: Failure mechanism #2

$$EW = IW \rightarrow V_{\text{flex}} = \frac{4\sqrt{2}}{\cos(\frac{\pi}{8}) - \frac{b_c\sqrt{2}}{l}} m$$

For $l = 10$ ft (7620 mm) and $b_c = 12$ in. (305 mm), $V_{\text{flex}} = 7.23m$

### 3. *Failure Mechanism 3*

$$EW = V_{\text{flex}} \times \delta$$

$$IW = 4(m \times l)\frac{\delta}{\text{r}}$$

$$= 4m \frac{l}{\frac{l}{2}\cos\left(\frac{\pi}{8}\right) - \frac{b_c}{2}} \times \delta$$

$$= \frac{8}{\cos(\frac{\pi}{8}) - \frac{b_c}{l}} m \times \delta$$

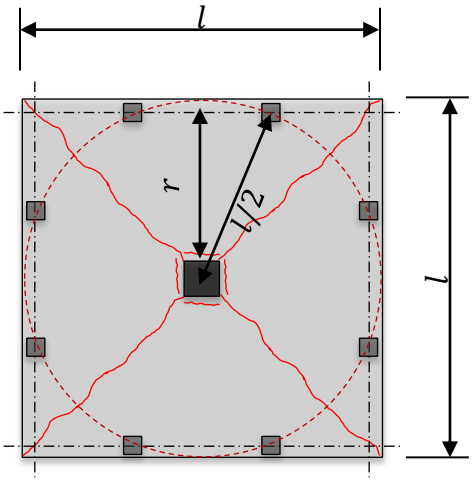


Fig. A-3: Failure mechanism #3

$$EW = IW \rightarrow V_{\text{flex}} = \frac{8}{\cos(\frac{\pi}{8}) - \frac{b_c}{l}} m$$

For $l = 10$ ft (7620 mm) and $b_c = 12$ in. (305 mm), $V_{\text{flex}} = 9.71m$

### 4. *Failure Mechanism 4*

$$EW = V_{\text{flex}} \times \delta$$

$$IW = 8(m \times \text{Z})\frac{\delta}{\text{r}}$$

$$= 8m\frac{\frac{l}{2}\cos\left(\frac{\pi}{8}\right)}{\frac{l}{2} - \frac{b_c\sqrt{2}}{2}} \times \delta$$

$$= \frac{8}{1 - \frac{b_c\sqrt{2}}{l}} m \times \delta$$

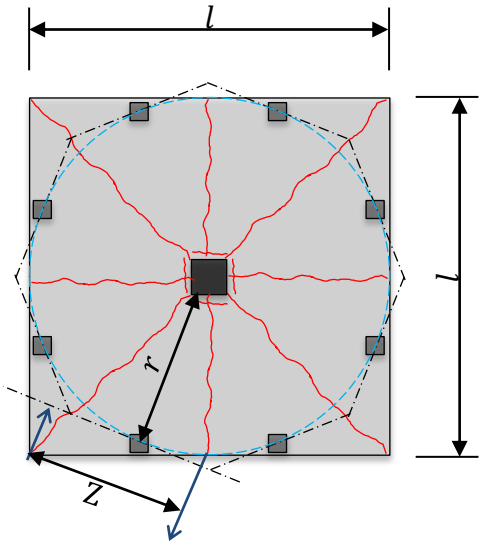

Fig. A-4: Failure mechanism #4

$$EW = IW \rightarrow V_{\text{flex}} = \frac{8}{1 - \frac{b_c\sqrt{2}}{l}} m$$

For $l = 10$ ft and $b_c = 12$ in. then $V_{\text{flex}} = 9.32m$

## A.2: READY-MIX CONCRETE DESIGN

DOAN COMPANIES

| | |
|---|---|
| CONTRACTOR: | U-M CIVIL ENGINEERING DEPT |
| MIX DESIGN NO : | 4026NAM |
| DESIGN STRENGTH : | 4000 PSI 28 DAYS |
| DESIGN SLUMP : | 5" +/-1" |
| DESIGN AIR : | 2% ENTRAPPED |
| UNIT WEIGHT: | 150.5 |
| USE : | BEAM |
| W/C RATIO: | 0.54 |
| PROJECT: | U-M NORTH CAMPUS<br>ANN ARBOR PLANTS |

| MATERIALS | SIZE/TYPE | SOURCE | ASTM |
|---|---|---|---|
| FLY ASH: | TYPE F | HEADWATERS RESOURCES | C-618 |
| CEMENT: | TYPE I | ST MARYS CEMENT | C-150 |
| FINE AGGREGATE: | 2NS | BARRETT PIT #9 | C-33 |
| COARSE AGGREGATE: | 26-A | AGGREGATE INDUSTRIES | C-33 |
| MID-RANGE: | MRX | EUCLID CHEMICAL | C-494 |
| WATER: | POTABLE | MUNICIPAL | C-94 |

**MATERIAL PROPORTIONS:** (PER CUBIC YARD)

| | SSD WEIGHTS | SP.G. | ABS. VOL. |
|---|---|---|---|
| CEMENT : | 325 LBS. | 3.15 | 1.65 |
| FLY ASH: | 120 LBS. | 2.54 | 0.76 |
| FINE AGGREGATE: | 1640 LBS. | 2.67 | 9.84 |
| COARSE AGGREGATE: | 1740 LBS. | 2.69 | 10.37 |
| ENTRAPPED: | 2 % | | 0.54 |
| WATER: | 241 LBS. | 1.00 | 3.86 |
| MID-RANGE: | 4.0oz CWT. | | |
| TOTAL: | 4066 LBS. | | 27.02 CU.FT. |

THIS MIX DESIGN WILL MEET THE PROJECTS SPECIFICATIONS IN 28 DAYS WHEN HANDLED, PLACED, AND TESTED IN ACCORDANCE WITH CURRENT ASTM AND ACI STANDARDS AND RECOMMENDED PRACTICES.

---

NOTE : ASTM C-94 STATES : "WHEN THE STRENGTH OF CONCRETE IS USED AS A BASIS FOR ACCEPTANCE THE MANUFACTURER SHALL BE ENTITLED TO COPIES OF ALL TEST REPORTS ". PLEASE PLACE US ON THE DISTRIBUTION LIST FOR COPIES. THANK YOU.

---

SUBMITTED:DOAN COMPANIES

DATE: 19-Jul-14
GENERAL MANAGER TOM MCCURRY

# APPENDIX B
# PROCESSED DATA

## B.1: MEASURED CONCRETE PROPERTIES

Compressive strength ($f_c'$) of the slab concrete for all test specimens was measured when the concrete was 28 days old and when the specimens were tested. These measured compressive strengths are shown in Table B-1 to Table B-5.

Tensile strengths $f_{ct}$ and $f_r$ of the slab concrete were measured at the testing days, and they are presented in Table B-6 to Table B-10. Concrete properties, including compressive strength, splitting strength, and modulus of rupture, were measured.

Compressive strength of top column stub concrete was measured at the testing day of each specimen, and the results are presented in Table B-11.

*Table B-1: Slab concrete compressive strength for Specimen S08C*

| Cylinder | $f_c'$ at 28 days old psi (MPa) | $f_c'$ at 114 days old (testing day) psi (MPa) |
|---|---|---|
| 1 | 4455 (30.7) | 6182 (42.6) |
| 2 | 4719 (32.5) | 5788 (39.9) |
| 3 | 4636 (32.0) | 6326 (43.6) |
| Average | **4603** (31.7) | **6099** (42.1) |
| S.D. | 135 (0.932) | 278 (1.89) |

*Table B-2: Slab concrete compressive strength for Specimen S08O*

| Cylinder | $f_c'$ at 35 days old psi (MPa) | $f_c'$ at 62 days old (testing day) psi (MPa) |
|---|---|---|
| 1 | 4147 (28.6) | 5089 (35.1) |
| 2 | 4532 (31.2) | 4717 (32.5) |
| 3 | 4260 (29.4) | 4529 (31.2) |
| 4 | | 5387 (37.1) |
| 5 | | 5523 (38.1) |
| Average | 4313 (29.7) | **5049** (34.8) |
| S.D. | 198 (1.37) | 425 (2.93) |

*Table B-3: Slab concrete compressive strength for Specimen S08R*

| Cylinder | $f_c'$ at 19 days old psi (MPa) | $f_c'$ at 30 days old (testing day) psi (MPa) |
|---|---|---|
| 1 | 4780 (32.9) | 5519 (38.1) |
| 2 | 4700 (32.4) | 5196 (35.8) |
| 3 | 4750 (32.8) | 5024 (34.6) |
| 4 | () | 5231 (36.1) |
| 5 | () | 5488 (37.8) |
| 6 | () | 5368 (37.0) |
| 7 | () | 5722 (39.5) |
| Average | 4740 (32.7) | **5360** (37.0) |
| S.D. | 40 (0.27) | 234 (1.62) |

*Table B-4: Slab concrete compressive strength for Specimen S12O*

| Cylinder | $f_c'$ at 25 days old psi (MPa) | $f_c'$ at testing day psi (MPa) |
|---|---|---|
| 1 | 3155 (21.8) | 4639 (32.0) |
| 2 | 3279 (22.6) | 4509 (31.1) |
| 3 | | 4654 (32.1) |
| 4 | | 4240 (29.2) |
| 5 | | 4506 (31.1) |
| Average | **3217** (22.2) | **4510** (31.1) |
| S.D. | 87 (0.601) | 166 (1.15) |

*Table B-5: Slab concrete compressive strength for Specimen S12R*

| Cylinder | $f_c'$ at 31 days old psi (MPa) | $f_c'$ at testing day psi (MPa) |
|---|---|---|
| 1 | 3668 (25.3) | 4669 (32.2) |
| 2 | 4183 (28.8) | 4847 (33.4) |
| 3 | 4280 (29.5) | 4877 (33.6) |
| 4 | | 4767 (32.9) |
| 5 | | 4779 (33.0) |
| Average | 4040 (27.9) | **4780** (33.0) |
| S.D. | 329 (2.27) | 81.0 (0.558) |

*Table B-6: Concrete tensile strength for Specimen S08C at testing day*

| Cylinder or Beam | $f_{ct}$ psi (MPa) | $f_r$ psi (MPa) |
|---|---|---|
| 1 | 469 (3.24) | 543 (3.47) |
| 2 | 523 (3.60) | 674 (4.64) |
| 3 | 524 (3.61) | 447 (3.08) |
| 4 | | 405 (2.79) |
| Average | **505** (3.48) | **517** (3.57) |
| S.D. | 31.1 (0.215) | 119 (0.822) |

*Table B-7: Concrete tensile strength for Specimen S08O at testing day*

| Cylinder or Beam | $f_{ct}$ psi (MPa) | $f_r$ psi (MPa) |
|---|---|---|
| 1 | 514 | 351 |
| | (3.54) | (2.42) |
| 2 | 549 | 479 |
| | (3.16) | (3.30) |
| 3 | 455 | 500 |
| | (3.14) | (3.45) |
| Average | **476** | **443** |
| | (3.28) | (3.06) |
| S.D. | 33.1 | 80.8 |
| | (0.228) | (0.557) |

*Table B-8: Concrete tensile strength for Specimen S08R at testing day*

| Cylinder or Beam | $f_{ct}$ psi (MPa) | $f_r$ psi (MPa) |
|---|---|---|
| 1 | 543 | 495 |
| | (3.74) | (3.41) |
| 2 | 608 | 510 |
| | (4.19) | (3.52) |
| 3 | 590 | 544 |
| | (4.07) | (3.75) |
| 4 | 496 | |
| | (3.42) | |
| 5 | 621 | |
| | (4.28) | |
| Average | **571** | **516** |
| | (3.94) | (3.52) |
| S.D. | 51.4 | 25.2 |
| | (0.355) | (0.174) |

*Table B-9: Concrete tensile strength for Specimen S12O*

| Cylinder or Beam | $f_{ct}$ at testing day (43), psi (MPa) | $f_r$ at 76 days old, psi (MPa) |
|---|---|---|
| 1 | 486 | 653 |
| | (3.35) | (4.50) |
| 2 | 595 | 584 |
| | (4.10) | (4.03) |
| 3 | 652 | 655 |
| | (4.50) | (4.52) |
| 4 | 498 | 741 |
| | (3.43) | (5.11) |
| 5 | 572 | |
| | (3.95) | |
| Average | 561 | **658** |
| | (3.87) | (4.54) |
| S.D. | 69.3 | 64.1 |
| | (0.478) | (0.442) |

*Table B-10: Concrete tensile strength for Specimen S12R at testing day*

| Cylinder or Beam | $f_{ct}$ psi (MPa) | $f_r$ psi (MPa) |
|---|---|---|
| 1 | 545 | 465 |
| | (3.76) | (3.21) |
| 2 | 562 | 575 |
| | (3.87) | (3.96) |
| 3 | 527 | 486 |
| | (3.64) | (3.35) |
| 4 | 515 | |
| | (3.55) | |
| Average | 537 | **509** |
| | (3.70) | (3.51) |
| S.D. | 20.4 | 58.4 |
| | (0.14) | (0.403) |

*Table B-11: Compressive strength of the top column stub concrete*

| Cylinder | $f_c'$ measured at testing day psi (MPa) |
|---|---|
| S08-C | 7170 (49.5) |
| S08-O | 7520 (51.9) |
| S08-R | 6900 (47.5) |
| S12-O | 6890 (47.5) |
| S12-R | 7120 (49.1) |

## B.2: SPECIMEN TEST DATA

## B.2.1 Specimen S08C

### *B.2.1.1 Cracks*

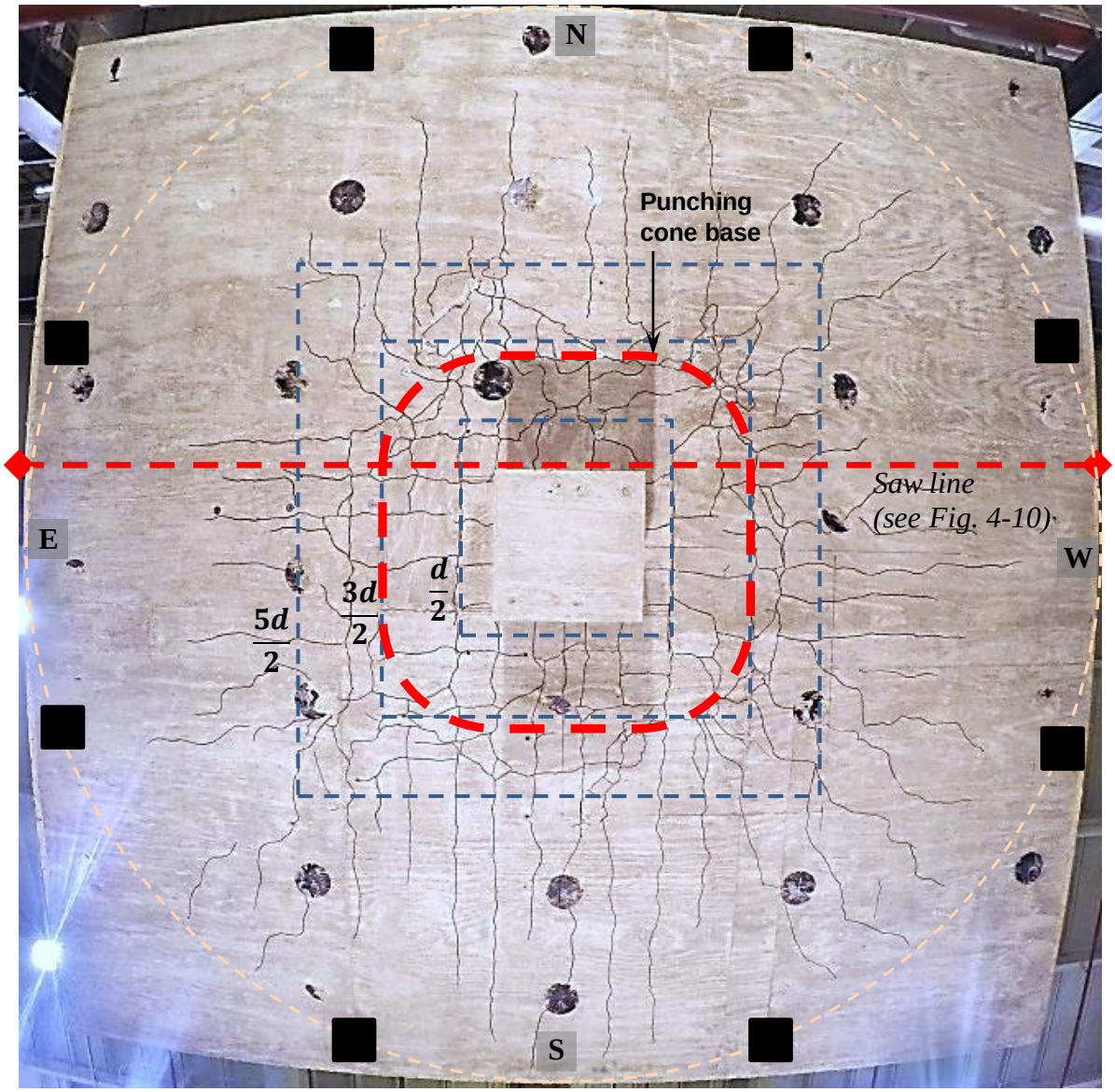


*Fig. B-1: Cracks on the bottom of slab S08C*

### *B.2.1.2 Strains in Slab Flexural Reinforcing Bars*

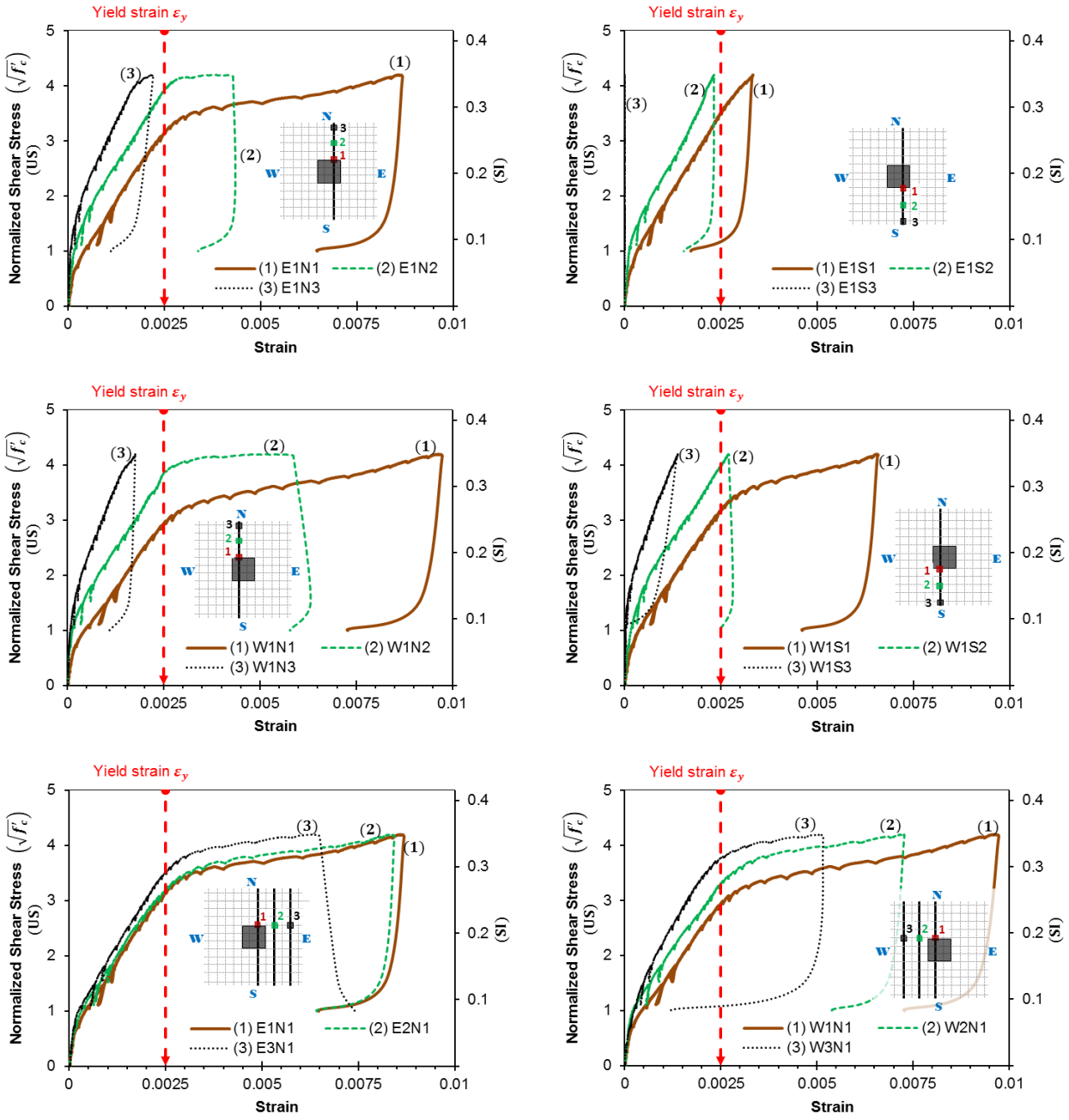


*Fig. B-2: Measured strains in the slab reinforcing bars of Specimen S08C*

*(see Fig. 3-25 for strain gauge labels and locations)*

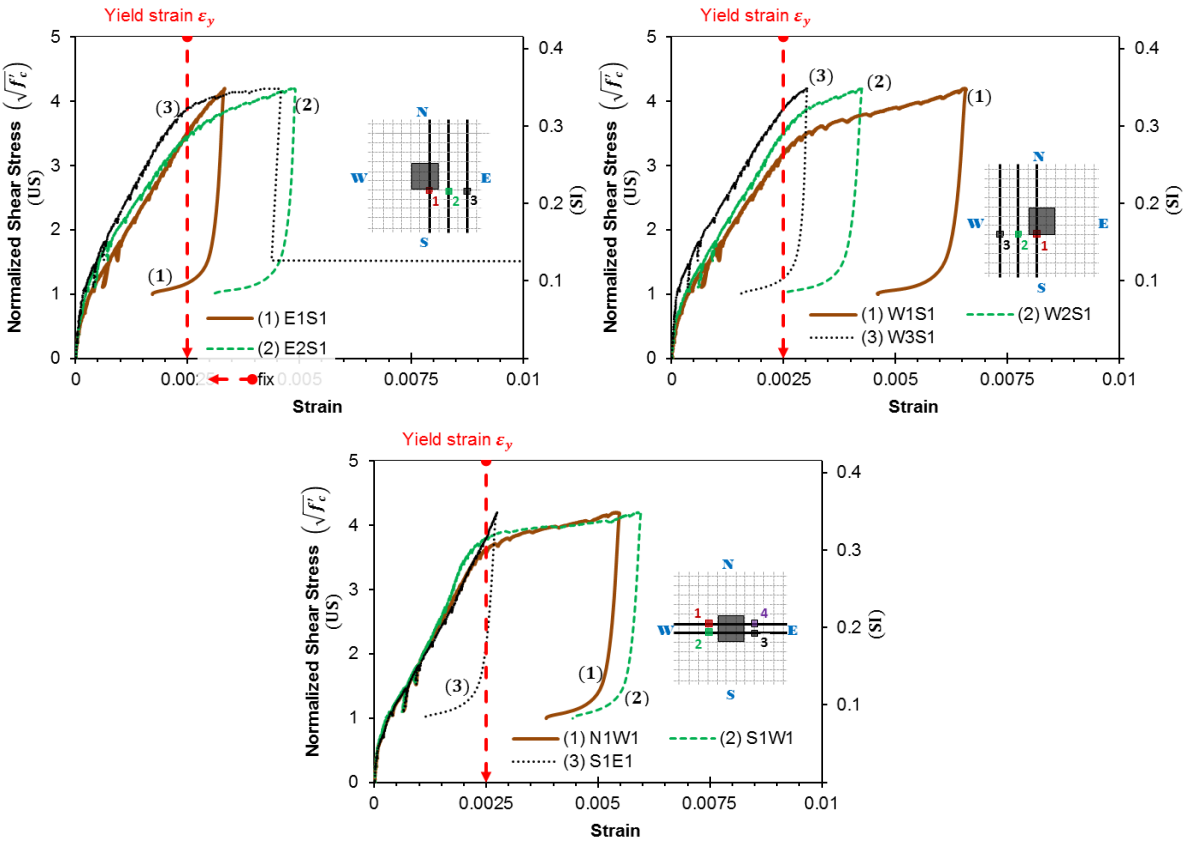


*Fig. B-2: Measured strains in the slab reinforcing bars for Specimen S08C (continue)*

*(see Fig. 3-25 for strain gauge labels and locations)*

### *B.2.1.3 Slab Through-thickness Expansions*

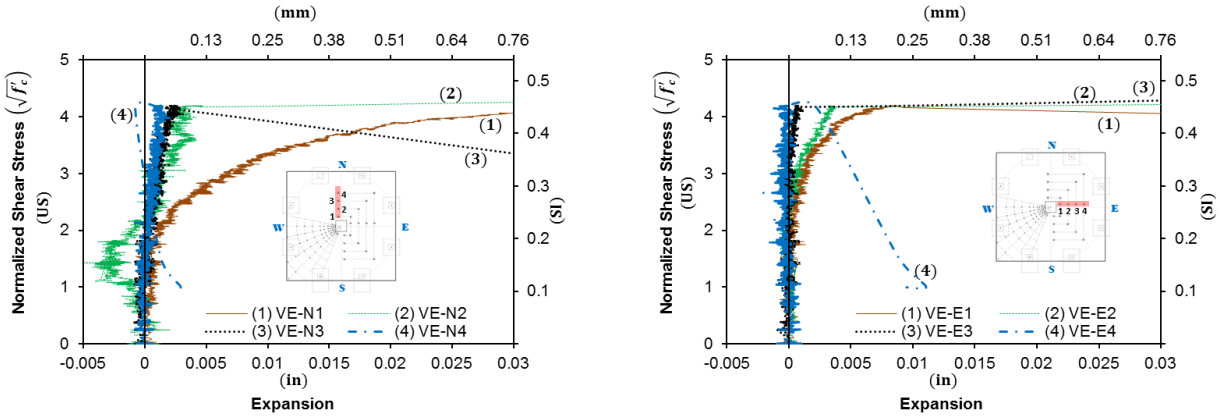


*Fig. B-3: Measured slab through-thickness expansion for Specimen S08C*

*(see Fig. 3-24 for strain gauge labels and locations)*

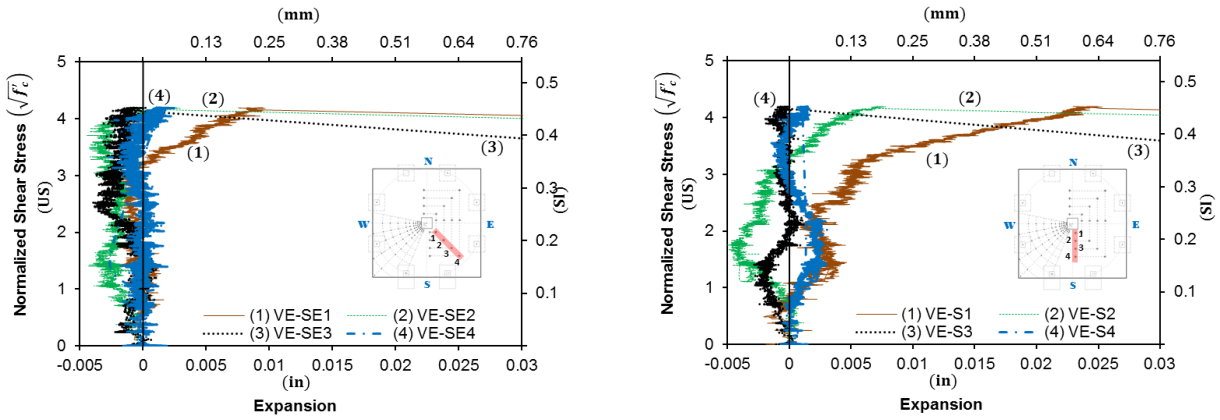


*Fig. B-3: Measured slab through-thickness expansion for Specimen S08C (continue)*

(Labels in Fig. 3-24)

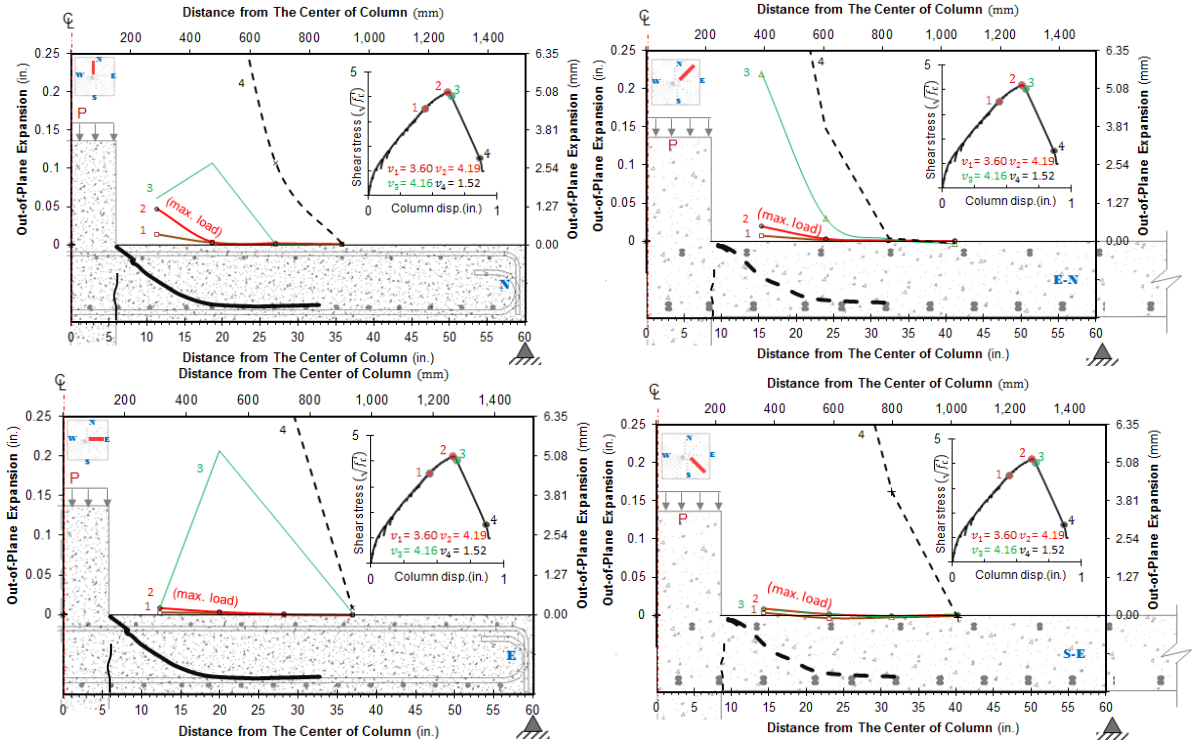


*Fig. B-4: Measured slab through-thickness expansions at different loads for Specimen S08C*

### *B.2.1.4 Top Surface Vertical Displacement*

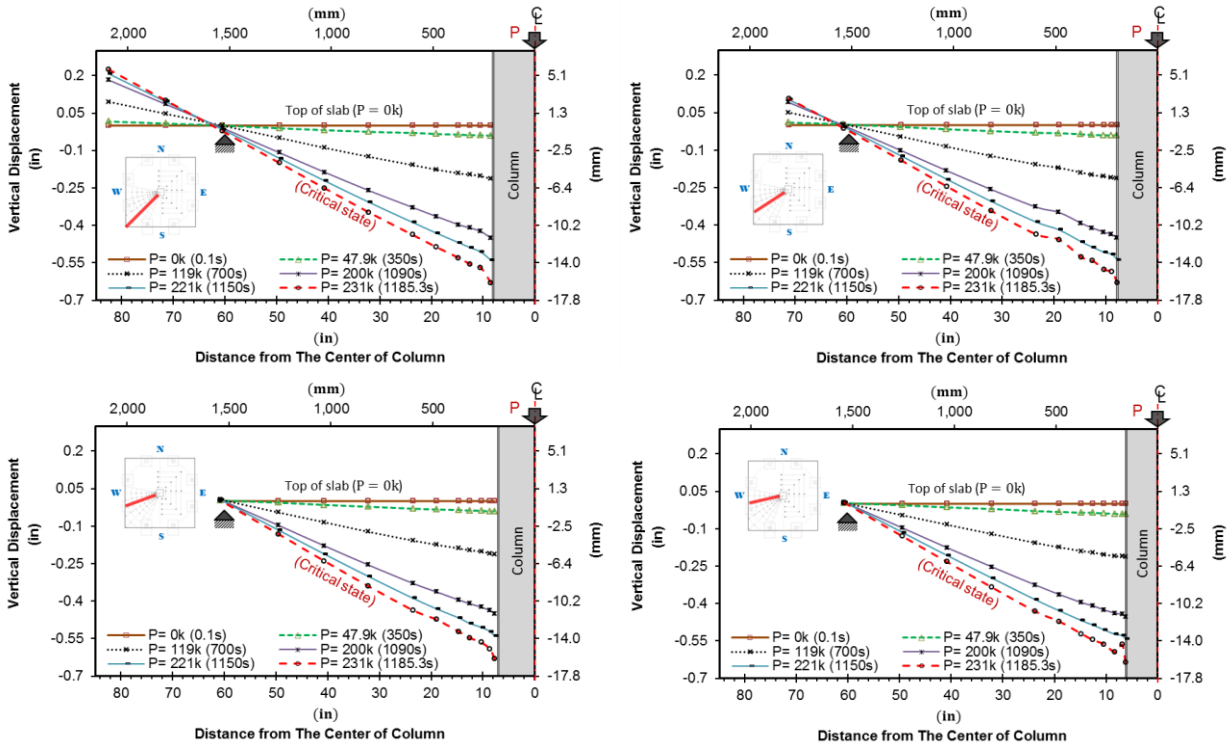


*Fig. B-5: Vertical displacement of the top surface of the slab*

## B.2.2 Specimen S08O

### *B.2.2.1 Cracks*

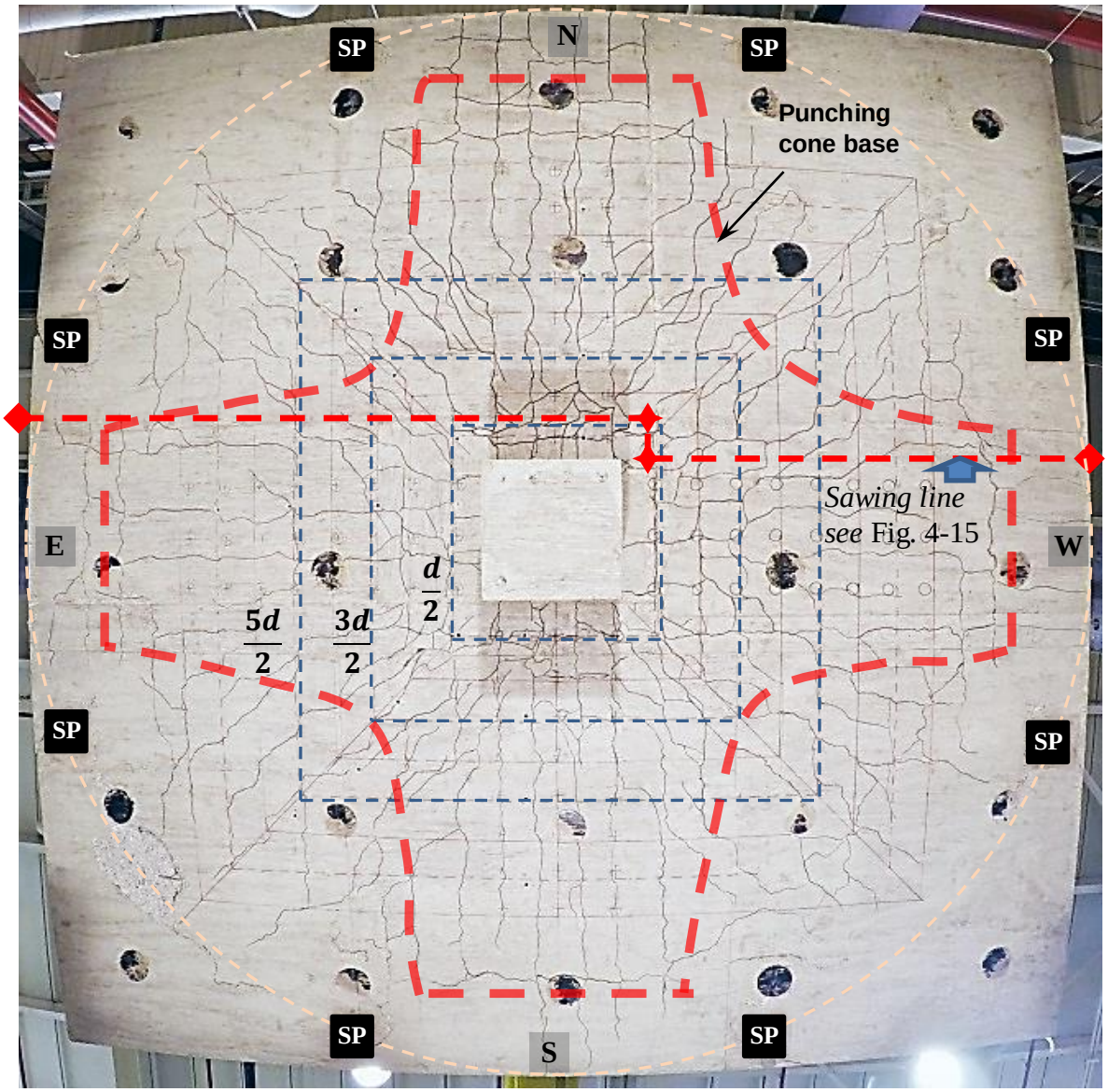


*Fig. B-6: Cracks on the bottom of slab S08O after the completion of the test*

### *B.2.2.2 Strains in Slab Flexural Reinforcing bars*

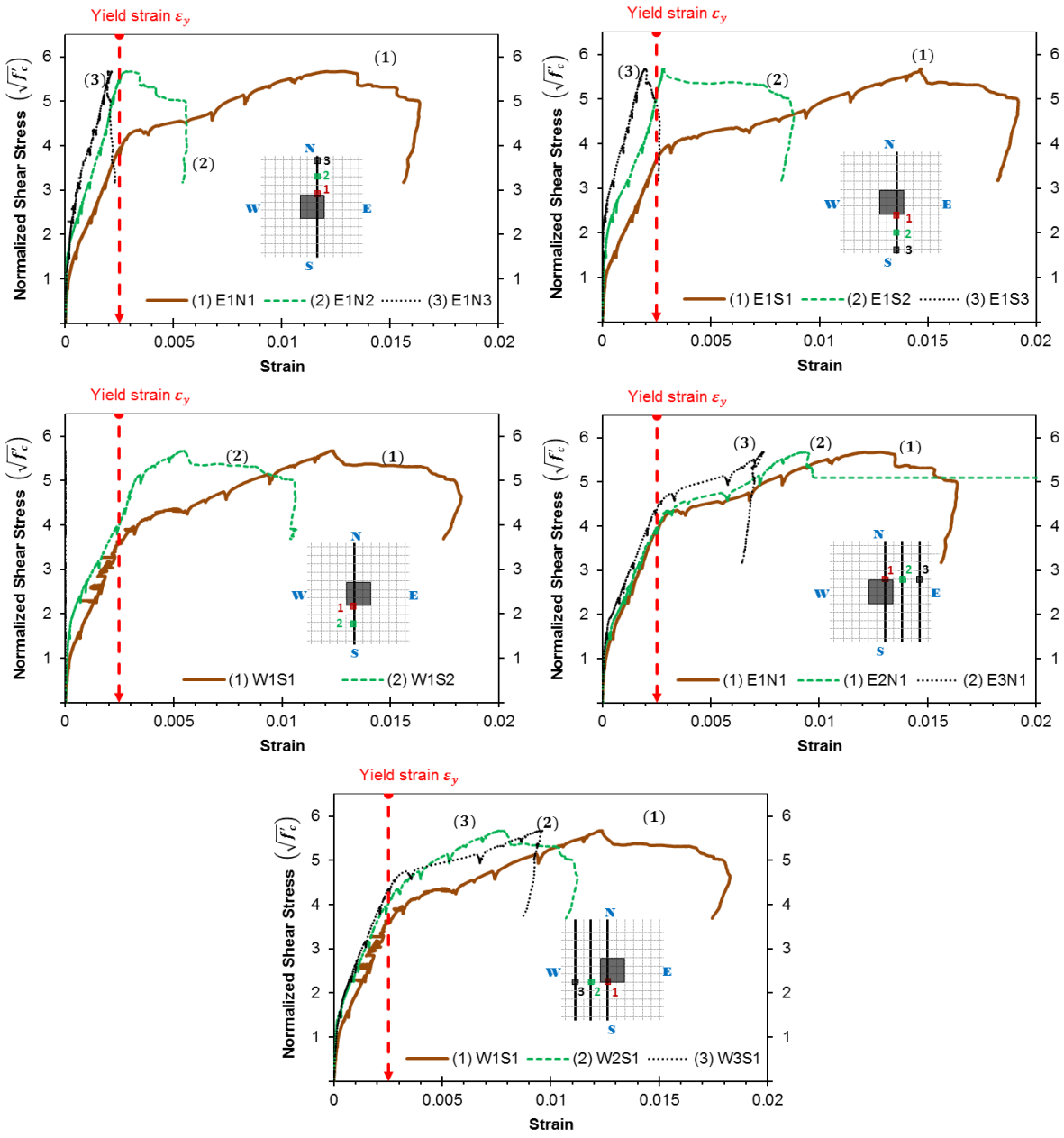


*Fig. B-7: Measured strains in the slab flexural reinforcing bars of Specimen S08O*

*(see Fig. 3-25 for strain gauge labels and locations)*

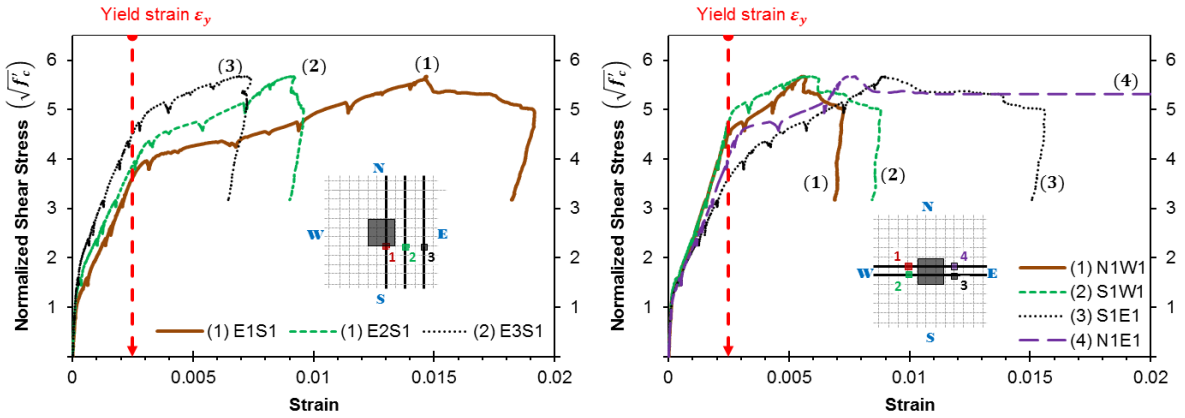


*Fig. B-7: Measured strains in the slab flexural reinforcing bars of Specimen S08O (continued)*

*(see Fig. 3-25 for strain gauge labels and locations)*

### *B.2.2.3 Strains in Shear Studs*

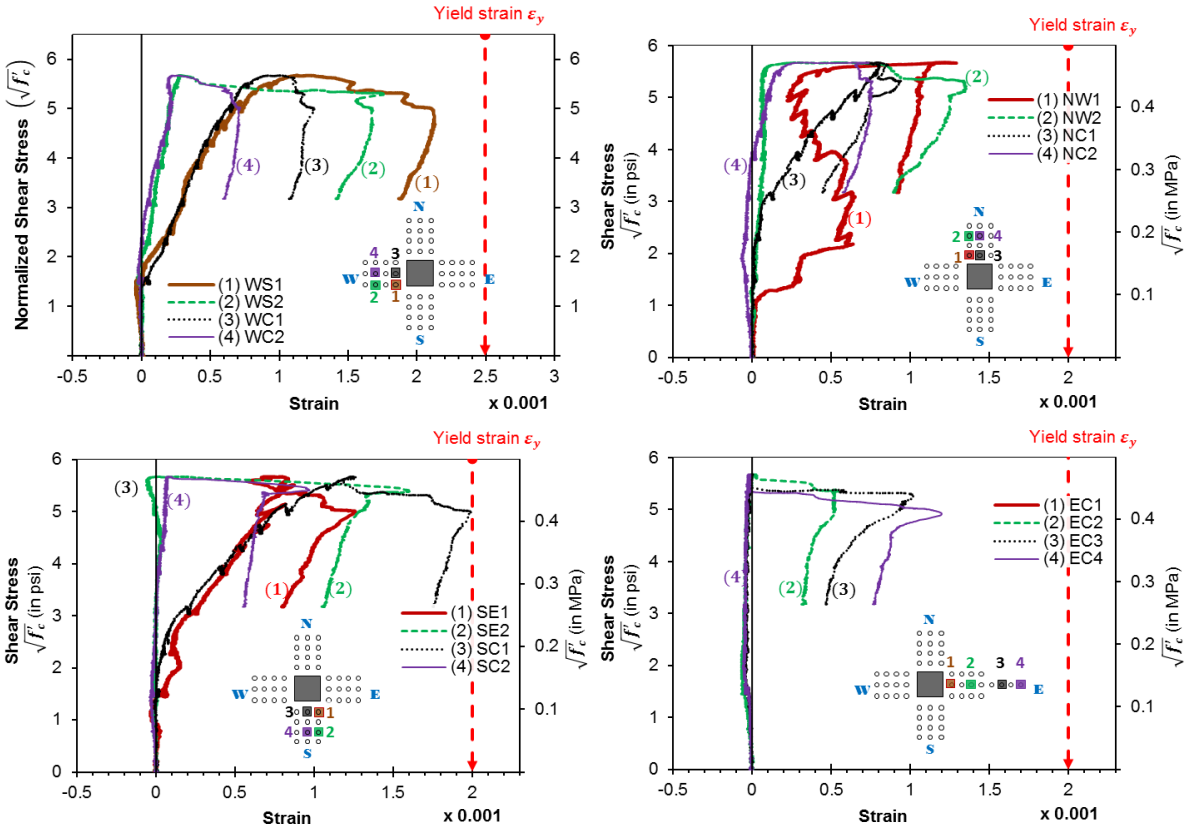


*Fig. B-8: Measured strains in the shear studs for Specimen S08O*

*(see Fig. 3-26 for strain gauge labels and locations)*

### *B.2.2.4 Slab Through-thickness Expansions*

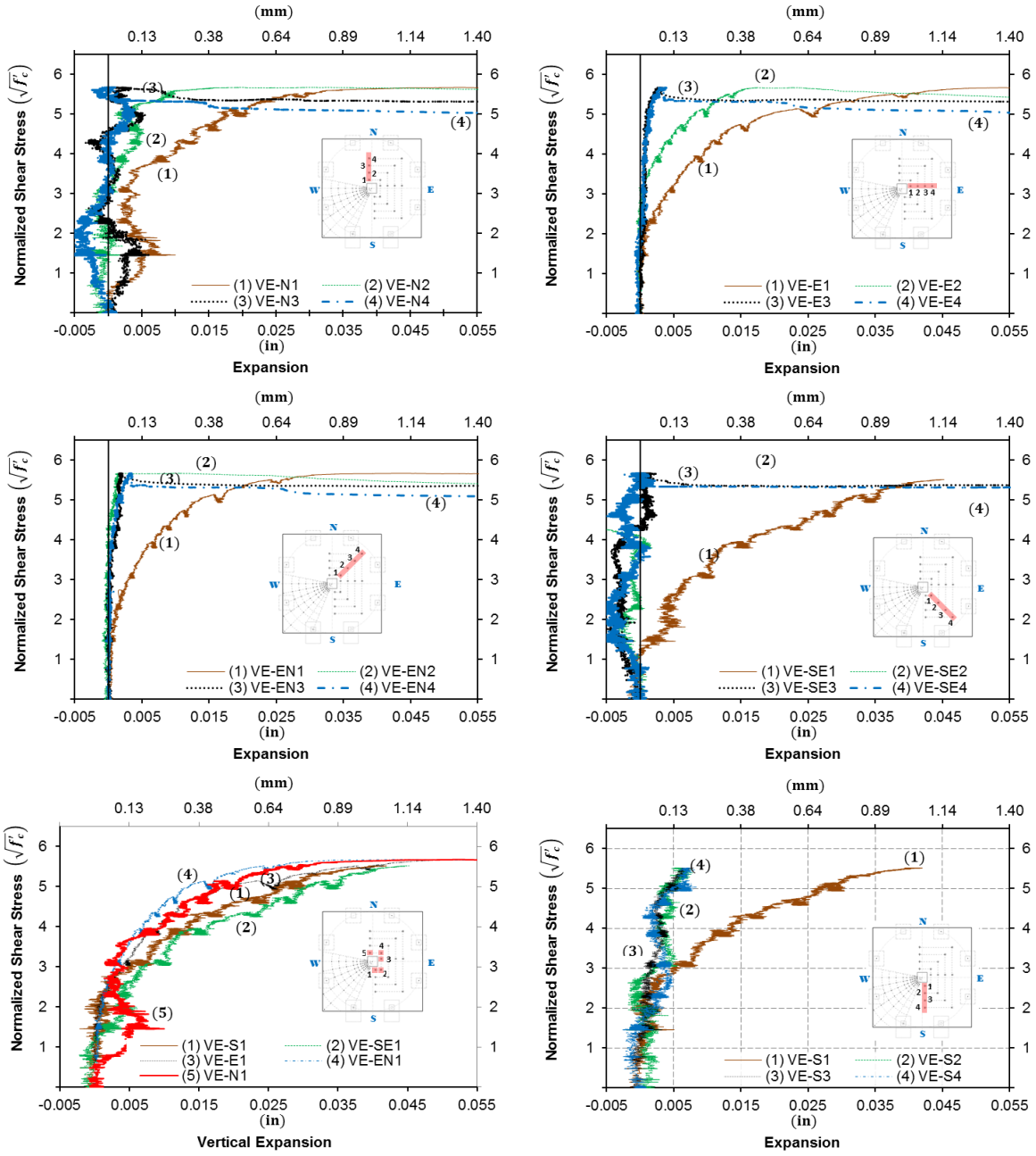


*Fig. B-9: Measured slab through-thickness expansion for Specimen S08O*

*(see Fig. 3-24 for labels and locations)*

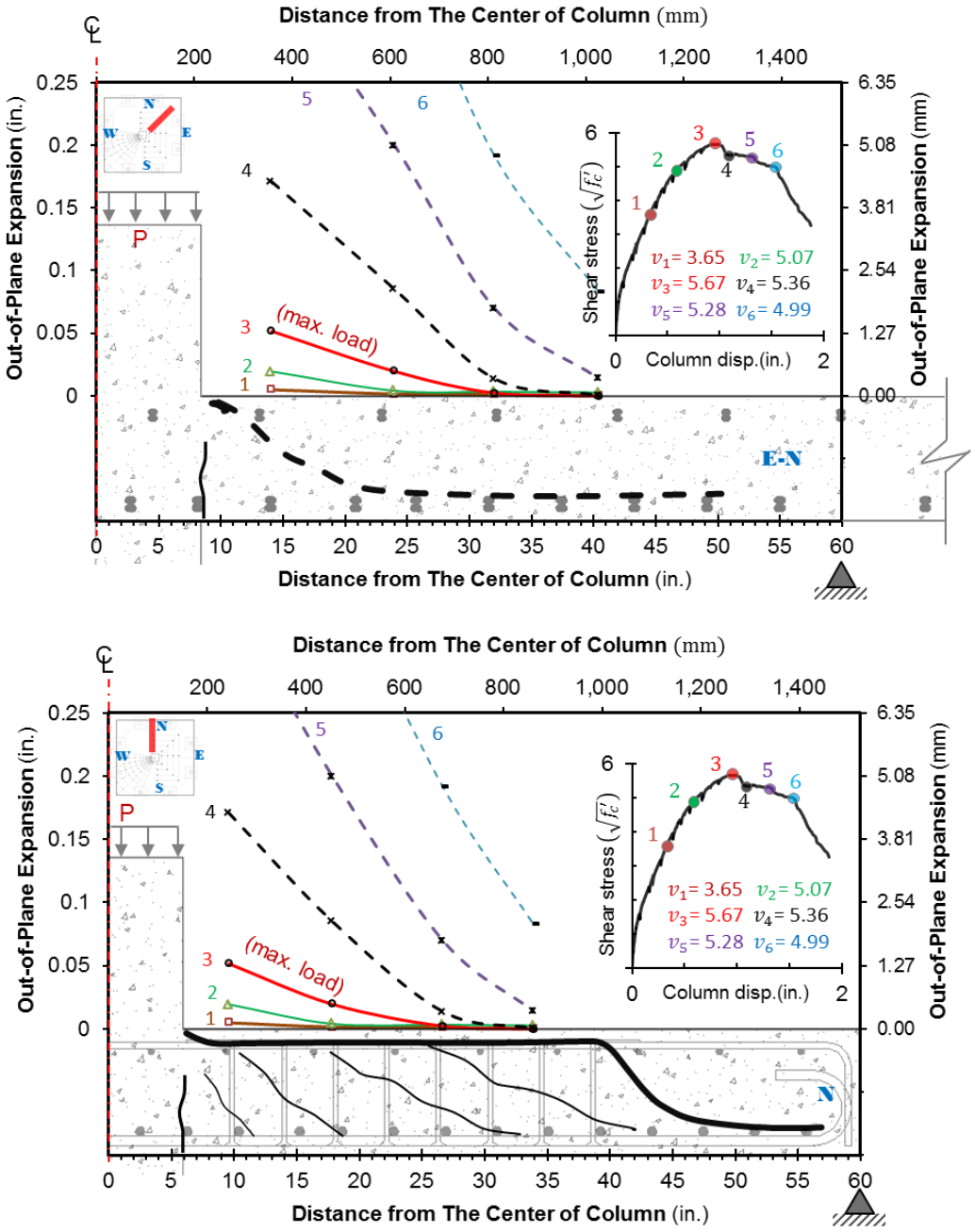


*Fig. B-10: Measured slab through-thickness expansion at different loads*

## B.2.3 Specimen S08R

### *B.2.3.1 Cracks*

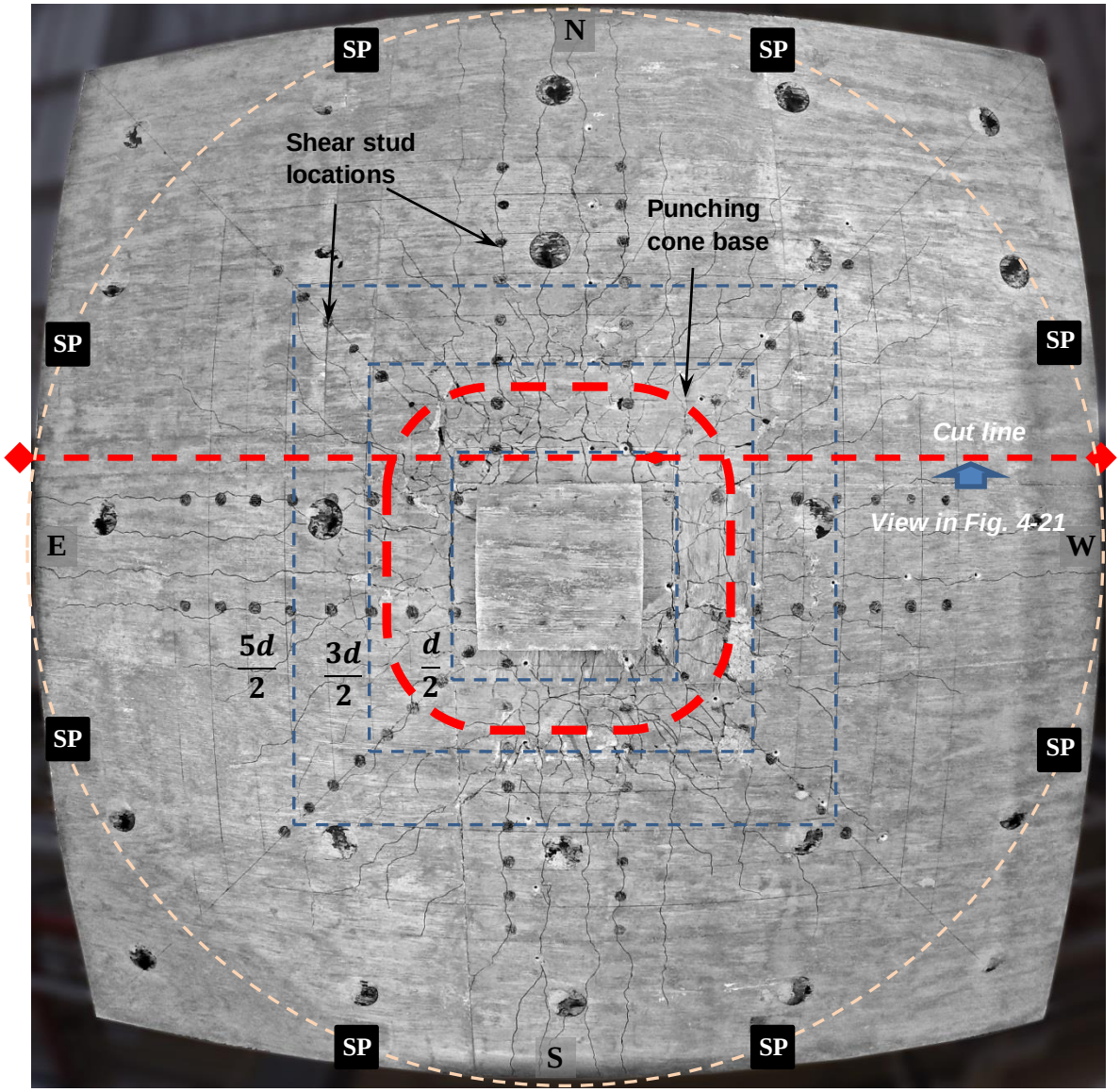


*Fig. B-11: Cracks on the bottom of slab S08R after the Test*

### *B.2.3.2 Strains in Slab Flexural Reinforcing bars*

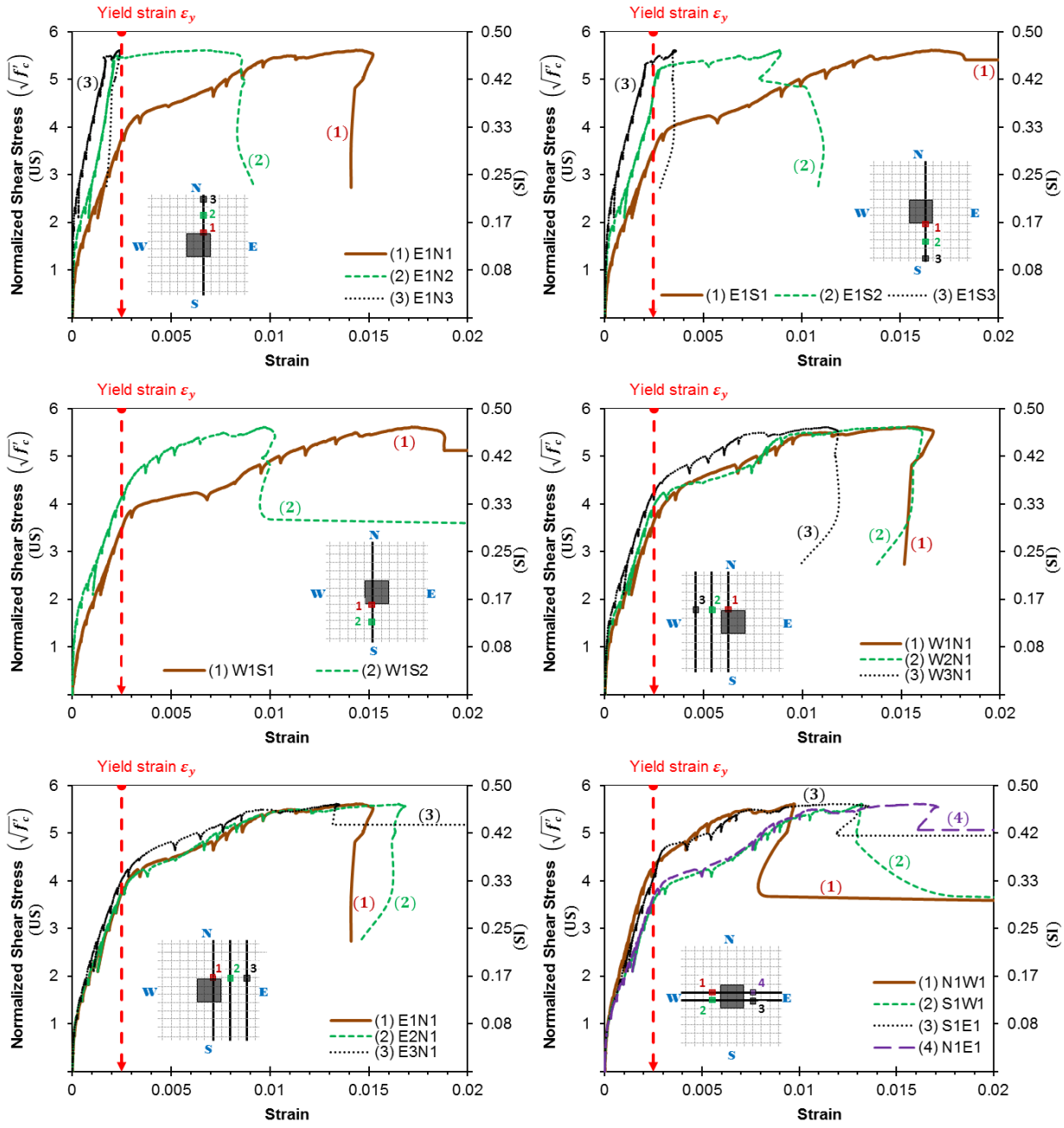


*Fig. B-12: Measured strains in the slab flexural reinforcing bars of Specimen S08R*

*(see Fig. 3-25 for strain gauge labels and locations)*

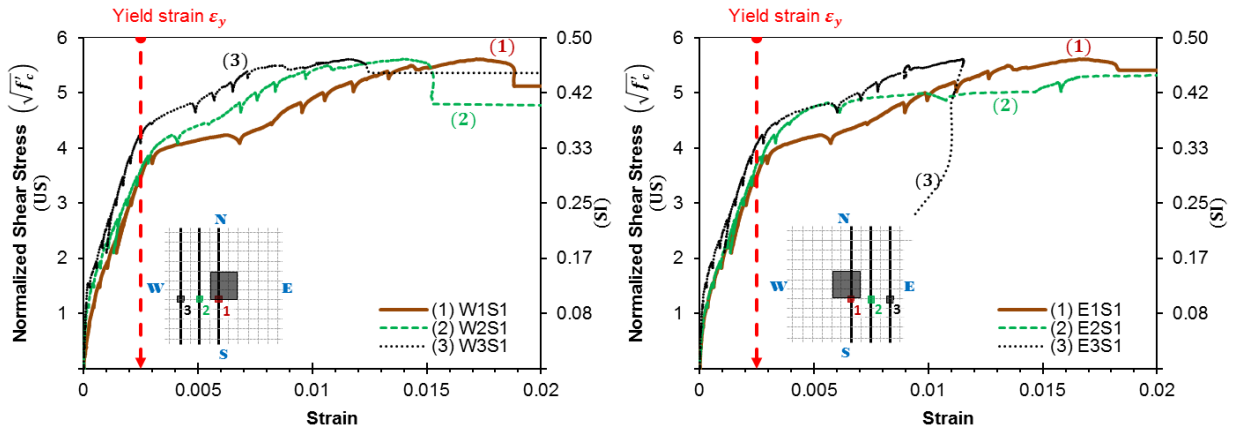


*Fig. B-12: Measured strains in the slab flexural reinforcing bars of Specimen S08R (continued)*

*(see Fig. 3-25 for strain gauge labels and locations)*

### *B.2.3.3 Strains in Shear Studs*

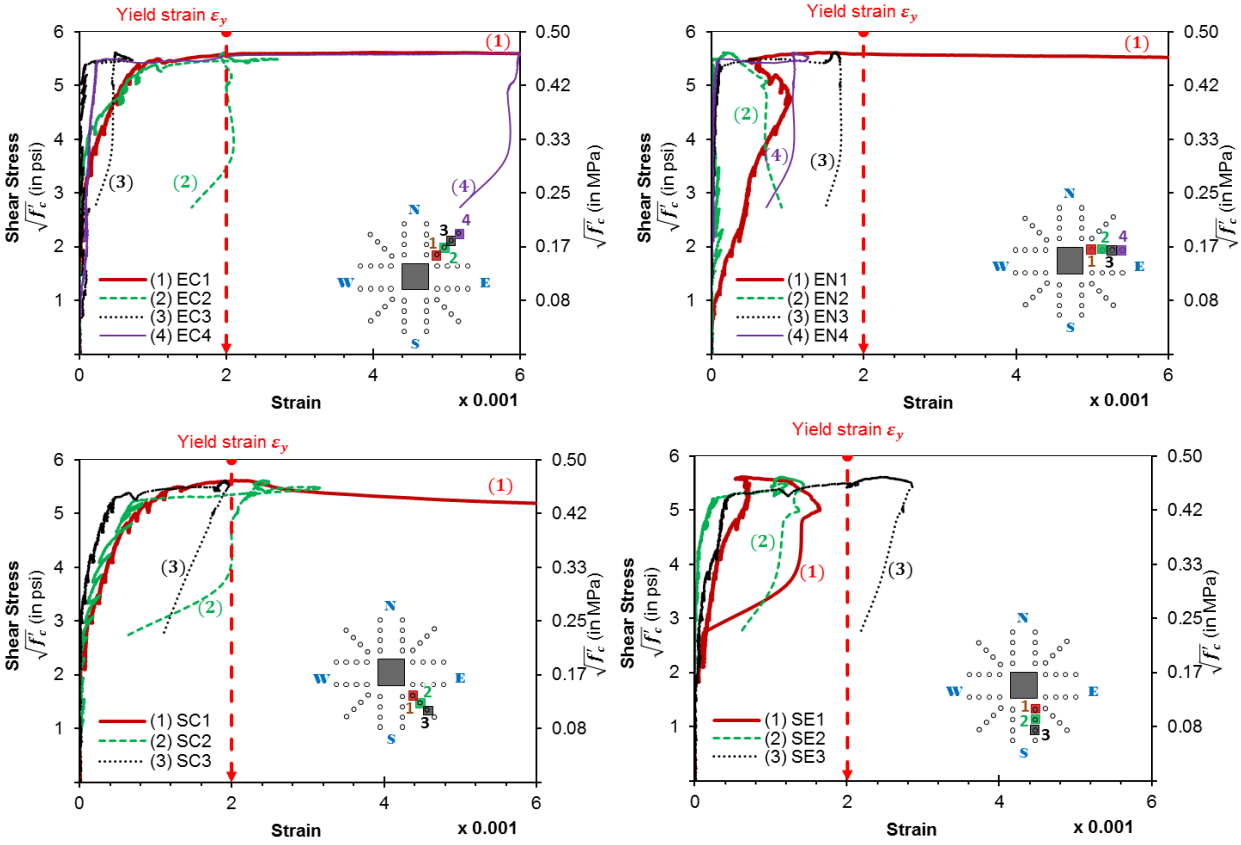


*Fig. B-13: Measured strains in the shear studs for Specimen S08R*
*(see Fig. 3-26 for strain gauge labels and locations)*

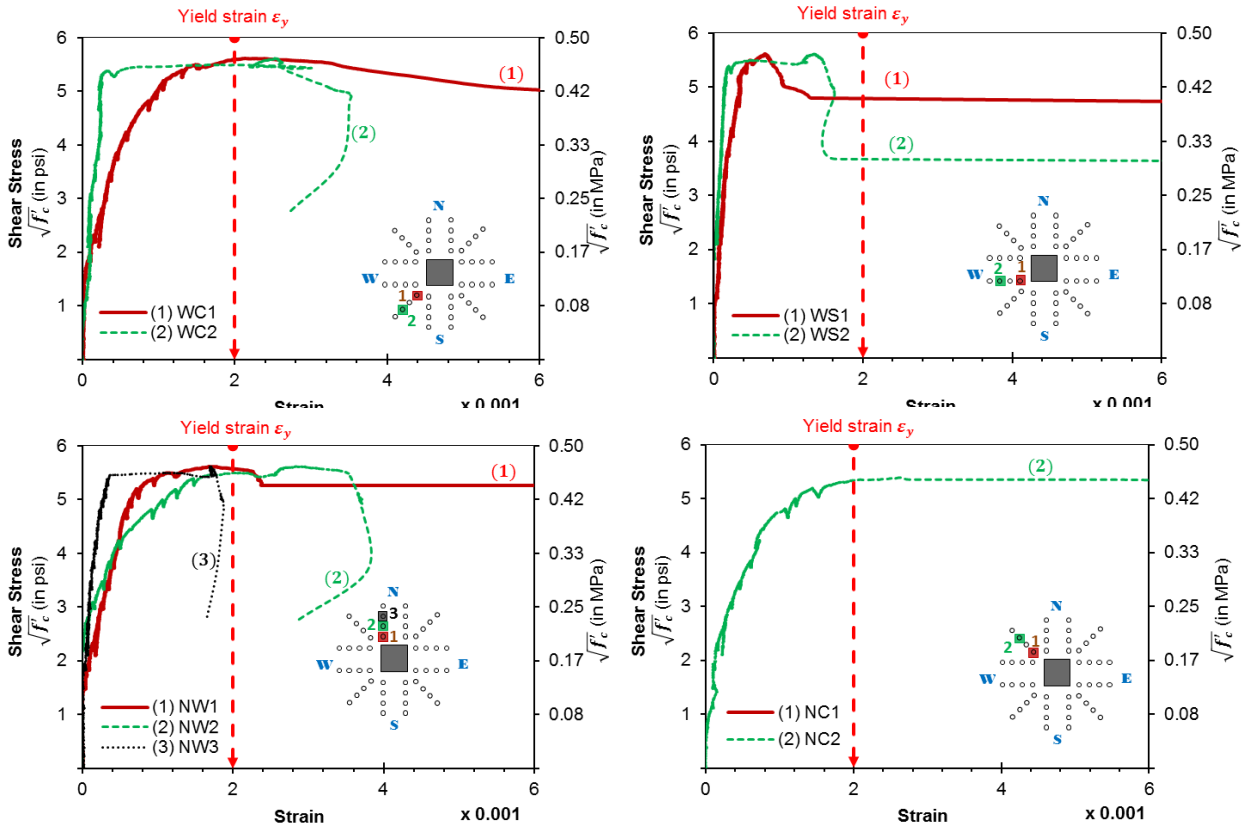


*Fig. B-13: Measured strains in the shear studs for Specimen S08R (continued)*

*(see Fig. 3-26 for strain gauge labels and locations)*

### *B.2.3.4 Slab Through-thickness Expansions*

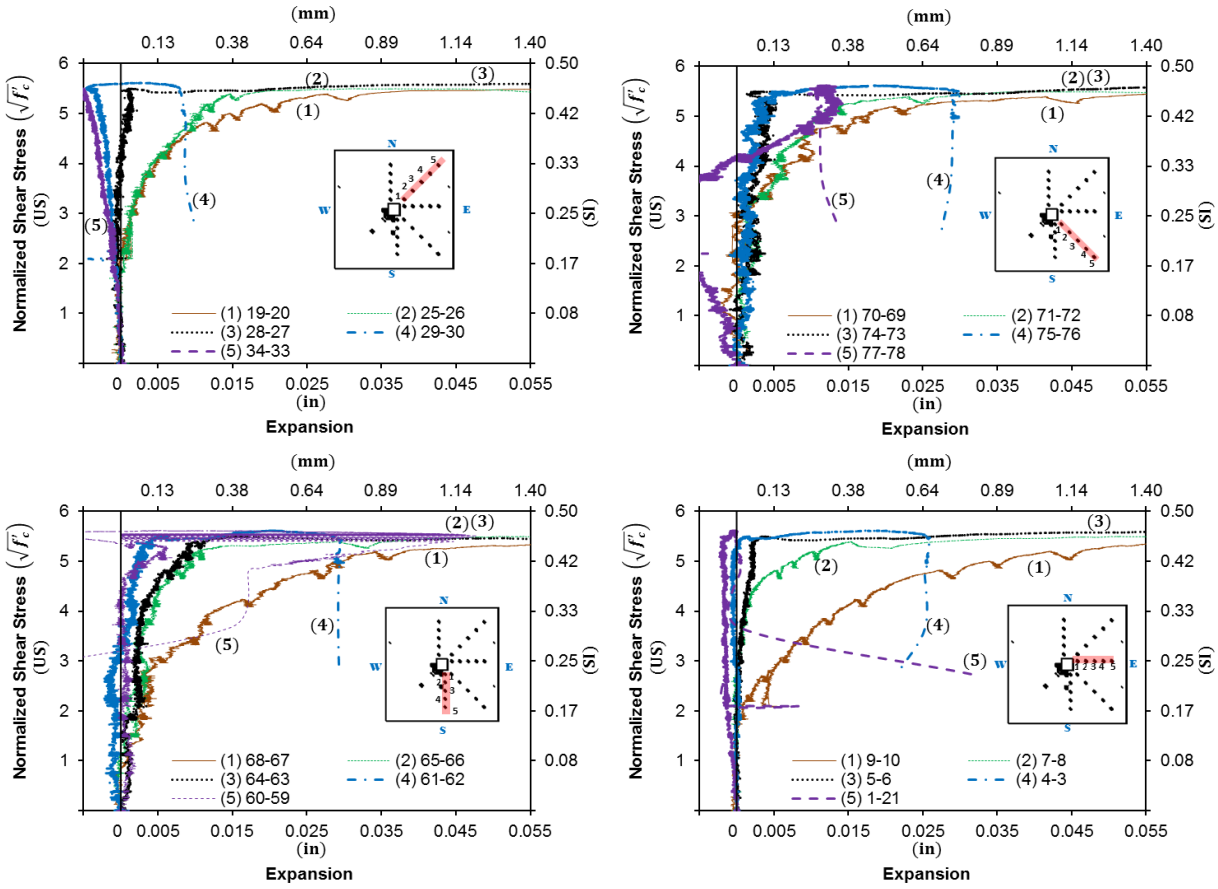


*Fig. B-14: Measured slab through-thickness expansion for Specimen S08R*

*(see Fig. 3-24 for labels and locations)*

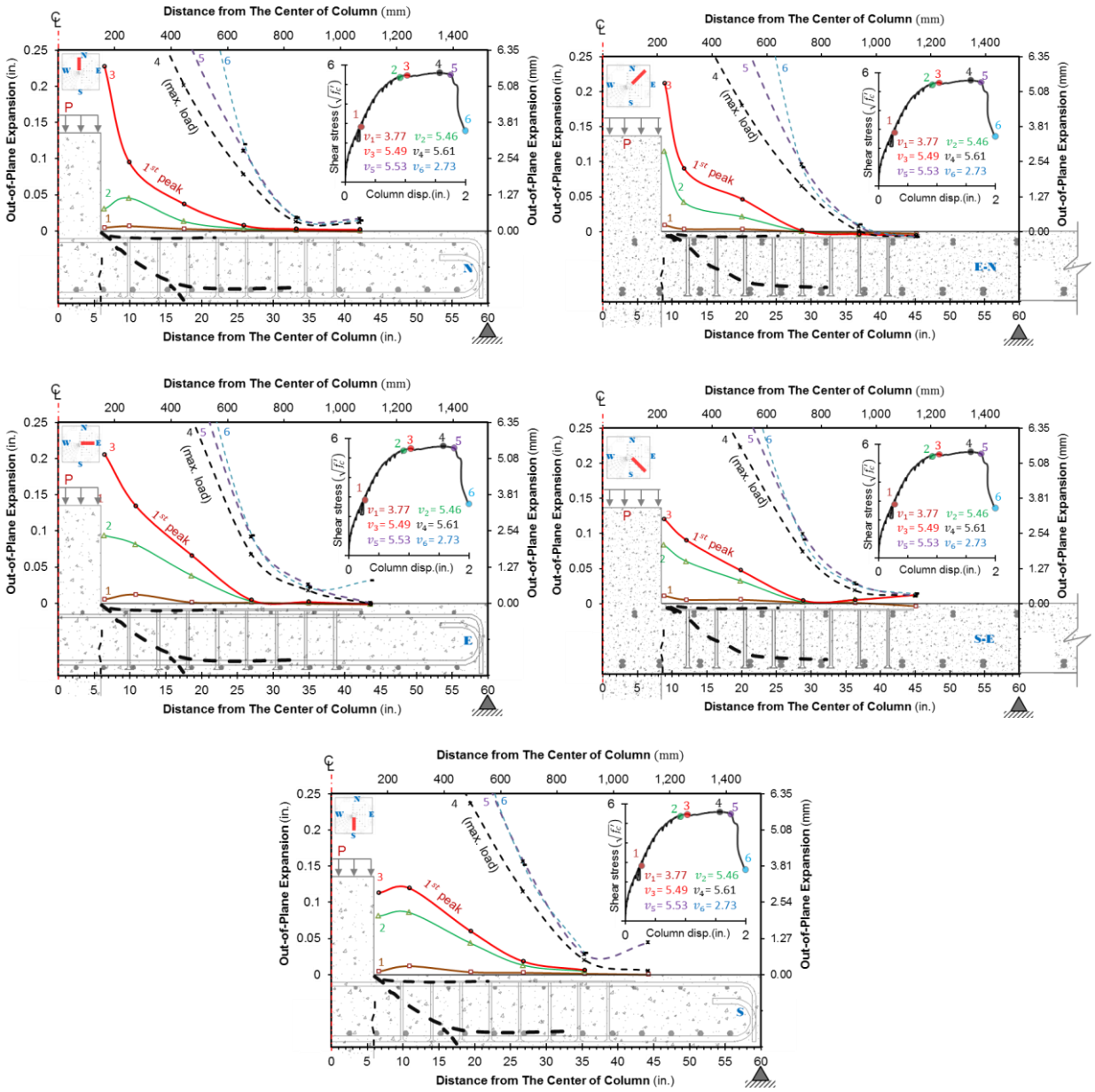


Fig. B-15: Measured slab through-thickness expansions for Specimen S08R at different loads

## B.2.4 Specimen S12O

### *B.2.4.1 Cracks*

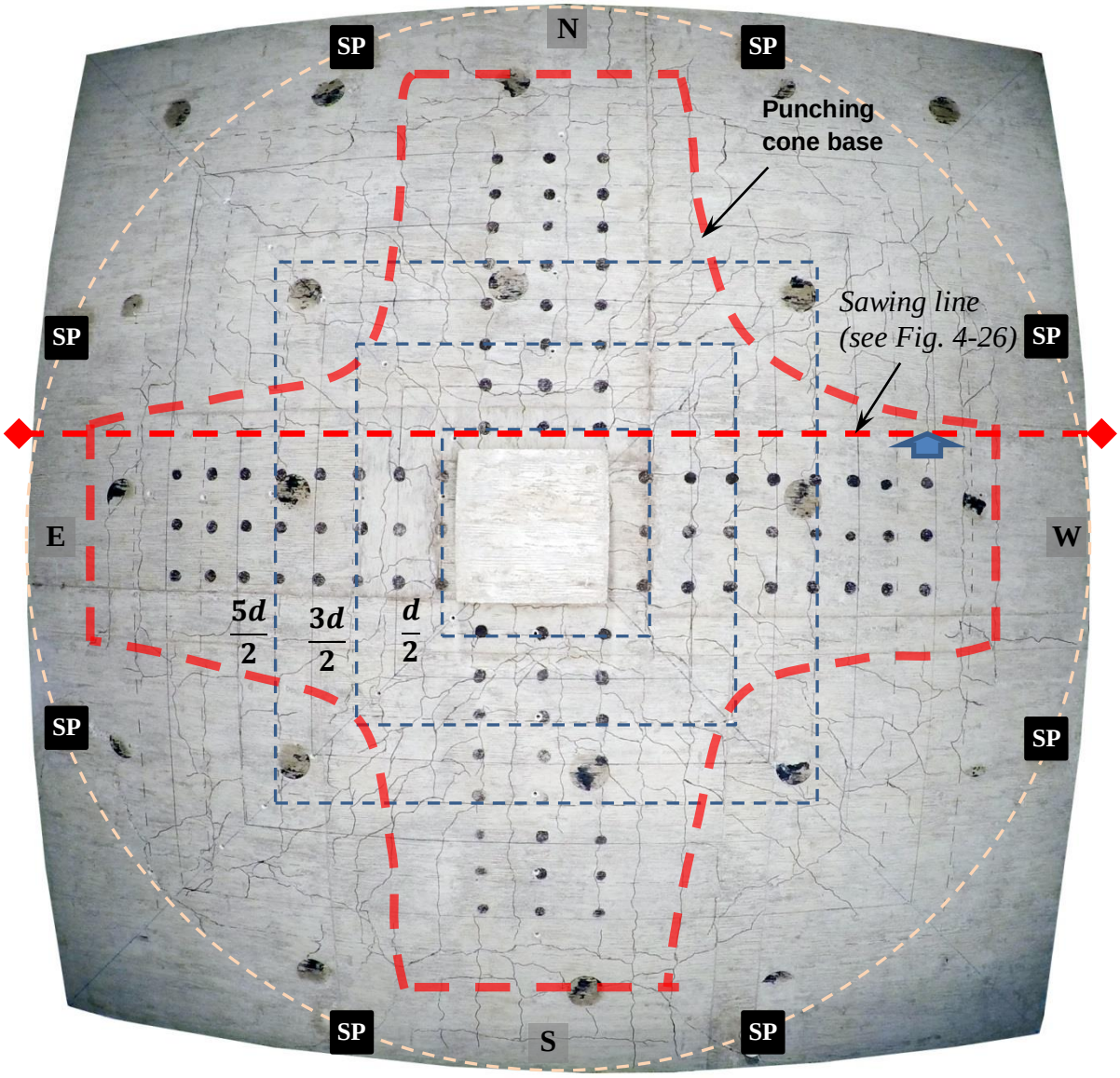


*Fig. B-16: Cracks on the bottom of slab S12O after the Test*

### *B.2.4.2 Strains in Slab Flexural Reinforcing bars*

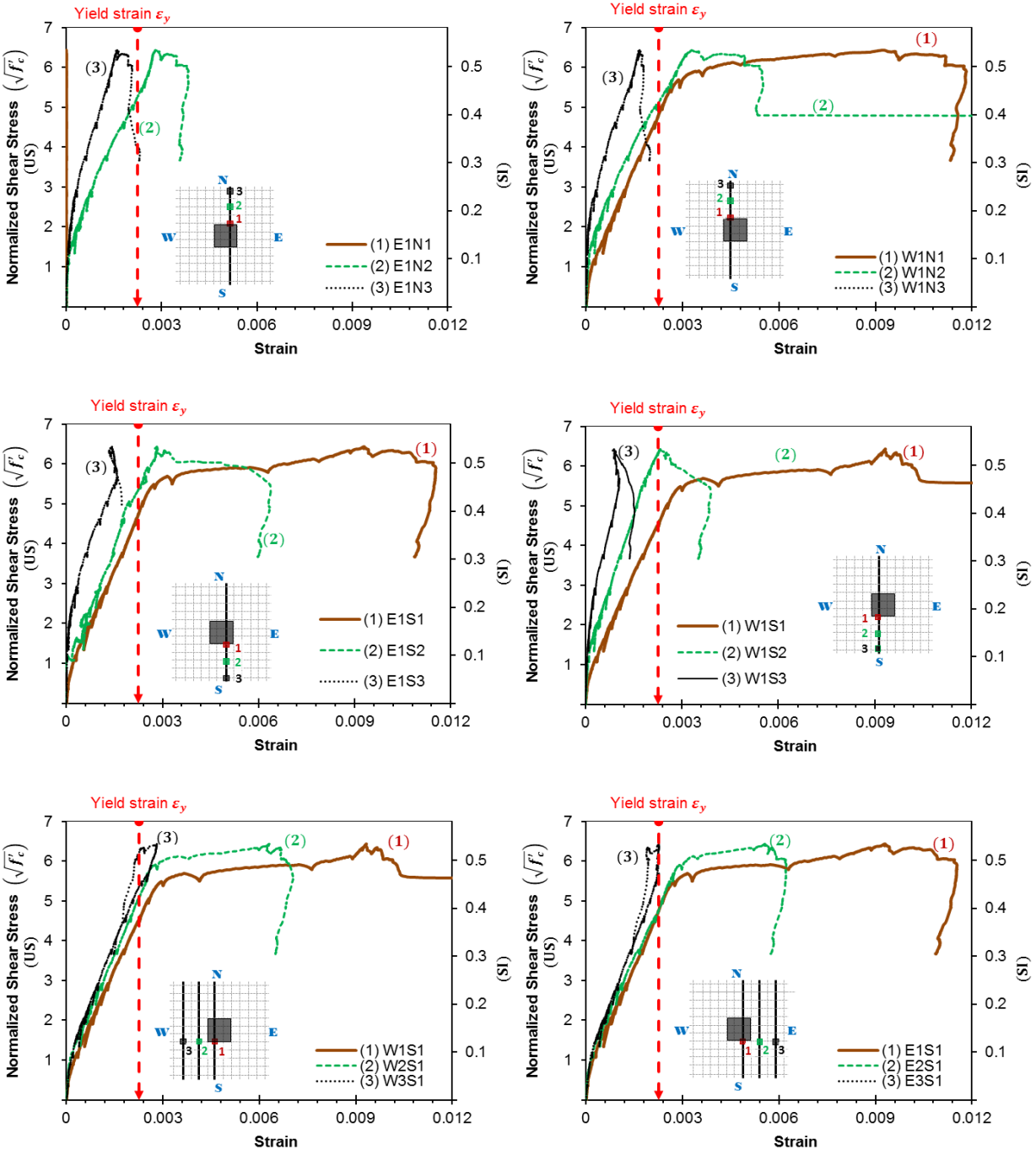


*Fig. B-17: Measured strains in the slab flexural reinforcing bars of Specimen S12O*

*(see Fig. 3-25 for strain gauge labels and locations)*

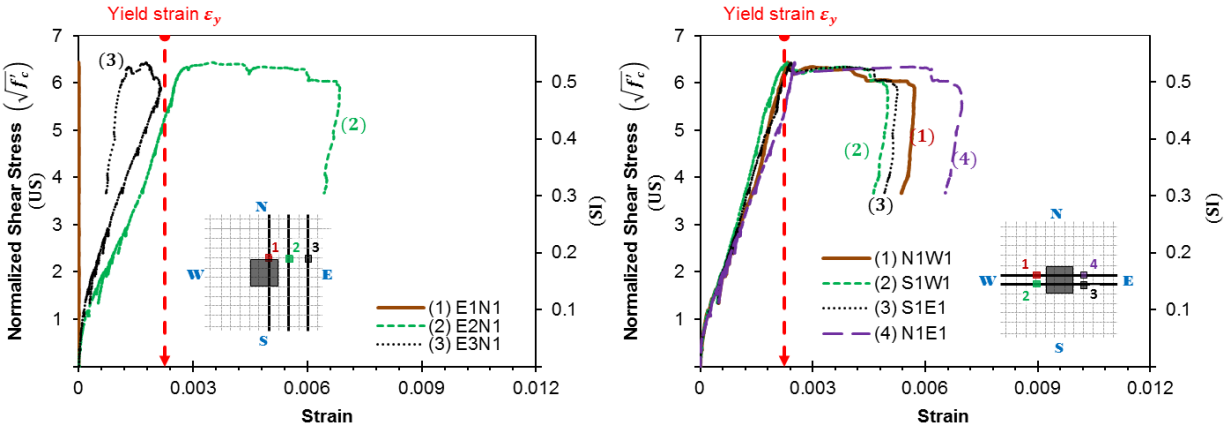


*Fig. B-17: Measured strains in the slab flexural reinforcing bars of Specimen S12O (continued)*

*(see Fig. 3-25 for strain gauge labels and locations)*

### *B.2.4.3 Strains in Shear Studs*

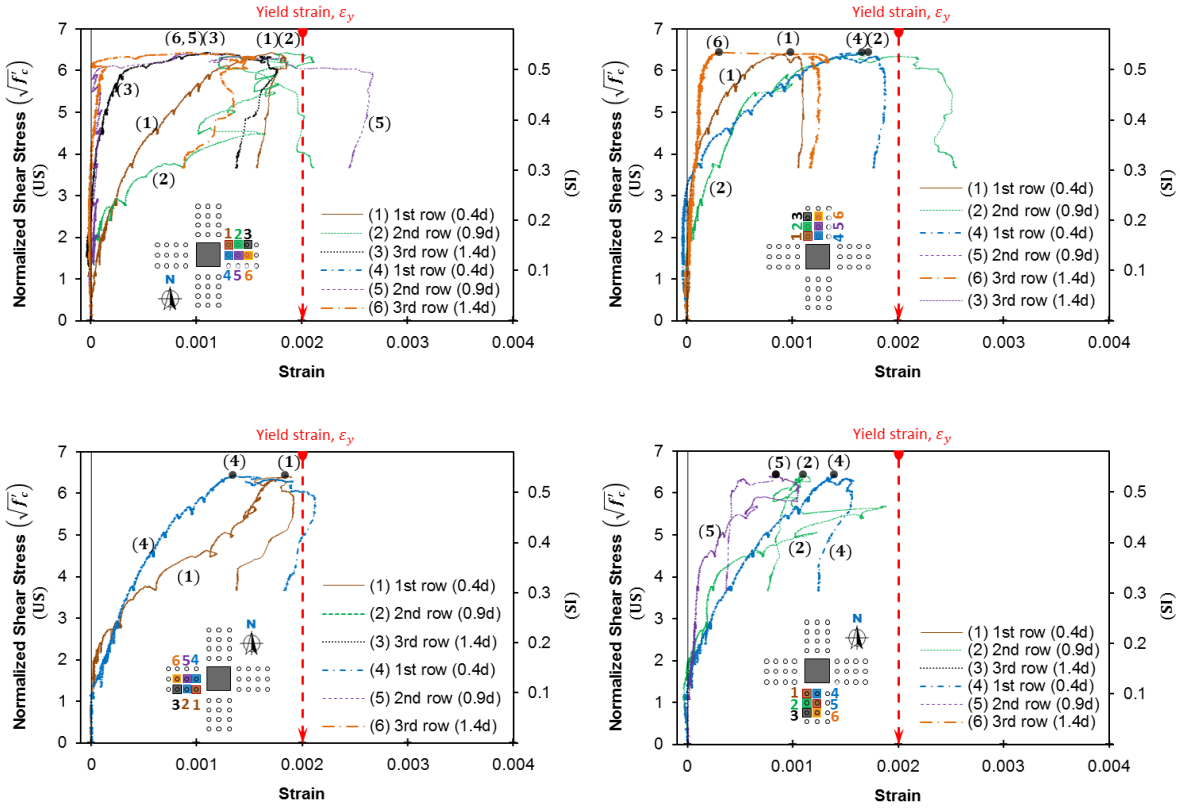


*Fig. B-18: Measured strains in the shear studs for Specimen S12O*

*(see Fig. 3-26 for strain gauge labels and locations)*

### *B.2.4.4 Slab Through-thickness Expansions*

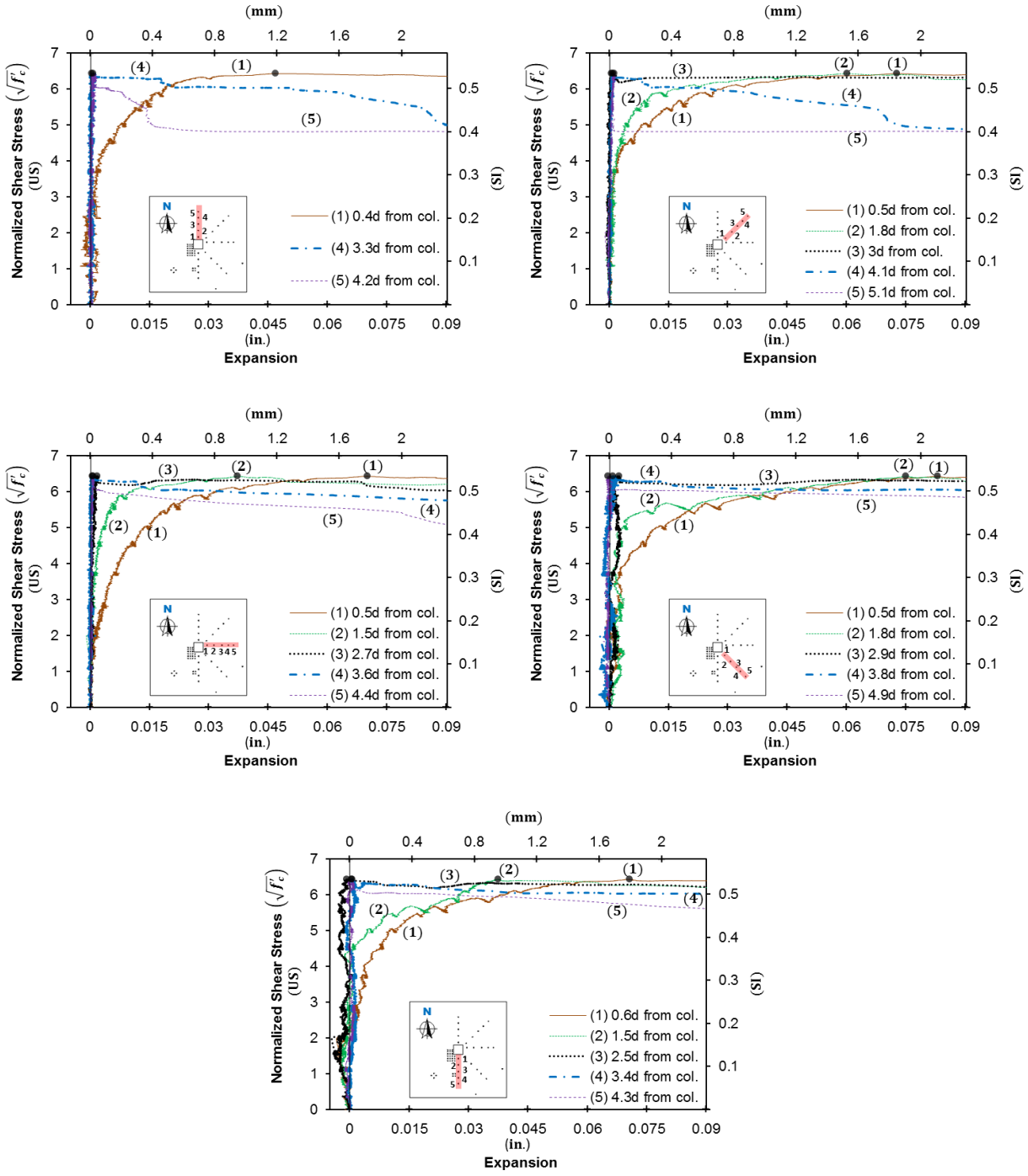


*Fig. B-19: Measured slab through-thickness expansion for Specimen S12O*

*(see Fig. 3-24 for labels and locations)*

## B.2.5 Specimen S12R

### *B.2.5.1 Cracks*

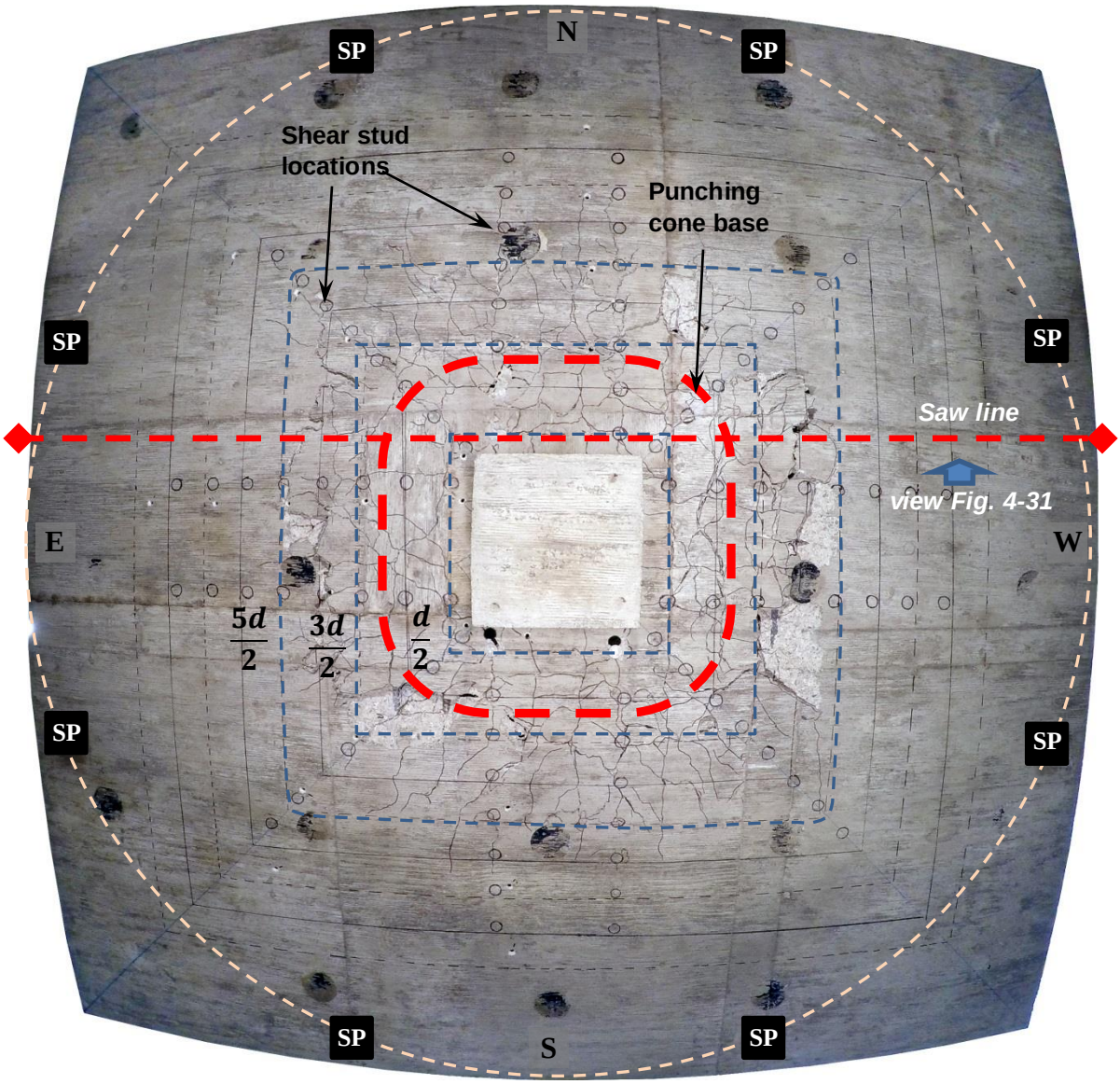


*Fig. B-20: Cracks on the bottom of slab S12R after the completion of the test*

### *B.2.5.2 Strains in Slab Flexural Reinforcing bars*

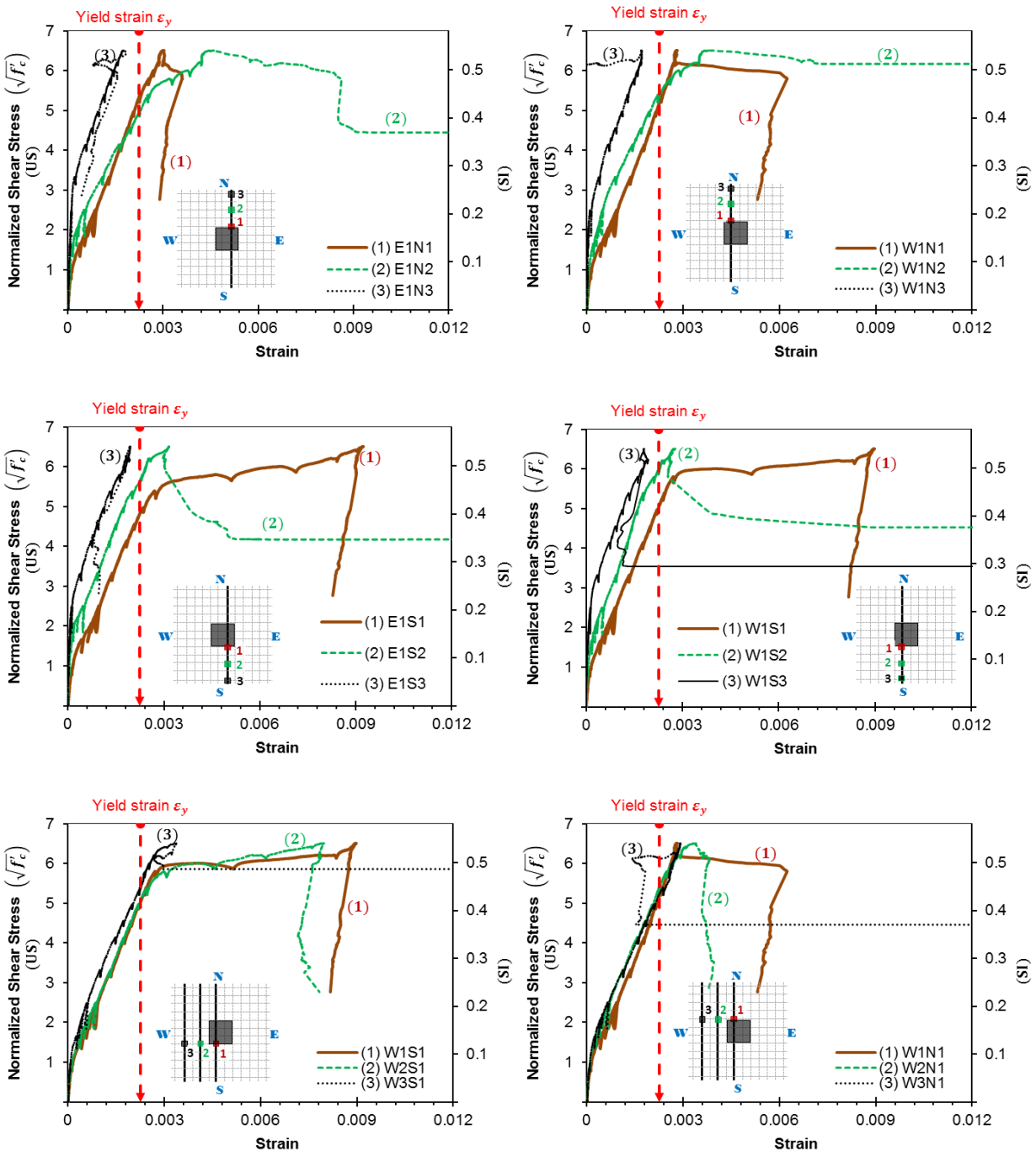


*Fig. B-21: Measured strains in the slab flexural reinforcing bars of Specimen S12R*

*(see Fig. 3-25 for strain gauge labels and locations)*

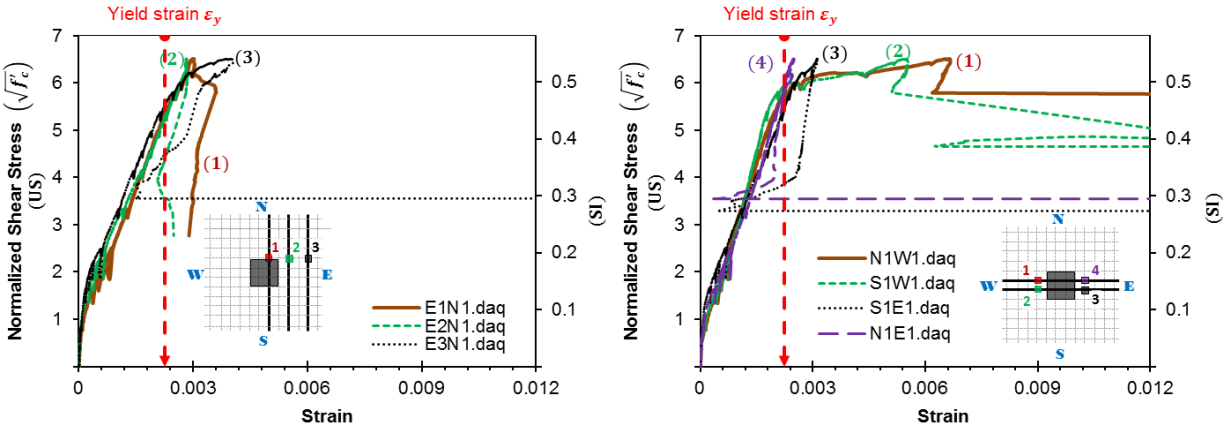


*Fig. B-21: Measured strains in the slab flexural reinforcing bars of Specimen S12R (continue)*

*(see Fig. 3-25 for strain gauge labels and locations)*

### *B.2.5.3 Strains in Shear Studs*

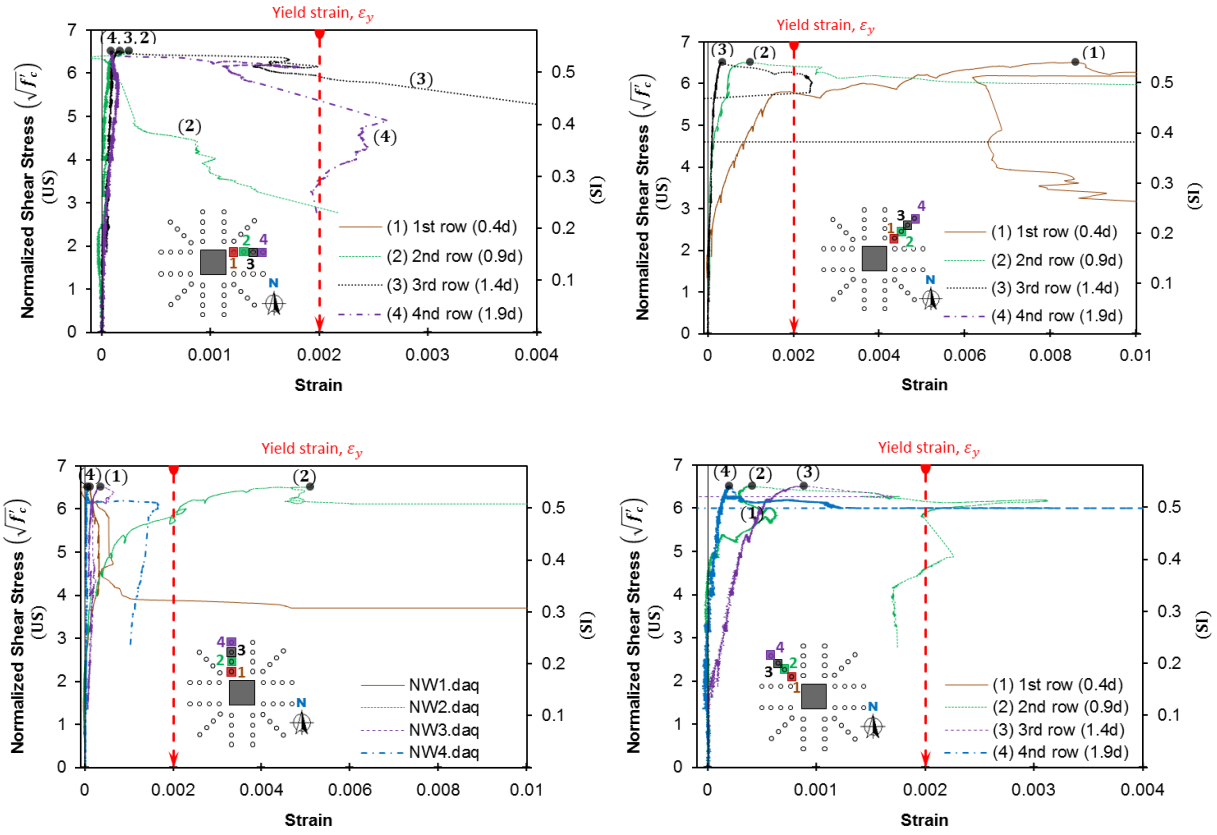


*Fig. B-22: Measured strains in the shear studs for Specimen S12R*

*(see Fig. 3-26 for strain gauge labels and locations)*

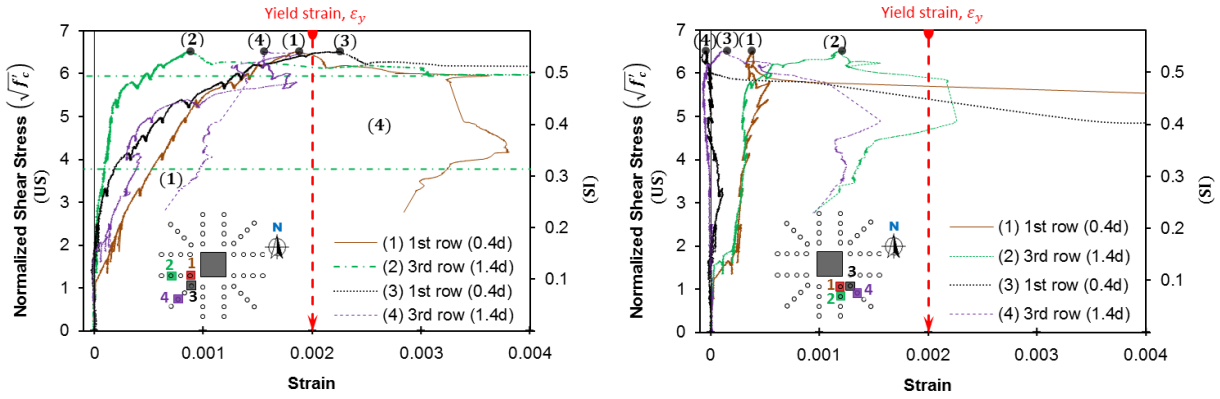


*Fig. B-22: Measured strains in the shear studs for Specimen S12R (continue)*

*(see Fig. 3-26 for strain gauge labels and locations)*

### *B.2.5.4 Slab Through-thickness Expansions*

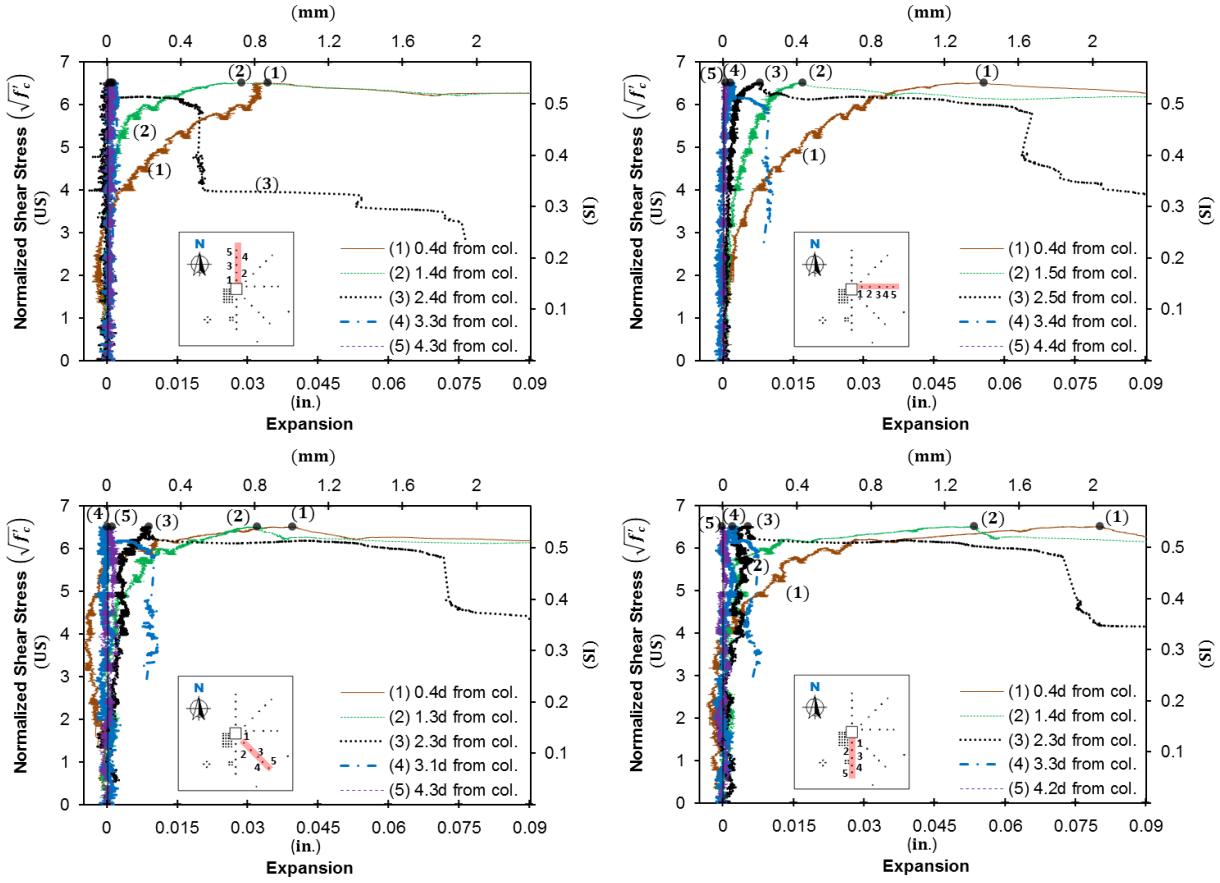


*Fig. B-23: Measured slab through-thickness expansion for Specimen S08R*

*(see Fig. 3-24 for labels and locations)*

# APPENDIX C

# CALCULATION OF $V_{fn}$ FOR FLAT PLATE SYSTEMS

## C.1 HATCHER ET AL[57] TEST OF A FLAT PLATE SYSTEM

Top flexural reinforcing bars for the slab in the Hatcher et al[57] test is shown in Fig. C-1, and this section presents a calculation of the local flexurally-induced shear strength (Eq. 43) for an interior slab-column connection at Column 7.

Span $L := 5ft = 1.524 \cdot m$

Column width $h_c := 6in = 152.4\,mm$ Thus, $\beta := \frac{h_c}{L} = 0.1$

Slab thickness $t := 1.75in = 44\,mm$

Slab flexural effective depth, $d := 1.438in = 37\,mm$

Concrete properties (at test date) $f_c := 2680psi = 18.5\,MPa$

Flexural reinforcement properties $f_y := 36700psi$ [146]

1/8 in. square rebar $A_s := \left(\frac{1in}{8}\right)^2 = 10 \cdot mm^2$

***1. Calculation of Vfn for slab-column connection 7***

The ACI transfer width $b_{tfw} := h_c + 2 \cdot (1.5 \cdot t) = 11.25 \cdot in$ $b_{tfw} = 286\,mm$

Thus, two bar spacings were used in this transfer width.

*a. 1st spacing* $s_1 := \left(\frac{3}{4}\right)in = 0.75 \cdot in$ within the width of $w_1 := 13 \cdot s_1 = 9.75\,in$

$s_1 = 19\,mm$ $w_1 = 248\,mm$

Reinforcement ratio $\rho_1 := \frac{A_s}{s_1 \cdot d} = 1.45 \cdot \%$

Slab unit moment strength $m_1 := \rho_1 \cdot f_y \cdot \left(1 - \frac{\rho_1 \cdot f_y}{1.7 \cdot f_c}\right) \cdot d^2 = 971.2 \cdot \frac{lbf \cdot in}{in}$

$m_1 = 4320\,\frac{N \cdot m}{m}$

*b. 2nd spacing* $s_2 := \left(1 + \frac{1}{2}\right)in = 1.5 \cdot in$ within the width of $w_2 := b_{tfw} - w_1 = 1.5\,in$

$s_2 = 38\,mm$ $w_2 = 38\,mm$

Reinforcement ratio $\rho_2 := \frac{A_s}{s_2 \cdot d} = 0.72 \cdot \%$

Slab unit moment strength $m_2 := \rho_2 \cdot f_y \cdot \left(1 - \frac{\rho_2 \cdot f_y}{1.7 \cdot f_c}\right) \cdot d^2 = 518 \cdot \frac{lbf \cdot in}{in}$

$m_2 = 2303 \frac{N \cdot m}{m}$

Unit moment strength for slab with the ACI transfer width

$m := \frac{m_1 \cdot w_1 + m_2 \cdot w_2}{b_{tfw}} = 911 \frac{lbf \cdot in}{in}$ $\quad m = 4051 \frac{N \cdot m}{m}$

Thus, the local flexurally-triggered shear strength

$V_{fn} := (6.5 + 20 \cdot \beta) \cdot m = 7.74 kip$ $\quad V_{fn} = 34.4 kN$

***2. Measured shear strength Vu***

$V_u := 7.5 kip$ $\quad V_u = 33.4 kN$

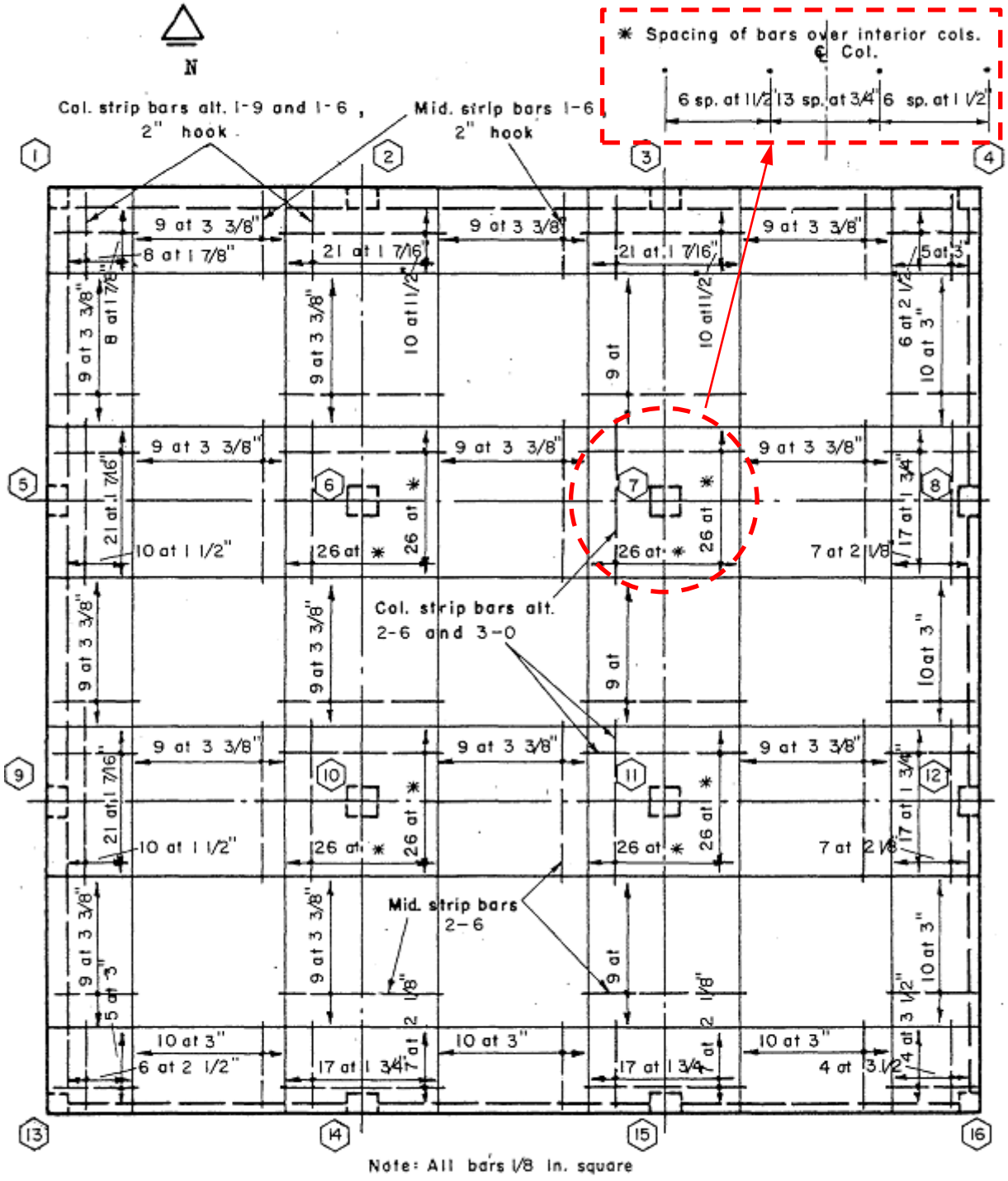


*Fig. C-1: Top flexural rienforcing bars for the slab in the Hatcher et al[57] test*

## C.2 GURALNICK AND LA FRAUGH[58] TEST OF A FLAT PLATE SYSTEM

Top flexural reinforcing bars for the slab in the Guralnick and La Fraugh[58] test is shown in Fig. C-2, and this section presents a calculation of the local flexurally-induced shear strength (Eq. 43) for an interior slab-column connection at Column 7.

Span $L := 15ft = 4.57 \cdot m$

Column width $h_c := 18in = 457\,mm$ Thus, $\beta := \frac{h_c}{L} = 0.1$

Slab thickness $t := 5.25in = 133\,mm$

Slab flexural effective depth, $d := 4.563in = 116\,mm$

Concrete properties (at test date) $f_c := 4715psi = 32.5\,MPa$

Flexural reinforcement properties $f_y := 44500psi$

#4 bars $A_s := 0.2in^2 = 129 \cdot mm^2$

***1. Calculation of Vfn for slab-column connection 7***

The ACI transfer width $b_{tfw} := h_c + 2 \cdot (1.5 \cdot t) = 33.75 \cdot in$ $b_{tfw} = 857\,mm$

Thus, two bar spacings were used in this transfer width.

*a. 1st spacing* $s_1 := \left(3 + \frac{1}{8}\right)in = 3.125 \cdot in$ within the width of $w_1 := 9 \cdot s_1 = 28.1\,in$

$s_1 = 79\,mm$ $w_1 = 714\,mm$

Reinforcement ratio $\rho_1 := \frac{A_s}{s_1 \cdot d} = 1.4 \cdot \%$

Slab unit moment strength $m_1 := \rho_1 \cdot f_y \cdot \left(1 - \frac{\rho_1 \cdot f_y}{1.7 \cdot f_c}\right) \cdot d^2 = 12 \cdot \frac{kip \cdot in}{in}$

$m_1 = 53 \frac{kN \cdot m}{m}$

*b. 2nd spacing* $s_2 := \left(6 + \frac{3}{8}\right)in = 6.375 \cdot in$ within the width of $w_2 := b_{tfw} - w_1 = 5.625\,in$

$s_2 = 162\,mm$ $w_2 = 143\,mm$

Reinforcement ratio $\rho_2 := \frac{A_s}{s_2 \cdot d} = 0.69 \cdot \%$

Slab unit moment strength $m_2 := \rho_2 \cdot f_y \cdot \left(1 - \frac{\rho_2 \cdot f_y}{1.7 \cdot f_c}\right) \cdot d^2 = 6 \cdot \frac{kip \cdot in}{in}$

$m_2 = 27 \frac{kN \cdot m}{m}$

Unit moment strength for slab with the ACI transfer width

$$m := \frac{m_1 \cdot w_1 + m_2 \cdot w_2}{b_{tfw}} = 11 \frac{kip \cdot in}{in} \qquad m = 49 \frac{kN \cdot m}{m}$$

Thus, the local flexurally-triggered shear strength

$$V_{fn} := (6.5 + 20 \cdot \beta) \cdot m = 93.6\,kip \qquad V_{fn} = 416\,kN$$

***2. Measured shear strength Vu***

$$q_u := 369psf$$

Estimate shear transfer at column 7 when failure, using factor 1.15 for shear at the first interior support [5]

$$V_u := q_u \cdot \left( \frac{L}{2} + 1.15 \cdot \frac{L}{2} \right)^2 = 95.9\,kip \qquad V_u = 427\,kN$$

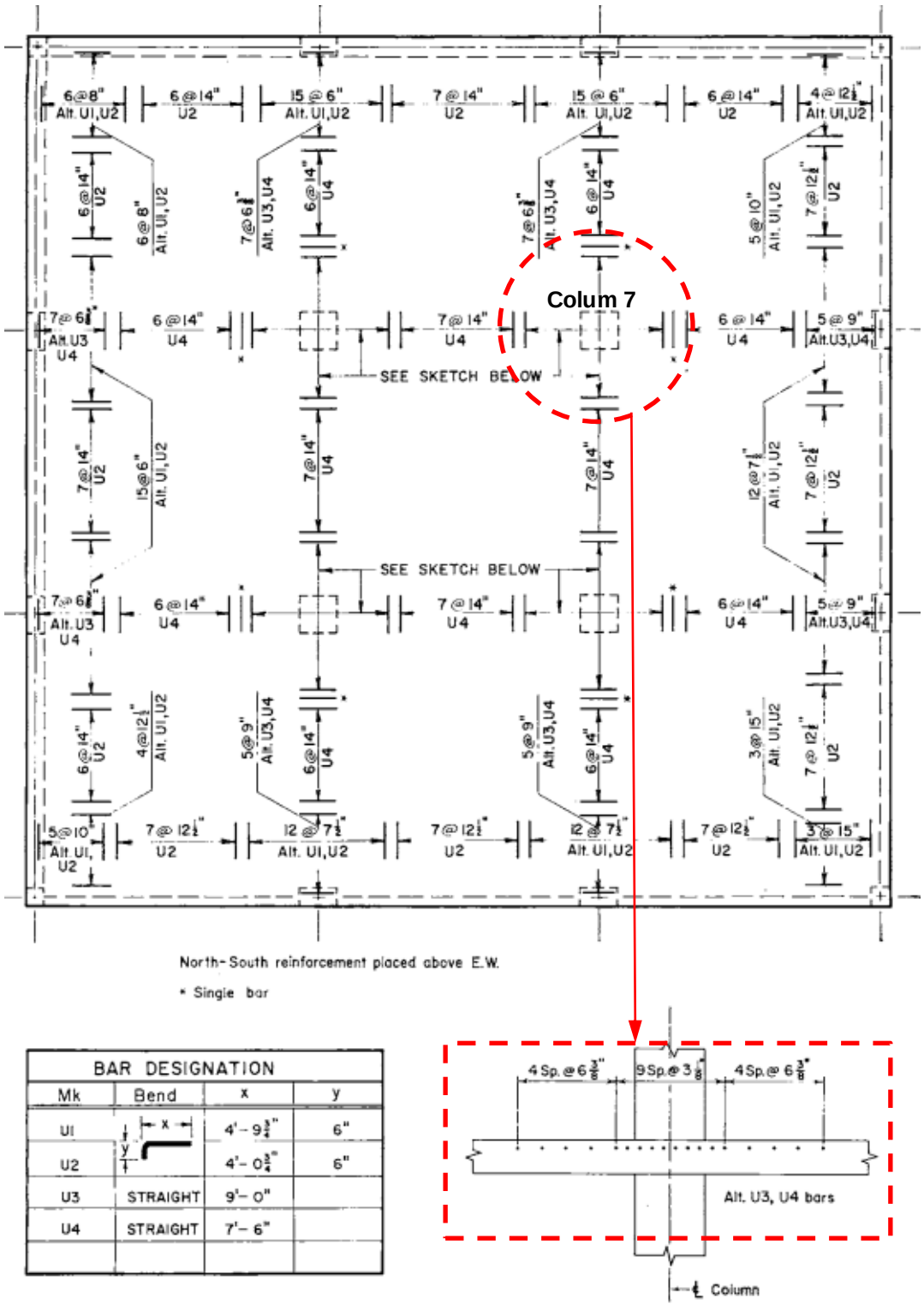


*Fig. C-2: Top flexural rienforcing bars for the slab in the Guralnick and La Fraugh[58] test*

# APPENDIX D
# CONCRETE DAMGAGED PLASTICITY MODEL

This appendix describes the Concrete Damaged Plasticity model used in Abaqus[19]. This model was based on the models proposed by Lubliner et al[100] in 1989 and developed by Lee and Fenves[138] in 1998.

## D.1 STRAIN DECOMPOSITION AND EFFECTIVE STRESS

The strain tensor ($\boldsymbol{\varepsilon}$, rank two tensor $\varepsilon_{ij}$) is decomposed into elastic part ($\boldsymbol{\varepsilon}^e$) and plastic part ($\boldsymbol{\varepsilon}^p$) as follows.

$$\boldsymbol{\varepsilon} = \boldsymbol{\varepsilon}^e + \boldsymbol{\varepsilon}^p \qquad (D1)$$

The plastic strain ($\boldsymbol{\varepsilon}^p$) represents all irreversible deformations in due to both compression and tension loading. The elastic part ($\boldsymbol{\varepsilon}^e$) is computed using the elastic stiffness $\boldsymbol{E}$, a rank four tensor ($E_{ijkl}$),

$$\boldsymbol{\varepsilon}^e = \boldsymbol{E}^{-1} : \boldsymbol{\sigma} \qquad (D2)$$

in which $\boldsymbol{\sigma}$ is a stress tensor (rank two, $\sigma_{ij}$). Substituting Eq. (D1) into Eq. (D2), the stress tensor is computed as follows.

$$\boldsymbol{\sigma} = \boldsymbol{E} : (\boldsymbol{\varepsilon} - \boldsymbol{\varepsilon}^p) \qquad (D3)$$

Using the concept of the continuum damage theory, degradation of the elastic stiffness $\boldsymbol{E}$ due to damages in compression and tension loadings is accounted for using a rank four tensor $\boldsymbol{D}$, as given in Eq. (D4). For practical reasons isotropic degradation damage is assumed and presented by a scalar damage variable $D$, which varies from 0 to 1. The tensor $\boldsymbol{D}$ is then written as Eq. (D5). By substitution Eq. (D5) into Eq. (D4), the elastic stiffness $\boldsymbol{E}$ can be computed using Eq. (48).

$$\boldsymbol{E} = \boldsymbol{D}: \boldsymbol{E}_0 \tag{D4}$$

$$\boldsymbol{D} = \frac{1}{(1-D)}\boldsymbol{I} \tag{D5}$$

$$\boldsymbol{E} = (1-D)\boldsymbol{E}_0 \tag{48}$$

Substituting Eq. (D3) into Eq. (48), the stress tensor $\boldsymbol{\sigma}$ is computed from Eq. (D6). In this model, the effective stress tensor $\overline{\boldsymbol{\sigma}}$ is defined in Eq. (D7). This effective stress is dependent on plastic strain ($\boldsymbol{\varepsilon}^p$). The yielding (failure) surface and plastic potential are developed in the effective stress space ($\overline{\boldsymbol{\sigma}}$) instead of the stress space ($\boldsymbol{\sigma}$).

$$\boldsymbol{\sigma} = (1-D)\boldsymbol{E}_0 : (\boldsymbol{\varepsilon} - \boldsymbol{\varepsilon}^p) \tag{D6}$$

$$\overline{\boldsymbol{\sigma}} = \boldsymbol{D}: \boldsymbol{\sigma} = \frac{\boldsymbol{\sigma}}{1-D} \tag{D7}$$

$$\overline{\boldsymbol{\sigma}} = \boldsymbol{E}_0 : (\boldsymbol{\varepsilon} - \boldsymbol{\varepsilon}^p) \tag{D7a}$$

## D.2 HARDENING VARIABLE, $\boldsymbol{\kappa}$

In the concrete damaged plasticity model, the hardening variable $\boldsymbol{\kappa} = [\kappa_{\mathrm{t}} \quad \kappa_{\mathrm{c}}]$ is used to control the evolution of yield surface and to compute stress ($\boldsymbol{\sigma}$). This variable, a so-called equivalent plastic strain, consists of two independent variables $\kappa_{\mathrm{t}}$ and $\kappa_{\mathrm{c}}$ for tension and compression, respectively. In Abaqus/Standard[19], the evolution (rate) of the variable $\boldsymbol{\kappa}$ is defined as follows.

$$\dot{\boldsymbol{\kappa}} = \hat{\boldsymbol{h}}(\hat{\overline{\boldsymbol{\sigma}}}) \cdot \hat{\dot{\boldsymbol{\varepsilon}}}^p \tag{D8}$$

In which $\hat{\overline{\boldsymbol{\sigma}}} = [\bar{\sigma}_1 \quad \bar{\sigma}_2 \quad \bar{\sigma}_3]$ is the eigenvalue matrix of the effective stress tensor ($\overline{\boldsymbol{\sigma}}$), and $\hat{\dot{\boldsymbol{\varepsilon}}}^{\mathrm{p}} = \left[\dot{\varepsilon}_1^p \quad \dot{\varepsilon}_2^p \quad \dot{\varepsilon}_3^p\right]$ is the eigenvalue matrix of the plastic strain rate tensor ($\dot{\boldsymbol{\varepsilon}}^{\mathrm{p}}$), which is defined using a nonassociated plastic flow discussed latter. The matrix $\hat{\mathbf{h}}(\hat{\overline{\boldsymbol{\sigma}}})$ is defined in the following equation.

$$\hat{\boldsymbol{h}}(\hat{\overline{\boldsymbol{\sigma}}}) = \begin{bmatrix} r(\hat{\overline{\boldsymbol{\sigma}}}) & 0 & 0 \\ 0 & 0 & -(1-r(\hat{\overline{\boldsymbol{\sigma}}})) \end{bmatrix} \tag{D9}$$

The scalar quantity $r(\hat{\overline{\boldsymbol{\sigma}}})$ in Eq. (D9) is a weight factor (varies from 0 to 1) and computed using Eq. (D10),

$$r(\hat{\boldsymbol{\sigma}}) = \frac{\sum_{i=1}^{3}\langle\bar{\sigma}_i\rangle}{\sum_{i=1}^{3}|\bar{\sigma}_i|} \tag{D10}$$

in which the Macauley bracket $\langle\cdot\rangle$ is defined as $\langle\hat{\bar{\sigma}}_{\mathrm{i}}\rangle = (\bar{\sigma}_{\mathrm{i}} + |\bar{\sigma}_{\mathrm{i}}|)/2$. Thus, $r(\hat{\boldsymbol{\sigma}}) = 0$ if all principal stresses ($\bar{\sigma}_i$) are negative, $r(\hat{\boldsymbol{\sigma}}) = 1$ if they are all positive.

The damage variable ($D$), which is assumed to be a function of $\boldsymbol{\kappa}$ in Abaqus/Standard, is defined as follows.

$$D = D(\boldsymbol{\kappa}) = 1 - \big(1 - s_c D_t(\boldsymbol{\kappa})\big)\big(1 - s_t D_c(\boldsymbol{\kappa})\big) \tag{D11}$$

In which $0 \le D_t \le 1$ and $0 \le D_{\mathrm{c}} \le 1$ are tensile and compressive damage variables, respectively. The parameters $\mathrm{s_t}$ and $\mathrm{s_c}$ are given in terms of function $r(\hat{\boldsymbol{\sigma}})$, as shown in Eqs. (D12) and (D13).

$$s_t = 1 - w_t r(\hat{\boldsymbol{\sigma}}) \tag{D12}$$

$$s_c = 1 - w_c[1 - r(\hat{\boldsymbol{\sigma}})] \tag{D13}$$

In which, factors $w_t$ and $w_{\mathrm{c}}$, control the recovery of the tensile and compressive stiffness for load reversal, are assumed to be material properties. In Abaqus/Stardard, $w_t = 0$ and $w_{\mathrm{c}} = 1$ are the default values. Degradation damage variables $D_{\mathrm{t}}$ and $D_{\mathrm{c}}$ in Eq. (D11) are defined in uniaxial tensile and compressive load conditions, respectively.

### D.2.1 Uniaxial Tensile Stress Conditions

For uniaxial tensile stress conditions principal stresses are $\bar{\sigma}_1 > 0$ and $\bar{\sigma}_2 = \bar{\sigma}_3 = 0$, and thus, $r(\hat{\boldsymbol{\sigma}}) = 1$. This value leads to $\mathrm{s_c} = 1$, $\mathrm{s_t} = 1 - w_{\mathrm{t}}$, $\dot{\kappa}_{\mathrm{t}} = \dot{\varepsilon}_1^{\mathrm{p}} = \dot{\varepsilon}_{\mathrm{t}}^{\mathrm{p}}$, and $\dot{\kappa}_{\mathrm{c}} = 0$. So, damage variable in compression ($\kappa_{\mathrm{c}}$) and degradation damage variable ($\mathrm{D_c}$) are equal to zero for these loading conditions. Damage variable in tension ($\kappa_{\mathrm{c}}$) is set as plastic tensile strain ($\varepsilon_{\mathrm{t}}^{\mathrm{p}}$, Fig. D-1), and degradation damage variable ($D$) is a function of only $\kappa_{\mathrm{t}}$ (or $\varepsilon_{\mathrm{t}}^{\mathrm{p}}$), as shown in Eq. (D14).

$$D = D_t(\kappa_t) = D_t\big(\varepsilon_t^p\big) \tag{D14}$$

In Abaqus/Stardard, tensile degradation damage variable ($D_t$) and tensile stress ($\sigma_{\mathrm{t}}$) are inputted as a tabular function of a cracking strain ($\varepsilon_{\mathrm{t}}^{\mathrm{cr}}$). The cracking strain is defined as $\varepsilon_{\mathrm{t}}^{\mathrm{cr}} =$

$\varepsilon_t - \sigma_t/E_0$ and shown in Fig. D-1. The damage variable ($\kappa_t$), or plastic tensile strain ($\varepsilon_t^p$), is converted from the cracking strain ($\varepsilon_t^{cr}$) using Eq. (D15).

$$\varepsilon_t^p = \varepsilon_t^{cr} - \frac{D_t}{1 - D_t}\frac{\sigma_t}{E_0} \tag{D15}$$

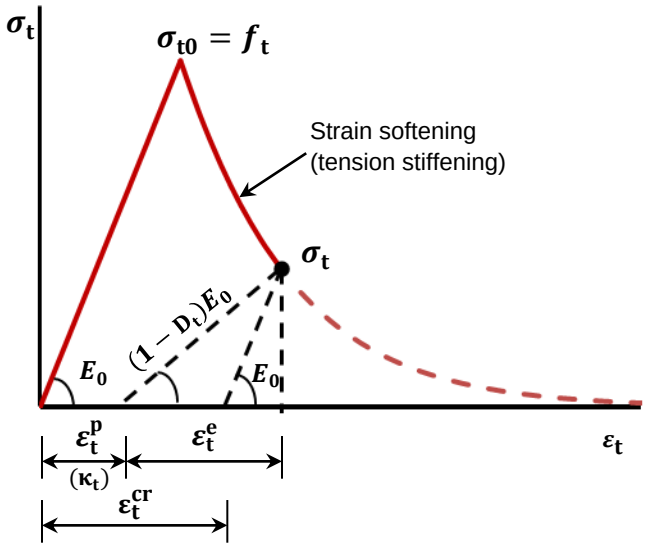


*Fig. D-1: Uniaxial tensile stress and strain relationship*

### D.2.2 Uniaxial Compressive Stress Conditions

For uniaxial compressive stress conditions principal stresses are $\bar{\sigma}_3 < 0$ and $\bar{\sigma}_1 = \bar{\sigma}_2 = 0$, and thus, $r(\hat{\boldsymbol{\sigma}}) = 0$. This value leads to $s_c = 1 - w_c$, $s_t = 1$, $\dot{\kappa}_c = \dot{\varepsilon}_1^p = \dot{\varepsilon}_c^p$, and $\dot{\kappa}_t = 0$. So, damage variable in tension ($\kappa_t$) and degradation damage variable ($D_t$) are equal to zero for these loading conditions. Damage variable in tension ($\kappa_t$) is set as plastic strain ($\varepsilon_c^p$, Fig. D-2), and degradation damage variable ($D$) is a function of only $\kappa_c$ (or $\varepsilon_c^p$), as shown in Eq. (D17).

$$D = D_c(\kappa_c) = D_c\left(\varepsilon_c^p\right) \tag{D16}$$

In Abaqus/Stardard, compressive degradation damage variable ($D_c$) and compressive stress ($\sigma_c$) are inputted as a tabular function of a crushing strain ($\varepsilon_c^{in}$). The crushing strain is defined as $\varepsilon_c^{in} = \varepsilon_c - \sigma_c/E_0$ and shown in Fig. D-2. The damage variable ($\kappa_c$), or plastic tensile strain ($\varepsilon_c^p$), is converted from the crushing strain ($\varepsilon_c^{in}$) using Eq. (D17).

$$\varepsilon_c^p = \varepsilon_c^{in} - \frac{D_c}{1 - D_c}\frac{\sigma_c}{E_0} \tag{D17}$$

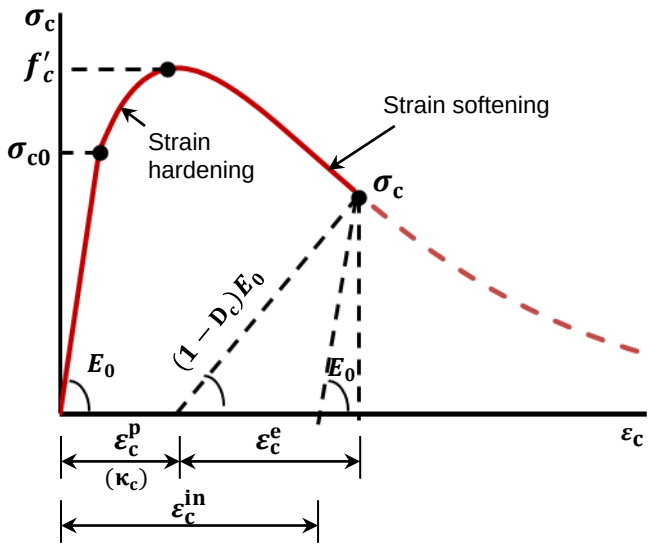


*Fig. D-2: Uniaxial compressive stress and strain relationship*

## D.3 PLASTICITY

### D.3.1 Yield Condition

In Abaqus/Stardard, a yield condition, which is developed by Lee and Fenves[138] to account for different evolution of strength under tension and compression, is used for Concrete Damaged Plasticity model. This yield condition is presented in term of effective stresses ($\bar{\boldsymbol{\sigma}}$) as follows.

$$F(\bar{\boldsymbol{\sigma}}, \boldsymbol{\kappa}) = \frac{1}{1-\alpha}(\bar{q} - 3\alpha\bar{p} + \beta_d(\boldsymbol{\kappa})\langle\bar{\sigma}_{max}\rangle - \gamma_d\langle-\bar{\sigma}_{max}\rangle) - \bar{\sigma}_c(\boldsymbol{\kappa}) \leq 0 \tag{D18}$$

In which $\bar{\mathrm{p}} = -\bar{\boldsymbol{\sigma}}:\boldsymbol{I}/3 = I_1/3 = \xi/\sqrt{3}$ is the effective hyrostatic pressure ($\xi$ is the hyrostatic axis in the principle stress space, Fig. D-3), $\bar{q} = \sqrt{3\bar{\boldsymbol{S}}:\bar{\boldsymbol{S}}/2}$ is the effective Von Mises stress ($\bar{\boldsymbol{S}}$ is the effective deviatoric stress tensor), $\bar{\sigma}_{\max}$ is the maximum principle effective stress ($\bar{\sigma}_i$), $\bar{\sigma}_{\mathbf{c}}(\boldsymbol{\kappa})$ is the effective compressive cohesion stress, and $\alpha$ and $\gamma_{\mathrm{d}}$ are dimensionless material constants.

Function $\beta_{\mathrm{d}}(\boldsymbol{\kappa})$ is given in Eq. (D19), in which $\bar{\sigma}_t(\boldsymbol{\kappa})$ is the effective tensile cohesion stress. For biaxial compression conditions ($\bar{\sigma}_{\max} = 0$), Eq. (D19) becomes to the well-known Drucker-Prager yield condition. The constant $\alpha$ is determined from the initial equibiaxial and uniaxial

compressive yield stresses (e.g., $\bar{\sigma}_1 = 0$ and $\bar{\sigma}_2 = \bar{\sigma}_3 = -\sigma_{b0}$, and $\bar{\sigma}_1 = \bar{\sigma}_3 = 0$ and $\bar{\sigma}_2 = -\sigma_{c0}$, respectively), and it is given in Eq. (D20). Typical experimental values of the ratio $\sigma_{b0}/\sigma_{c0}$ for concrete varies from 1.10 to 1.16, and the constant α is thus in the range from 0.08 to 0.12.

$$\beta_d(\boldsymbol{\kappa}) = \frac{\bar{\sigma}_c(\boldsymbol{\kappa})}{\bar{\sigma}_t(\boldsymbol{\kappa})}(1-\alpha) - (1+\alpha) \qquad (D19)$$

$$\alpha = \frac{\sigma_{b0} - \sigma_{c0}}{2\sigma_{b0} - \sigma_{c0}} \qquad (D20)$$

Constant $\gamma_d$ enters the yield function only for triaxial compression conditions (i.e. $\bar{\sigma}_{max} < 0$), and it is computed from the ratio $K_c$ given in Eq. (D21).

$$K_c = \frac{\bar{q}_{(TM)}}{\bar{q}_{(CM)}} \qquad (D21)$$

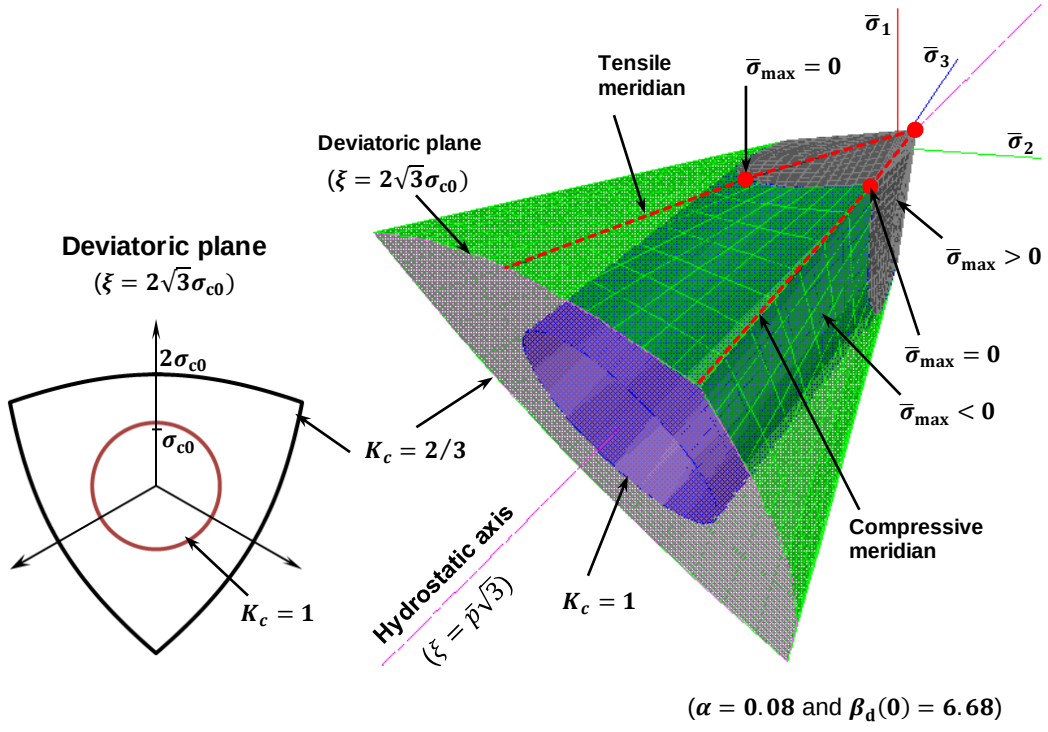


*Fig. D-3: Initial yield surfaces for different values of $K_c$*

In which, $\bar{q}_{(TM)}$ and $\bar{q}_{(CM)}$ are effective Von Mises stresses for the tensile meridian (TM, e.g. $\bar{\sigma}_3 = \bar{\sigma}_2 < \bar{\sigma}_1 = \bar{\sigma}_{max} < 0$) and compressive meridian (CM, e.g. $\bar{\sigma}_3 < \bar{\sigma}_2 = \bar{\sigma}_1 = \bar{\sigma}_{max} < 0$), respectively (Fig. D-3). For any given value of the hydrostatic pressure $\bar{p}$, $K_c$ is given in Eq.

(D22). Solving this equation, $\gamma_d$ is given in Eq. (D23). The typical experimental value of $K_c$ is 2/3, resulting in $\gamma_d = 3$.

$$K_c = \frac{\gamma_d + 3}{2\,\gamma_d + 3} \tag{D22}$$

$$\gamma_d = \frac{3(1 - K_c)}{2\,K_c - 1} \tag{D23}$$

### D.3.2 Flow Rule

Direction of the evolution (rate) of the plastic strain ($\dot{\boldsymbol{\varepsilon}}^p$) is determined using a nonassociated potential flow $G(\bar{\boldsymbol{\sigma}})$,

$$\dot{\boldsymbol{\varepsilon}}^p = \dot{\lambda}\frac{\partial G(\bar{\boldsymbol{\sigma}})}{\partial \bar{\boldsymbol{\sigma}}} \tag{D24}$$

in which $\dot{\lambda}$ is a positive scalar factor of proportionality, which is nonzero only when plastic deformations occur. The potential flow $G(\bar{\boldsymbol{\sigma}})$ is defined as follows.

$$G(\bar{\boldsymbol{\sigma}}) = \sqrt{(\epsilon\sigma_{t0}\tan\psi)^2 + \bar{q}^2} - \bar{p}\tan\psi \tag{D25}$$

In Eq. (D25), $\psi$ is the dilation angle measured in the $\bar{p}$-$\bar{q}$ plane at high confining pressure ($\bar{p}$), $\sigma_{t0}$ is the uniaxial tensile strength, and parameter $\epsilon$, referred to as the eccentricity, is used to define the rate at which the function of the potential G approaches the asymptote. The potential defined in Eq. (D25) is continuous and smooth, thus the flow direction ($\dot{\boldsymbol{\varepsilon}}^p$) is defined uniquely. The default value for $\epsilon$ is 0.1, while $\psi$ is often taken as approximately 30 degrees[101].

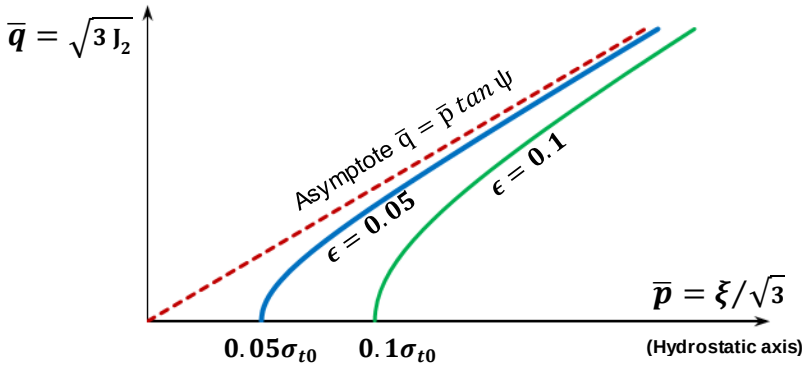


*Fig. D-4: Potential flow $G$ in $\bar{p}$-$\bar{q}$ plane for different values of $\epsilon$*

### D.3.3 Viscoplastic Regularization

In implicit analysis programs, material nonlinearities, including softening behavior and stiffness degradation, and the plastic consistency condition (Eq. D18) often cause severe convergence difficulties, and thus the simulation results are strongly dependent on mess refinement and alignment. Abaqus/Standard overcomes some of these difficulties by embedding a viscoplastic concept (rate-dependent model) in the concrete damaged plasticity model. This concept, which is developed from the Duvault-Lions model, permits a viscoplastic stress ($\boldsymbol{\sigma}_{\upsilon}$) to be outside of the yield surface,

$$\dot{\boldsymbol{\varepsilon}}_{\upsilon}^{p} = \begin{cases} \frac{1}{\mu}\boldsymbol{E}_{\upsilon}^{-\mathbf{1}}\colon(\boldsymbol{\sigma}_{\upsilon} - \boldsymbol{\sigma}^{*}) & If\ F(\boldsymbol{\sigma}_{\upsilon}, \boldsymbol{\kappa}) > 0 \\ 0 & otherwise \end{cases} \tag{D26}$$

in which $\dot{\boldsymbol{\varepsilon}}_{\upsilon}^{\mathrm{p}}$ is a viscoplastic strain rate tensor, $\mu$ is a viscosity parameter representing the relaxation time ($\tau$) of the viscoplastic system, and $\mathbf{E}_{\upsilon}$ is a viscoplastic stiffness given in Eq. (D27), which is a function of a viscous stiffness degradation variable ($\mathrm{D}_{\mathrm{v}}$). Stress $\boldsymbol{\sigma}_{\upsilon}$ in Eq. (D26) is a stress of viscoplastic system, and $\boldsymbol{\sigma}^{*}$ is defined to be a function of the stress computed from the rate-independent backbone model (damaged plasticity model presented in Sections D.3.1 and D.3.2) for the current strain $\boldsymbol{\varepsilon}$. The stresses $\boldsymbol{\sigma}_{\upsilon}$ and $\boldsymbol{\sigma}^{*}$ are given in Eqs. (D28) and (D29), respectively.

$$\boldsymbol{E}_{\upsilon} = (1 - D_{v})\boldsymbol{E}_{0} \tag{D27}$$

$$\boldsymbol{\sigma}_{\upsilon} = (1 - D_{v})\boldsymbol{E}_{0}\colon\left(\boldsymbol{\varepsilon} - \boldsymbol{\varepsilon}_{\upsilon}^{p}\right) \tag{D28}$$

$$\boldsymbol{\sigma}^{*} = (1 - D_{v})\overline{\boldsymbol{\sigma}} \tag{D29}$$

$$\overline{\boldsymbol{\sigma}} = \boldsymbol{E}_{0}\colon(\boldsymbol{\varepsilon} - \boldsymbol{\varepsilon}^{p}) \tag{D7a}$$

Substituting Eqs. (D28) and (D29) into Eq. (D26) and using $\overline{\boldsymbol{\sigma}}$ from Eq. (D7a) lead to Eq. (D30), an expression for the viscoplastic strain rate ($\dot{\boldsymbol{\varepsilon}}_{\upsilon}^{\mathrm{p}}$). The rate of the viscous stiffness degradation variable ($\dot{\mathrm{D}}_{\mathrm{v}}$) is defined similarly to Eq. (D30) and given in Eq. (D31). Eqs. (D28), (D30), and (D31) transform the concrete damaged plasticity model presented in previous sections into a viscoplastic model.

$$\dot{\boldsymbol{\varepsilon}}_v^p = \begin{cases} \frac{1}{\mu}(\boldsymbol{\varepsilon}^p - \boldsymbol{\varepsilon}_v^p) & If\ F(\boldsymbol{\sigma}_v, \boldsymbol{\kappa}) > 0 \\ 0 & \text{otherwise} \end{cases} \quad (D30)$$

$$\dot{D}_v = \begin{cases} \frac{1}{\mu}(D - D_v) & If\ F(\boldsymbol{\sigma}_v, \boldsymbol{\kappa}) > 0 \\ 0 & \text{otherwise} \end{cases} \quad (D31)$$

For each increment in an incremental approach, results obtained using the viscoplastic model can represent the results obtained using the inviscid model if the time relaxation parameter ($\tau$) defined in the former model is selected appropriately. Fig. D-5 presents the effect of $\tau$ on the solution of the viscoplastic model. For an increment $i$ with a time step of $\Delta t_i$, if an incremental strain ($\Delta\varepsilon_i$) is hold constantly, the stress ($\sigma_{vi}$) will reduce exponentially (stress relaxation) with time to $\boldsymbol{\sigma}^*$, which is computed from the inviscid model. Fig. D-5 shows the stress decreases more quickly as the time relaxation decreases, and thus the stress can be assumed to be close to the yield surface at the end of the increment $i$ if the ratio $\tau/\Delta t_i$ is small enough. In Abaqus/Standard, the time relaxation is set through the viscosity parameter ($\mu$). Lee and Fenves[101], based on their numerical study of reinforced concrete structures, suggested that $\mu$ may be set to 15 percent of the time step ($\Delta t_i$). The default value for the viscosity parameter ($\mu$) is set equal to 0 in Abaqus/Standard.

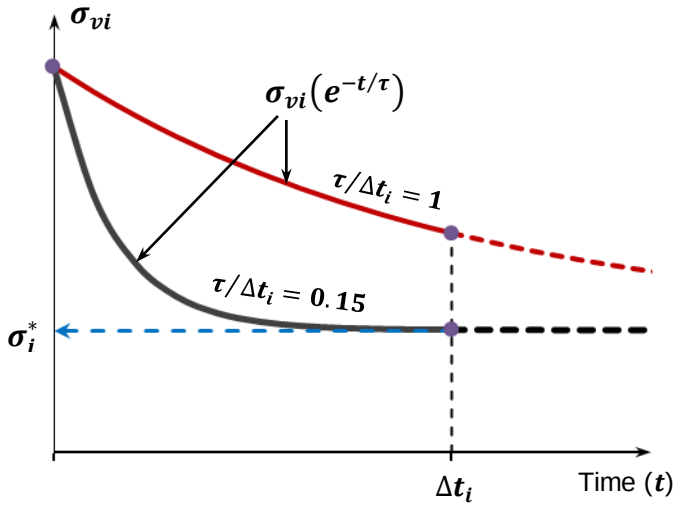


*Fig. D-5: Effect of the time relaxation parameter($\tau$)*

# REFERENCES


1. Sozen, M.A. and C.P. Siess. *Investigation of multiple panel reinforced concrete floor slabs*. in *ACI Journal Proceedings*. 1963. ACI.
2. Gasparini, D., *Contributions of C. A. P. Turner to Development of Reinforced Concrete Flat Slabs 1905–1909.* Journal of Structural Engineering, 2002. **128**(10): p. 1243-1252.
3. Wight, J.K., *Reinforced Concrete: Mechanics and Design*. 7 th. ed. 2015: Prentice Hall.
4. Naaman, A.E., *Prestressed concrete analysis and design: fundamentals*. 2004: Techno Press 3000.
5. ACI 318, *Building Code Requirements for Structural Concrete and Commentary*. 2014, Reported by ACI Committe 318. American Concrete Institute, Detroit, Michigan.
6. Eurocode 2, *Design of concrete structures*. 2004: BS EN 1992-1-1:2004.
7. CAN/CSA A23.3, *Design of concrete structures*. 2014, Canadian Standards Association.
8. ACI-ASCE Committee 426, *The Shear Strength of Reinforced Concrete Members - Slabs.* Journal of the Structural Division, 1974. **100**(ST8): p. 50.
9. Dam, T.X., J.K. Wight, and G. Parra-Montesinos, *Behavior of Monotonically-loaded Slab-Column Connections with Shear Studs.* ACI structural Journal, 2016. **(Accepted)**.
10. Wood, J.G., *Pipers row car park collapse: Identifying risk.* Concrete, 2003. **37**(9).
11. Wilkinson, S., et al., *Observations and implications of damage from the magnitude Mw 6.3 Christchurch, New Zealand earthquake of 22 February 2011.* Bulletin of Earthquake Engineering, 2013. **11**(1): p. 107-140.
12. Langohr, P.H., A. Ghali, and W.H. Dilger, *Special Shear Reinforcement for Concrete Flat Plates*, in *ACI Journal Proceedings*. 1976, ACI.
13. Mokhtar, A.S., A. Ghali, and W. Dilger, *Stud shear reinforcement for flat concrete plates*, in *ACI Journal Proceedings*. 1985, ACI.
14. Decon USA. *North American manufacturer of Studrails®*. Available from: http://www.deconusa.com/en/.
15. Birkle, G. and W. Dilger, *Shear Strength of Slabs with Double-Headed Shear Studs in Radial and Orthogonal Layouts.* ACI Special Publication, 2009. **265**.
16. Ferreira, M.P., G.S. Melo, P.E. Regan, and R.L. Vollum, *Punching of Reinforced Concrete Flat Slabs with Double-Headed Shear Reinforcement.* ACI Structural Journal, 2014. **111**(1-6).
17. Broms, C.E., *Ductility of flat plates: Comparison of shear reinforcement systems.* ACI structural Journal, 2007. **104**(6).

18. Post, N.M., *Tests Show Premature Failure of Shear-Stud Reinforcement*, in *Engineering News-Record*. 2011.

19. ABAQUS 6.13, *ABAQUS Analysis User's Guide Version 6.13, Hibbitt, Karlsson and Sorensen*. http://50.16.176.52/v6.13/books/usb/default.php.

20. CEB-FIB Bulletin 12, *Punching of Structural Concrete Slabs*, ed. S. Kinnunen. Vol. 12. 2001: FIB-Féd. Int. du Béton.

21. Timoshenko, S. and S. Woinowsky-Krieger, *Theory of plates and shells*. Vol. 2. 1959: McGraw-hill New York.

22. Broms, C.E., *Tangential Strain Theory for Punching Failure of Flat Slabs.* ACI Structural Journal, 2016. **113**(1): p. 95.

23. The Joint Committee on Concrete and Reinforced Concrete, *Report on Concrete and Reinforced Concrete, Revised at the Meeting of the Joint Committee on Concrete and Reinforced Concrete, November 20, 1912*, in *Proceedings, American Society for Testing Materials*. 1912. p. 224-273.

24. Moe, J., *Shearing strength of reinforced concrete slabs and footings under concentrated loads*. 1961: Portland Cement Association, Research and Development Laboratories.

25. Joint Committee of 1916, *Report of the Committee on Reinforced Concrete Building Laws*, in *Proceedings,American Concrete Institute, 12, 171-180*. 1916.

26. ACI Standard Specifications. *No. 23, "Standard Building Regulations for the Use of Reinforced Concrete,"*. in *ACI JOURNAL, Proceedings*. 1920.

27. Joint Committee on Concrete and Reinforced Concrete, *Final Report of the Joint Committee on Concrete and Reinforced Concrete,.* Proceedings, American Society for Testing Materials, 1917. **17**(Part I): p. 202-262

28. Joint Committee of 1924, *Standard Specifications for Concrete and Reinforced Concrete.* , in *Proceedings, American Sociey for Testing Materials*. 1924. p. 312-385.

29. ACI 318, *Building Regulations for Reinforced Concrete*. 1941, Reported by ACI Committe 318. American Concrete Institute, Detroit, Michigan. p. 913-986.

30. ACI 318, *Building code requirements for reinforced concrete*. 1947, Reported by ACI Committe 318. American Concrete Institute, Detroit, Michigan: Detroit.

31. ACI 318, *Building code requirements for reinforced concrete*. 1951, Reported by ACI Committe 318. American Concrete Institute, Detroit, Michigan: Detroit.

32. ACI 318, *ACI Standards, Building Code Requirements for Reinforced Concrete.* Proceedings, Journal of the American Concrete Institute., 1956. **52**: p. 913-986.

33. ACI-ASCE Committee 326, *Shear and Diagonal Tension: Report of ACI-ASCE Committee 326*, ed. A.C.I. Shear Diagonal Tension, American Society of Civil Engineers. 1962: American Society of Civil Engineers.

34. ACI 318, *Building code requirements for reinforced concrete (ACI 318-63)*, in *ACI publications ; 318-63*. 1963, Reported by ACI Committe 318. American Concrete Institute, Detroit, Michigan: Detroit, Mich. p. 144 p.

35. ACI 318, *Building code requirements for reinforced concrete*. 1971, Reported by ACI Committe 318. American Concrete Institute, Detroit, Michigan: Detroit. p. 78 p.

36. ACI 318, *Building code requirements for reinforced concrete*. 1977, Reported by ACI Committe 318. American Concrete Institute, Detroit, Michigan: Detroit. p. 78 p.

37. ACI 318, *Building code requirements for reinforced concrete*. 1989, Reported by ACI Committe 318. American Concrete Institute, Detroit, Michigan: Detroit.

38. Vanderbilt, M.D., *Shear strength of continuous plates.* Journal of the Structural Division, 1972. **98**(5): p. 961-973.

39. Hawkins, N.M., *Shear Strength of Slabs with Shear Reinforcement.* ACI Special publication, 1974(SP 42-34).

40. Polak, M., E. El-Salakawy, and N. Hammill, *Shear reinforcement for concrete flat slabs.* ACI Special Publication, 2005. **232**.

41. ACI 318, *Building Code Requirements for Structural Concrete And Commentary*. 2008, Reported by ACI Committe 318. American Concrete Institute, Detroit, Michigan.

42. Corley, W.G. and N.M. Hawkins. *Shearhead reinforcement for slabs*. 1968. ACI.

43. ACI 421.1R-99, *Guide to Shear Reinforcement for Slabs*. 1999, The American Concrete Institute.

44. ACI 421.1R-08, *Guide to Shear Reinforcement for Slabs*. 2008, American Concrete Insitute.

45. Seible, F., A. Ghali, and W.H. Dilger, *Preassembled shear reinforcing units for flat plates*, in *ACI Journal Proceedings*. 1980, ACI.

46. Voet, A.F.V.D., W.H. Dilger, and A. Ghali, *Concrete flat plates with well-anchored shear reinforcement elements.* Canadian Journal of Civil Engineering, 1982. **9**(1): p. 107-114.

47. Dilger, W., *Flat slab–column connections.* Progress in Structural Engineering and Materials, 2000. **2**(3): p. 386-399.

48. Bu, W. and M.A. Polak, *Effect of openings and shear bolt pattern in seismic retrofit of reinforced concrete slab–column connections.* Engineering Structures, 2011. **33**(12): p. 3329-3340.

49. Gomes, R. and P. Regan, *Punching strength of slabs reinforced for shear with offcuts of rolled steel I-section beams.* Magazine of Concrete Research, 1999. **51**(2): p. 121-129.

50. Carvalho, A.L., G.S. Melo, R.B. Gomes, and P.E. Regan, *Punching shear in post-tensioned flat slabs with stud rail shear reinforcement.* ACI Structural Journal, 2011. **108**(5).

51. Cheng, M.-Y. and G.J. Parra-Montesinos, *punching shear strength and deformation capacity of fiber reinforced concrete slab-column connections under earthquake-type loading.* 2009. **UMCEE 09-01**.

52. Hognestad, E. *Shearing strength of reinforced concrete column footings*. in *ACI Journal, Proceedings*. 1953. ACI.

53. Richart, F.E. *Reinforced concrete wall and column footings*. in *ACI Journal Proceedings*. 1948. ACI.

54. Johansen, K.W., *Yield-line theory*. 1962: Cement and Concrete Association.

55. Hawkins, N., M. Criswell, and F. Roll, *Shear strength of slabs without shear reinforcement.* ACI Special Publication, 1974. **42**.

56. Ospina, C.E., G. Birkle, and Widianto. *Databank of Concentric Punching Shear Tests of Two-Way Concrete Slabs without Shear Reinforcement at Interior Supports*. in *Structures Congress 2012*. 2012. ASCE.

57. Hatcher, D.S., M.A. Sozen, and C.P. Siess, *A study of tests on a flat plate and a flat slab*. 1961, University of Illinois Engineering Experiment Station. College of Engineering. University of Illinois at Urbana-Champaign.

58. Guralnick, S.A. and R.W. La Fraugh. *Laboratory study of a 45-foot square flat plate structure*. in *ACI Journal Proceedings*. 1963. ACI.

59. Sherif, A., *Relation Between Structure and Test Set-up*, in *Punching of Structural Concrete Slab, Fédération Internationale du Béton, Comite Euro-International du Beton. Bulletin 12. Technical Report.* 2001.

60. Elstner, R.C. and E. Hognestad. *Shearing strength of reinforced concrete slabs*. 1956. ACI.

61. Birkle, G. and W.H. Dilger, *Influence of slab thickness on punching shear strength.* ACI structural Journal, 2008. **105**(2).

62. Rankin, G. and A. Long. *PREDICTING THE ENHANCED PUNCHING STRENGTH OF INTERIOR SLAB-COLUMN CONNECTIONS*. in *ICE Proceedings*. 1987. Thomas Telford.

63. Model Code 90, *Design of concrete structures.* CEB-FIP Model Code 90. British Standard Institution, London, UK, 1993.

64. Marzouk, H. and A. Hussein, *Experimental investigation on the behavior of high-strength concrete slabs.* ACI structural Journal, 1992. **88**(6).

65. Sherif, A. and W. Dilger, *Punching failure of a full scale high strength concrete flat slab.* Trita-BKN. Bulletin, 2000. **57**: p. 235-243.

66. Wight, J.K. and J.G. MacGregor, *Reinforced Concrete: Mechanics and Design*. 6th ed. 2011: Prentice Hall.

67. Guandalini, S. and A. Muttoni, *Punching Tests on Concrete Slabs without Shear Reinforcement.* Swiss Federal Institute of Technology, Lausanne, Switzerland., 2004: p. 129.

68. Regan, P.E., *Behaviour of reinforced concrete flat slabs*. 1981: Construction Inudstry Research and Information Association.

69. Bazant, Z.P. and Z. Cao, *Size effect in punching shear failure of slabs.* ACI structural Journal, 1987. **84**(1).

70. Sherif, A.G. and W.H. Dilger, *Critical review of the CSA A23. 3-94 punching shear strength provisions for interior columns.* Canadian Journal of Civil Engineering, 1996. **23**(5): p. 998-1011.

71. Alexander, S.D. and S.H. Simmonds, *Tests of column-flat plate connections.* ACI structural Journal, 1992. **89**(5).

72. Braestrup, M.W., *Central Punching of Reinforced Concrete Slabs.* Comite Euro International du Beton Bulletin d'information 1995. **No 223, June**: p. 233-243.

73. Regan, P.E. and M.W. Bræstrup, *Punching Shear in Reinforced Concrete: A State of Art Report. Bulletin D'information No. 168*. [Contribution À la 24e Session Plenière Du CEB, Rotterdam, Juin 1985]. 1985: CEB, Comité Euro-International du Béton.

74. Gardner, N., *Relationship of the punching shear capacity of reinforced concrete slabs with concrete strength.* ACI structural Journal, 1990. **87**(1).

75. Einpaul, J., J. Bujnak, M.F. Ruiz, and A. Muttoni, *Study on Influence of Column Size and Slab Slenderness on Punching Strength.* ACI Structural Journal, 2016. **113**(1): p. 135.

76. Ngo, D. and A. Scordelis. *Finite element analysis of reinforced concrete beams*. in *ACI Journal Proceedings*. 1967. ACI.

77. Hueste, M.B.D. and J.K. Wight, *Nonlinear punching shear failure model for interior slab-column connections.* Journal of Structural Engineering, 1999. **125**(9): p. 997-1008.

78. Tian, Y., *Behavior And Modeling of Reinforced Concrete Slab-column Connections*. 2007, The University of Texas at Austin.

79. Menetrey, P., *Numerical analysis of punching failure in reinforced concrete structures*. 1994, École Polytechnique Fédérale de Lausanne.

80. Kinnunen, S. and H. Nylander, *Punching of concrete slabs without shear reinforcement*. 1960, Meddelande No. 38, Institution foKr Byggnadsstatik, Kungliga Tekniska HoKgskolan, Stockholm: Elander.

81. Menetrey, P. and K. Willam, *Triaxial failure criterion for concrete and its generalization.* ACI structural Journal, 1995. **92**(3): p. 311-318.

82. De Borst, R. and P. Nauta, *Non-orthogonal cracks in a smeared finite element model.* Engineering Computations, 1985. **2**(1): p. 35-46.

83. Vidosa, F.G., M.D. Kotsovos, and M.N. Pavlovic, *Symmetrical Punching of Reinforced Concrete Slabs: An Analytical Investigation Based on Nonlinear Finite Element Modeling.* ACI Structural Journal, 1988. **85**(3): p. 241-250.

84. Kheyroddin, A., S.H. Vaez, and H. Naderpour, *INVESTIGATION OF FINITE ELEMENT MODEL OF SLAB COLUMN CONNECTIONS UNDER ECCENTRIC LOAD*, in *The 14th World Conference on Earthquake Engineering*. 2008: Beijing, China.

85. Hallgren, M. and M. Bjerke, *Non-linear finite element analyses of punching shear failure of column footings.* Cement and Concrete Composites, 2002. **24**(6): p. 491-496.

86. Polak, M.A., *Modeling punching shear of reinforced concrete slabs using layered finite elements.* ACI structural Journal, 1998. **95**(1).

87. Hand, F.R., D.A. Pecknold, and W.C. Schnobrich, *Nonlinear layered analysis of RC plates and shells.* Journal of the structural division, 1973. **99**(7): p. 1491-1505.

88. Jofriet, J.C. and G.M. McNeice, *Finite element analysis of reinforced concrete slabs.* journal of the structural division, 1971. **97**(3): p. 785-806.

89. Lin, C.-S. and A.C. Scordelis, *Nonlinear analysis of RC shells of general form.* Journal of the Structural Division, 1975. **101**(3): p. 523-538.

90. Scordelis, A. and E. Chan, *Nonlinear analysis of reinforced concrete shells.* Special Publication, 1987. **98**: p. 25-58.

91. Hu, H.-T. and W. Schnobrich, *Nonlinear finite element analysis of reinforced concrete plates and shells under monotonic loading.* Computers & Structures, 1991. **38**(5): p. 637-651.

92. Di, S. and Y. Cheung, *Nonlinear analysis of RC shell structures using laminated element. II.* Journal of Structural Engineering, 1993. **119**(7): p. 2074-2094.

93. Phuvoravan, K., *A finite element for the nonlinear analysis of reinforced concrete slabs*. 2003, Purdue University.

94. MINDLIN, R., *Influence of rotary inertia and shear on flexural motions of isotropic, elastic plates.* J. of Appl. Mech., 1951. **18**: p. 31-38.

95. Yamada, T., A. Nanni, and K. Endo, *Punching shear resistance of flat slabs: Influence of reinforcement type and ratio.* ACI Structural Journal, 1992. **89**: p. 555-555.

96. Marzouk, H. and Z. Chen, *Finite element analysis of high-strength concrete slabs.* ACI Structural Journal, 1993. **90**(5).

97. Xiao, R. and T. O'Flaherty, *Finite-element analysis of tested concrete connections.* Computers & Structures, 2000. **78**(1): p. 247-255.

98. Kheyroddin, A., S. Hoseini Vaez, and H. Naderpour, *Numerical Analysis of Slab-Column Connections Strengthened with Carbon Fiber Reinforced Polymers.* Journal of Applied Sciences, 2008. **8**(3).

99. Winkler, K. and F. Stangenberg. *Numerical Analysis of Punching Shear Failure of Reinforced Concrete Slabs*. in *Proceedings of the ABAQUS User's Conference, Newport, RI. Dassault Systemes, USA, Lowell, MA*. 2008.

100. Lubliner, J., J. Oliver, S. Oller, and E. Oñate, *A plastic-damage model for concrete.* International Journal of Solids and Structures, 1989. **25**(3): p. 299-326.

101. Lee, J. and G.L. Fenves, *A plastic-damage concrete model for earthquake analysis of dams.* Earthquake engineering & structural dynamics, 1998. **27**(9): p. 937-956.

102. Model Code 2010, *Fédération Internationale du Béton Model Code for Concrete Structures 2010.* . 2013: Wiley.

103. Hordijk, D.A., *Tensile and tensile fatigue behaviour of concrete; experiments, modelling and analyses.* Heron, 1992. **37**(1).

104. Li, K.K.L., *Influence of size on punching shear strength of concrete slabs*, in *McGill University, Montreal, Canada*. 2000.

105. Xiao, R. and C. Chin, *Flat Slabs at Slab-Column Connection: Nonlinear Finite Element Modelling and Punching Shear Capacity Design Criterion.* Advances in Structural Engineering, 2007. **10**(5): p. 567-579.

106. Malvar, L., *Punching shear failure of a reinforced concrete pier deck model.* ACI Structural Journal, 1992. **89**(5).

107. Wosatko, A., J. Pamin, and A.M. Polak. *Comparison of simulation results for 3D punching shear problem*. in *Recent Advances in Computational Mechanics*. 2014. CRC Press.

108. Adetifa, B. and M.A. Polak, *Retrofit of slab column interior connections using shear bolts.* ACI structural journal, 2005. **102**(2).

109. Genikomsou, A. and M. Polak. *Finite Element Analysis of a Reinforced Concrete Slab-Column Connection using ABAQUS*. in *Structures Congress 2014*. 2014. ASCE.

110. Genikomsou, A.S. and M.A. Polak, *Finite element analysis of punching shear of concrete slabs using damaged plasticity model in ABAQUS.* Engineering Structures, 2015. **98**: p. 38-48.

111. Yan, P.Y., *Behaviour of shearhead system between flat reinforced concrete slab and steel tubular column*, in *Faculty of Engineering and Physical Sciences, School Of Mechanical, Aerospace And Civil Engineering*. 2011, The University of Manchester.

112. Genikomsou, A., G. Balomenos, and M. Polak. *FEA of flat slabs retrofitted with shear bolts*. in *Presented in Session of Research in Progress. The ACI Fall 2014 Convention at Washington, D.C. USA*. 2014.

113. ASTM A615, *Standard Specification for Deformed and Plain Carbon-Steel Bars for Concrete Reinforcement.* Annual book of ASTM standards, 2015. **3**: p. 57-72.

114. ASTM A29, *Standard Specification for General Requirements for Steel Bars, Carbon and Alloy, Hot-Wrought*. 2015, American Society for Testing and Materials (ASTM).

115. ASTM A1044, *Standard Specification for Steel Stud Assemblies for Shear Reinforcement of Concrete*. 2010, American Society for Testing and Materials (ASTM).

116. Doan Companies.

117. ACI 211.1-91, *Standard Practice for Selecting Proportions for Normal, Heavyweight, and Mass Concrete*. 2002.

118. ASTM C39, *Standard Test Method for Compressive Strength of Cylindrical Concrete Specimens.* 2014.

119. ASTM C496, *Standard Test Method for Splitting Tensile Strength of Cylindrical Concrete Specimens*. 2011, American Society for Testing and Materials (ASTM).

120. ASTM-C78, *C78 / C78M - 10e1 Standard Test Method for Flexural Strength of Concrete (Using Simple Beam with Third-Point Loading).* ASTM International, 2013.

121. Barnsco Michigan. p. 975 Ladd Rd. Walled Lake, MI 48390. Phone: (248) 668-1010.

122. ASTM E8, *Standard Test Methods for Tension Testing of Metallic Materials.* Annual book of ASTM standards, 2004. **3**: p. 57-72.

123. NDI Measurement Sciences. Available from: http://www.ndigital.com/msci/products/optotrak-certus/.

124. Dam, T.X. and J.K. Wight, *Flexurally-Triggered Punching Shear Failure of Reinforced Concrete Slab-Column Connections Reinforced with Headed Shear Studs Arranged in Orthogonal and Radial Layout.* Engineering Structures, 2015. **110**: p. 258-268.

125. Lips, S., M.F. Ruiz, and A. Muttoni, *Experimental Investigation on Punching Strength and Deformation.* ACI structural Journal, 2012. **109**(6): p. 889-900.

126. Ruiz, M.F. and A. Muttoni, *Applications of Critical Shear Crack Theory to Punching of Reinforced Concrete Slabs with Transverse Reinforcement.* ACI Structural Journal, 2009. **106**(4).

127. Regan, P. and F. Samadian, *Shear Reinforcement against punching in reinforced concrete flat slabs.* Structural Engineer, 2001. **79**(10).

128. Peiris, C. and A. Ghali, *Flexural reinforcement essential for punching shear resistance of slabs.* ACI Special Publication, 2012. **287**.

129. Birkle, G., *Punching of Flat Slabs: The Influence of Slab Thickness and Stud Layout*. 2004, Department of Civil Engineering, University of Calgary, Calgary, AB, Canada.

130. Beutel, R., *Punching of Flat Slabs with Shear Reinforcement at Inner Columns.* Rheinisch-Westfälischen Technischen Hochschule Aachen, Aachen, Germany, 2002.

131. Stein, T., A. Ghali, and W. Dilger, *Distinction between punching and flexural failure modes of flat plates.* ACI Structural Journal, 2007. **104**(3).

132. Pan, A. and J.P. Moehle, *Lateral displacement ductility of reinforced concrete flat plates.* ACI Structural Journal, 1989. **86**(3).

133. Widianto, O.B. and J.O. Jirsa, *Two-way shear strength of slab-column connections: Reexamination of ACI 318 provisions.* ACI Structural Journal, 2009. **106**(2).

134. Guandalini, S., O.L. Burdet, and A. Muttoni, *Punching tests of slabs with low reinforcement ratios.* ACI structural Journal, 2009. **106**(1): p. 87-95.

135. 352.1R-11, *Guide for Design of Slab-Column Connections in Monolithic Concrete Structures*. 2011, The American Concrete Institute: Farmington Hills, Michigan, USA.

136. Mitchell, D. and W.D. Cook, *Preventing progressive collapse of slab structures.* Journal of Structural Engineering, 1984.

137. Hawkins, N.M. and D. Mitchell. *Progressive collapse of flat plate structures*. in *ACI Journal Proceedings*. 1979. ACI.

138. Lee, J. and G. Fenves, *Plastic-Damage Model for Cyclic Loading of Concrete Structures.* Journal of Engineering Mechanics, 1998. **124**(8): p. 892-900.

139. Hillerborg, A., M. Modéer, and P.-E. Petersson, *Analysis of crack formation and crack growth in concrete by means of fracture mechanics and finite elements.* Cement and concrete research, 1976. **6**(6): p. 773-781.

140. Chen, W.-F. and D.-J. Han, *Plasticity for structural engineers*. 2007: J. Ross Publishing.

141. Oller, S., *Nonlinear dynamics of structures*. 2014: Springer.

142. Vermeer, P.A. and R. De Borst, *Non-associated plasticity for soils, concrete and rock.* HERON, 29 (3), 1984, 1984.

143. Kupfer, H., H.K. Hilsdorf, and H. Rusch. *Behavior of concrete under biaxial stresses*. 1969. ACI.

144. McGuire, W., R.H. Gallagher, and R.D. Ziemian, *Matrix structural analysis*. 2000.

145. Hognestad, E. *Yield-line theory for the ultimate flexural strength of reinforced concrete slabs*. in *ACI Journal Proceedings*. 1953. ACI.

146. Mayes, G.T., M.A. Sozen, and C.P. Seiss, *Tests on a quarter scale model of a multiple-panel reinforced concrete flat plate floor*. 1959: University of Illinois.